MULTIDIMENSIONAL HYBRID NANOMATERIALS FOR ADVANCED THERAGNOSTIC APPLICATIONS

By

LETAO YANG

A dissertation submitted to the

School of Graduate Studies

Rutgers, The State University of New Jersey

In partial fulfillment of the requirements

For the degree of

Doctor of Philosophy

Graduate Program in Chemistry and Chemical Biology

Written under the direction of

Ki-Bum Lee

And approved by

_____

_____

_____

_____

New Brunswick, New Jersey

January 2019

ABSTRACT OF THE DISSERTATION

Multidimensional Hybrid Nanomaterials for Advanced Theragnostic Applications

By LETAO YANG

Dissertation Director:
Prof. Ki-Bum Lee

Nanomedicine is a multidisciplinary field that develops and translate biologically functionalized nanomaterials for the treatment or diagnosis of injuries and diseases. Taking advantage of the high surface-to-volume ratio and the unique physicochemical properties of nanomaterials, nanomedicine has shown great potential for many clinical theragnostic applications. In this dissertation, to further advance nanomaterials-based medical applications, multidimensional hybrid nanomaterials were developed by addressing the critical challenges of current nanotherapeutics. For cancer treatment, 0D-2D hybrid nanomaterials were synthesized and applied for the photothermal therapy-based cancer ablation by combining the surface property of 2D nanomaterials and the optical properties of plasmonic and carbon nanomaterial. To address the slow- or non-biodegradability of 2D carbon nanomaterials, 3D nanoscaffolds assembled from MnO_2-based 2D nanomaterials were designed and synthesized for stem cell therapy. By further developing a 1D-2D hybrid nanostructure, highly sensitive biosensing platform was also fabricated using graphene and gold nanoarrays. Lastly, a method to high throughput print 0D, 1D and 2D nanostructures in a single platform was developed for providing quantitative design principles of

nanomaterials-based medical applications. Collectively, by showcasing the design and synthesis of multidimensional nanomaterials for theragnostic applications, this dissertation is aimed to provide useful insights for the next generation precision and personalized medicine based on hybrid nanomaterials.

ACKNOWLEDGEMENTS

First, I would like to thank the alumni and members of KBLee group, not only for the scientific collaborations but also for the inspiring discussions. Dr. Aniruddh Solanki's question on "can we make graphene mesh" guide me through my rotation. Dr. Shreyas Shah's question on "can you make degradable graphene" led to the development of MnO_2 nanoscaffolds. Dr. Tae-Hyung Kim and Dr. Jinping Lai mentored me differently, by directly involving me in the project and taught me how to handle projects. I also feel lucky to have worked with Dr. Perry Yin, whose advices are always sharp and to the point. I'm grateful to Dr. Birju Shah to manage the lab so well and Dr. Sahishnu Patel for his motivational talks. It has also been a great time to work with An, Tian, Dr. Prasad, Dr. Pasquale and Dr. Yea. To our current group members, I want to give special thanks to Dr. Dean Chueng, who is always willing to help and always helped, and Yixiao Zhang, who brought so many enjoyable moments and encouragement to my Ph.D. life. Dr. Hyeon-Yeol Cho, Dr. Jin-Ho Lee and Dr. Jin-Ha Choi, who has given me a lot of advice, helped me with experiments and generously involved me in their exciting projects. It's an invaluable experience to work with these super postdocs. Christopher Rathnam, Thanapat Pongkulapa, Brian Conley and Hudifah Rabie, who are my excellent collaborators, I'm grateful for their hardworking and valuable insights. I also want to thank Shenqiang Wang, Jeffery Luo, Shaivin Patel, Brandon Conklin, Skylar Chuang, and Yannan Hou for their strong support for developing the projects with me.

It is Prof. Ki-Bum Lee established such a great group culture that I'm lucky to have worked with so many great scientists. I'm also very grateful to Prof. Lee for his great patience, his encouragement on highly risky projects, the invaluable insights into the experiments and

his strong support in collaboration outside the field of chemistry. It is because of Prof. Lee that I'm trained to have an organized scientific structure, proper scientific communication abilities and the big picture in chemistry, and also gain perspectives from multiple disciplines. None of my achievements in my Ph.D. studies will be possible without him and his advice have shaped many of my philosophies for my life and research. Here I would like to express my most appreciation for all his help, support and guidance.

I want to thank my committee members, Prof. Jing Li and Prof. Eric Garfunkel for their advice in the annual meetings and qualifications. Many of the comments, even the out-field-research-presentation that is five years ago, I still remember clearly. These comments taught me how to be a good scientist and will be invaluable experiences to my scientific career.

I want to acknowledge my collaborators outside of KBLee lab, who provided not only tremendous help on my project but also new perspectives from different fields. I want to thank Prof. Li Cai, who is also my committee member, and his students, Dr. Ying Li and Misaal Patel for their help and suggestions on the animal experiments. It is a great pleasure to work with Prof. Cai's group and I learned a lot in spinal cord injury surgeries and histological analysis. I want to thank Prof. Jae K. Lee from the University of Miami for introducing many interesting aspects of neuroscience and supporting the scaffold transplantation work. Prof. Wise Young also generously allowed me to get training for the spinal cord injury workshop and I'm also grateful to Prof. Sun and Dr. Xiaowen Qiu from Prof. Young's lab for generously testing the hydrogel and cell transplantation for me. Dr. Jong-Min Lee and Prof. Bong Geun Chung for their great help on design the microfluidics and teaching me the spheroids fabrication for the cancer photothermal therapy. Lastly, I

want to gratefully thank Prof. Lu Wang and Dr. Gangotri Dey for the great help on the DFT simulation studies. It is such an exciting experience to see how the computational and experimental work support and guide each other.

Lastly, I want to thank my family for their love and support. My family has given me incredible support and freedom to pursue whatever I feel enthusiastic. Without such strong support, I would not be able to focus and finish my Ph.D. study. It is never possible to say enough thanks to my family and return the support and love they give me. However, I hope I can develop strong science to make their dedication more worthwhile.

Table of Contents

List of Figures

List of Tables

Chapter 1: Introduction

1.1 Current progress in nanomedicine

1.1.1 What is nanomedicine

In the past three decades, nanotechnology has revolutionized many fields of biology and medicine[2-5]. More specifically, the design, functionalization, and utilization of materials to provide solutions for biomedical applications now have been termed as nanomedicine[6]. In general, nanomedicine has impacted broad areas of disease treatment and the way how people understand biology. So far, nanomedicine has been mostly associated with the formulations of pharmaceutics for the drug delivery or diagnosis[7-9]. More recently, broader areas of nanomedicine such as biosensing, drug delivery, regenerative medicine and smart therapeutics have been established[6]. Taking advantages of the unique physical properties of nanomaterials and large surface-to-area ratios, now people can detect pathogens in complex biological samples down to the femtomolar, attomolar level or even at the single molecular level[10-15]. By engineering the composition, size, shape and surface of nanomaterials, nanoparticle-based drug delivery systems (DDS) can successfully control the drug distribution in the sites of action precisely in a spatiotemporal controlled manner[2,7,16,17]. The nanoengineered matrix can also direct the stem cell fates to specific lineages by simply modulating the mechanical, optical, electrical, topographical and other physical properties through pathways such as integrin-mediated mechanotransduction[18-23]. More recently, as nanoparticles are typically within similar size ranges of many biological units and objects such as proteins, virus, sugars and extracellular matrix, scientists have also developed a variety of smart nanotherapeutics to mimic the natural biological units for

specific control over cellular behaviors[24-28]. These new biomedical fields enabled by nanomaterials have dramatically influenced translational medicine and the way how people understand diseases and injuries.

1.1.2 How does nanomedicine work?

In general, the ability of nanomaterials performs fantastically in the complex systems of disease and injury treatment and biological sensing often originates from their unique physical, chemical and biological properties at the nanometer scale[5,6,29]. These physical, chemical and biological properties can manipulate or detect cellular behaviors by providing soluble cues, physical cues or cell-cell interactions, thereby improving the therapeutic and diagnostic – also known as "theragnostic" outcome[30]. As the target of nanomedicine and any other types of medicine, cellular behaviors that have been widely associated with diseases and injuries have included: i) apoptosis; ii) proliferation/growth; iii) polarization; iv) differentiation; and v) migration. For example, cancer is characterized by abnormal growth of cells and by delivering soluble factors such as small molecule anti-cancer drugs by nanoparticles, we're hoping to inhibit such abnormal growth by turn on tumor suppressor genes and proteins or turn off tumor growth-related genes or pathways[31]. Stem cells, which is critical in regenerative medicine, are characterized by self-renewal and the ability to differentiate[32]. And utilizing nanoengineered matrix, the physical cues of stem cell microenvironment can be controlled by manipulating the integrins, which is typically in the scale between sub-hundred to a few hundred nanometers[33]. Such control over the microenvironment of stem cell eventually enabled the programmed growth and differentiation under in vitro and in vivo conditions, which are two most critical factors in stem cell-based regenerative medicine. On the other hand, monitoring the cellular

behaviors by nanomaterials-based biosensors, which by itself does not necessarily lead to the microenvironment changes, receive the changes of soluble, physical or intercellular microenvironments of target cells. After converting these biological signals back to physical output by nanosensors, scientists and clinicians can better design the therapeutic routes for treating the patients. There are a myriad of examples on how nanomaterials have improved the control of cell apoptosis, proliferation/growth, polarization, differentiation and migration by modulating the soluble, physical and intercellular cues in a different manner with conventional therapeutics; the underlying mechanism of why nanomedicine would be special to achieve such cellular control can vary significantly in different biological systems; however, similar to many other fields of nanotechnology, most nanotherapeutic systems become unique in functions in the following three aspects: i) the quantum effects originating from the quantum confinement phenomenon at the nanoscale; ii) the high surface-to-volume ratio compared to the bulk and macroscopic materials; and iii) the unique shapes and dimensions of nanostructures interfacing biology. Most of the unique optical, electrical, magnetic and thermal properties of nanomaterials that are used for theragnostics in nanomedicine are built up on quantum effects. For example, the localized surface plasmonic resonance effects taking place at the nanometer scale have laid the fundamentals of gold nanoparticles-based plasmonic biosensors in pathogen detection[34]. On the other hand, the high surface-to-volume ratio of nanomaterials strongly influence the surface chemistry and the interactions with biomolecules. For instance, as nanomaterials have significantly higher surface-to-volume ratio compared to bulk materials, nanoparticles can load more drugs, better control the degradation rates, induce integrin clustering more effectively and have more functionality sites to interfacing biological

systems and regulate cell behaviors[6,8,33]. The third property, the shapes and dimensions of nanostructures, are more influential in the interfacing with cellular, extracellular or other biological objects[35]. Given that cells are composed of different biological units with varying shapes and dimensions, many of which are at the nanoscale, a proper design on the shapes of nanomaterials can substantially change how cells recognize and respond to nanomaterials. The quantum effects, high surface-to-volume ratio and the biomimicry size and shapes of nanomaterials have represented distinctive advantages of nanomedicine and can significantly improve the treatment of many challenging diseases and injuries.

1.1.3 0D, 1D and 2D nanomaterials in nanomedicine

There are a few ways to categorize nanomaterials such as dimensionality, surface function, degradability and compositions, which are all critical factors influencing the behaviors of nanomedicine in biological systems. Among them, dimensionality that directly and simultaneously describes two of the most important characters of nanomaterials – the size and shapes, determines the quantum effects, high surface-to-volume ratio and the interactions with biological systems of nanomaterials to a large extent[35,36]. For example, many reports have supported the strong relation between the anisotropy of nanomaterials and the anisotropy of optical and electrical properties[16,36-38]. These concepts have laid the fundamentals in silicon-nanowire-based nanoelectronics and plasmonic materials-based nanophotonics. Also, the dimensionality of nanomaterials is also one of the determining factors in the endocytosis process in vitro and the clearance rates in vivo, which are critical in clinical applications[35,39,40]. Given its important role in a wide variety biological and physical processes, nanomaterials with different dimensionalities were reviewed to achieve

a systematic understanding on how nanotechnology contributed to the three fields of medicine: cancer therapy, regenerative medicine and biosensing.

1.1.4 The structure of this thesis

Overall, as a chemist, I have always been fascinated by the big question on how the control of chemical and physical structures of nanocrystalline with different compositions can eventually benefit human health and environmental sustainability[1,41-57]. Therefore, I have developed and involved in many projects covering different fields of nanomedicine. As a Ph.D. student supervised by Prof. Lee, my major contributions during my Ph.D. research have been on the development of 2D-nanomaterials based hybrid nanoscaffolds for regenerative medicine with a particular focus on central nervous system (CNS) diseases[42,58,59]. The work on this topic is inspired by identifying the scientific question that: 2D-nanomaterials-based nanoscaffolds have demonstrated great potential in regenerative medicine, but they're mostly non- or slow- biodegradable. Focusing on this topic, several versions of MnO_2-based hybrid nanoscaffolds have been developed in the past a few years. More recently, to provide solutions and design principles to scaffold systems beyond 2D nanomaterials, I further developed a nanoscaffold that contains 0D, 1D and 2D nanotopographies to interface cells and instructed the design of broad fields of nanomedicine-based regenerative therapy. Other parts of my work have also included the 2D nanomaterials-based cancer therapy and biosensing, which will also be described in this thesis as well. Therefore, multidimensional nanomaterials-based cancer and biosensing applications will also be briefly overviewed.

1.2 Multidimensional nanomaterials-enabled cancer therapy

1.2.1 Nanomedicine for advanced cancer therapy

Increasing interests on the application of nanotechnology in the last two decades can be largely attributed to the unique advantages of nanomaterials for cancer diagnosis, drug delivery, imaging, artificial vaccines, nanoscale medical devices and some nanomaterials being therapeutic reagents by themselves[8,16,60]. Some of the developed nanomedicine approaches have been used for clinical applications and there are many others that show great potential and undergo clinical trials[4]. Representative nanomedicine products on the market already have included albumin nanoparticles, micelles and liposomes. More recently developed therapeutic approaches based on nanomedicine include nanoparticle-based hyperthermia, gene delivery, radiation therapy and immunotherapy. Many excellent reviews have well summarized the progress in the field of nanomedicine, and it's such a broad, fast-changing and important topic that apparently cannot be covered comprehensively[61-110]. Here I highlight several important topics on several recently developed nanomaterials that have been less covered in the reviews and could potentially contribute to the cancer treatment in unconventional manners.

1.2.2 0D nanomaterials-based smart therapeutics for cancer nanomedicine

Most of the nanoparticles applied clinically for cancer treatment are based on 0D nanomaterials, which indicate the nanomaterial have similar sizes less than 100 nm in all three dimensions. Compared to the 1D and 2D nanomaterials, 0D nanomaterials don't have anisotropy in their shape and physical properties, thereby representing less complex systems in vitro and in vivo. To synthesize polymeric 0D nanomaterials, emulsion and nanoprecipitation method have been mostly used based on the micelle formation in a bi-

solvent system[111-113]. There are also self-assembly methods to generate 0D nanomaterials from peptides, biomolecules or polymers, where specific hydrophobic, hydrophilic and covalent binding domains need to be integrated into the monomers to initiate a non-anisotropic assembly process. On the other hand, the 0D inorganic nanomaterials are often synthesized based on the crystal growth nature, where all phases of the crystal grow at similar speeds to form the nanoparticles. When the certain phase of the crystal grows at a faster speed, specific capping ligands can be introduced to selectively slow down the crystal growth in that direction[114,115]. More specifically, there are many synthetic techniques based on different mechanisms, such as thermo-decomposition, sol-gel, hydrothermal, solid-state, chemical vapor deposition, atomic layer deposition for the synthesis of inorganic and organic 0D nanomaterials[116-124]. A variety of the 0D nanomaterials have been applied for drug delivery, imaging, and diagnosis of cancer[29]. Most of them are conjugated with anti-cancer drugs, either covalently or non-covalently, for drug delivery applications by taking advantages of the EPR effect. However, there are more functions that nanoparticles can provide other than drug delivery. Here, one example that demonstrates the recently demonstrated unique applications of nanoparticles will be provided, which focus on the gold nanoparticles-based biomimicry and smart therapeutics. Gold colloidal particles are first synthesized and characterized about 40 years ago[125]. Due to the facile control of crystals in multiple dimensions and the size, and the shape dependent plasmonic properties, gold nanoparticles are one of the mostly investigated materials for nanomedicine. When the gold nanoparticles are above 10 nm, a strong scattering of the near IR (NIR) light start to occur due to the localized surface plasmonic resonance of the nanoparticle[126-128]. Taking advantage of this unique phenomenon, high contrast dark-field-

imaging and surface-enhanced Raman spectroscopy has been developed for in vitro and in vivo cancer imaging. Photothermal therapy that converts the scattered NIR light into thermal energy has also been widely reported for gold nanoparticles with larger sizes, which is also based on the LSPR[129-138]. Compared to the water-bath based hyperthermia strategy, gold nanoparticle-based NIR photothermal hyperthermia can be made target specific and can achieve deeper tissue penetration. Such NIR-based photothermal effects have been further extended to the NIR-triggered drug release. For example, gold nanoparticles can be linked by drug intercalated complementary DNA sequences, and the NIR-triggered heating can lead to the melting of DNA followed by releasing of drugs in a spatiotemporal controlled manner[139-142].

Moreover, the drug releasing process can also be monitored by the SERS. By combining the heat-triggered and chemotherapy-based anti-cancer pathways, synergistic cancer therapy can be achieved in vitro and vivo[17]. The monitoring of the drug delivery process using in vivo imaging modalities enabled by gold nanoparticle makes the nanoparticle-based cancer treatment more attractive for personalized medicine by providing drug administration information to the doctors[143,144].

In addition to these unique physical properties for cancer theranostics, gold nanoparticles that have widely tunable sizes and gold-thiol-based simple and robust surface conjugation strategy have also been applied for many biomimicry smart therapeutics. Two of the many examples is the gold-nanoparticle-based nanozyme and [145,146]. One of the fundamental process to create protein diversity using identical genetic codes in cells is through the modification of RNA by editing or splicing[146]. Conventional chemical biology-based approaches for the modification of RNA have been mainly based on ribozymes, tRNA

endonuclease and adenosine deaminase. However, each of them has intrinsic limitations. For example, RNA acting adenosine deaminases can correct RNA errors by creating point mutations from A to G by changing adenosine into inosine. Guide RNA-based RNA correction is achieved by cleaving bulge-helix-bulge (BHB) areas. However, these approaches need to deliver plasmid to synthesize endonuclease as well as the guide RNA, leading to the highest efficiency of 30% for splicing. A third method to edit RNAs is based on ribozymes, which currently achieve a 10-50% efficiency at its best due to the instabilities of ribozymes or the difficulties occurred in plasmid delivery. To this end, people have developed a gold nanoparticle-based biomimetic system that mimics enzymatic structure and functions through the control over ligands on the gold nanoparticle. This system is known as enzyme. Briefly, three different ligands are conjugated onto a single gold nanoparticle, which are two different DNAzyme ligands and one RNA ligase domain. DNAzyme is a type of divalent metal ion based nuclei acids that bind to target specific RNAs through base pair recognition and then cleave the sequences that are not matching and inside the metal ion core region. RNA ligase is an enzyme that catalyzes the ligation of two ribonucleotides in an ATP-dependent manner. To better mimic the natural enzyme-based RNA editing, 10 nm gold nanoparticle was used. When the DNAzyme in the nanozyme recognizes target RNA sequence that needs to be corrected, the target RNA will be cleaved and lead to the formation of 2’-3’-cyclic phosphates. The 2’-3’-cyclic phosphates then can be further recognized by RNA ligase to produce corrected RNA. Using this modular system, people can demonstrate the splicing of RNA targets with a yield above 10%. The efficiency can increase to 45-66% when excess RNA ligase existent in solution.

Also, As a modular system, people can use the nanozyme-based system for editing unlimited RNA sequences.

Other than nanozyme, there have been several other nuclei acid-based biomimetic systems for the control of biochemical pathways in cancer cells as well as others. For example, biomimetic RNA-silencing nanocomplexes have been applied for overcoming multidrug resistance in cancer cells[145]. The famous spherical nucleic acid concept developed by Chad Mirkin group has also been applied as an RNAi-based therapy for glioblastoma treatment. Compared to simply using 0D nanoparticles as delivery vehicles, these nanoparticle-based smart therapeutics can directly function as signaling macromolecules to perform the functions of tumor-suppressors and can even behave beyond the natural cancer regulator systems.

1.2.3 1D nanomaterials-based macromolecule delivery for cancer nanomedicine

1D nanomaterials refer the nanostructures with one dimension substantially larger than the other two dimensions. Attention to the application of 1D nanomaterials such as nanotubes, nanorods, nanobelts and nanoneedles for biological applications started two decades ago. In general, the synthesis of such 1D nanostructures can be achieved by self-assembly (e.g., lipid nanotubes), crystal growth facet control (CTAB-capped gold nanorods), soft templating (e.g., mesoporous silica nanorods) and hard templating (e.g., AAO templated metal nanotubes). Due to their unique one dimensional shape, the shear force during blood circulation and the cellular uptake of the 1D nanomaterials can be substantially different from the 0D and 2D nanomaterials during drug delivery into the tumor sites. For example, 1D nanomaterials tend to accumulate more in the tumor site and adhere to the vessel wall lining endothelial cells more effectively compared to 0D nanomaterials[62-64,82,104,112].

Therefore, 1D nanomaterial overall has better potential in the passive targeting of the tumor during cancer therapy. Also, due to the anisotropic structure of 1D nanomaterials, unique optical and electrical properties occur and can be used for cancer therapy or imaging[147]. For instance, gold nanorods show a significantly higher scattering of NIR light, which could be either applied for SERS-based cancer detection by enhancing the local electromagnetic field, or for photothermal therapy-based cancer killing, by converting the optical energy into thermal energy efficiently[148]. Despite these intriguing properties for cancer killing and diagnosis, one particular field that is unique for 1D nanomaterials is the intracellular delivery of macromolecules such as plasmids, proteins and siRNA. Effective delivery of genetic and protein materials to specific sites of tissues have been a major challenge in drug delivery. Conventional methods such as diffusion and cationic polymer-based have been limited by the wide applicability due to the high variance of delivery efficiency in different cell types, concerns on safeties due to the toxicity of cationic polymers, and perhaps most importantly, the insufficient transfection efficiency due to the negative charge and large size of genetic materials and giant proteins. To this end, scientists discovered that 1D nanomaterials-based injection of nucleic acids and proteins into the cytoplasm can directly bypass the critical barrier of tissue junctions and cell membranes, thereby significantly increasing the delivery efficiency[147,149-151]. Taking nanoneedles as an example, bioactive agents can be loaded onto the tips of nanoneedles, then transfer them to unlimited cell types on a single patch, can sense the electrical activities of cells in a dynamic manner, or regulate the behaviors of cancer cells by providing optical or other physical signals without significantly impacting the viability and metabolic pathways. These vertical nanoneedle-based delivery system can be a generalized platform to

introduce a variety of large-sized biomolecules into different types of cells in a high-throughput manner. By performing cell viability assay, scientists have confirmed that 1D nanomaterials such as silicone nanowires can penetrate cell membrane without significantly sacrificing cell viability no matter what is coated on the surface of silicone wires[152]. In an intracellular transfection assay using mammalian cells, plasmid DNA and siRNA can be delivered to over 95% of the cells with a high transfection efficiency. Most importantly, the delivered genetic materials remain functional and can effectively manipulate cellular pathways. Also, as the spatial distributions of genetic materials can be controlled on the substrate, scientists can also achieve patterned cellular control by simply patterning the genetic materials. After the first study in 2010, this field has spurred intense interest in both tissue engineering and cancer nanomedicine[153]. For example, by developing a biodegradable porous silicone nanoneedle patch, Stevens group delivered VEGF-165 gene for the induction of neovascularization in the muscle tissues[154]. For cancer application, Gu group used a degradable microneedle patch and delivered aPD1, which is an antibody for the programmed death01 (PD-1) encapsulated dextran nanoparticles for highly efficient cancer immunotherapy in vivo[155]. aPD1 that effectively delivered into the tumor site can induce strong immune responses using a murine melanoma model. Such a delivery method for aPD1 is significantly more effective compared to the direct injection of free aPD1 and the aPD1 delivered by non-biodegradable microneedle patches. While the nanoneedles-based intracellular delivery of biomolecules has triggered intense interests, they are still limited to the delivery of biomolecules that absorbed or conjugated to the nanoneedles or nanowires, which is undesired for drug delivery to cancer cells. To this end, Melosh group has further developed another hollow 1D nanostructure, where they termed nanostraws, for

the more generalized delivery of biomolecules[156-163]. Using their nanostraw-based platform, ions and small molecules can be efficiently delivered into the cytosols of cancer cells with 40-70% delivery efficiency. Larger biomolecules such as plasmids are also successfully delivered into cancer cells to manipulate the genes inside cancer cells. The same group has further applied the nanostraw-based platform for the delivery of protein glycosylation and for monitoring cell in a long period. Other progress achieved in this field also include the interfacing of nanowires with tissues for monitoring tissue activities. Given the wide variety of genetic pathways and anti-cancer drug developed and discovered for cancer treatment, these 1D nanomaterial-based nanoarrays represent universal platforms for effective treatment of cancer and applications beyond cancer.

1.2.4 2D nanomaterials as a prodrug for cancer theranostics

In most cases, 2D nanomaterials, or nanosheets refer to the single or few atomic thin layered nanomaterials which include 2D graphene, boron nitride, transition metal dichalcogenides, transition metal trichalcogenides, metal halides, oxides, III-VI layered semiconductors, layered αand γzirconium phosphates and phosphonates, layered double hydroxides, ternary transition metal carbides and nitrides and clays [164]. The unique atomic-thin layered structure has made 2D nanomaterials particularly interesting materials for catalysts, due to their rich surface defects, which is desired for drug delivery; due to its extraordinary high surface-to-volume ratio for self-assembly; and due to their mechanical flexibilities. Because of the unique light-matter interactions between many 2D nanomaterials and NIR light, there have also been several 2D nanomaterial-based photothermal therapeutic systems for the ablation of tumor in vitro and vivo[165-168]. Additionally, the high surface area and rich defective sites compared to 0D and 1D

nanomaterials further make 2D nanomaterials ideal for surface functionalization with tumor homing ligands to target cancer cells in vivo. Moreover, compared to 0D nanomaterials, 2D nanomaterials, which have anisotropic structures, could better target the tumor sites through passive targeting effects due to the similar mechanism with 1D nanomaterial[62,63,66]. Lastly, 2D nanomaterials can degrade faster than 0D and 1D nanomaterials due to their large surface-to-volume ratio, and the degradability has been an increasing evaluation factor for the clinical applications of nanomaterials to treat cancer[169]. Even though there are many unique advantages of 2D nanomaterials for drug delivery, one particularly interesting application is based on the 2D nanomaterials providing therapeutic effects by themselves, which can also be called "prodrug 2D nanomaterials". For example, metal oxides with relatively high oxidative potential that does not reduce normal cell viabilities but significantly affect the growth of cancer cells by modulating metabolic and redox pathways. One of the examples is Mn(IV)O2 nanosheet-based cancer therapeutic systems[170-194]. Oxidative stress and ROS are tightly associated with the induction, the protection and the apoptosis of cancer cells[195-200]. As a defensive mechanism towards the high level of ROS in cancer, higher concentrations of glutathione, which is a representative intracellular bioreductant, are typically observed in cancer cells. Such elevated glutathione leads to strong protection mechanisms by eliminating excessive ROS and suppress the apoptotic pathways such as BAK and BAX in cancer undergoing chemotherapy. To this end, people have developed photodynamic therapy, which induces ROS by light, to synergistically work with chemotherapeutic agents. However, light-based manipulation of cancer apoptosis is not always practical in clinical treatments. Therefore, people developed the concept of chemodynamic therapy, which either reduces the glutathione levels or

increases the ROS levels by chemical alone without requiring light, to assist the cancer treatment[201-203]. One of the most promising nanomaterials that can reduce the glutathione levels is the MnO_2-based nanomaterials. More specifically, Mn(IV)O2 can accept two electrons from glutathione to form Mn2+ and oxidized glutathione, thereby affecting the defensive mechanisms developed by cancer cells towards ROS. Also, the released Mn2+ can bind to the calcium receptors and act as an effective MRI imaging contrast agent in the tumor area. Using 2D MnO_2 nanosheets, scientists can simultaneously deliver anti-cancer drugs that induce apoptosis and ROS in the cancer cells to synergistically kill the cancer cells. By further hybridizing MnO_2 nanosheets with other nanomaterials, multifunctional cancer theragnostic systems can be further developed. For example, upconversion nanoparticles encapsulated by MnO_2 nanosheets can selectively detect the high level of glutathione in cancer[204-207]. Before the reaction between MnO_2 and glutathione, the NIR activated fluorescence from upconversion is quenched. After the degradation of MnO_2, the fluorescence is recovered, thereby detecting glutathione in the form of a turn-on sensor. Also, by hybridizing MnO_2 nanosheets with photothermal reagents such as gold nanostructures, photothermal therapy, which is a stress regulator, can be further incorporated with chemotherapeutic modalities to suppress the tumor growth and enhance the cancer killing. Recently, Chen group has further identified a unique mechanism for MnO_2-based sensitization of cancer cells towards chemotherapy[191,194]. Their studies on Mn2+ as a degradation product suggests that Mn2+ alone can induce the ROS generation in the presence of bicarbonate due to Fenton reaction. Fenton reaction is the conversion of less toxic intracellular oxidants such as H2O2 into a more toxic form of radicals. And by

utilizing Mn2+ catalyzed Fenton reaction, higher cancer apoptosis was achieved using MnO_2 nanosheets combining with chemotherapeutic reagents.

1.3 Multi-dimensional nanomaterials-enabled stem cell therapy

Note: This section is adapted from a publication that I co-authored[1]. I mainly wrote the section for 2D nanomaterials-based stem cell therapy.

Stem cell therapy, as an emerging topic of regenerative medicine, is the treatment of diseased or injuries based on the delivery of stem cells or the engineering of endogenous stem cells. Currently, a major drawback in stem cell therapy is the limited control over stem cell fate, which leads to low efficiency in giving rise to mature differentiated cells that can replace the originally damaged cells[208,209]. On the other hand, ex vivo differentiation of stem cells have been proven to be very low in efficiency and has poor cell survival upon transplantation into the body. To overcome these challenges, various multidimensional nanomaterials that are capable of precisely controlling stem cell fate in the nanometer range have been developed rapidly. Furthermore, nanomaterials are highly versatile; they enable us to effectively and dynamically control the differentiation of stem cells solely through the biophysical cues of nanomaterial[58]. As demonstrated, subtle changes in the physical microenvironment such as the surface material orientation, ECM protein composition, and shape can significantly influence the therapeutic potential of stem cell[210].

This section covers novel nanomaterials used for stem cell differentiation in multidimensional approaches. Nanotechnology-based approaches to selectively guide stem-cell-based regeneration include 1) soluble microenvironmental factors; 2) insoluble physical microenvironment, and 3) Nano-topographical features (Figure 1). Soluble

microenvironment describes the growth factors, cytokines, and chemokines associated with nanomaterials delivered to the stem cells. Insoluble physical microenvironment describes the biochemical cues given to extracellular matrix (ECM) protein for enhanced attachment and orientation. Lastly, nano-topographical feature describes the physical, topographical cues nanomaterial provides to the stem cell. Overall, nanotechnology-based approaches offer physicochemical control required to differentiate stem cells into cell lines of interest. With the increasing interest to develop innovative tools and technologies, we can also expect creative solutions for the complex problems associated with stem cell biology and their applications.

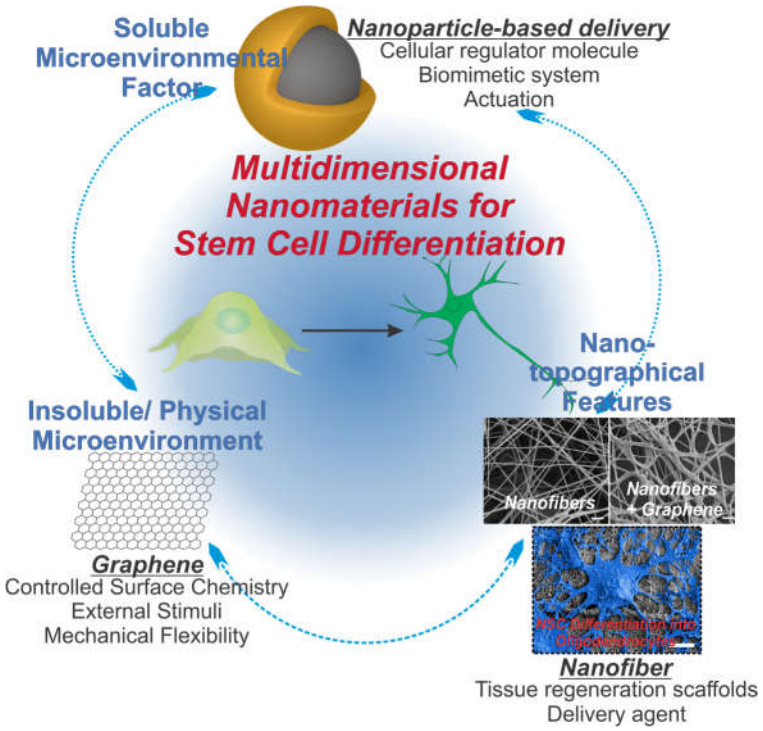

Figure 1-1. Illustrative diagram representing the multidimensional nanomaterials discussed in this section of introduction: 0D soluble microenvironmental factors, 2D insoluble physical microenvironment, and 1D nano-topographical features[1].

1.3.1 0D Nanomaterials-based Soluble Factors

With their unique sizes in the range of viruses and proteins, nanomaterials can interact with biological systems at the molecular level with high specificity[211]. Nanoparticles, different bulk materials, possess significant surface to volume ratio, composition, shape, surface, and unique optical and magnetic properties that are advantageous in solving biomedical challenges. Apart from numerous biomedical applications like imaging and drug/gene delivery, application of directing stem cell differentiation through nanoparticles is lacking. However, the unique properties of nanoparticles are met with strong enthusiasms from researchers for modulating stem cell behaviors and understanding stem cell signaling mechanisms[212].

Regulator molecules including growth factors and signaling molecules are major factors with the key ability to regulate stem cell behaviors, However, naturally occurring regulator molecules suffer from short circulation half-life and fast degradation rate under in vivo circumstances. These drawbacks together with low diffusivity render the real application of stem cell therapy inefficient due to the ineffective delivery and non-specific distribution. As such, a delivery system with spatial-temporal precision is of significance for utilizing signaling molecules to guide stem cell differentiation. With tremendous surface-to-volume ratio, high loading capacity and targeting delivery modality, nanoparticles have been used frequently as signaling molecule carriers. Owing to their intrinsic properties, the nanoparticle can provide prolonged growth factor releasing profile to treat stem cells effectively above concentration threshold. For example, hepatocyte growth factor (HGF) was loaded into chitosan nanoparticles (CNPs), formed by an ionotropic gelation method through strong electrostatic interactions between the CNPs and proteins, to show the

successful steady release of 85% HGF for five weeks. As shown in vitro differentiation experiments, the treated mesenchymal stem cells (MSCs) adapted to a round-shape hepatic cell characteristic morphology with upregulated expression of albumin[213]. Further in vivo study was done by co-injection of MSCs with HGF-CNPs into cirrhotic mice[214]. The in vivo differentiation from MSCs of hepatocytes was confirmed by the expression of albumin and cytokeratin 19. The increased level of alpha-fetoprotein and decreased expression of alpha-smooth muscle actin and type-I collagen suggested the reversal of fibrosis of hepatic extracellular matrix.

Inorganic nanoparticles, especially nanoporous/mesoporous silica nanomaterials have been used as biomolecule carrier for stem cell differentiation in bone tissue regeneration. Neumann et al. coupled Bone morphogenetic protein 2 (BMP2) on nanoporous silica nanoparticle through an amino-silane linker to test the osteoinductive effect on adipose-derived human mesenchymal stem cells (ADMSCs)[215]. Apart from osteogenesis, Kolzova and colleague used nanoporous silica particles to deliver exogenous trophic mimetics Cintrofin and Gliafin, peptide mimetics for the ciliary and glial cell-derived neurotrophic factors, to embryonic stem cells (ESCs). Confirmed by immunostaining, the embryonic stem cells were driven into motor neurons with the delivery of two peptide mimics. The function of the differentiated motor neuron was also characterized through electrophysiology and voltage-sensitive fluorescent protein imaging. Furthermore, the differentiated motor neurons were transplanted into mice, showing long-term survival, demonstrating the potential application in ESC differentiation for stem cell therapy[216].

By incorporating small molecules into polyelectrolyte, nanoparticles consist of polyethyleneimine (PEI) and dextran sulfate (DS), Santos et al. delivered retinoic acid into

the subventricular zone (SVZ) to induce neural stem cells differentiation[217]. The differentiated neuronal function was assessed through intracellular calcium variations upon KCL depolarization and histamine stimulation. Additionally, nanoparticle-based genetic manipulation has also been shown as an alternative strategy to guide stem differentiation. The versatility of nanoparticles also allows target delivery of genetic molecules into the cells. Lee and coworkers have first demonstrated that using magnetic core-shell nanoparticles (MCNPs) to guide neural stem cells (NSCs) differentiate into different lineages (neurons and oligodendrocytes) with the delivery of genetic materials of small interfering RNA (siRNA) or plasmid DNA. The controlled differentiation of neural stem cell was succeeded in RNA interference-based approach by suppressing two key "neural switch" genes CAVEOLIN-1 and SOX9 for oligodendrocyte and neuron differentiation respectively[218]. Chen et al. also demonstrated the hepatic differentiation of induced pluripotent stem cells (iPSCs) using mesoporous silica nanoparticles (MSNs) as a non-viral gene carrier and cell imaging agent. The mesoporous silica nanoparticle based carrier showed minimal cytotoxicity and fast cellular uptake for iPSCs. Upon treatment of MSNs loaded with hepatocyte nuclear factor 3β(HNF3β) plasmid DNA, the iPSCs went into mature hepatocyte lineage differentiation with functions like low-density lipoprotein uptake and glycogen storage[55].

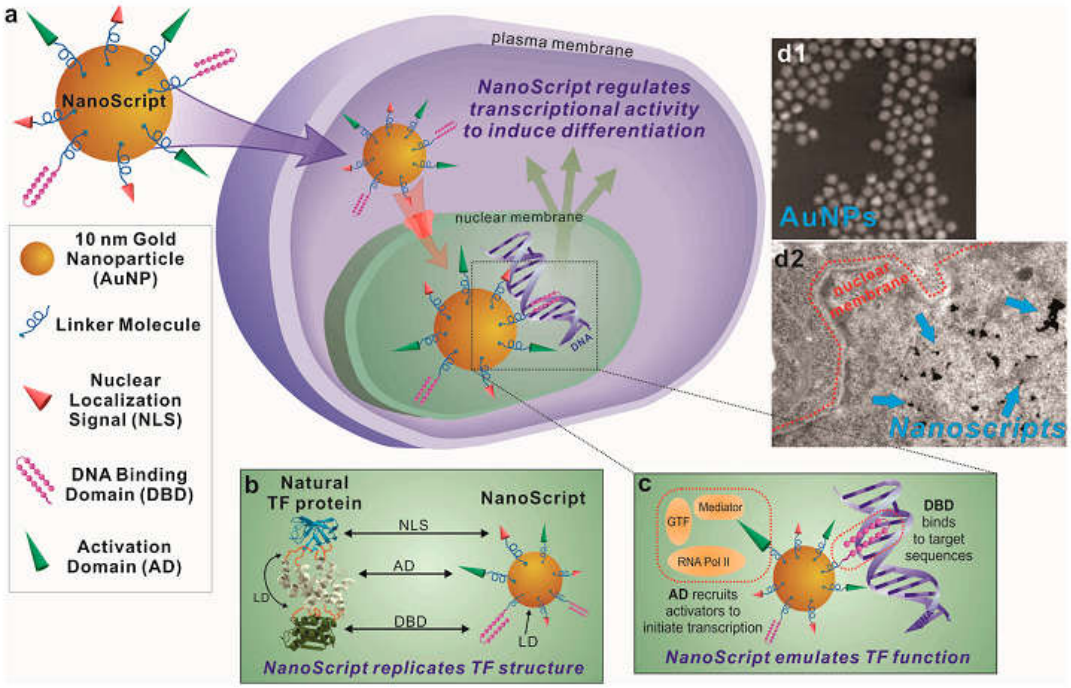

Figure 1-2. General design scheme of NanoScript. (a) NanoScript is consist of a single 10 nm gold nanoparticle, DNA binding Domain (DBD), Activation Domain (AD), and Nuclear Localization Signal (NLS), which forms assembly to mimic natural transcription factor. (b) Comparison of NanoScript with natural transcription factor. The assembly of the three essential domains of natural transcription factors is replicated by NanoScript. (c) The DBD and AD domains on NanoScript works synergistically to mimic natural transcription factors for transcriptional modulation on expression of targeted genes (d) NanoScript shows high mono-dispersity, efficient uptake and nuclear localization.

As shown, small molecule dosing and genetic manipulation are equally significant for directing stem cell fate in tissue engineering and regenerative medicine[219]. With this merit, Lee et al. demonstrated the co-delivery of small molecules and RNA interference agents to differentiate neural stem cells into neurons using a single vehicle delivery system based on the cyclodextrin-modified dendritic polyamine. Through the binding of small molecule retinoic acid with β-cyclodextrin and electrostatic interaction between siRNA and a dendritic polyamine, the combination of small molecule and RNA interference synergistically targeted multiple cellular pathways to induce stem cell differentiation. The controlled and reliable neuronal differentiation was confirmed through immunostaining of GFAP and TuJ1 markers[220].

Nanomaterial Biomimetic System

Transcription factors are master regulators in orchestrating basic cellular behaviors and are responsible for critical cellular functions and cellular fate. Therefore, by modulating the expression of specific genes, the differentiation of stem cell can also be modulated through manipulating the key transcription factors[221,222]. Contrary to a traditional viral-based delivery system with drawbacks such as cytotoxicity, immunogenicity, and undesirable for clinical applications, Lee has developed NanoScript, a nanoparticle-based synthetic transcription (Figure 2)[223]. Specifically, NanoScript consists of 1) a nanoparticle core, usually gold nanoparticle due to its biocompatibility and ease of functionalization; 2) functional peptides for nuclear localization; 3) an activation domain mimic, and 4) a Py-I'm hairpin polyamide as synthetic DNA binding domain. To demonstrate stem cell differentiation, NanoScript was designed to mimic myogenic regulatory factors (MRFs),

which are a group of four transcription factors, MyoD, myogenin, Myf5, and Mrf4, functioning as a crucial regulator of muscle cell differentiation. The NanoScript-MRF successfully guided ADMSCs to differentiate into mature muscle cells showing upregulated myogenin and myosin expression and myofibrils formation[224].

Furthermore, with the ability to activate endogenous gene expression activity, NanoScript was conjugated with N-(4-Chloro-3-(trifluoromethyl) phenyl)-2-ethoxybenzamide (CTB) derivative, an epigenetic modulator, to enhance chondrogenic differentiation from adipose-derived mesenchymal stem cells. Specifically, the CTB derivatives conjugated on NanoScript, triggering the p300 signaling pathway as a histone acetyltransferase (HAT) activator will induce an increase in HAT activity, transforming the chromatin structure from “tight” into “loose” form. One gene that is regulated by the p300 signaling pathway is Sox9, a key chondrogenic promoting gene. Thus, the combination of CTB derivatives and Sox9 activation, NanoScript showed enhanced chondrogenic differentiation from ADMSCs[225].

In addition to previously mentioned advantages, NanoScript can be flexibly functionalized with interchangeable components to mimic different transcription factors as well. Once natural transcription factors bind to their target genes, they can activate or repress gene transcriptions. Contrasting gene activation using the NanoScript platform, a gene repressing NanoScript was made to emulate the repression ability of natural transcription factor to downregulate gene expression at the transcription level in late 2015. By designing the repression NanoScript to downregulate Sox9 expression, neural stem cells were

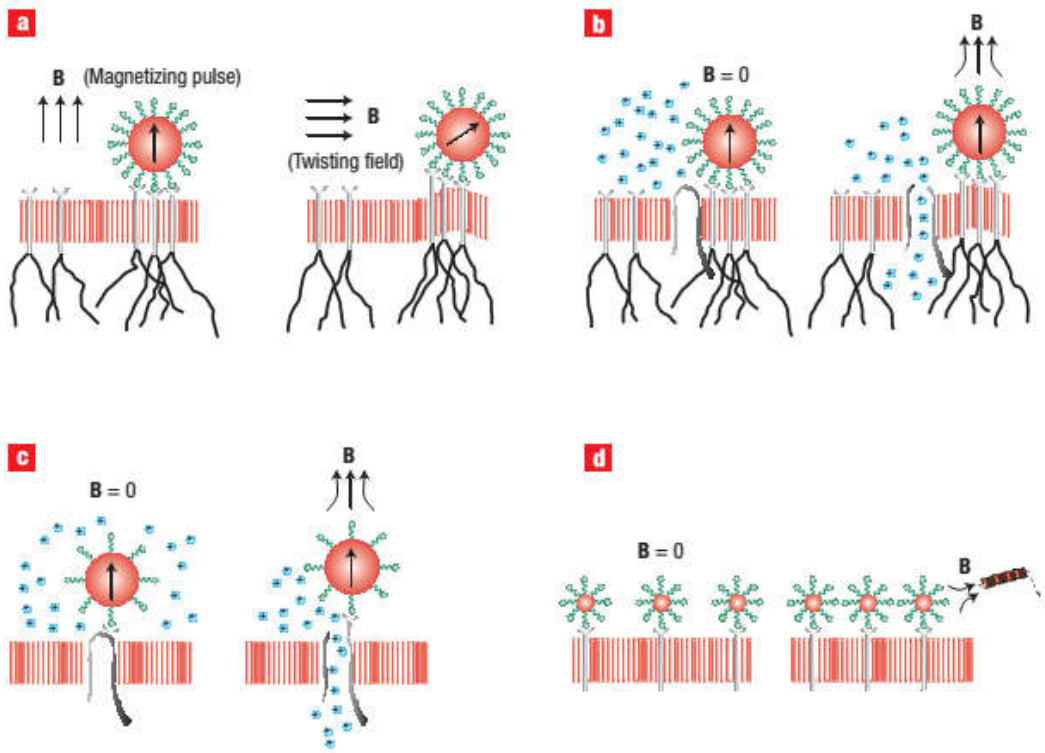

Figure 1-3. Different type of magnetic actuation. (a) magnetic twisting cytometry; (b) mechano-sensitive ion-channel activation; (c) targeted ion-channel activation; (d) receptor clustering. [22]

successfully differentiated into neurons. The mature neuron function, calcium ion flux, was observed[226].

Other than providing soluble cues, nanoparticles have also been shown to provide mechanical cues responsible for stem cell fate determination, tissue formation, and organ regeneration. Recently, remote magnetic actuation (Figure 3) has been demonstrated to provide mechanical stimulation to biological cells[227]. Upon mechanical stimulations, the integrin receptors at the focal adhesion of cells have been shown to correlate with cell biochemistry, morphology, and even epigenetic chromosomal activity[228,229]. With the

development of magnetic nanoparticles, cellular or even receptor level magnetic actuation can be achieved to activate different mechanosensors existing in the cell membrane[230]. Through facile surface functionalization, nano-actuators can bind to the cell surfaces and manipulate cell function or even guide stem cell differentiation with an external magnetic field. Magneto actuation technology offers a method to isolate single receptor-mediated cellular mechanotransduction process which can bring insights to related cellular-matrix interactions[231].

Among the very first demonstrations of this approach, Ingber and his colleagues attached magnetic nano/microbeads to cell-surface through integrin receptors with applied tensional forces. The cellular responses were recorded with different kinds of mechanic stimuli: pulse, oscillation, static stress, and prolonged stress. Through the cellular adaption to the mechanotransduction, several pathways related mechanisms like Rho signaling and mechanosensitive ion channels were identified to be responsible for the different adoption for static and dynamic mechanical changes applied to integrin[232]. Later, similar magnetic nanoparticle-based approach was applied to generate a mechanical stress to specific ion channel of interest (i.e. TREK-1). The study demonstrated the specific activation of mechanosensitive ion channel in real time through force generated on targeting nanoparticle on the extracellular region of TREK-1[233]. More recently, magnetic nanoparticles have been utilized to generate magneto-mechanical stimulation on cell surface receptors for stem cell differentiation. Henstock, et al. targeted the same receptor mentioned above, TREK-1, with delivery of 4pN per nanoparticle for mechanotransduction in mesenchymal stem cells, resulting in a 2.4 fold increase in the mineralization in the chick fetal femur[234]. Furthermore, due to facile functionalization on the magnetic nano-actuators,

different mechano-sensitive receptors can be modulated simultaneously to study receptor interactions and pathway interplays. Hu et al. demonstrated higher mineralization ratio with the help of osteogenic culture medium and stimulating two specific cell membrane receptors: platelet-derived growth factor receptor α (PDGFRα) and integrin αvβ3[235]. Another example of this combined receptor mechanical stimulation was demonstrated by Haj and his colleague by targeting PDGFRα and PDGFRβ. Upon cyclical magneto-mechanical stimulation, human bone marrow-derived mesenchymal stem cells (hBMSCs) differentiated into a smooth muscle cell lineage[236]. Overall, the unique size range and properties of nanoparticles enable nanoparticle-based stem cell regulatory approach with molecular level specificity, improved interaction efficiency, and spatial-temporal resolution. A nanoparticle based stem cell differentiation system with the ability to interact with cellular processes and deliver regulator molecules remotely on demand would be of significance for translating the current research to the next stage. Moreover, development of such nanomaterials with desirable degradability would be a key step for the advancement in clinical applications of nanoparticle based stem cell therapy and tissue engineering.

1.3.2 2D Nanomaterial-based Insoluble Physical Microenvironments

During stem cell differentiation, cells exerts forces to and simultaneously receive forces from the surrounding extracellular matrix (ECM) proteins. Therefore, mechanical properties from the ECM play a significant role in regulating stem cell behaviors. Moreover, the physical stimulations (e.g. electrical, mechanical, and photochemical stimulation) from the substrate can provide additional dimension of control over the differentiation process of stem cells. Furthermore, the physical microenvironments of the ECM also influence the

clinical transplantation potential of stem cells. To this end, a variety of organic and inorganic scaffolds, insoluble physical microenvironments, that can mimic the ECM have been developed to have precise control over stiffness, surface topography, shear forces, degradability, and retractability. Among the various types of nanomaterials, tremendous interest has been focused on two-dimensional structured nanomaterials in the last decade since the discovery of graphene – an sp2 bonded carbon nanomaterial[237,238]. A variety of graphene derivatives and graphene mimics have been rapidly designed, synthesized, and studied. In 2008, graphene was reported as a drug delivery vehicle for the first time and generated intense interest in graphene-based bioapplications, ranging from biosensing, cancer therapy, drug delivery, and regenerative therapy[225,239]. For stem cell culturing and differentiation, graphene and its derivatives have been found universally to be versatile, biocompatible, and highly stable scaffolds for promoting stem cell differentiations with low inflammatory induction[240]. The broad interest generated from graphene nanosheet-based scaffolds have further inspired the development of scaffolds based on other two-dimensional nanomaterials such as ultrathin polymeric nanosheets, which is biocompatible and biodegradable. For example, the high mechanical flexibility would allow sufficient tolerance of mechanical stresses for tissue regeneration. Also, the highly absorptive and porous architecture of 2D nanomaterial constructed scaffold would be advantageous for efficient mass transport. Moreover, the high electrical conductivity of graphene-based scaffold allows electrical stimulation, monitoring, and detection of differentiated neurons or cardiomyocytes. With high mechanical flexibility and versatile surface functionalities, graphene and their derivatives can be facilely engineered into scaffolds with tunable

geometrical and mechanical cues to direct stem cell fate and further enhance stem cell differentiation.

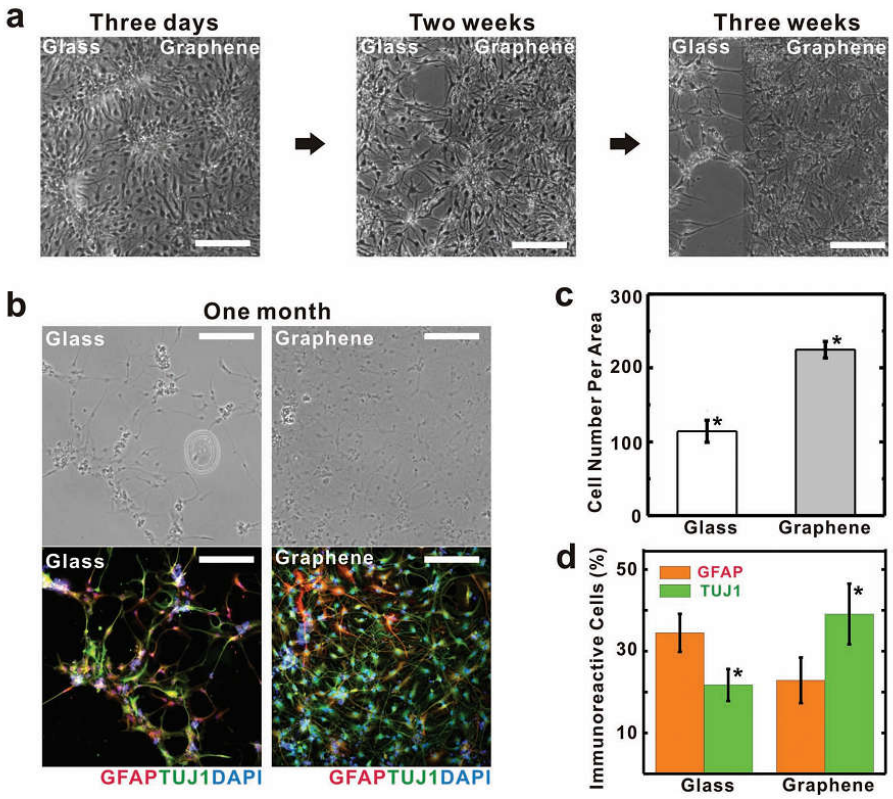

Figure 1-4. Enhanced neural differentiation of hNSCs on CVD grown graphene substrate: a) Bright-field images of the hNSCs after a differentiation process of 3 days (left), two weeks (middle) and three weeks (right). b) Bright field (top) and fluorescence (bottom) images of hNSC after differentiation on glass (left) and graphene (right) after a differentiation process of one month. Immunostaining on GFAP (red) and TUJ1 (green) for astroglial and neural cells were conducted on hNSCs. c) Cel density (per 0.64 mm^2) on graphene substrate and glass after differentiation for one month. d) Percentage of GFAP (red) and TUJ1 (green) on glass and graphene. All scale bars are 200 μm. [36]

Enhancing stem cell differentiation through substrate surface chemistry

Graphene has been demonstrated as a biocompatible and promising substrate for electrical and optical interfacing devices due to their high mechanical flexibility, transparency, and conductivity. Hong et al. reported that graphene substrate fabricated by chemical vapor deposition (CVD) effectively enhanced the differentiation of human neural stem cells into neurons (Figure 4)[241]. While the mechanism remains unclear, laminin-related cellular pathways were found to be significantly enhanced and the graphene substrates were observed to act as an excellent cell-adhesion layer especially for the long-term differentiation process. Later on, also using a CVD method, Cheng et al. found that mouse hippocampal neurons cultured on graphene showed enhanced neurite sprouting and outgrowth, which could act through the GAP43 related pathways[242]. As the cell adhesion and growth factor is highly related to the surface functional groups of graphene, fluorinated graphene sheets have been developed as a scaffold to guide neural stem cell growth and differentiation as well. Loh et al. observed a further enhancement of neuronal differentiation from MSCs after they introduced neuron-inductive agent, retinoic acid, which could be attributed to enhanced absorption and binding of retinoic acid towards the fluorinated substrate[243]. Similar to the observations in neurogenesis, enhanced cellular adhesion and proliferation on scaffolds constructed from graphene and its derivatives have also been found in the osteogenic, myogenic, chondrogenic, cardiomyogenic, and other differentiation processes in MSCs[224,244-247].

While the mechanism is still unclear, hydrophilicity, surface functionality, roughness, surface area, and nanotopographical features such as ripples were proposed to be the reasons for such enhanced adhesion. Loh et al. reported the chemical roles of graphene and

graphene oxide (GO) in guiding stem cells towards specific cell lineages. They suggested that the strong noncovalent binding towards osteogenic inducers of graphene make it act as a preconcentration platform for enhanced osteogenesis[248]. They also found that differentiation into adipocytes was suppressed on graphene-based scaffolds as insulin, a key adipogenic growth factor was denatured through the π-π interaction on graphene scaffold. GO, on the other hand, did not interfere with the adipogenesis because they bind with insulin through electrostatic interaction. For chondrogenic differentiation, Lim et al. fabricated a cell-assembled graphene 3D biocomposite and showed enhanced chondrogenic differentiation[224]. Kim et al. later discovered that GO plays a dual role, both as an excellent cell-adhesion substrate but also as a growth factor protein preconcentration platform during the chondrogenic differentiation process[246]. In contrast to the conventional chondrogenic pellet culturing and differentiation of MSCs, the incorporation of GO preloaded with transforming growth factor-β3 (TGF-β3) can overcome the diffusion limitation of TGF-β3 that occurs inside the pellet. Chondrogenic marker, SOX-9, and Aggrecan expression were enhanced more than two-fold and three-fold respectively compared to the control group. Among the different types of stem cell differentiation, preliminary investigation on the graphene-based scaffolds for osteogenesis and neurogenesis has been conducted in vivo, confirming their high biocompatibility and promising applications in tissue engineering.

Electrical and optical stimulation for enhanced stem cell differentiation and detection

In addition to its surface chemistry and high aspect ratio, graphene also has unique optical and electrical properties that can stimulate stem cells and further assist differentiation.

Pulse electrical stimulation has been proven to enhance the neuronal regeneration efficiently. However, it would be more practical to integrate a power supply inside body instead of inserting electrodes. Recently, to address this challenge, Wang et al. constructed a self-powered electrical stimulation system (high effective triboelectric nanogenerator, TENG) that utilized a graphene-based hybrid microfiber to enhance the differentiation of neural stem cells through electrical stimulation (Figure 5)[249].

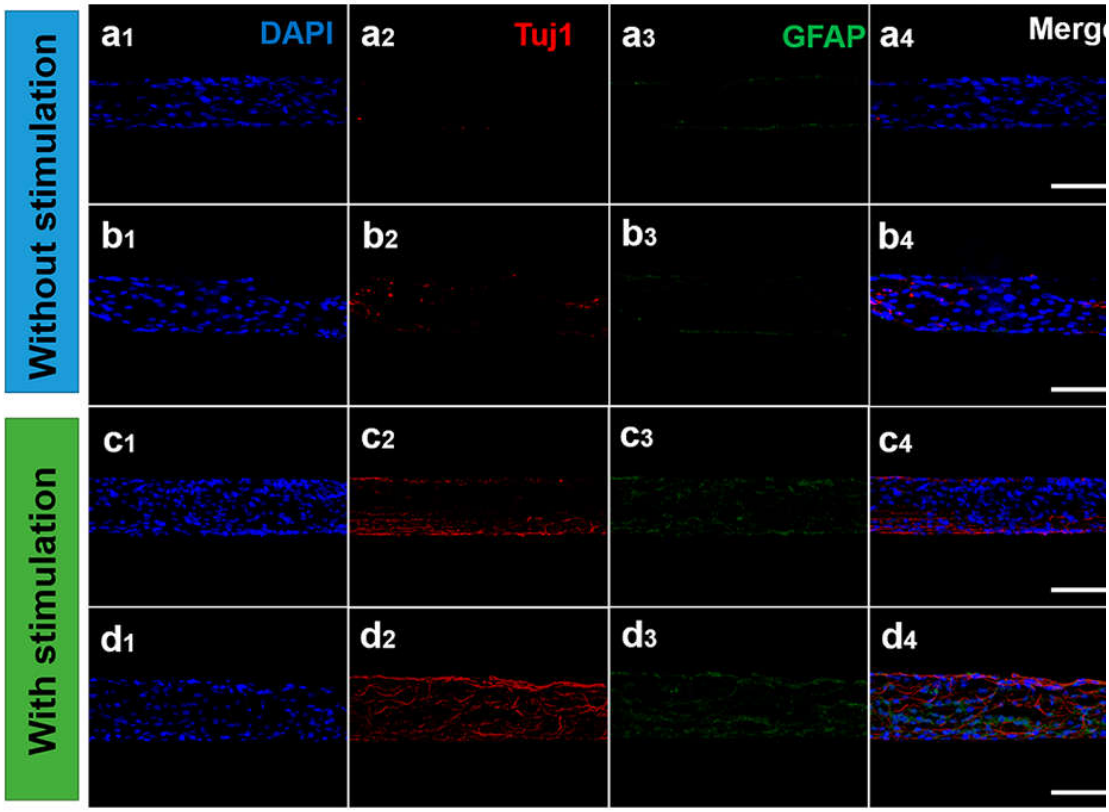

Figure 1-5. Electrical and optical stimulation for enhanced stem cell differentiation. (a, b) After cultured under stimulation and without electrical stimulation for 21 days, cells were immunostained with DAPI (blue) for nucleus, Tuj1 (red) and GFAP (green). (c, d) After cultured under TENG electrical stimulation and without TENG electrical

Another study has also successfully utilized electrical field stimulation to control neural cell-cell interactions through alternating the protein synthesis related to cell mobility and cytoskeleton. More importantly, the graphene substrate also provides a good electrical coupling with the neurons for electrical stimulations. Ghaderi et al. demonstrated the differentiation of human neural stem cells (hNSCs) into neurons using reduced graphene oxide (rGO); while under pulsed laser stimulation, the photothermal effect induced radial thermal flow and resulted in the organization of the neuronal network by elongating the differentiated neurons in the radial directions[250]. In contrast, unreduced graphene oxide (GO), where there is a weaker photothermal effect or quartz, no obvious enhanced differentiation was observed. The same group has also reported the photo-catalytical stimulation on hNSCs by utilizing a rGO/TiO2 hybrid scaffold[251]. They found that the flash photostimulation not only promoted proliferation (by a factor of ~2.5) of the stem cells but also guided stem cells differentiation into neuronal lineage versus glial cells. Recently, the stimulation of cardiomyocytes differentiated from ADSCs has also been demonstrated on the graphene scaffold[247].

In addition to stimulating and enhancing differentiation of stem cells, the excellent electrical and optical properties have also been utilized for detecting the behaviors of differentiated cells and for monitoring the differentiation process. For example, it is reported that the neural network can be successfully formed on graphene films and the neural signals can be effectively enhanced on graphene films[252]. Graphene can act as a conductive substrate and transfer the electrical signals to the neural cells cultured and effectively modulate neural cell behaviors. Furthermore, Choi et al. also synthesized a scaffold assembled from GO encapsulated gold nanoparticles (Au@GO NPs) that is

applicable for monitoring the differentiation of NSCs based on electrochemical detection and surface-enhanced Raman Spectroscopy (SERS)[253]. It has been reported that during the stem cell differentiation, C=C bonds gradually decrease, which can be reflected from the Raman bands at 1656 cm-1. Based on this mechanism, Au@GO NPs monitored the differentiation in a non-destructive manner. By taking advantage of electrical properties of graphene, electrochemical detection of the C=C bonds was also achieved in a single platform.

When acting as a coating material, the high flexibility of graphene can effectively take on the geometry, pattern, and morphology of the underlying scaffolds. Lee et al. demonstrated a silica nanoparticle-graphene oxide hybrid scaffold to promote axonal alignment of differentiated neurons[254]. Recently, Lee also developed micro-contact printing technique and fabricated combinatorial patterns of GO for the effective control over the differentiation of human adipose-derived mesenchymal stem cells[58] (ADMSCs). The morphology of ADMSCs was effectively modulated by the GO patterns. It was found that ADMSCs preferentially differentiate into osteoblasts and the grid pattern selectively guides the ADMSCs into neuronal lineage with highly elongated axons. Not only the aforementioned 2D scaffolds, 3D scaffolds based on graphene and its derivatives have also been fabricated by taking advantage of their high flexibility. These 3D scaffolds could accelerate the application of graphene for tissue engineering due to the recent interest in 3D cell culture in the biological field. For example, based on layer-by-layer (LBL) assembly, Shin et al. reported a GO-embedded GelMA hybrid hydrogel scaffold that forms multiple layers of cardiomyocyte cell sheet[255]. The high flexibility of GO was proposed to facilitate cell separation and stack for the highly dense, organized 3D complex tissue

architectures. Most importantly, this tissue-like cell construct demonstrated synchronous and spontaneous beating after 24-hour culture process.

Recently, scientists have fabricated a variety of 3D nanostructures based on GO and graphene using hydrothermal, electrostatic assembly, and soft templating methods. Liu et al. reported three-dimensional hydroxyapatitete – graphene hybrid forms assembled from graphene for enhanced osteogenesis[244]. Moreover, the mineralized 3D scaffold further accelerated and enhanced osteogenesis of MSCs through the increased deposition of inorganic minerals. In addition to graphene-based nanosheets, polymeric nanosheets also present a high level of flexibility, which is highly advantageous for performing transplantation and adapting to local injured areas. Recently, Fujie et al. reportedly inserted magnetic nanoparticles embedded PGA nanosheets scaffold along with in vitro cultured monolayer retinal pigment epithelial cell (RPE) for retinal recovery [256]. Due to its ultrathin nature and flexibility, the polymer nanosheet scaffold was proposed to avoid vitreous fluid leakage and minimize postsurgical infection.

Overall, the unique surface chemistry, binding toward biomolecules, fascinating electrical and optical properties of graphene-based nanosheets, and the excellent mechanical flexibilities of 2D nanomaterial have demonstrated high biocompatibility, enhanced cellular adhesion, proliferation, stem cell differentiation, detection, and transplantations. Future research would call for further investigations, especially in simulation studies on the mechanism on how graphene binds to bio-molecules and how graphene enhances and accelerate the differentiation process. Furthermore, development of novel 2D nanomaterials assembled in 3D scaffold with biodegradable properties and studying the

stem cells in vivo would further boost the clinical application of 2D nanomaterials in tissue engineering.

1.3.3 1D Nanofiber-based Nanotopographical Features

In addition to soluble cues, stem cells are very sensitive to the surrounding physical topographical microenvironment as well. The act of modifying the underlying substrates allows researchers to control and regulate cell adhesion, spreading, shape, elongation, and ultimately cell fate[257]. As tissue formation is heavily dependent on the recruitment of progenitor cells from the surrounding area, biomaterials introduced as implants are critical in bridging the gap when the defects are too severe to heal autogenously. Therefore, it is important for biomaterials to be able to orchestrate the biochemical and biophysical cues to facilitate cell-cell and cell-ECM interactions to facilitate stem cell therapy.

Nanofiber technology has gained significant attentions and excitement in the research and development field as a potential solution to overcome some of the current challenges such as burn and wound care, tissue and organ regeneration, and various degenerative diseases in biomedical engineering. Compared to traditional bulk material, nanofiber substrates offer tremendous amount of surface area for enhanced cell adhesion, protein adhesion, and drug loading. Furthermore, nanofibers offer topographical features mimicking the macrophysical structure of natural ECM proteins in both animals and humans. Lastly, nanofibers can be fabricated through various processes and materials which have the industrial potential to be regulated and scaled up easily for mass production[258].

Typically, a nanofiber can be generated through various methods including molecular self-assembly, electrospinning, and thermally induced phase separation[259]. With rational

material design, through the use of biodegradable polymer, a nanofiber can provide time-dependent temporary support until the regenerated tissue is matured. Through the introduction of interconnected porous network, nanofibers have also been shown to promote cell-cell interaction through deep cell penetration. Additionally, a nanofiber can be fabricated by ECM protein to promote stem cell adhesion and differentiation. Moreover, a nanofiber can be controlled through fabrication to either be random or aligned to give anisotropic topographical guidance. Furthermore, bioactive compounds (growth factors, nucleic acids, and integrin-binding ligands) have also been shown to be embedded into nanofiber scaffolds. To realize the potential of nanofiber biomedical application, numerous works have been focused on the topic of tissue regeneration.

During the early stages of nanofiber technologies in biomedical applications, many natural polymers were used. For example, in skin tissue regeneration, Park and Min et al. had demonstrated through type I collagen nanofiber[260] and surface modification of silk fibroin (SF) nanofibers with oxygen gas to increase surface hydrophilicity[261], they were able to promote the cellular activity of human dermal keratinocytes and fibroblasts. Nie group[262] and Sethuraman group[263] had used a different blend of biodegradable chitosan materials to form nanofibers that are comparable in tensile strength of normal human skin to evaluate for skin regeneration in vitro. By attaching bone-marrow-derived mesenchymal stem cells (BM-MSCs), Ma group demonstrated that by increasing the density of BM-MSCs, thanks to the biomimetic nanofiber scaffolds, wounds treated with BM-MSCs attached nanofibers closed more than a week earlier than untreated controls[264].

Through a co-self-assembling peptide of phosphorylated serine peptide amphiphile and RGDS peptide amphiphile, Stupp and coworkers inserted the peptides based nanofiber into

a 5mm rat femoral critical-size defect to demonstrate bone formation and mineralization within four weeks[265]. To form the self-assembling nanofiber, the nanofiber-forming molecules contain a peptide segment with one domain that has a strong propensity to form extended β-sheets and the second domain with residues for bioactivity. The β-sheets domain is crucial for promoting assembly of fibrous aggregate instead of spherical aggregate[266]. By combining synthetic biodegradable polymers, Ramakrishna was able to increase the porosity of polycaprolactone/hyaluronic acid/gelatin to over 93% and maintain tensile strength to support osteoblast for mineralization.[267] This interconnecting porous composite nanofibrous scaffold provided large surface area for cell attachment, cell activity, and cell proliferation. Similar to the previous study[264], MSCs have also been cultured on to completely synthetic polycaprolactone nanofiber to show deep penetration of cells and the presence of abundant ECM after one week[268]. In the same report, Vaccanti group also showed that the cultured MSCs on the surface of PCL nanofibers were inclined to differentiate into osteogenic lineages as mineralization had occurred after four weeks[268].

Nanofibers have also been applied to ligament regeneration. Unlike other tissues, tendon and ligament have a very low propensity to regenerate due to their high ECM density and low vascularity[269]. The body typically relies on scar tissue mediated healing process which is inadequate to replace the functions of damaged or diseased tendon and ligament. As mentioned, owning to its high porosity nature, nanofiber allows for high cell infiltration rate and also allow for uniaxial alignment to mimic the anisotropic structure of native tendon and ligament. In this report[270], Ouyan and coworkers demonstrated that by seeding human tendon progenitor cells (hTSPCs) on top of aligned Poly(lactic acid) (PLLA) nanofibers higher tendon gene expression similar to native tissue was observed compare to

randomly aligned fiber control which is significantly lower. The reason is that ECM production of tendon and ligament fibroblasts have specific uniaxial direction. In another approach[271], Shin stretched the nanofiber at 12 cycles/min frequency for 24h and found that human ligament fibroblast-produced more ECM collagen on longitudinally stretch axis than the transverse axis.

Typical nanofibers have sizes above 400 nm in diameters. However, through rational design, by functionalizing chitosan nanofiber with galactose to make galactosylated chitosan (GC) and shrinking the nanofiber to ~160nm, Gu and coworkers showed the enhanced bioactivity and mechanical stability of primary hepatocytes through mimicking the ECM properties of hepatocytes[272]. Through topographical properties of nanofibers, Baharvand[273] was able to enhance the generation of hepatocyte-like cells from mesenchymal stem cells with commercially available Ultra-WebTM nanofiber with the help of inducing bio-agents. From his finding, hepatocyte markers ALB, CYP7a1, and HNF4α were consistently upregulated compared to regular tissue culture condition.

The brain has long been considered to be more complex than the universe, and yet this spectacular piece of "organic machinery" has fascinated the scientists and clinicians endlessly. When there are subtle disturbances to the brain, complications in physical, motor, psychological, and cognitive functions can occur. Therefore, the understanding of how the central nervous system (CNS) functions and developing therapies to repair this intricate system after damages caused by diseases and injuries has been longed-for by the scientists and clinicians. In order to differentiate into specialized neural cells of interest (e.g. neurons and oligodendrocytes), researchers have been exploring the 3D microenvironment for gradient diffusion of bio-agents, cell migration, and cell-cell interaction. Zhang and

coworkers[274] have developed a 3D culture system by attaching several functional motifs to self-assembling peptide RADA16. Comparing to recombinant ECM proteins, peptide-based nanofiber offers not only topographical bio-mimic but also the high in purity and amount of desired functional motifs. In the region with higher biological motifs, neural cells are significantly enhanced in survival. Similarly by presenting neurite-promoting IKVAV motif through 3D self-assembled peptide nanofiber, Stupp group had also shown his artificial nanofiber scaffold can rapidly induce neuronal differentiation from neural progenitor cells[275].

For the CNS regeneration, a number of studies have been focused on the differentiation of neurons, while oligodendrocyte – a myelinating cell lineage involved in many neuronal circuits, was underappreciated. In combination with two-dimensional nanomaterial, Lee group reported a polycaprolactone (PCL) – GO hybrid scaffold for guiding stem cell differentiation into oligodendrocytes (Figure 6)[276]. The scaffolds were fabricated from electrospinning of nanofiber scaffolds, followed by drop-casting GO solutions. The nanofiber morphology, which is a mimic of oligodendrocyte ECMs, was found to be well maintained after GO drop-casting, and the GO provides an excellent surface for cell adhesion and differentiation (Figure 7). From polymer chain reaction (PCR) analysis, while the PCL only and GO only (control groups) only has 1-3-fold enhancement of oligodendrocyte markers compared to the control group (glass), the PCL-GO hybrid scaffold enhanced the oligodendrocyte differentiation by over 10 folds (Figure 8). We have also proposed that such effective control over oligodendrocyte differentiation and development originate from integrin-mediated pathways, mainly FAK, Akt, ILK, and Fyn.

Nanofiber-based delivery of bioactive agents

To turn nanofibers into drug carries, bioactive agents are typically immobilized into the polymer matrix for their control release. Depending on the polymer material, typical procedure consists of entrapment[277] or binding[278] as demonstrated by Stupp et al.. By

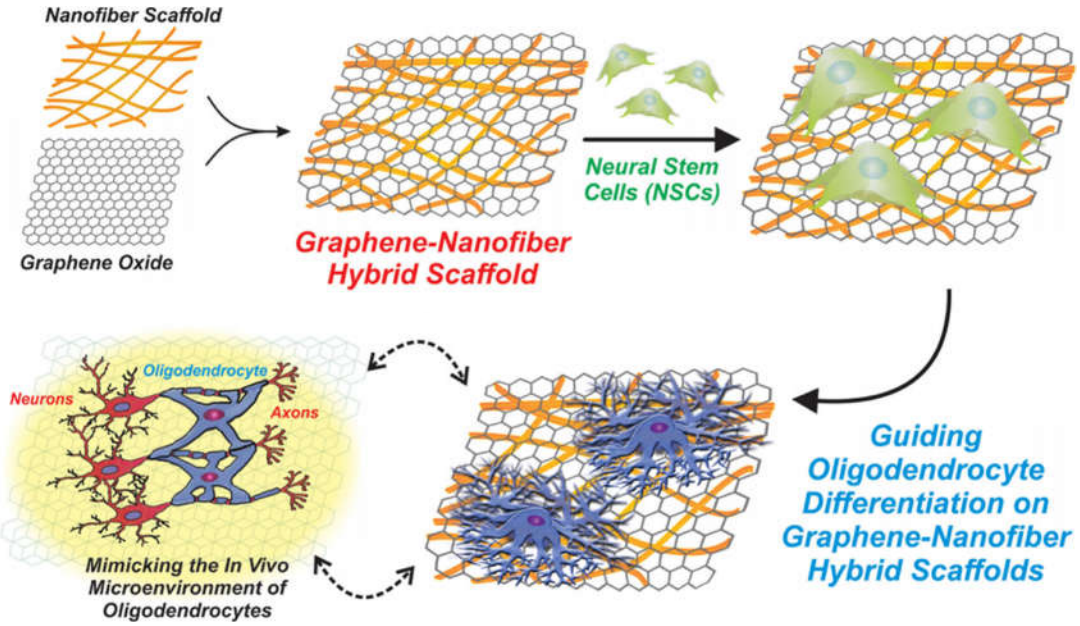

Figure 1-6. Schematic diagram depicting the fabrication and application of graphene-nanofiber hybrid scaffolds. Polymeric nanofibers generated using electrospinning were subsequently coated with graphene oxide (GO) and seeded with neural stem cells (NSCs). NSCs cultured on the graphene-nanofiber hybrid scaffolds show enhanced differentiation into oligodendrocyte lineage cells. [69]

entrapping the bioactive agents in an intermediate state, bioactive agents are physically encapsulated inside of the cross-linked polymers. Another method of loading bioactive agents into nanofiber is to bind the bioactive agents chemically onto the polymer structure of nanofiber through hydrogen bonds, covalent bonds, hydrophobic, and electrostatic interactions.

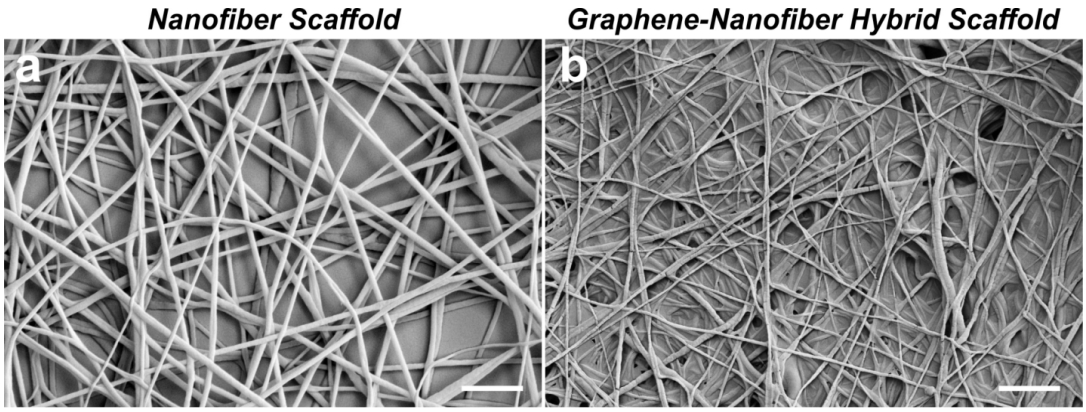

Figure 1-7. Morphology of plain scaffold and graphene oxide (GO) coated nanomaterial-nanofiber hybrid scaffold. (a,b) Field emission scanning electron microscopy (FE-SEM) images of PCL nanofibers (a) and PCL nanofibers coated with 1.0 mg/mL GO solution (b). Scale bars: 2 μm. [69]

Drug release from nanofibers can be described through three mechanisms: desorption from fiber surface, diffusion through fibers, and in vivo fiber degradation[279]. When the nanofiber carrier is subjected to a physiological condition, body fluid or tissue culture media will penetrate the space in between individual nanofibers. When the nanofiber drug carrier is swollen by the aqueous phase, drugs or proteins attached to the fiber surfaces can be released. Upon desorption from fiber surface, drugs will be disused into the aqueous phase.

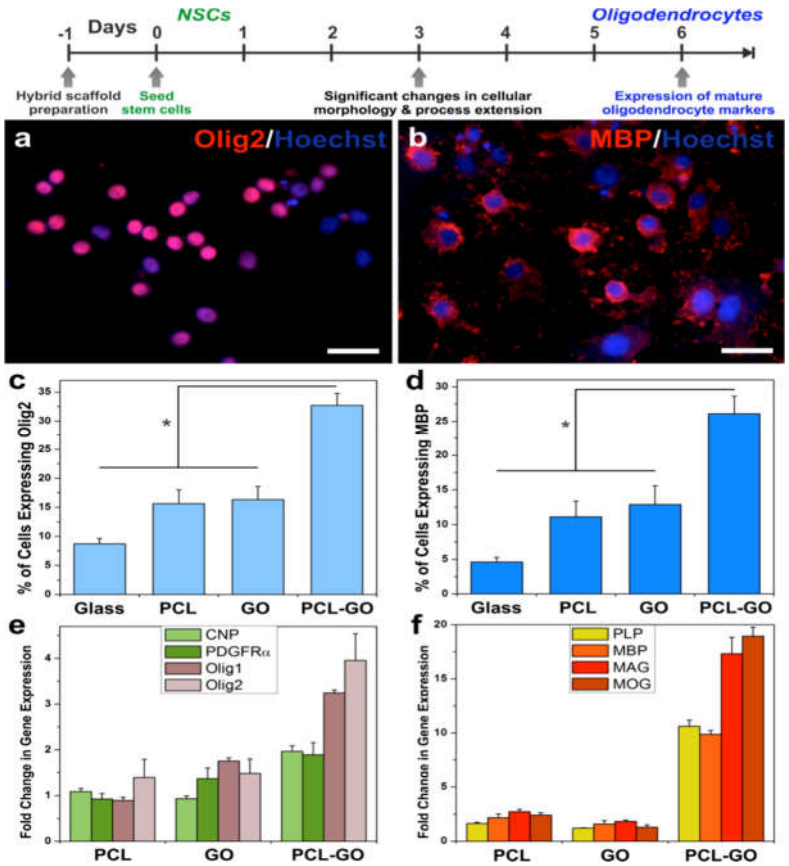

Figure 1-8. Enhanced oligodendrocyte differentiation on PCL-GO nanofiber-nanomaterial hybrid scaffold. (a,b) Immunocytochemistry image of NSCs after six days of culture on hybrid scaffolds, stained for the early oligodendrocyte marker Olig2 (a) and the mature oligodendrocyte marker MBP (b). Scale bars: 20 µm. (c,d) Quantitative comparison on various substrates of the percentage of cells expressing Olig2 (c) and MBP (d). (e,f) Quantitative PCR analysis showing gene expression of early oligodendrocyte markers including CNP, PDGFR, Olig2 and Olig2 (e), and mature oligodendrocyte markers including PLP, MBP, MAG and MOG (f). The gene expression is relative to GAPDH, and normalized to the PLL-coated glass control. [69]

Conclusions

Stem cell therapy holds the key of regenerative medicine for functional recovery from various injuries and diseases. Addressing the current challenges, nano-chemists and biologists have invested in various nanomaterials and their assembly in multidimensional domains to mimic the properties of the natural microenvironment to promote and dictate stem cell differentiation into desired lineages. In this review, the benefits of nanomaterial in the field of stem cell biology are clearly shown to be advantageous over traditional methods including bio-reagent delivery, in vivo imaging modality, and transplantation platform. Although much has been investigated to this point, there remains more investigation to be done in the clinical applications of multi-dimensional nanomaterials.

1.4 Multi-dimensional nanomaterials-enabled biosensors

Biosensors that provide information on the disease-relevant biological targets and cell signals have been valuable tools for biologists and clinicians. There have been many biosensors that successfully detect different biomolecules based on approaches such as Raman spectroscopy, cyclic voltammetry, Field-emission transistors, mass spectroscopy, high performance chromatography (HPLC), reflectometer, IR spectrometer, UV-Vis absorption spectrometer, magnetic resonance imaging and microbalance. The fundamental mechanism of these biosensors are based on the conversion of biochemical signals to electrical, optical, magnetic, thermal and mechanical signals, which can be visualized or measured directly. To this end, many nanomaterials that have these unique physical properties and simultaneous large surface areas for signal conversion can provide excellent solution to improve the sensitivity of biosensors. Currently, the trend of biosensor development is towards the real-life implementation, for example, the cost-effective, highly reproducible, highly mobile and throughput, miniaturization, real-time and wearable devices. In this regard, nanomaterials-based biosensors are still far from satisfactory, despite the huge promise they hold for the improved healthcare solutions. Therefore, it is critical to understand the representative biosensing systems and what are the critical steps for them towards next-generation biosensors. Comprehensive reviews have been done by many other great scientists focusing on different types of biosensors or varying categories of nanomaterials. Here I mainly highlight several representative biosensor systems for different dimensional nanomaterials.

1.4.1 0D plasmonic nanomaterials-based optical sensors

Surface plasmonic resonance refers to the coherent oscillations of electron cloud of the metal surface under the electromagnetic radiation field and at a dielectric-metal interface[34] [280-289]. The field focusing on such unique light-matter interactions is termed "plasmonics." In metal nanoparticles, the plasmon resonance can be localized and non-propagating, which is known as "localized surface plasmonic resonance (LSPR)" [280,281]. It has been well studied that the spectrum and the intensity of LSPR are highly dependent on the shape, dimension, surrounding dielectric environment and metal of the nanoparticles[13]. The dependence on the local dielectric properties has been used as principles for a variety of plasmonic biosensors. On the other hand, the utilization of LSPR with the enhanced electromagnetic field has been applied for surface enhanced spectroscopies such as surface-enhanced Raman spectroscopy (SERS), and metal enhanced fluorescence (MEF) assay in the biosensing [290-299]. Overall, the broad applications of 0D plasmonic nanostructures in biosensing mainly include particle-particle coupling-based colorimetric biosensing, metal nanoparticle-enhanced LSPR, Rayleigh scattering-based sensing, LSPR-based refractive index sensing, SERS and MEF. Among them, SERS-based biosensors are one of the most investigated as they can be used for label-free and label-based detection of biomolecules both in solution, in vitro and in vivo. Also, they can have high sensitivity down to single-molecule level and an amplification factor above 10^{14} fold for ultrasensitive biosensors [280,281,283,289,297,299]. Moreover, SERS, as a special type of Raman spectroscopy, can be performed in aqueous-based environments and have sharp fingerprint peaks for multi-color detection. Furthermore, the SERS signals are highly sensitive to the change of nanostructures and such signal changes are often non-linear, thereby providing a unique signal amplification strategy. In this regard, 0D nanoparticles are particularly useful.

Before the induction of aggregation, 0D nanoparticles typically have low SERS signals, due to a weak amplification of the electromagnetic field. However, once a target biomolecule was introduced to induce the aggregation of nanoparticles, the SERS signals will dramatically increase, which are also known as the increase of "hot spots". This process has been applied for detecting low concentrations of targets in a highly sensitive and selective manner. One of the representative biosensor based on 0D plasmonic nanoparticles is the SERS-based DNA and RNA detection, which is initially developed by Mirkin group[300].

Gene detection based on DNA or RNA sensing is fundamental for the understanding of many biological processes and for probing diseases[301-308]. While biological methods such as qRT-PCR have been widely used for detecting DNA or RNA, multiple steps are required to achieve a highly sensitive detection[300]. To this end, people have developed and incorporated several other gene detection methods with high sensitivities without requiring amplification. Scanometric DNA detection, for example, can achieve a sensitivity of 50 fM. However, such scanometric DNA detection usually can only detect a single gene at one time, thereby limiting their applications in multiplex gene monitoring, which is essential for gene analysis. Fluorescence-based detection, which monitors multiple genes based on different colors, micrometer-sized probes are still needed to obtain the encoded structures with proper uniformity. To this end, Mirkin group developed a gold nanoparticle-based SERS biosensor for the detection of genes with high sensitivity at 20 fM[300]. First, a 10 nm gold nanoparticle functionalized by Cy3 labeled and thiol-functionalized DNA with complimentary sequence to one end of the target gene, was fabricated through thiol-gold binding. This 10 nm gold nanoparticle has relatively low

scattering and enhancement effects on the local electromagnetic field; thereby no significant Raman signals will exist in the solution.

Meanwhile, a planar gold substrate that is also functionalized with DNA with complementary sequences to the other end of the target gene was also prepared. When the target DNA was added into the solution, the DNA functionalized gold nanoparticle and planar gold substrate will recognize each end of the target DNA, then forming a conjugated structure using the target DNA as a bridge. At this stage, the distance between a gold nanoparticle and gold substrate will be substantially decreased down to few nanometers, forming a sandwich structure with Cy3 dye in between two gold structures, which is also known as the hot spot. This unique structure is known to induce a few order strong enhancement of electromagnetic field and leading to a dramatic change of SERS signals. Thus, DNA or RNA concentrations as low as 20 fM can be effectively detected. Moreover, as SERS signals include a variety of sharp fingerprint peaks, different Raman dyes other than Cy3 can be used for multiplex gene detection by simply using different probe DNA sequences. For example, from a single DNA or RNA detection assay, DNA sequences from six different viral sources (HVA, HVB, HIV, EV, VV and BA) can be detected and differentiated from each other at low concentrations, suggesting its high selectivity, high sensitivity and multiplex gene detection. This system provides strong arguments on the nanoparticle-based next-generation biosensing applications and has inspired many works on exploring SERS-based gene detection.

1.4.2 1D silicon nanowire-based bioelectronic sensors

Silicon nanowire and carbon nanotube are probably the two mostly representative 1D nanostructures for bioelectronic applications and are fundamental building blocks of the field of nanoelectronics. 1D silicon nanowire was first synthesized by Lieber group at Harvard at 1997 and Lee group at Hong Kong University at 1998 using vapor-liquid-solid (VLS) mechanism[309]. VLS mechanism is typically achieved by using nanocatalyst such as gold nanoparticles, which absorb the vapor reactant (e.g., SiH4) at high temperature[310]. Then the continuous absorption of the reactant on gold nanoparticles lead to the saturation and precipitation of the semiconductor materials at the VLS interface to achieve a most energy stable form. Based on this unique 1D nanostructure of silica, many interesting applications have been developed. Among them, biosensing based on silicon nanowire-enabled field-effect transistor (FET) has been one of the most representative areas, which I will focus on in this part of the introduction.

As a basic building unit for high density integrated circuits, FET is composed of the semiconductor substrate such as silicon, the gate, drain and source electrodes[311-321]. The drain and source electrodes that collect and inject currents are doped oppositely to the semiconductor substrate. The gate, which is coupled to the semiconductor substrate capacitively, influences the current flow by applying different voltages (Vg). When no voltage is applied, the p-n junction will have no current flow. When a certain voltage is applied, the current start to appear due to the induction of charge carriers and the decrease of the potential barrier. To apply for biosensors, the conductivity of silicon nanowire can change based on the changes of charge densities[309]. In another word, when we functionalize the silicon nanowires with surface receptors to specifically bind to the target biomolecule, the charge density will change and lead to current changes, which is a similar process of

applying a voltage to the semiconductor layer in the planar form of FET. When p-type Si-nanowire was used, the recognition and absorption of a target with a negative charge will increase conductance, thereby increasing the signals in FET current. Comparing to other semiconductor materials that have been used in FET biosensors such as indium oxides and zinc oxide, Si Nanowires have sub 10 nm sized diameter and versatile surface functionalities while maintaining high hole or electron mobility. Thus, Silicon nanowire-based FET biosensors for the detection of nucleic acid, protein, virus have been widely developed. One of the pioneering work is the detection of proteins using such FET biosensors. The silicon nanowires, which typically have a SiO2 coated surface, can be functionalized with amino propyl triethoxysilane (APTES), which further conjugate to NHS ester terminated biotin receptor. Using this functionalized silicon nanowires, the FET biosensor can selectively detect streptavidin that specifically binds to biotin receptors and leads to a current change[6]. The concentration of streptavidin as low as 10 pM can be sensitively detected. Recent advancements have included the development of reversible binding and detection of protein through reversible bonds such as biotin- antibiotic binding, the success of multiplex protein detection based on high-intensity FET biosensor arrays, and the incorporation of a top-down method to fabricate silicon nanowire-based FET biosensors.

1.4.3 2D nanosheets-based optical and electronic sensors

Compared to the 1D silicon and other nanowires-based biosensors, 2D nanomaterial-based bioelectronic sensors have higher surface areas, which not only increase the binding sites for the binding towards analytes but also increase the sensitivity of the device[164]. For

graphene more specifically, graphene-based FET is advantageous regarding the high conductivity compared to 1D nanomaterials[322-346]. However, different from the silicon-based biosensors, graphene-based FET biosensors require more complex surface functionalization. This is because the direct covalent functionalization usually causes changes of the sp2 lattice of the graphene, leading to a decrease of conductivity. Therefore, non-covalent binding of probes through π-π stacking or hydrophobic interactions are widely used. On the other hand, covalent conjugation of probes on graphene lattice will improve the selectivity and reproducibility of the biosensor. Based on these strategies, in 2008, Mohanty and Berry's lab reported the first graphene-based FET biosensor by covalently conjugating single strand DNA probes to the graphene oxide (GO)-based substrate[347]. After the binding towards complimentary DNA, the conductivity of GO changes, leading to signal a change of the FET biosensor. By using graphene substrate grown by chemical-vapor-deposition (CVD), scientists improved the sensitivity to 10 pM for the DNA detection, which is benefited from the significantly higher conductivity of graphene. By further decorating the graphene with gold nanoparticles by improving the binding sites and surface ratio on graphene-based detection systems. Using peptide nucleic acid (PNA) instead of DNA was found to improve the sensitivity to the range of 100 fM level, due to the stronger binding affinity of PNA towards target DNA and a less strict requirement on ionic strengths of detection environment. There have been many other works ongoing to apply graphene-based electronic sensors to detecting biomolecules in a highly sensitive and selective manner. The requirement on detecting environment also become less. For example, people now are interested in the detection of biomolecules under cell culture conditions or even under in vivo conditions. Despite the great advancement in

the nanomaterial-based biosensor systems, there are still plenty of room to study important questions such as how to achieve ultrasensitive detection under complex biological fluids, how to improve the selectivity when the target analytes are low in concentration in the solution and how to develop implantable biosensors that is wearable, flexible, biodegradable and biocompatible for next-generation healthcare solutions. These critical challenges will be solved in the next decade by improving the fabrication of nanomaterial-based biosensors, the surface functionalization of biosensors and the advancement in nanomaterial synthesis.

Chapter 2: 0D-2D hybrid nanomaterials for advanced cancer therapy

2.1 Graphene-Plasmonic Hybrid Nanoparticles-based Photothermal Therapy

Note: This is a published work published in Scientific Reports[50]. As a co-first author, my major contribution is on the synthesis and characterization of the nanoparticles and evaluate their therapeutic effects in cancer spheroids.

2.1.1. Introduction

The American Cancer Society predicts 1.6 million new cancer cases and 600,000 Americans to die of cancer in 2017. This corresponds to 1,650 death per day, making cancer the second most common cause of death in the USA.[348] The mortality rates are still high despite a high level of spending on cancer therapy.[349] Despite many new drugs developed with higher anti-cancer therapeutic potential, the key challenge lies in high throughout the screening and explicitly understanding the effects of these new drugs in more clinically relevant models. Currently, two-thirds of all drugs that enter Phase II clinical screening and a third of drugs entering Phase III clinical trials fail to transit into the next stage.[350] To obtain a higher success rate in clinical trials, there is an urgent need for the development of drug screening methods which could predict the toxicity and efficacy with higher accuracy and better represent tumor microenvironment.[351] One promising approach for drug screening applications is the use of three-dimensional (3D) cell culture systems. In conventional two-dimensional (2D) cell cultures based on tissue culture plates, cell-cell and cell-matrix interactions are less prevalent compared to in vivo 3D environments, thereby failing to mimic tumor precisely. Additionally, the cells in 2D cultures can be

stretched leading to cytoskeletal rearrangements and artificial polarity.[352] In 3D cultures, in contrast, the cell environment can be reproduced with higher accuracy including cell-cell, cell-matrix interactions.[353] Ma et al. compared the chemotherapy and nanoparticle penetration properties of different culture systems.[354] They observed that 3D spheroids of HeLa cells displayed similar morphologic characteristics as solid human tumors. 3D spheroids also showed some characteristics of solid tumors, such as resistance to chemotherapeutics that could not be observed in 2D cultures.

Spheroids are generally formed using pellet culture[355], liquid overlay[356], hanging drop[357], spinning flask[358], and magnetic levitation methods.[359] However, these conventional methods have limitations, such as lack of reproducibility and wide distribution of spheroid sizes. To this end, advances in microfabrication techniques provide a promising solution.[360] Microwell arrays can provide a facile method to produce uniform-sized spheroids in a high-throughput manner.[361] For example, concave poly(dimethylsiloxane) (PDMS)-based microwells have been used to generate cancer spheroids which were used for screening anticancer drug-loaded nanoparticles.[362] Due to their biocompatibility and widely tunable physical properties and biodegradabilities, hydrogels have also recently been used as a microwell material.[363] One such example is poly(ethylene glycol)(PEG) based hydrogel microwells, based on which uniform-sized embryoid bodies can be reliably created and cultured.[364] Alternatively, cell spheroids have also been formed by encapsulating cells into a PEG hydrogel with restricted volumes, which can further achieve a higher control over cell-cell interactions.[365] Lee et al. found that the spheroid size and functionality could be modulated by the stiffness of the encapsulating hydrogel.[366] Utilizing cell spheroids

encapsulating hydrogel particles for self-assembling, macroscopic 3D structures have been further achieved.[367] Still, given that usually multiple cell types are involved during tissue and tumor genesis, and considering the complex and heterogenous microenvironment during tumor genesis, it is challenging to utilize previously developed single-cell spheroids for accurately mimicking organs or tumors for precision drug screening. To this end, reliable methods for creating multicellular spheroids are of particular value. For example, HepG2 and NIH3T3 fibroblast cells in spheroids were co-cultured in a digital microfluidic device to better mimic in vivo liver functions.[368] Also, progenitor cells and mesenchymal stem cells were co-cultured in PDMS microwells to form spheroids.[369] Moreover, spheroids of rat hepatocytes and fibroblasts were formed on electrospun scaffolds[370] and colonic adenocarcinoma cells in co-culture with normal colonic fibroblasts were formed using a rotary orbit shaker.[176] Despite the development of these co-culture spheroid systems, the methods are still either labor intensive or produce spheroids in a non-homogeneous manner, which can lead to inconclusive results when applied for screening anti-cancer therapeutics. Therefore, a high throughout and reliable approach that can produce homogeneous multicellular spheroids is needed.

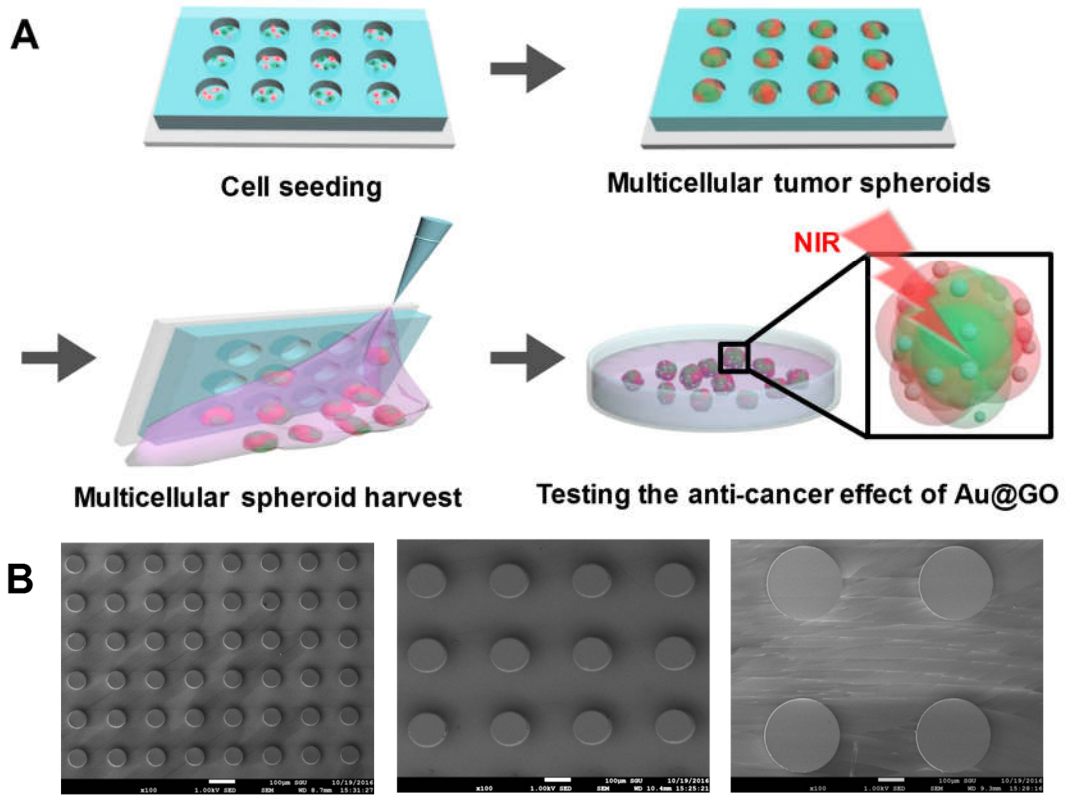

Figure 2-1. Schematics of uniform-sized 3D tumor spheroid culture inside of PEG hydrogel microwells, spheroid harverst and use of spheroids in for PTT experiments (A). SEM images of PDMS stamp for the PEG hydrogels with microwell diameters of 75 (left), 150 (middle), and 300 μm (right) (B).

Recently, nanomaterials (e.g., graphene nanosheet[371], gold nanoparticle) have been used to explore the cancer biology.[372] Compared to a conventional small molecule for anti-cancer therapy, the unique physical and chemical properties not only made these nanomaterials excellent drug delivery platform, but also unique anti-cancer reagents and imaging reagents. Through a further hybridization of the two nanomaterials using surface engineering, unique physiochemical properties from every single nanoparticle can be dynamically integrated into a single platform for versatile biological applications.[373] For example, gold nanoparticles encapsulated by graphene oxide (GO) nanosheets can be used to detect changes on a cellular level using Surface Enhanced Raman Spectroscopy (SERS)[374], or a gold nanocluster-functionalized reduced GO nanosheets were used for combined drug delivery and imaging of cancer cells.[375] However, despite being a highly potent cancer theragnostic reagent, its therapeutic effects have not yet been evaluated in well defined 3D culture systems. This is further compounded by the generally dramatically increased sizes and more heterogenous surface chemistries from nanomedicinal reagents, which could lead to higher complexity during drug screening as compared to conventional small molecules. Addressing these challenges, we developed a high throughout hydrogel microwell array-based method for generating uniform-sized multicellular tumor spheroids. The microwell array is successfully demonstrated in multiple co-cultures including HeLa/human umbilical vein endothelial cells (HUVEC) and HeLa/Ovarian cancer cells. While the HeLa/HUVEC co-culture acts as a tumor/endothelium model, HeLa/Ovarian co-culture can be used to simulate metastasis in carcinomas. Based on the spheroids based drug screening platform, we investigate the potential of a novel hybrid gold nanoparticle-

functionalized graphene oxide (Au@GO) for photothermal therapy (PTT) based anti-cancer applications.

2.1.2 Materials and Methods

Hydrogel Microwell Fabrication

Hydrogel microwell arrays were fabricated using a PDMS stamp as previously described.[364,376] Briefly, photomasks were designed using Autocad (Autodesk, USA), printed on a photomask, and transferred onto silicon wafers (Wanxiang SiliconPeak Electronics Co., China) using SU-8 negative photoresist (MicroChem Corp., USA) according to manufacturer's instructions. After ultraviolet (UV) light exposure, wafers were treated with the SU-8 developer (MicroChem Corp., USA). PDMS prepolymer solution (10:1, monomer: curing agent, Sylgard 184, Dow Corning Corp., USA) was poured onto the silicon molds and air bubbles were removed in a vacuum chamber for 30 minutes, followed by curing in an oven at 85°C for 2 hours. The glass slide, acting as a substrate for supporting the hydrogel microwell array, was then treated with 3-(trimethoxysilyl) propyl methacrylate (TMSPMA, Sigma-Aldrich Co., USA) for 30 minutes and further heated for 1 hour at 70°C afterwards to provide better adhesion to the hydrogel. An aqueous solution containing 10% (w/w) PEG 1,000 dimethacrylate (Polysciences, USA) and 1% (w/w) of the photoinitiator, 2-hydroxy-2-methyl propiophenone (Sigma-Aldrich Co., USA), was poured between the glass slide and the PDMS stamp. The hydrogel was crosslinked by a radical chain growth reaction for 20 seconds using a UV light source (320-350 nm, Omnicures Series 1500, EXFO, Canada). Lastly, the PDMS mold was carefully peeled from the glass slide and hydrogel microwell

arrays washed with ethanol followed by overnight storage in phosphate buffered saline (PBS, Thermo Fisher Scientific, USA).

Spheroid Culture

For spheroid culture, green fluorescent protein (GFP)-labeled HeLa cells and red fluorescent protein (RFP)-labeled ovarian cells, were cultured in Dulbecco's Modified Eagle's Medium (DMEM, Thermo Fisher Scientific, USA) with 10% fetal bovine serum (FBS, Thermo Fisher Scientific, USA) and 1% penicillin-streptomycin (Thermo Fisher Scientific, USA). Further HUVEC-labeled with cell trace violet cell proliferation kit (Molecular Probes, USA) were cultured in Endothelial Cell Growth Medium-2 (EGM-2, Lonza, Switzerland). The cells were seeded into the hydrogel microwell arrays with a concentration of $1x10^6$ cells/mL and incubated for one day at 37°C. The tumor spheroids formed in the hydrogel microwells were replated onto polystyrene confocal dishes (Ibidi, Germany) and were subsequently incubated for one more day at 37°C.

Synthesis of Au@GO Nanoparticles

Au@GO nanoparticles with 40 nm size 40 nm and spherical shape were synthesized from positively charged nanoparticles and negatively charged GO using an electrostatic enabled assembly method.[253] All the reagents used were from Sigma Aldrich. Briefly, to synthesize positively charged nanoparticles, 5.0 mg of $HAuCl_4 \cdot 3H_2O$ solution was prepared at 4 degrees, then 1.0 mL of 3.0 mg/mL cysteamine was quickly added to the gold yellow solution.[377] The solution should turn orange immediately, and then was further stirred under room temperature. After 15 minutes' stirring, under dark conditions, 15 μL of 3.8

mg/mL $NaBH_4$ was quickly injected into the solution under rapid stirring. One hour later, the stirring was slowed down and the reaction was continued overnight to obtain dark red colored cysteamine-functionalized gold (Au-CA) nanoparticles. To synthesize the negatively charged GO, a modified two-step Hummer's method was used.[47] By adding 1.0 g of graphite, 2.5 g $K_2S_2O_8$, 2.5 g P_2O_5, and 12 mL concentrated H_2SO_4 (98%) step by step with caution, the viscous solution was stirred overnight at 80°C. Then, the mixture was slowly added to 500 mL of distilled water and further stirred overnight. Pre-oxidized graphite was obtained by filtering the 500 mL solution and was dried for 24 hours. To obtain graphite oxide, the pre-oxidized graphite oxide was added into 120 mL H_2SO_4 (98%), and 15 g of $KMnO_4$ powder was slowly added into the solution under 10°C, and the mixture was stirred under 35°C for 4 hours, followed by a slow addition of 250 mL distilled water. After further stirring for 3 hours, the reaction was quenched by the drop-by-drop addition of 20 mL 30% H_2O_2, with the appearance of shining yellow colored graphite oxide. GO was obtained by first purifying graphite oxide by 10% HCl and distilled water, then the graphite oxide was exfoliated by a Brandson ultrasonicator. To synthesize the GO core-shell nanoparticle, 1.0 mL of diluted solution (100 μg/mL) of cysteamine functionalized gold nanoparticle was slowly added (2 mL/h) into 10 mL of concentrated (1.0 mg/mL) of GO under vigorous stirring. After 2 hours, the particles were purified by centrifugation at 10,000 rpm for 10 minutes, followed by distilled water washing 3 times. The final concentration of nanoparticles was adjusted accordingly by adding the proper amount of water. To characterize the nanoparticles, a Philips CM12 electron microscope with an AMT-XR11 digital camera was used for transmission electron microscopy (TEM) characterization; a Malvern Nano series Zeta sizer was used for measuring the

hydrodynamic sizes and surface charges; Agilent Cary 60 UV-Vis was used to measure the UV-Vis spectrum.

Cell Viability Analysis

The cell viability was measured using 3-(4,5-Dimethylthiazol-2-yl)-2,5-Diphenyltetrazolium Bromide (MTT) assays (Roche, Germany). Fluorescent-activated cell sorting (FACS, FACS Calibur, BD Bioscience, USA) analysis was further conducted. FACS results were visualized using the Flow-Jo software (BD Bioscience, USA).

Photothermal Therapy

After replating the spheroids onto the polystyrene confocal dish and further incubation for one day, the culture medium was exchanged with medium containing 1 vol% Au@GO and was subsequently incubated for one day. Lastly, the spheroids were irradiated with near infrared (NIR) laser (808nm, 5W/cm^2, BWF2, B&W, Denmark) for 10 minutes.

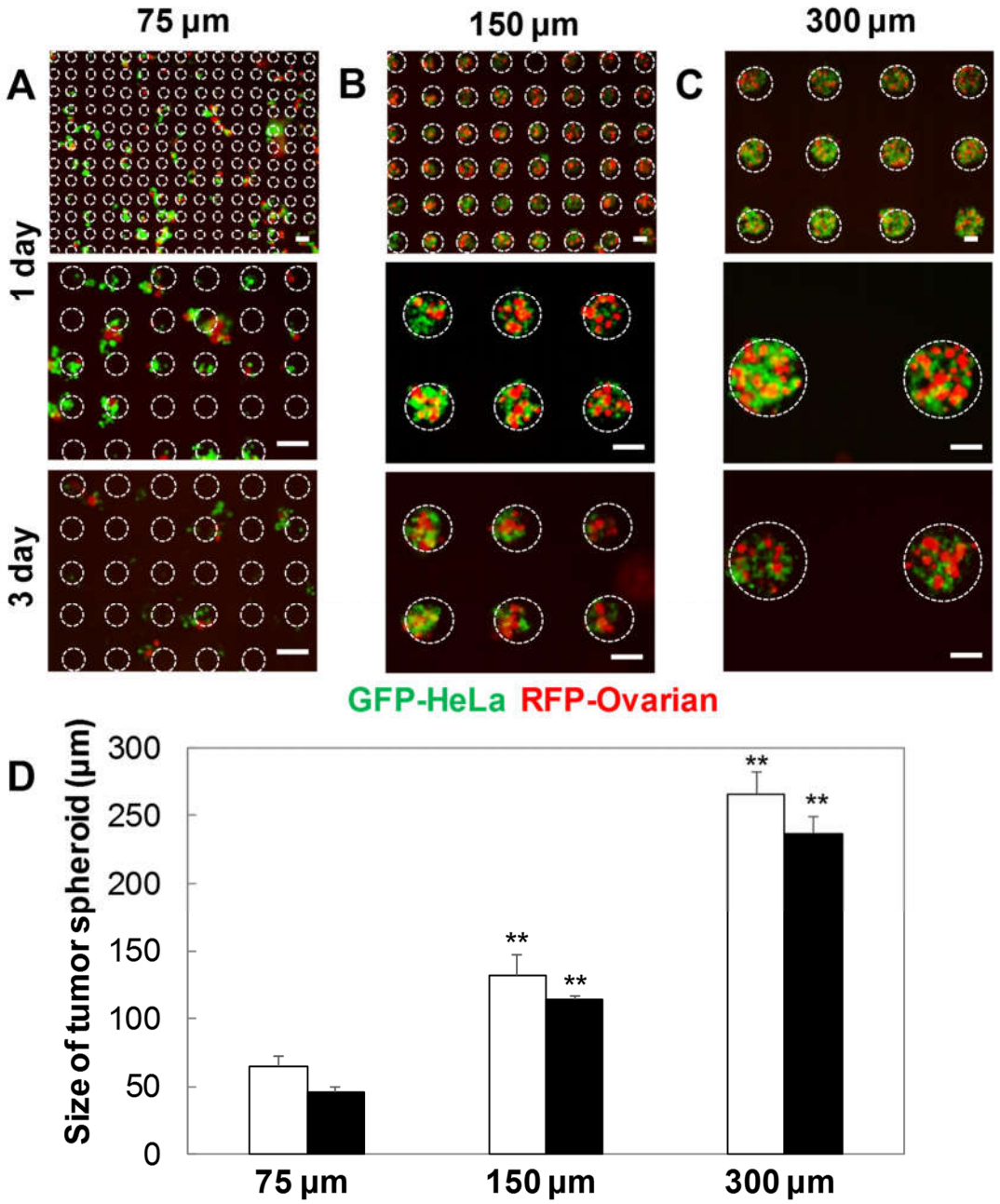

Figure 2-2. Fluorescent microscopy images of HeLa (green) and Ovarian (red) spheroid co-cultures inside of 75 (A), 150 (B), and 300 µm microwells (C). Scale bars are 100 µm. Analysis of spheroid diameter after one (white bars) and three days (black bars) of culture inside hydogel microwells with different sizes (D).

2.1.3 Results and Discussion

Hydrogel Microwell Fabrication for Multicellular Tumor Spheroids

We developed PEG hydrogel microwells to generate uniform-sized multicellular tumor spheroids (Figure 2-1). The PDMS stamps were able to reproduce microwells with diameters of 75, 150, and 300μm as shown by scanning electron microscopy (SEM) (Figure 2-1B). Co-culture of tumor spheroids inside of the hydrogel microwells was facile and it could be observed that after one day of culture spheroids had formed for all three microwell sizes (75, 150, and 300μm, Figure 2-2, A-C). While the cells grew exclusively inside the larger microwells (150 and 300 μm in diameter), cell growth could also be observed around the smallest microwells (75μm in diameter) (Figure 2-2A). This is probably due to the growing spheroids becoming too large for the microwells and consequently fail to precisely follow the shapes of microwells in early stages of spheroid growth, indicating a lower size limit for spheroid size. It could be observed that the co-culture spheroids inside of the microwells reduced in size after three days of culture (Figure 2-2D). This observation corresponds to the observations of spheroid formation made by Lin et al..[378] Three stages in spheroid formation were observed, an initial rapid aggregation, a delay period, and a final tight compaction phase. While the first rapid phase is usually completed within the first 12 hours, it can take up to 36 hours for the final phase to complete. In this paper, the first measurement of spheroid size falls within the delay period after the first aggregation phase. The second measurement of spheroid size, however, is after the final aggregation phase which leads to the observed decrease in spheroid size.

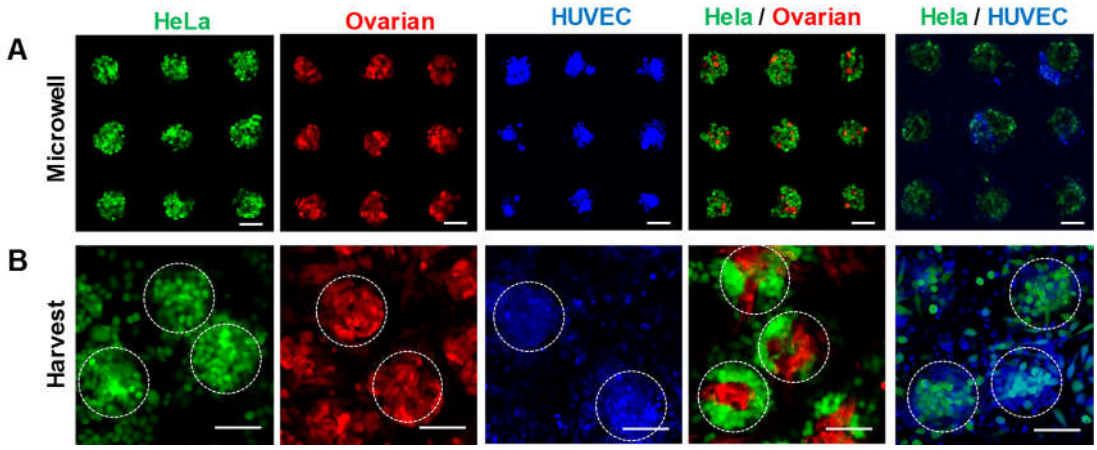

Figure 2-3. Flourescent micoscopy images of tumor spheroids, consisting of HeLa (green), Ovarian (red), HUVEC (blue), and co-cultures of HeLa/Ovraian and HeLa/HUVEC inside of the 150 µm hydrogel microwells after one day of culutre (A) and after harvesting (B). Scale bars are 100µm.

Here, we decided to harvest the spheroids onto polystyrene confocal microscopy dishes after one day for the final aggregation steps to occur on the substrate that will be used for PTT experiments. Figure 2-3 shows spheroids in 150µm microwells before and after harvesting. We observed that the spheroids get distorted in their shape when changing from a 3D hydrogel microwell to a 2D culture substrate. This can be attributed to the lacking support of the 2D substrate. The confocal microscopy images showed that both HeLa and Ovarian spheroids, as well as the HeLa/Ovarian co-culture spheroids, retained their original sphere shape well after replating. In contrast, HUVEC and HUVEC/HeLa co-culture spheroids became significantly more disturbed in their shape. This can be explained by HUVEC cells, showing a lower tendency to self-aggregate, further HUVEC spheroids are

slower to form strong intercellular connections than HeLa and Ovarian cells.[379] Despite these morphological deformations, all spheroids preserve their 3D characteristics as shown by confocal z-stack microscopy (Supplemental FigureS1).

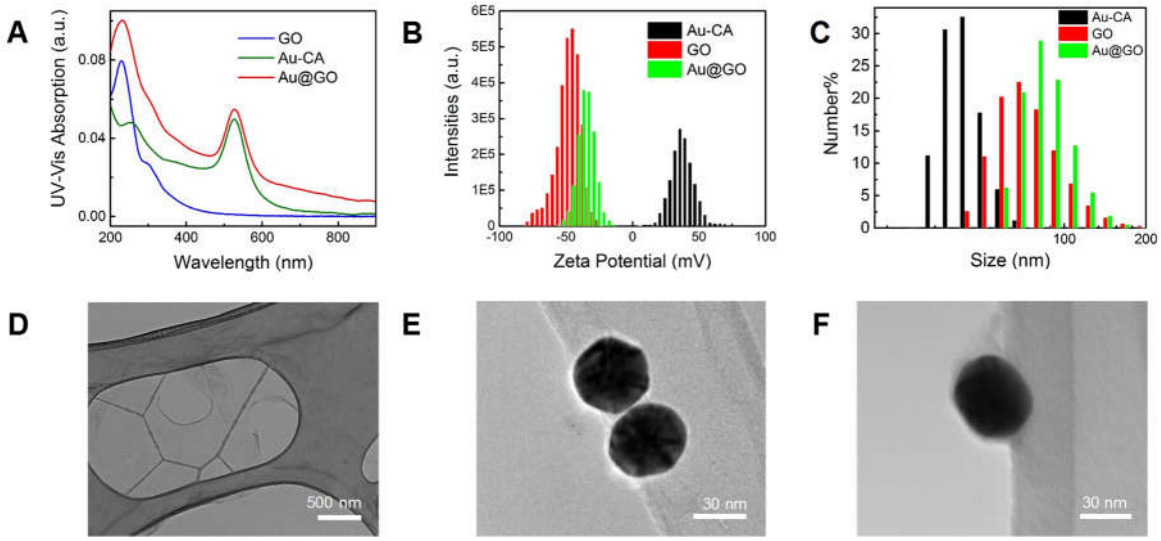

Figure 2-4. Characterasations of the Au@GO nanomaterial. UV-Vis spectra of GO, Au-CA nanoparticle, and Au@GO nanoparticle (A), corresponding Zeta potentials (B), and size distributions (C). TEM images of GO (D), gold nanoparticles (E), and Au@GO nanoparticles (F).

Synthesis of Nanoparticles

To investigate the therapeutic potential of hybrid nanomaterials using our generated 3D spheroid co-culture model, we synthesized 40 nm hybrid Au@GO nanoparticles with a core-shell structure. This core-shell nanoparticle was synthesized based on the electrostatic assembly between positively charged gold nanoparticles (+32 mV, cysteamine functionalized) and negatively charged nano-sized GO (110 nm, -49 mV). A 40 nm was selected to achieve a balance between cellular uptake and efficient photothermal therapy.[380]

To obtain the positively charged gold nanoparticles, cysteamine was used simultaneously as a reductant and capping reagent in an aqueous based reaction with $HAuCl_4$. Nano-sized GO with high oxidation levels, on the other hand, was synthesized from a modified Hummer's method. Electrostatic assembly between these two nanoparticles was initiated by the slow addition of positively charged gold nanoparticle solution into a concentrated GO solution. A reversed addition sequence from GO to gold nanoparticles would lead to unstable colloidal aggregations with large sizes, which would be less suitable for delivery-based applications as well as for cancer targeting. The successful formation of our core-shell hybrid structure was characterized by UV-Vis spectroscopy, zeta potential, hydrodynamic sizes and TEM, respectively (Figure 2-4A-C). In the UV-Vis spectrum collected from the Au@GO nanoparticles, it shows two representative absorption peaks from gold nanoparticles at a wavelength of 530 nm (surface plasmon resonance peak) and goes at a wavelength of 225 nm (π-π^* transition).[381] Meanwhile, after encapsulated by the GO to form the Au@GO nanoparticles, the positive zeta potential of CA-Au nanoparticles dramatically changed from a highly positive charge of 32 mV to a negative value of -35 mV, indicating the successful GO coating on its surface. This encapsulation of GO on gold nanoparticles is also supported by an increase of hydrodynamic size for the Au@GO nanoparticles to 92 nm, as compared to the GO (81 nm) and gold nanoparticles (45 nm). TEM images of Au@GO nanoparticles provide even more direct evidence on the core-shell hybrid structure, where thin-layered GO films enwrap the surface gold nanoparticles with a significantly different shape as compared to TEM images of individual GO or gold nanoparticles (Figure 2-4D-F). These characterizations of Au@GO nanoparticles

collectively well support the successful synthesis of Au@GO nanoparticles assembled from positively charged gold nanoparticles and negatively charged GO.

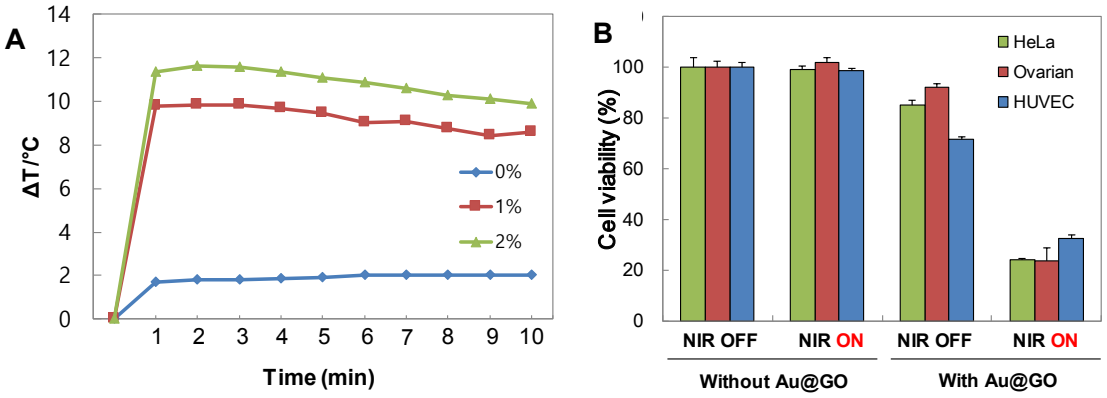

Figure 2-5. Photothermal effect of the Au@GO nanoparticle. Photothermal heating with different concentrations of Au@GO nanoparticles (A). Cell viability of HeLa, Ovarian, and HUVEC cells after NIR treatment with Au@GO nanoparticles and control experiments without Au@GO nanoparticles (B).

Photothermal Therapy Effect

A temperature of above 47°C is desirable to achieve thermal ablation of the cancer cells. First, it was tested which concentration of Au@GO nanoparticles is required to reach this temperature starting. As shown in Figure 2-5A, after one minute of NIR irradiation, temperatures differences of 10°C (starting from body temperature at 37°C) are reached, with only 1 vol% of Au@GO nanoparticles. Increasing the concentration to 2 vol% only leads to a marginally higher temperature, which is not relevant for PTT applications. Hence, a concentration of 1 vol% was chosen for the following experiments. Subsequently, PTT experiments with 2D mono-cultures and spheroids were carried out to test the photothermal effect on the individual cell types (Figure 2-5B). Control experiments without the addition of Au@GO nanoparticles showed no negative effects of NIR irradiation on cell viability in 2D cultures. The addition of Au@GO nanoparticles leads to low dark toxicity before NIR treatment as also observed in toxicity experiments (Supplemental FigureS2). After NIR treatment, the viability of cells reduced drastically to 20% in the case of HeLa and ovarian cells, and 32% in the case of HUVEC cells. These results were confirmed by fluorescent microscopy images, taken of the corresponding spheroids before and after NIR treatment (Supplemental Figure 2-S3). In the fluorescent microscopy images, it was observed that the HUVEC spheroids displayed higher viability after NIR treatment compared to HeLa, and Ovarian spheroids similar to the observations made in 2D cultures. We believe that the difference in viability can be explained by two different mechanisms. Fast dividing cells, such as HeLa cells, have a higher chance to be in the G2/M phase of the cell cycle. It was previously found, with similar size nanoparticles, that cells in the G2/M phase have a faster uptake of nanomaterials.[382] Thus, in our experiments the HUVEC

cells might have a lower uptake of Au@GO nanoparticles compared to HeLa and Ovarian cells. Another possible explanation for the lower sensitivity of HUVEC cells could be a higher thermo-sensitivity for fast dividing cancer cells.[383,384]

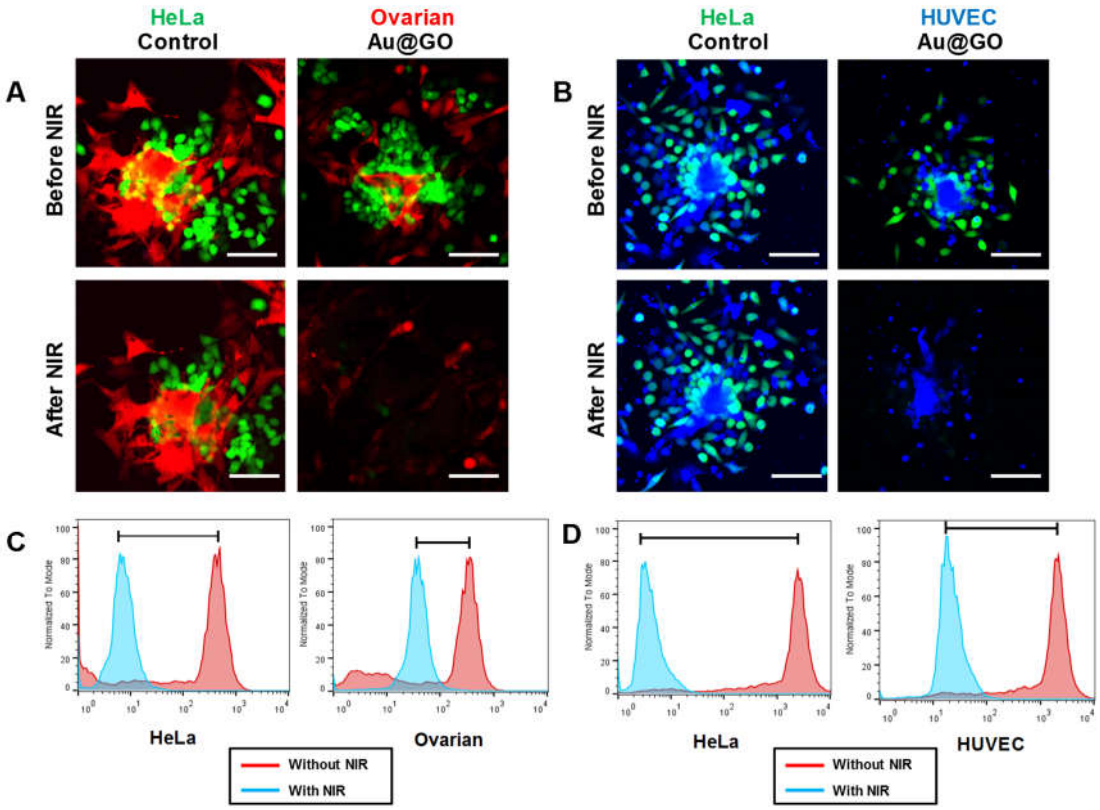

Figure 2-6. Analysis of co-culture spheroids after PTT. Confocal flurescent microscopy images of HeLa (Green)/Ovarian (Red) co-culture spheroids before and after NIR treatment (A). FACS analysis of cell viability of HeLa/Ovarian co-culture spheroids in PTT (B). Confocal flurescent microscopy images of HeLa (Green)/HUVEC (blue) co-culture spheroids before and after NIR treatment (C). Analysis of cell viability by FACS of HeLa/HUVEC co-culture spheroids in PTT (D). All scale bars are 100µm.

Co-culture spheroids of HeLa/Ovarian and HeLa/HUVEC were further used to test the photothermal effect of the nanomaterial (Figure 6). As in the experiments using 2D cultures and mono-culture spheroids, NIR irradiation without the addition of Au@GO nanoparticles had no observable effects on the cell viability, as seen from the fluorescent confocal microscopy images (Figure 2-6A,C). Conducting PTT experiments with 1 vol% Au@GO nanoparticles and the co-culture spheroids leads to similar results as already observed in 2D cultures and mono-culture spheroids. However, the deviations in the viability for Ovarian and HUVEC cells could be observed. The PTT efficiency on HeLa cells was high for both types of co-culture spheroids killing all HeLa cells, as expected from previous experiments. The viability of Ovarian cells, however, was higher than expected from previous experiments. While in 2D culture experiments the PTT effect of Au@GO nanoparticles on Ovarian cells was similar to the effect on HeLa cells, with the same cell viability after PTT, the viability was higher in 3D co-culture spheroids (Figure 2-6A,B). Further, higher viability of HUVEC cells was observed in HeLa/HUVEC co-culture spheroids (Figure 2-6 C,D). The higher PTT effect of the Au@GO nanoparticles in the co-culture situation most likely is due to the higher thermo-sensitivity of the fast-dividing HeLa cells.[383,384] A further explanation might be competitive uptake from HeLa cells, reducing the number of particles that can be taken up by HUVEC or Ovarian cells. This effect would be stronger in 3D cultures compared to 2D cultures, as there are more directly neighboring cells competing for uptake.

Conclusions

In conclusion, addressing the critical challenges of 3D spheroids based novel anti-cancer therapeutics screening, we developed a hydrogel microwell array-mediated approach for high throughout producing uniform-sized multicellular 3D tumor spheroids. The co-culture spheroids were harvested from the hydrogel microwell array and can be cultured on 2D substrates while retaining their 3D structures. Furthermore, spheroids generated with our hydrogel microwells were successfully used to test the effectiveness of newly developed Au@GO nanoparticles as PTT agents for cancer therapy. Through the use of the co-culture spheroids, we demonstrated not only the high therapeutic potential of Au@GO nanoparticles for inducing cancer apoptosis but also a high selectivity of the nanoparticles towards fast-growing cancer cells in 3D culture. Overall, this method of generating uniform-sized multicellular 3D tumor spheroids could be a powerful tool for conducting in vitro drug screening applications.

2.2 Graphene-Plasmonic Hybrid Nanoparticle-based Photothermal–Gene Therapy

2.2.1 Introduction

The recent development of nucleic acid conjugated nanoparticles and their derivatives has rapidly inspired a myriad of novel nanoparticle-based molecular diagnostic, therapeutic, and self-assembly systems[223,226,385-392]. Nanoparticles in such nucleic acid conjugates not only provide novel physical and chemical properties (e.g., catalytic, magnetic, quenching, plasmonic, photodynamic) but also act as scaffolds that assemble the nucleic acids[386,387]. This novel approach gives rise to a variety of highly robust biosensing functionalities and provides effective gene regulating capability with high bio-compatibility. Specifically, for cancer theranostics, recent studies have demonstrated the effective killing of several cancer cell lines, including those with high levels of multi-drug resistance using gene regulating nucleic acid conjugated nanoparticles[393-396]. However, despite the promising results from nucleic acid – nanoparticle conjugates and other nanoparticle-based drug delivery systems, several deadly cancers can adapt through multiple pathways and complex mechanisms, leading to inefficient ablations of tumors in vivo. For example, upregulated drug efflux and DNA repair lead to the development of multi-drug resistance in cancer cells[395,397-399]. Also, many of the conventional therapy has been limited by the abnormally up-regulated pro-survival genes such as BCL2 and Caspase families in highly deadly cancers[400-403]. Moreover, although nanoparticle-based therapeutics provide the potential for cancer imaging and treatment monitoring, cancer imaging in such nanoparticle conjugates still heavily rely on fluorescence[30,123,402-407], which frequently provides poor imaging contrasts due to auto-fluorescence of cells and limits cancer behavior studies in vitro as well as in vivo.

Graphene – plasmonic hybrid, as a type of newly discovered nanostructure, has been proposed for use in a myriad of fields, including photocatalysis, photovoltaics, photodetectors, biosensing, stem cell differentiation, and drug delivery[253,390,408-417]. As a single-layered nanomaterial bonded by an sp^2 hybridized carbon atom, graphene possesses extraordinary chemical, electrical, optical and physical properties[237,238,276,418-424]. For instance, graphene is an excellent drug delivery platform and has been demonstrated to load a variety of different therapeutic biomolecules such as small molecule drugs and nucleic acids[425-429]. Additionally, graphene has been used in NIR induced photothermal therapy to induce cell apoptosis, likely through the unselective regulation of variety pathways, including apoptotic caspase family genes and impairing DNA repairing mechanisms, following the induction of HSPs[410,430-432]. Furthermore, graphene is highly biocompatible, amphiphilic and therefore has been reliably applied to transfect different types of cells[433]. On the other hand, noble metal-based plasmonic nanostructures, non-linearly amplify optical properties such as photoelectric, photocatalytic and photothermal effects from graphene through localized surface plasmonic resonance (LSPR)[136,434,435]. LSPR from plasmonic nanoparticles has also enabled NIR based SERS imaging in the hybrid system[436], which overcome the limitation of low contrast in fluorescence imaging as graphene quenches the fluorescent agents through Förster resonance energy transfer (FRET)[437,438]. As such, these intriguing properties make graphene – plasmonic a unique and promising solution to circumvent the aforementioned challenges faced by nucleic acid – nanoparticle conjugates. Still, there are several hurdles that need to be addressed for graphene -plasmonic hybrids to realize their full potential for cancer treatment. For example, previously synthesized hybrid nanoparticles frequently suffer from bulkiness and

have poor colloidal stabilities, limiting their cellular uptake. Also, the strong photothermal effects from the hybrid nanoparticle unselectively target multiple cellular apoptotic pathways. As a result, both cancer cells and surrounding normal tissues are killed unselectively, leading to a strong concern of nanoparticle cytotoxicity in vitro and in vivo.

Herein, we report the development and application of nucleic acid conjugated graphene – plasmonic hybrid nanoparticle for the targeted, multifunctional suppression and imaging of cancer cells (Figure 2-7). The graphene encapsulated hybrid nanoparticles have a core-shell structure (plasmonic – graphene core-shell nanoparticle, PGNP for short) that is an optimal size for cellular uptake and selective transfection into cancer cells was achieved by conjugating the surface of the PGNPs a PEG-RGD ligand through lipid-graphene interactions. Also, LSPR from the gold core nanoparticles significantly improved the efficacy of the hybrid's photothermal effect, and a non-fluorescent based, high-contrast dark field imaging (DFI) modality was incorporated as the first demonstration of its kind. On the other hand, to more effectively treat cancer, we designed oligonucleotides that assembled on the hybrid nanoparticles to target-specifically bind to BCL2 mRNAs, aiming to restore the pro-apoptotic balance in cancer. Specifically, we hypothesized that through the combination of selective BCL2 inhibition and the photothermal therapy, the NIR irradiated PGNP nucleic acid conjugate would be able to synergistically sensitize cancer through multiple cellular pathways, including induction of HSPs and pro-apoptotic Caspase families, to clinically used anti-cancer drugs in vitro as well as in vivo.

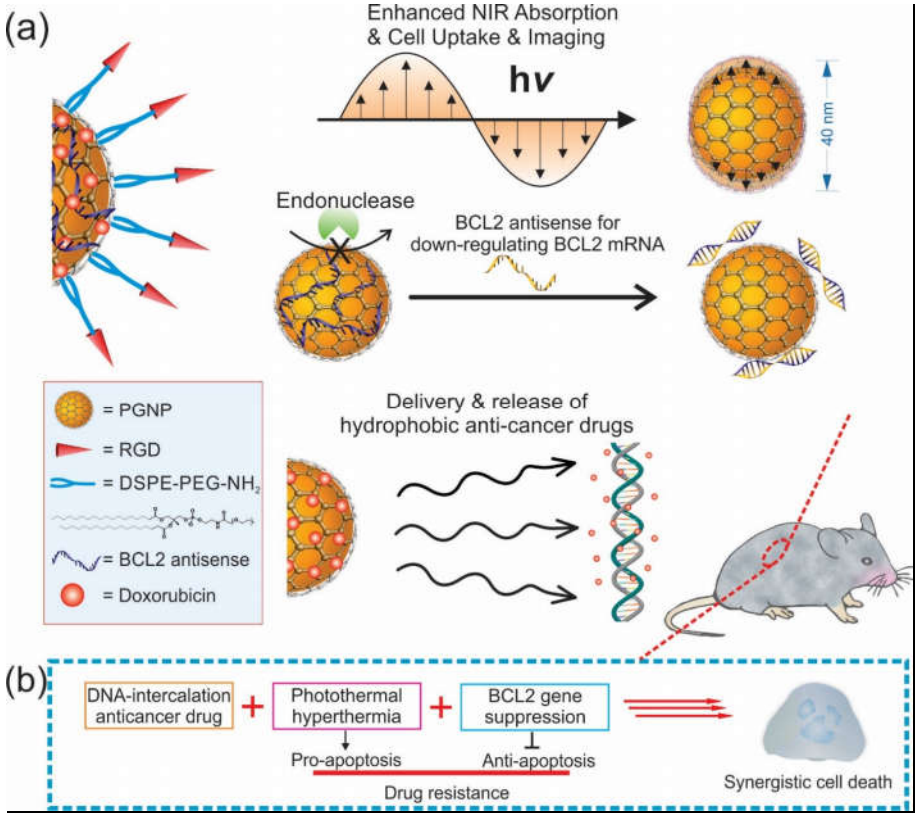

Figure 2-7. Schematic diagram illustrating the PGNP (plasmonic core-graphene shell hybrid nanoparticle) based DDS for combinatorial therapy. (a) The PGNP with sizes around 40 nm i) has enhanced NIR absorption, photothermal hyperthermia, good cellular uptake efficiency and enabled the high contrast dark field imaging (DFI); ii) delivers BCL2 ASON for selective suppression of the anti-apoptotic BCL2 gene, which is overexpressed in a variety of cancer cells, and iii) delivery of anti-cancer drugs. (b) Synergistic co-sensitization of chemotherapy based on a novel photothermal hyperthermia-gene combined therapy. This photothermal-BCL2 ASON combined therapy synergistically sensitize cancer cells towards anti-cancer drug induced apoptosis through a collective induction of intracellular pro-apoptotic pathways and a suppression of anti-apoptotic pathways, therefore enhances cancer cell apoptosis in vitro and tumor ablation in vivo.

2.2.2 Methods

Synthesis of nano-sized, negatively charged Graphene oxide (NGO). Graphene oxide with sizes around 100 nm was synthesized based on a previously reported method with minor modifications. 1.0 g of graphite flakes were added into a mixture of 12.0 ml concentrated sulfuric acid (98%), 2.5 g P_2O_5 and 2.5 g $K_2S_2O_8$ then stirred and heated at 83 ºC for 6 hours to get the pre-oxidized graphite oxide. After washing with 500 ml distilled water, the pre-oxidized graphite oxide was dried in vacuum overnight and used for exfoliation. In the ice water bath, 1.0 g pre-oxidized oxide was added into 120 ml concentrated H_2SO_4, then 15.0 g $KMnO_4$ was slowly added in 10 minutes with the temperature kept below 20 °C. After another 20 minutes stirring, the temperature of the reaction was slowly raised to 35 °C and continued to be heated for 3.5 hours. Then 250 ml distilled water was carefully added with temperature kept below 50 °C. After 3 hours, the reaction was quenched by adding 700 ml distilled water followed by 20 ml 30% H_2O_2 aqueous solution, with the appearance of shining yellow color in the solution. The as-synthesized graphite oxide was washed with 10% HCl solution and distilled water for 3 times. After exfoliated under tip ultrasonication for 3 hours under water bath, the graphene oxide solution was centrifuged at 13300 rpm for 1 hour for twice and the supernatant solution was used.

Synthesis of cysteamine functionalized nanoparticles (GNP). 40 nm (TEM size) cysteamine functionalized gold nanoparticles were synthesized using cysteamine as a ligand from $HAuCl_4$. 20.0 ml 0.53 mg/ml $HAuCl_4$ solution was prepared and 2.4 mg cysteamine hydrochloride salt was added into the solution in a 50 ml round bottom flask and stirred in the dark at a speed of 1200 rpm using a magnetic bar at room temperature. The solution turned from yellow to orange instantly. After one hour, 10.0 µl 0.38 mg/ml

$NaBH_4$ solution was rapidly injected into the $HAuCl_4$ solution and a faint purple color appear after the injection of $NaBH_4$ solution. The solution continues to be stirred for 2 hours at a speed of 1200 rpm and then stirred overnight at a speed of 500 rpm. Then the nanoparticles were centrifuged down at 4000 rpm for 5 minutes using a micro-centrifuge and washed with water twice to remove free cysteamine molecules. The concentration of cysteamine functionalized gold nanoparticles were estimated by drying 1.0 ml solution in an oven and then correlated to the absorption at 527 nm in the UV-Vis spectrum.

Synthesis of PGNPs and gold nanoparticle-decorated graphene. Into 5 ml highly concentrated NGO solution (3.0 mg/ml), 1.0 ml cysteamine functionalized gold nanoparticles solution (0.2 mg/ml) was added drop by drop (10 μl for each drop) under vigorous stirring (800 rpm). After the addition, the solution was transferred to a 10 ml glass vial, sealed, sonicated and vortexed at 2000 rpm for 1 hour and a dark red solution was obtained. The PGNPs were centrifuged at 8000 rpm and washed with distilled water for three times to get rid of any suspended NGO. To synthesize the gold nanoparticle-decorated graphene, 0.1 ml cysteamine functionalized gold nanoparticles solution was added into 1.0 ml 0.2 mg/ml NGO solution followed by 20 minutes of bath sonication. The solution turned purple 1 minute after the addition of gold nanoparticles. After sonication, the gold nanoparticle-decorated graphene was then washed with distilled water 3 times.

Evaluation of photothermal effect from PGNPs nanoparticles. 2.0 μg/ml NGO, 20 μg/ml cysteamine functionalized nanoparticles, 20 μg/ml citric acid functionalized nanoparticles and 20 μg/ml PGNPs were measured with photothermal effect under identical conditions. Concentrations were normalized based on their UV-Vis absorption intensity (227 nm for GO and 527 nm for gold nanoparticles). 1.0 ml nanoparticle solution was added into a pre-

cleaned quartz cuvette with a thin metal thermal probe. A NIR laser (wavelength at 808 nm) was fixed with laser output touching the quartz surface at 45 °C. The temperature of the solution was first stabilized for 5 minutes, then the laser with a pre-set power density of 6.6 W/cm^2 was turned on and the temperature of the solution was recorded every one minute for 8 minutes. The setup remained the same during the photothermal test for all four solutions and water only was used as a control.

Dark field imaging for the glioblastoma cells. For dark field imaging and SERS imaging, a glioblastoma U87-EGFP cell line were used. The cells were seeded into 24 well plates with cover glass with a cell density of 6×10^4 per well. After 24 hours incubation with cell confluency percentage 30%-50%, the PGNPs nanoparticles and gold nanoparticle decorated graphene were delivered using opti-MEM cell media at a concentration of 50 µg/ml followed by 6 hours incubation. Then the cell media was changed to 10% FBS DMEM and continued with incubation for 12 hours. For dark field imaging, the cells were then washed with PBS and fixed using formalin. An Olympus IX83 inverted motorized microscope was used to obtain the dark-field images.

Mild photothermal hyperthermia performed in glioblastoma cells. U87-EGFR VIII cells were seeded in 96 well plates at a cell density of 20k per well. PGNPs nanoparticles in opti-MEM were then delivered into the cells at a concentration of 50 µg/ml and incubated for 3 hours. Then the cell media was changed back to 10% FBS DMEM cell media. Different laser powers were applied to the cells vertically with a distance of 0.5 cm for 5 minutes in each well. After laser exposure, the cell media was changed and the cells were incubated for 48 hours before measuring the cell viability using a standard Prestro blue assay. For the qRT-PCR analysis, the cells were trizoled and extracted with RNA using a

standard procedure. A hyperthermia stimulated HSP family and cellular apoptotic family Caspase 3 were analyzed.

Study on the antisense loading on the PGNPs nanoparticles using FRET. A 100 pmol/1.0 ml Cy5-labelled oligonucleotide (sequence: 5'-/Cy5/TGC GCT CCT GGA CGT AGC CTT -3') solution was first prepared and measured with fluorescence. Then 100 µl 0.5 mg/ml PGNPs solution was added to the oligonucleotide solution. After incubation in room temperature for 15 minutes, the fluorescence from the solution was measured. To prove the quenching wasn't from the extinction of PGNPs nanoparticles, 1 nmol/100 µl of a complementary DNA (sequence: 5'- AAG GCT ACG TCC AGG AGC GCA -3') was added into the solution and was incubated for 15 minutes. The fluorescence from the solution was then measured.

GFP & BCL2 knockdown in glioblastoma cells using PGNPs nanoparticles loaded with GFP antisense. Into 0.5 ml 0.1 mg/ml PGNPs nanoparticles and 0.5 ml 10 µg/ml NGO, 10 µl aqueous solution with 1 nmol of GFP antisense (5'-TGC GCT CCT GGA CGT AGC CTT -3') and 0.1 ml 10x PBS was added. After incubation and shaking for 24 hours, the nanoparticles and NGO were filtered through a filter with 100k MW cut-off. Then they were washed with the enzyme-free water and re-dissolved in opti-MEM cell media to get the desired concentrations (PGNPs nanoparticles at 50 µg/ml and NGO at the concentration of 5 µg/ml). These two groups, with control groups: no addition, 50 µg/ml PGNPs nanoparticles, five µg/ml NGO, and 100 pmol/1 ml antisense DNA, were then delivered into U87-EGFP cells in 24 well plates, at a cell density of 60k cells/well. After 6 hours, the cell media was changed into 10% FBS DMEM cell media and cultured for another 48 hours. The GFP fluorescence of these experimental groups was then checked under the Nikon Ti

eclipse microscope. The GFP knockdown efficiency was calculated based on the average GFP fluorescence intensity in the fluorescent images. BCL2 antisense (sequence: 5'-TCT CCC AGC GTG CGC CAT-3' was loaded in PGNPs nanoparticles and delivered using the same method described for GFP antisense. After 48 hours of delivery, the cells were trizoled and the mRNA extractions were analyzed with qRT-PCR following a standard procedure.

Performing photothermal-gene co-sensitized chemotherapy on glioblastoma cells. 100 μg PGNPs nanoparticles were firstly loaded with excess BCL2 antisense (1 nmol) in PBS, then incubated for 24 hours, washed and re-dissolved in opti-MEM cell media. Afterward, a stock doxorubicin aqueous solution at a concentration of 1 mg/ml was added into 1 ml opti-MEM cell media to obtain different doxorubicin concentrations, 0, 0.1, 0.5, 1, 5 and ten μg/ml. After incubation at room temperature for 4 to 6 hours, the nanoparticles were delivered into U87-EGFR VIII cells. U87-EGFR VIII cells were seeded at a density at 20k cells/well in a 96 well plate. After incubation for 6 hours, the media was changed to 10% FBS. The cells were continued to be cultured for 24 hours, and then the 808 nm NIR laser was exposed to the cells, at a distance of 0.5 cm and laser intensity at 1.5 W/cm^2 for 5 minutes in each well (laser intensity measured with a Newport Powermeter). After the NIR laser exposure, the cell media was changed and Presto blue assay was performed after 48 hours of culturing. For control groups, nanoparticles with only doxorubicin loading, nanoparticles with only doxorubicin and BCL2 antisense, nanoparticles with only doxorubicin and NIR laser exposure were performed in parallel under identical conditions.

Synthesis of RGD functionalized PGNPs nanoparticles. 0.5 mg DSPE-PEG2000-NH_2 was dissolved in 0.5 ml 0.4 mg/ml PGNPs nanoparticle solution by careful pipetting, followed

by extensive bath sonication for 1 hour below 25 °C (changing water in the sonicator every 10 minutes). Then the nanoparticles were centrifuged down at 8000 rpm and washed with distilled water twice and then dissolved in PBS. To introduce maleimide group for sulfhydryl conjugation, 0.5 mg sulfo-SMCC crosslinker dissolved in 50 µl DMSO was added into the lipid functionalized PGNPs nanoparticles and the solution was shaken at room temperature for 2 hours to complete the reaction and then washed with PBS. Before conjugating the RGD with cysteine functionalities (RGDC) to the maleimide group on the nanoparticle, 2.0 mg TCEP dissolved in 20 µl 0.5 M $NaHCO_3$ (pH~6) was diluted to 0.2 mol/L by adding distilled water. After adding 25 µl 0.2 M TCEP into 200 nmol RGDC (in the form of lyophilized powder), 0.5 ml 0.4 mg/ml PGNPs nanoparticles functionalized with lipid and sulfo-SMCC were added into the RGDC solution. The reaction proceeded for 24 hours in the fridge at 4 °C. Finally, the RGD functionalized nanoparticles were washed with distilled water.

Targeted delivery of PGNPs nanoparticles functionalized with RGD peptides. MCF-7 and MDA-MB231 cells were seeded on cover glass in 24 wells at a cell density of 60k cells per well and cultured for 24 hours. When the cell proliferation percentages reach 30%-50% proliferation rate, RGD functionalized PGNPs nanoparticles were delivered to the two cell lines at a concentration of 20 µg/ml with 0.5 ml volume (option-MEM) each well. After 1 hour, the cell media was washed with PBS and changed to 10% FBS DMEM. After incubation for 6 hours, the cells were washed with PBS and fixed with formalin for dark field imaging analysis. To show the selective knockdown of MDA-MB 231 cells, 20 µg/ml RGD functionalized PGNPs nanoparticles were loaded with BCL2 antisense and doxorubicin as described in the tri-modal therapy part; then they were delivered into the

two cell lines, which were cultured in 96 well plates and cultured for 1 hour. After cell media change and incubation for 24 hours, the cells were exposed to NIR laser for 5 minutes at a laser density of 1.5 W/cm^2. Forty-eight hours after the laser exposure, the cell viability of the two cell lines under different concentrations of doxorubicin was measured using a standard Presto blue assay.

In vivo tumor suppression in mice: To examine anti-cancer effects of [Nanoparticle's name] in the breast cancer tissue, the 6-week-old BALB/c nude mouse was purchased from RaonBio (Kayonggi-do, Yongin-si, South Korea) (control, n=3; xenograft, n=3). All animals were acclimatized to the animal facility for at least 48 h before experimentation and maintained according to the Guide for the Care and Use of Laboratory Animals published by the NIH. They were housed in a barrier under HEPA filtration and provided with sterilized food and water ad libitum. Animal facility was maintained 12-hour light/dark cycles at room temperature 21 ± 2°C with 30~40% humidity. Approximately 5.0 × 10^6 cells of MDA-MB-231 were mixed with 354234-matrigel (BD, San Jose, California, USA) and subcutaneously injected in both shoulders and thighs (4 sites in mice). Studies were conducted when the tumors were ≈4 mm in diameter.

2.1.3 Results and Discussion

Synthesis of PGNPs and delivery into glioblastoma cells

To achieve optimal delivery efficiency and improve cancer imaging in graphene-based hybrids, PGNPs with a 40 nm diameter and a spherical shape were first synthesized, as this geometry has been previously shown to be advantageous not only for improved cellular uptake efficiency and superior colloidal stability but also for exceptional biocompatibility when compared to larger nanostructures (>100 nm)[380,439]. As such, we first synthesized

amine-functionalized gold nanoparticles (GNPs) with diameters around 40 nm as the plasmonic core, which was then used as a template for the synthesis of PGNPs. The synthesis of amine functionalized GNPs was achieved through a facile, single step, and aqueous reaction utilizing cysteamine as a capping reagent and $NaBH_4$ as a reducing reagent (Figure 2-8a). Through a single electrostatic assembly step, the as-synthesized amine functionalized GNPs (+33 mV) could then be readily enwrapped by negatively charged (-55 mV) nano-sized graphene oxide (NGO), as confirmed by transmission electron microscopy (TEM) (Figure 2-8a, b). To further confirm the presence of NGO enwrapping the PGNPs, Raman and UV-Vis spectroscopies were performed. In the Raman spectrum of the hybrid nanoparticles under a 633 nm laser, the distinct D, G, 2D Raman bands of graphene were present, and the intensities of these bands were significantly higher than the intensities of the spectrum from graphene without GNPs, indicating the nanometer level proximity of graphene from the plasmonic cores and the activation of Surface Enhanced Raman Spectroscopy (SERS). In the UV-Vis spectrum, the 240 nm absorption peak, which originated from the π-π^* transition of graphene, was also clearly identified as further evidence of the graphene-plasmonic hybrid structure[381].

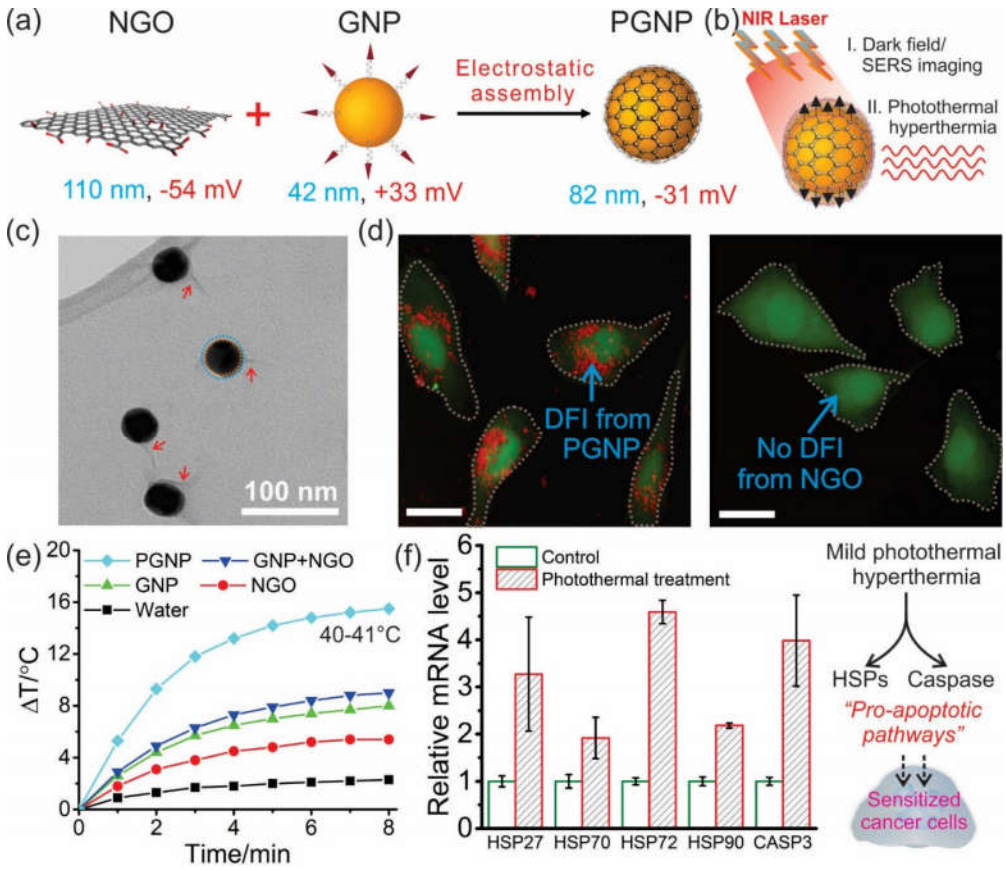

Figure 2-8. Synthesis of PGNPs for Dark Field Imaging (DFI) and enhanced photothermal hyperthermia. (a) Scheme for the synthesis of PGNPs based on electrostatic assembly. (b) An illustration of the plasmonic core enabled DFI and SERS imaging and the enhanced photothermal hyperthermia through a stronger light-matter interaction. (c) Representative TEM photograph of the as-synthesized PGNPs (red arrows indicating the NGO enwrapping plasmonic gold nanoparticles). (d) DFI imaging of a GFP labelled cell line using PGNP (left) and NGO (right) only (scale bar: 100 μm). (e) Enhanced photothermal effect from the PGNPs and control groups tested in aqueous solution. (f) qRT-PCR analysis and schematic diagram of the mRNA expression in glioblastoma cells treated with mild photothermal hyperthermia including HSP family and cellular apoptotic family (CASP3).

To evaluate the potential of PGNP for non-fluorescent based cancer imaging with improved contrast and suppressed quenching effects, we then transfected malignant glioblastoma cells with PGNP. It was found that two non-fluorescence based, orthogonal imaging modalities: DFI (Figure 2-8b) and NIR SERS, were both successfully observed with high contrast through the incorporation of plasmonic cores and induction of LSPR. In contrast, without the plasmonic core, cells transfected with the only graphene exhibited negligible DFI signals (Figure 2-8c). Using multiple sites analysis, it was determined that strong DFI signals were detected in over 90% of the glioblastoma cells studied, suggesting a high cell uptake efficiency. This is particularly interesting considering the existence of negatively charged surface of the hybrid nanoparticles, suggesting that the high uptake efficiency is likely due to the amphiphilic graphene coating on the nanoparticle surface. Equally important, we confirmed that the small size, the core-shell structure of our nanoparticles plays an important role in the cellular delivery process. For instance, as found when using another type of graphene - plasmonic core-shell structure with 200 nm TEM size and the absence of a core-shell structure, we constantly observed poor colloidal stability, extensive extracellular aggregations, and poor cellular uptake.

Mild photothermal hyperthermia by PGNPs

Building on our optimized hybrid nanoparticle geometry, the enhancement of the photothermal effect in nanoparticle-based drug delivery system directly increased the effect of photothermal therapy especially in deep tissues, leading to successful tumor ablation. To test our hypothesis that the incorporation of the plasmonic core in the PGNP improves the photothermal effect of the hybrid nanoparticle, we first tested the temperature

increase in aqueous solution (Figure 2-8e). Under a low power-density laser (1.5 W/cm^2) and short period (5 minutes) irradiation, temperature increase in 4 different solutions containing gold nanoparticle (GNP), nano graphene oxide (NGO) alone, GNP NGO mixture (GNP+NGO), and PGNPs at a fixed concentration (50 μg/ml) were measured at one-minute intervals for 10 minutes. As shown in Figure 2-8e, water exposed to NIR laser exhibited a negligible increase in temperature (<2 °C); however, in GNPs and NGO solutions mild temperature increases of 5 °C and 7 °C was observed, respectively. The PGNP solution, on the other hand, had the most significant heating, with a temperature increase up to 15 °C [ΔT=T-21 (°C), 21°C = room temperature]. In contrast, a mixture of negatively charged GNPs and negatively charged NGO, which did not form the hybrid structure, showed much lesser heating (ΔT=8°C) effect proving that the enhanced photothermal effect from PGNP truly benefited from the hybrid structure with the incorporation of plasmonic core, rather than from the simple mixing of each component.

The delivery of the PGNP with enhanced photothermal effects into malignant glioblastoma cells induced direct cell death up to 90% under a relatively high laser intensity. However, such highly efficient induction of cellular death simultaneously raises strong concerns for selective tumor treatment in vivo, since the surrounding normal tissues typically also undergo strong thermal stresses (above 5.9 W/cm^2) as well. To this end, we optimized the laser intensity exposed to the cells to 1.5 W/cm^2. Under this optimized laser intensity, PGNP was found to be highly biocompatible with negligible photothermal toxicity. Most importantly, PGNPs can still effectively upregulate pathways related to heat shock protein

and caspases, which we hypothesized to synergistically improve the performances of gene therapy and will be tested later in this study.

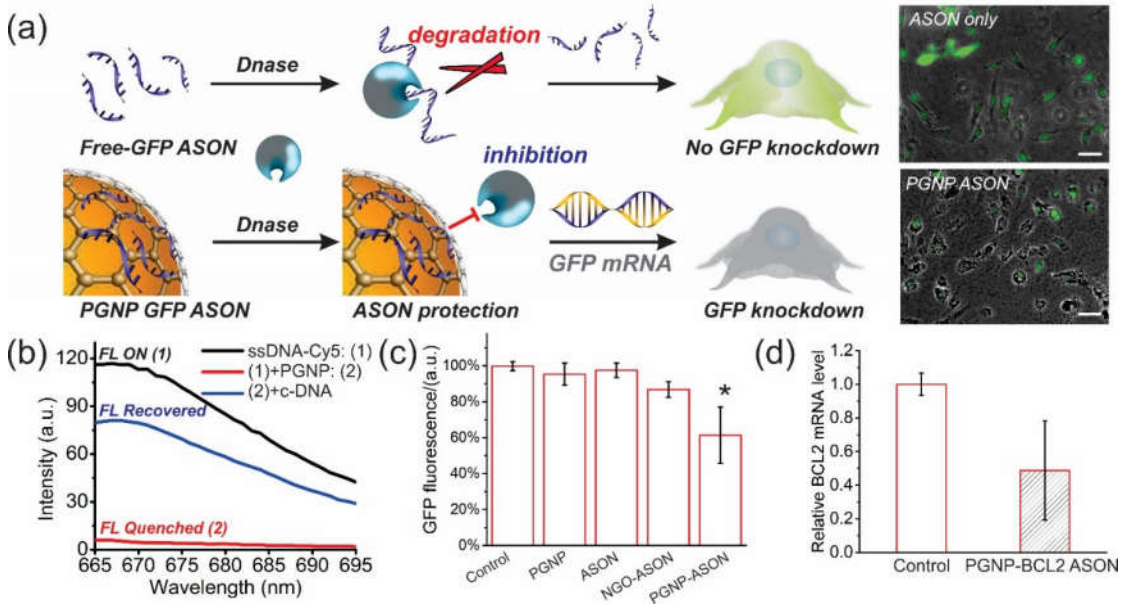

Figure 2-9. Delivery of antisense oligonucleotide (ASON) and the antisense effect. (a) Schematic diagram representing protection of the GFP ASON on the PGNP delivery platform and the GFP knockdown in the U87-EGFP cell line. Scale bar: 100 μm. (b) Fluorescence quenching of a Cy5 labelled single strand DNA during the absorption onto PGNP and the fluorescence recovery after the antisense binds to the complementary DNA. (c) Antisense effect of GFP ASON using different delivery vehicles. (d) BCL2 knockdown in glioblastoma cells using BCL2 ASON delivered by PGNP.

BCL2 downregulation Using PGNP – antisense oligonucleotide conjugates

In addition to photothermal hyperthermia that simultaneously induces a variety of intracellular pathways, BCL2 suppression through gene therapy can selectively regulate the cancer pro-apoptotic balance and has been shown to effectively improve the effect of

chemotherapy in several highly deadly cancers such as glioblastoma and breast cancer[396,400,440]. For graphene-based gene delivery systems, while several types of graphene - nucleic acid conjugates have been studied and delivered into cells, the formation of PGNP - antisense oligonucleotide (ASON) conjugates and its effect on intracellular genes remains unexplored. To this end, we first studied the assembly of a fluorescent dye (Cy5) labeled antisense oligonucleotide (ASON) onto PGNP in solution through fluorescence spectroscopy based on the FRET. When ASON was absorbed and conjugated onto the PGNP surface, the fluorescent dye would be near graphene and the fluorescence would be quenched. When the PGNP – ASON conjugate was incubated in the solution of complementary DNA, ASON would bind to its complementary sequences and the fluorescence of Cy5 would then be recovered. This FRET experiment not only indicated the success of conjugation of ASON on PGNP but also represented the binding of PGNP - ASON conjugate to the complementary DNA or mRNA sequences for gene regulation. After confirming the formation of the PGNP – ASON conjugate, the gene regulation of ASON loaded PGNP (PGNP-ASON) was then investigated in an EGFP-expressing U87 glioblastoma cell line (U87-EGFP), where GFP expression level could be directly monitored by fluorescence microscopy. After the delivery of PGNP-ASON targeting GFP genes into U87-EGFP cells for 48 hours, remarkably, cells showed 30% weaker GFP signals compared to the control group (non-treatment) (Figure 2-9a, c). Consequently, we delivered PGNP-ASON conjugates targeting BCL2 mRNA into U87-EGFR cells. After 6 hours of transfection and two days of incubation, gene expression was measured by qRT-PCR. We found significant BCL2 mRNA suppression (43%) using PGNP-ASON conjugate, normalized to untreated cells. These experimental results collectively supported

the application of PGNP-ASON for gene regulation, and similar therapeutic effect could also be likely expected on graphene-based drug delivery systems due to their similar surface functionalities.

Anti-cancer Efficiency of PGNPs with Combined Photothermal Hyperthermia and gene therapy

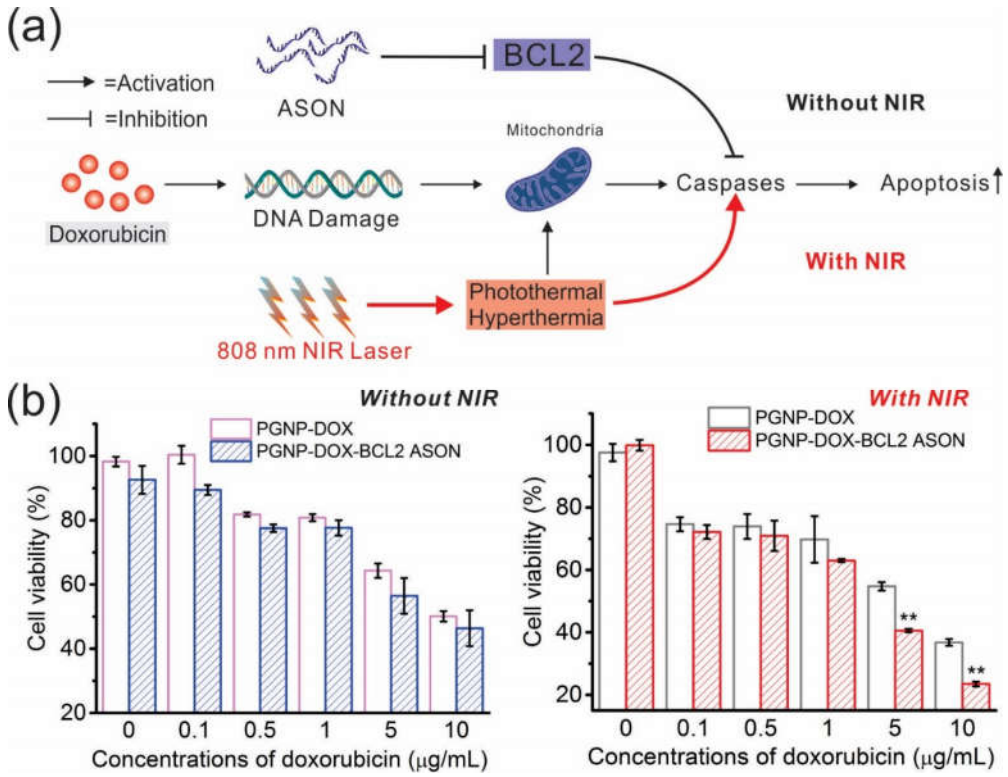

Figure 2-10. Synergistic effects of PGNPs-BCL2 ASON and doxorubicin (DOX) on glioblastoma (U87-EGFR VIII) cells. (a) Schematic diagram depicting synergistic co-sensitization of cancer cells towards anticancer drug (DOX) through combined photothermal hyperthermia (NIR laser) treatment and BCL2 ASON therapy. (b) Cell viability of glioblastoma cells treated with the PGNPs carrying DOX only or both DOX and BCL2 ASON with or without NIR exposure (** $p<0.01$, unpaired student's t-test).

To achieve optimal cancer killing, we hypothesized that the glioblastoma cells could be synergistically sensitized toward apoptotic pathway through the sequential suppression of BCL2 genes and mild photothermal hyperthermia, as shown in Figure 2-10a. First, doxorubicin delivered into the cells would intercalate with DNA thereby interfering with the biosynthetic activity of the cancer cells. Next, the activation of anti-apoptotic pathways preventing cancer cell apoptosis for survival would be blocked by initiating an anti-apoptotic gene (anti BCL2)[396,401,402,440]. Meanwhile, through the activation of HSPs and reactive oxygen species (ROS), cellular apoptosis related to the Caspase pathway could be triggered[59,394,441], and the cell activities to repair the damaged DNA, induced by doxorubicin, could also be suppressed by mild photothermal hyperthermia. Through this sequential combinatorial process, cancer cell apoptosis can be effectively triggered using a low NIR laser power and low concentrations of the chemotherapeutic agent, which would be advantageous for cancer therapies.

To test our hypothesis, we conducted a comprehensive apoptotic assay for cancer cells under four different groups: PGNP-Doxorubicin (PGNP-DOX) with and without BCL2 ASON in the absence of NIR and PGNP-DOX with and without BCL2 ASON under NIR. Consistent with the studies above, EGFR receptors-overexpressing malignant brain tumor cells (glioblastoma multiforme, U87-EGFR VIII) was used as a model tumor cell line. From the result shown in Figure 4b and Figure 4c, whereas NIR irradiation or BCL2 ASON conjugation on PGNP by itself triggered negligible cellular apoptosis, NIR irradiation and BCL2 ASON effectively sensitized the cancer cells toward chemotherapy, decreasing IC_{50} of doxorubicin from around 10.0 μg/ml to 5.4 μg/ml and 6.7 μg/ml, respectively. Through both modalities of NIR irradiation and BCL2 ASON conjugation, strikingly, the IC_{50} of

doxorubicin was further brought down to 2.4 μg/ml. While additional pathway studies are required to study the detailed mechanism, these results directly indicate the synergistic sensitization of U87-EGFR cells toward chemotherapy and strong cancer-killing potency of the PGNP based drug delivery systems.

Targeting Cancer Cells Using RGD Peptide-Conjugated PGNP-ASONs

When using such a highly potent cancer killing platform, selective delivery of PGNPs into cancer cells would be extremely important towards optimal anti-cancer efficiency as well as minimal cytotoxicity to surrounding non-malignant cells[442-444]. For the targeted delivery of PGNP into malignant cancer cells, we utilized the arginine-glycine-aspartic acid (RGD) peptide, which specifically binds to $\alpha_v\beta_3$ and $\alpha_v\beta_5$ integrins that are normally over-expressed on the surface of malignant tumor cells[443]. The RGD peptide was functionalized on the surface of PGNP using DSPE-PEG2000-NH_2 through lipid-graphene interactions (Figure 2-11a)[410,445]. The PEG modules in the linker molecule also prolong the circulation, reduce the protein immunogenicity, and increase the solubility of the PGNPs based DDS. To confirm the targeting effect of the RGD conjugated PGNPs toward malignant tumor cells, we used two different cell line pairs: MDA-MB-231 (high integrin expressing level) and MCF-7 cells (low integrin expressing levels), U87-EGFR VIII (high integrin expressing level) and astrocytes (low integrin expressing levels) (Figure 2-11b) as a proof-of-concept.

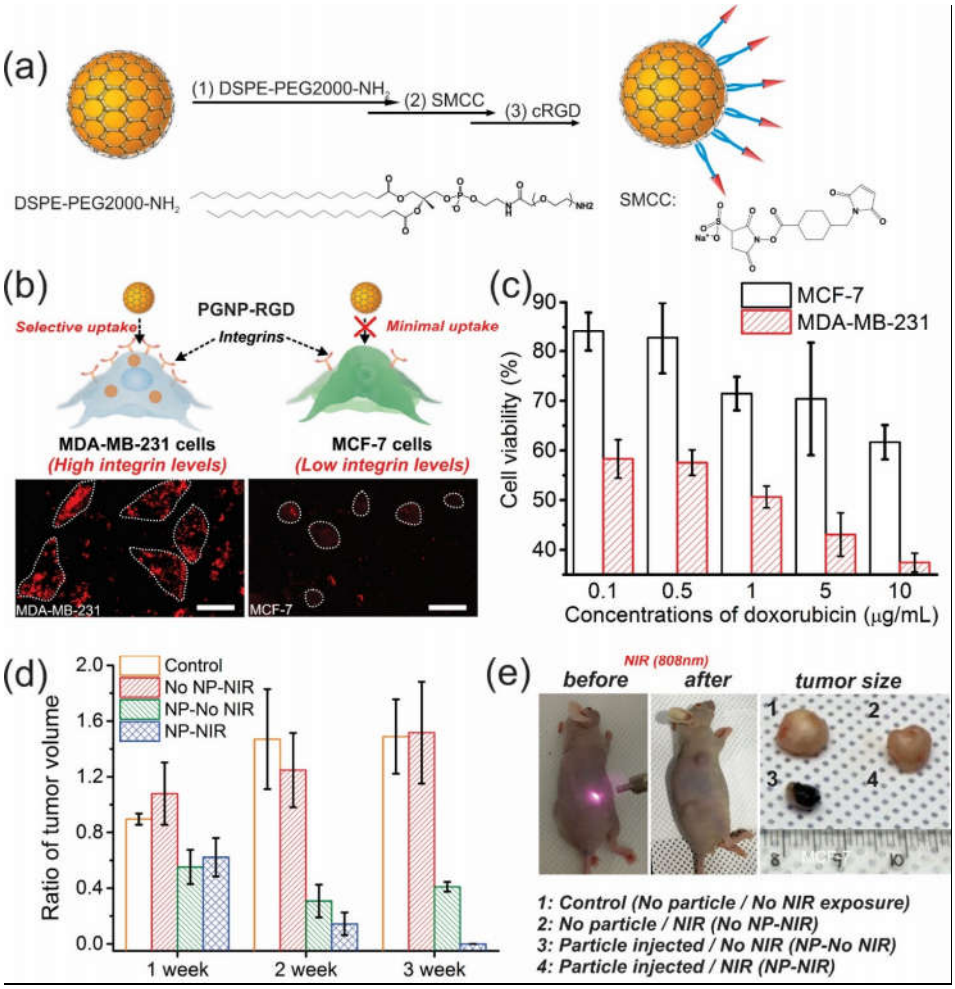

Figure 2-11. Targeting metastatic cancer cells by PGNP-RGD and the in vivo suppression of tumor in a mouse modal. (a) Scheme representing the functionalization of PGNPs. (b) Scheme and DFI images (scale bar: 100 μm) showing the selective uptake of PGNP-RGD by high integrin cells. (c) Differential knockdown of the high integrin expressing cancer cell (MDA-MB-231) and low integrin expressing cancer cell (MCF-7) using PGNP-RGD loaded with BCL2 ASON, doxorubicin and performed mild photothermal hyperthermia. (d) Time dependent change of tumor volume under different treatment under different conditions. (e) Photograph of tumor after 3 weeks' treatment under different conditions.

From the DFI of the four cell lines, RGD-conjugated PGNP-ASON conjugates were found to locate preferably in the MDA-MB-231 and U87-EGFR VIII cells, indicated by significantly stronger signal intensities. As hypothesized, due to the high expression level of integrin on the surface of the malignant tumor, MDA-MB-231 cells were mostly damaged compared to MCF-7 cells upon NIR exposure (laser power = 1.5 W/cm^2), regardless of the concentrations of doxorubicin (Figure 2-11c). Remarkably, at ten μg/mL doxorubicin, the viability of MDA-MB-231 and MCF-7 cells were reduced to 65% and 37%, respectively, under identical conditions, indicating the success of our targeting strategy.

The ultimate goal for this study is to test whether the PGNP-ASON conjugates combined with photothermal therapy could strongly suppress tumor suppression in vivo. To this end, we have further evaluated the in vivo tumor suppression by injecting four conditions (No particle/No NIR and No particles/NIR exposure) into a mouse xenograft tumor model. As shown in Figure 2-11d and 2-11e, control groups showed consistent tumor growth throughout 3 weeks (nanoparticles treated once a week) that resulted in the increase of tumor volume by 50% at the end point. Tumors treated with the RGD conjugated PGNPs (loaded with doxorubicin and ASONs), however, showed a strong suppression of tumor growth activity with a 40% decrease in tumor size compared to that of the control group. On the other hand, tumors treated with the PGNP-ASON conjugates (doxorubicin loaded) combined with NIR irradiation induced significant decrease of the tumor size within two weeks, and finally, tumors were completely removed after three weeks of therapy. From the qRT-PCR results, a significant increase of several apoptosis-related gene expressions such as BID, BAX, Cyto-C, and Caspase 3 was also found. This suggested that the tumors

were ablated through collective induction of apoptosis, which matched the observations from the combinatorial therapy in the in vitro assay. Additionally, the conjugates injected were also found to accumulate stably at the tumor sites for more than three weeks. Furthermore, no signs of toxicity from the conjugates were detected. Hence, we can conclude that the RGD-conjugated PGNPs developed here has an outstanding performance in tumor ablation with minimal toxic effects on normal cells both in vitro and in vivo.

Conclusion and Outlook

In conclusion, we developed a PGNP – nucleic conjugates with high anti-cancer potency in vitro as well as in vivo. PGNP has sharp-contrast DFI, SERS imaging modalities, and improved photothermal effects due to LSPR. Mild NIR photothermal hyperthermia induced by PGNP was found to initiate HSP activation and the apoptotic Caspase pathway without induction of any direct cellular apoptosis. Through the suppression of BCL2 mRNA and the induction of NIR photothermal therapy in glioblastoma, synergistically sensitization of malignant cancer cells toward chemotherapy was successfully achieved and validated. By further conjugating RGD via lipid-graphene interactions, PGNP-ASON conjugate was able to selectively target malignant cancer cells with high killing efficiency. Most importantly, preliminary investigation of the therapeutic efficacy from the PGNP-ASON combined with photothermal therapy demonstrated an over 90% decrease in tumor volume after three weeks. In summary, we have demonstrated a novel DDS based on a plasmonic core graphene shell nanoparticles for effective sensitization of cancer chemotherapy through the successful induction of photothermal hyperthermia and gene therapy. With the versatile drug loading from the graphene shell and its multi functionalities from the hybrid nanoparticles, we believe PGNP can also be applied for

sensitizing other types of anti-cancer drugs; this would be particularly important with the rise of personalized medicine. Moreover, the sub-nanometer thickness of graphene shell and the highly uniform, monodisperse plasmonic structures also made PGNP a perfect SERS based sensing platform, and we're currently applying it for the highly sensitive gene detection for monitoring stem cell differentiation and detecting drug-resistant cancer cells.

2.3 MnO_2-Fe_3O_4 Hybrid Nanoparticle-based Photothermal-Photodynamic Therapy

2.3.1 Introduction

Reactive oxygen species (ROS) are a group of a chemically reactive natural byproduct of the normal metabolism of oxygen and encompass H_2O_2, superoxide (O^{2-}), and hydroxyl radical (×OH), which share crucial roles in cell signaling and homeostasis. Recent interest in reactive oxygen species (ROS)-based cancer treatment has been driven by the breakthroughs on the understanding of critical pro-survival mechanisms in cancer and the paradigm shift of anti-tumor strategies[196-200,248]. For several decades, scientists and pharmaceutical companies have developed many drugs targeting oncogenes and tumor suppressor genes to combine with clinically used anti-cancer therapeutics, which are also known as the "oncogene addiction" hypothesis. However, recent studies suggest that targeting the survival mechanisms of cancer such as intracellular redox and immune surveillance could be a more promising strategy to improve the outcome of chemotherapy or radiotherapy, as they directly target multiple cancer survival pathways in parallel rather than the individual upstream pathways. One such promising strategy shows robust effects on killing cancer by directly targeting the essential survival pathways in cancer is to induce a high level of ROS in cancer cells[196,197,199]. For example, by generating ROS species through photochemical and biochemical reactions, scientists have developed photodynamic therapy which has been clinically used for the treatment of skin cancer through multiple critical apoptotic pathways. On the other hand, several anti-cancer drugs have also successfully reduced the synthesis of reduced GSH of cancer for the indirect sensitization of cancer cells towards apoptosis by reversing the ROS defensive systems in cancer. Strategies combining the simultaneous production of ROS and turning down ROS

protection have also been tested with synergistic sensitization of cancer cells towards other stress regulators such as chemotherapy and hyperthermia, which are cancer killing approaches used clinically[41,163,309]. Although these results have been encouraging, critical limitations remain towards the ultimate goal of fully conquering tumors under in vivo conditions and clinical applications. First, the efficiency on regulating ROS and oxidative stress in vivo remain to be improved towards the maximal cancer killing. Second, while ROS-based sensitization of cancer towards chemotherapy is promising, there are other vital pathways that ensure the survival of cancer cells and reduce the outcome of ROS induction or chemotherapy. For example, cancer cells can develop strong drug efflux mechanisms that also fails many of the clinically used anti-cancer drugs in vivo. Lastly, it would be essential to deliver the anti-tumor reagents to the tumor site and release in a spatiotemporally controlled manner, given their side-effects on normal tissues and the multiple barriers existent in vivo for drugs to reach the tumor sites.

In the past decade, nanoparticle (NP) therapeutics have rapidly risen as a treatment modality for cancer[446]. For drug delivery, NPs can overcome multiple barriers and deliver anti-cancer drugs to the tumor sites in a spatiotemporally controlled manner. Also, certain NPs such as magnetic and carbon NPs can be multifunctional, as can directly present "stress regulators" to synergistically work with clinically used anti-cancer drugs for cancer treatment. Targeting ROS induction and related pathways, scientists have recently developed several NPs with high potential for killing cancers through chemical-based ROS induction, which is also known as the process of chemodynamic therapy (CDT). For example, degradable iron-based NPs can release Fe^{2+}/Fe^{3+}, which directly produce hydroxyl radicals through Fenton reactions with excessive intracellular H_2O_2[447]. There are

also MnO_2-based NPs developed for cancer treatment, which reduce GSH levels through redox reactions rather than direct generation of free radicals[21,39,41,43,52,59,62,68,73,80,81,104,121,124,145,159,162,171,179,184,185,188,191-194,197,204,228,229,234,236,246,247,250,255-257,276,309,370,376,388,393,394,412,423,424,428,429,436,446,448-451]. While these nanoparticle-based CDT shows great promise to better drug delivery and treatment of cancer, most of them still rely on single ROS-induction mechanisms. Therefore, achieving highly efficient CDT for in vivo cancer killing remain challenging. Also, considering the strong drug efflux mechanisms developed in many cancers, how to improve the synergistic effect between CDT and other clinically used anti-cancer drugs for synergistic induction of cancer apoptosis are still critical hurdles to win the war on cancer.

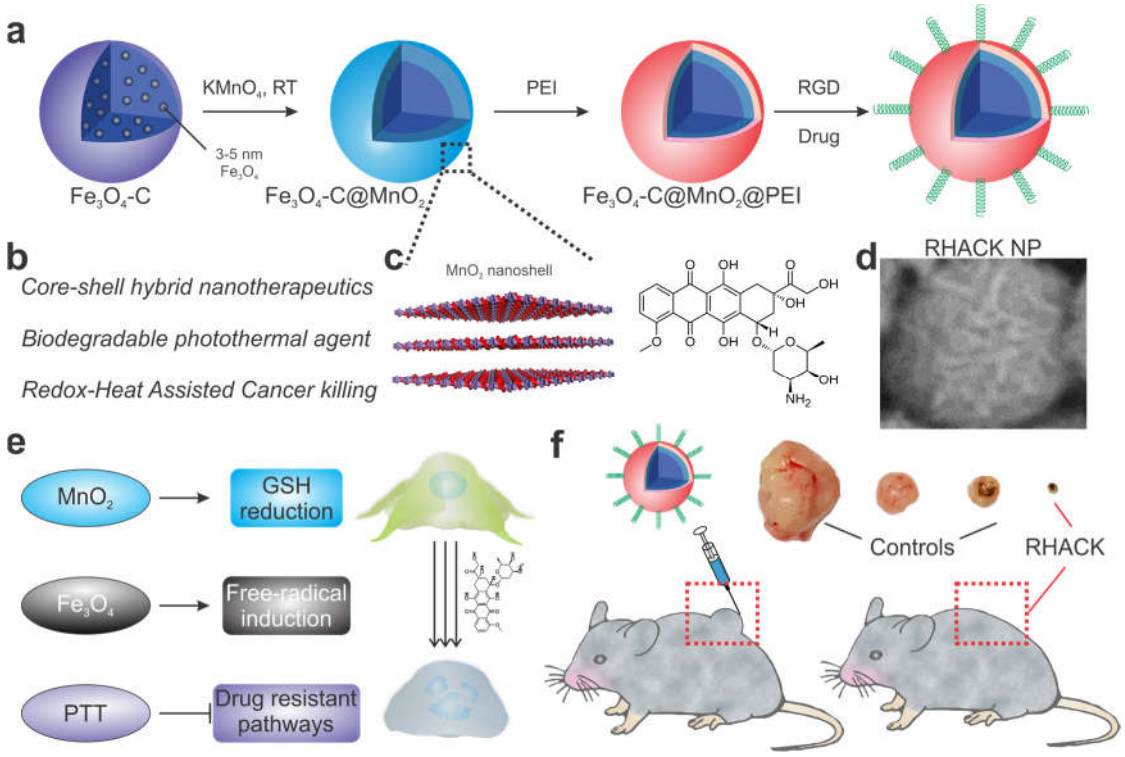

Figure 2-12. Redox and heat assisted cancer killing nanoparticles. a, Schematic diagram illustrating the synthetic route for the RGD-conjugated RHACK nanoparticles. b, Summary of the unique advantages of RHACK nanoparticle for cancer therapy. c, Detailed structure of the core-shell RHACK nanoparticles. d, Representative SEM images of RHACK nanoparticles showing the MnO2 nanosheets assembled shell on the surface of the core nanoparticle (image width of 200 nm). e, Mechanisms of synergistic induction of cancer apoptosis by GSH reduction, chemodynamic therapy and photothermal therapy. f, Schematic diagram showing the in vivo injection of RGD-conjugated RHACK nanoparticles successful lead to significant tumor suppression in vivo in a murine model.

Herein, we developed a multifunctional nanoparticle-based therapeutic platform for effectively killing cancer in vitro and in vivo through combined CDT, photothermal therapy (PTT) and the clinically used anti-cancer drugs (Figure 2-12). More specifically, our hybrid nanoparticle-based drug delivery system (DDS) integrate multiple CDT mechanisms of GSH reduction and ROS generation to induce ROS synergistically, thereby maximizing the ROS-based anti-cancer effects. Remarkably, our DDS is constructed from a biodegradable hollow iron oxide carbon core and a manganese dioxide shell and conjugated with a specific targeting modality iRGD (Fe_3O_4-C@MnO_2- iRGD NPs). Interestingly, when the Fe_3O_4-C@MnO_2- iRGD NPs are incubated with GSH that is rich in cancer cells, the NPs degrade in a controlled manner, which releases Mn^{2+} as a unique T1 MRI contrast agent for tumor imaging and Fe^{2+}/Fe^{3+} to generates highly toxic hydroxyl radicals through Fenton reaction. The degradation process is accompanied by the oxidization of GSH, leading to reduced ROS defensive mechanism in cancer cells, thereby increasing the effects of ROS generation on cancer cells synergistically. Also, such ROS-based cancer killing strategy is combined with other stress regulators, namely photothermal-enabled hyperthermia, to accelerate the intratumoral Fenton process and reduce the efflux of anti-cancer drugs to synergistically induce cancer apoptosis both in vitro and in vivo. Utilizing the multifunctional core-shell Fe_3O_4-C@MnO_2- iRGD NPs, which we termed as Redox and Heat Assisted Cancer Killing (RHACK) nanoparticles, we successfully demonstrated the strong anti-tumoral effect with over 99% tumor size reduction, which is 1.43 fold higher in efficiency compared to clinically used chemotherapeutics. These results indicate Fe_3O_4-C@MnO_2- iRGD NPs-based platform as a promising candidate for the efficient clinical tumor treatment and imaging.

2.3.2 Methods

Materials and Reagents

Ferrocene, acetone, carbamide, potassium permanganate, Methylene blue trihydrate (MB), 2', 7'-dichlorodihydrofluorescein diacetate (DCFH-DA), Doxorubicin (DOX), hydrogen peroxide (H2O2) and reduced glutathione (GSH) were purchased from Sigma-Aldrich Co. (St Louis, MO, USA). Calcein-AM and PI were bought from Invitrogen (USA). PBS (pH 7.4), fetal bovine serum (FBS), DMEM, RPMI, trypsin-EDTA and penicillin-streptomycin were purchased from Gibco Co., Ltd. (Carlsbad, CA, USA). All chemical agents were of analytical grade and were used directly with no further purification.

Characterization

The morphologies of the samples were observed using scanning electron microscopy (SEM, SIGMA, Zeiss, Germany) and transmission electron microscopy (JEOL JEM-2010F high-resolution TEM). The hydrodynamic diameter and zeta potential of the NPs were characterized using a Nano-ZS 90 Nanosizer (Malvern Instruments Ltd.) The UV-vis-NIR adsorption was recorded on a U-3310 spectrophotometer. The specific surface area and the pore size distributions were evaluated and calculated through the Brunauer-Emmett-Teller (BET) and Barrett-Joyner-Halenda (BJH) methods. The fluorescence (FL) emission and excitation spectra were acquired on a Hitachi F-7000 spectrophotometer under ambient conditions. Element concentration was determined by Agilent 700 Series Inductively coupled plasma mass spectrometry (ICP-MS). Raman spectra were obtained to confirm the structural nature of the carbon matrix of Fe3O4-C NPs using a Renishaw inVia Raman microscope. Powder X-ray diffraction (XRD) pattern was acquired on a Shimadzu XRD-

7000s diffraction instrument with Cu Kα radiation (λ=1.542 Å) over the scan range 10°-80°.

Synthesis of Fe_3O_4-C NPs and Fe_3O_4-C@MnO_2 NPs

The Fe_3O_4-C hollow nanoparticles were synthesized by a novel one-step hydrothermal method. In a typical synthesis, ferrocene (3.00 g) and carbamide (0.80g) were dissolved in acetone (300 mL). After intense sonication for 30 min, 2.5 mL of 30% H_2O_2 solution was slowly added into the above solution, which was vigorously stirred for 30 min with magnetic stirring apparatus. The precursor solution was transferred into a 500.0 mL Teflon-lined stainless steel autoclave. After sealing, the autoclave was heated to and maintained at 200 °C for 24 h. The autoclave was cooled naturally to room temperature. After intense sonication for 15 min, the products from the Teflon-lined stainless steel autoclave was magnetized for 10 min by a magnet of 0.20 T. The supernatant was discarded under a magnetic field. The precipitates were washed with acetone and DI water three times respectively. Finally, the black products were dried via lyophilization.

The synthesis of Fe_3O_4-C@ MnO_2 nanoparticles was based on the redox reaction. Firstly, 50 mg of Fe_3O_4-C nanoparticles were dispersed in 30 ml of 10 mM $KMnO_4$ aqueous solution. The solution was heated to 80 ℃ for 1h under stirring. The products were purified by DI water for three times. The as-obtained nanoparticles were dried via lyophilization.

Surface Modification with iRGD

To modify with targeting modality iRGD, the water-soluble Fe_3O_4-C@ MnO_2 NPs from above were first diluted with DPBS to reach a final concentration of 2 mg/mL. Afterward, excess ten kDa branched PEI (Sigma-Aldrich) was added dropwise (1 mg/mL) and spin overnight. After that, the PEI-coated MNPs were mixed with heterobifunctional linker

Sulfo-SMCC (0.1 mM) and incubate at room temperature for four h with continuous shaking. Simultaneously, SH-PEG-COOH moieties were linked to iRGD-NH_2 moieties using EDC/NHS coupling. After that, adding thiolated PEG-iRGD constructs to the thiol-reactive Sulfo-SMCC-linked MCNP-PEI complexes. The resulting mixture was allowed to react overnight, followed by purification by DI water for three times.

Drug loading and release.

The Fe_3O_4-C and Fe_3O_4-C@MnO_2 NPs were dispersed in an aqueous solution of DOX with a final concentration of 1 mg/ml. The solution was stirred overnight for DOX loading. Purification was performed twice, then the DOX-loaded Fe3O4-C NPs (Fe_3O_4-C -DOX) and Fe_3O_4-C@MnO_2 NPs (Fe_3O_4-C@MnO_2-DOX) were dispersed in Dulbecco's Phosphate Buffered Saline (DPBS). The loading and encapsulation efficiency was calculated based on the equations previously reported.

The Redox-triggered DOX release kinetics was further conducted. Two concentration groups of GSH was used. For each group, Fe_3O_4-C@MnO_2-DOX NPs (20 mg) were incubated in 20 ml GSH solution (2 μM or 10 mM) under stirring. At different time points, a portion of the solution (1 ml) was collected for centrifugation. The absorption of the supernatant was measured by a UV-Visible spectrometer (Varian Cary 50 spectrophotometer, CA) using maximum absorption of DOX at 480 nm. The DOX content in the solution was determined by a standard curve.

Degradation kinetics

Degradation of the Fe_3O_4-C@MnO_2 NPs (200 μg ml-1) was evaluated by mimicking intracellular GSH concentration (GSH, 10 mM) in deionized (DI) water under constant rotation. At predetermined time points (2 h, 4 h, 6 h, 8 h, 1 day, 2 days, 5 days, 7 days, 9

days), samples were collected for TEM, UV-vis-NIR adsorption, DLS, and the Fe, Mn concentration was measured by ICP-MS to quantitatively evaluate the degradation kinetics.

Photothermal Performance of Fe_3O_4-C and Fe_3O_4-C@MnO_2 NPs

Photothermal performance of Fe_3O_4-C and Fe_3O_4-C@MnO_2 NPs was assessed by 808 nm laser irradiation the individual holes of a 96-well culture plate containing 100 μl Fe_3O_4-C@MnO_2 or Fe_3O_4-C@MnO_2 NPs dispersion (PBS, pH=7.4) with varying concentrations. The temperature of the irradiated aqueous dispersion was recorded by a thermal probe.

Scavenging effect of GSH on ROS

10 Mm ROS (H_2O_2) with different concentration of GSH were incubated with 1 ml DCFH-DA (10 μM in PBS) at room temperature for 20 min, the variation of ROS was quantified by detecting the fluorescence of DCF (λex = 488 nm, λem = 525 nm) with fluorescence spectrum.

The intracellular concentration of GSH detection

MDA-MB-231 cells were seed in a six-well plate (10x105 per well) and cultured to be fully confluent. After treatment with a varied concentration of Fe_3O_4-C@MnO_2 NPs for six h at 37 °C, cells were harvested, washed with PBS and lysed on ice in 40 μl of Triton-X-100 lysis buffer. After 1h, lysates were centrifuged at 9800 g and 200 μl of the supernatant was mixed with 1000 μl of Ellman's reagent (0.5 mM DTNB). The amount of GSH was quantified by measuring the absorbance at 405 nm using a UV-vis-NIR spectrophotometer. Percentage of GSH content from treated cells were compared with untreated cells.

The ·OH generation, detection and the promotive effect of heat

Study of the ·OH generation was conducted by analyzing the degradation of methylene blue (MB) as reported previously. In brief, the absorbance at 644 nm of MB solution (50

μg ml-1) with or without 400 μM of H_2O_2 was measured before or after the addition of Fe^{2+} (100 μM). Electron paramagnetic resonance (EPR) spectroscopy was then employed to further ensure the generation of ·OH and the ability of heat-enhanced hydroxyl radical yield accurately using 5,5-Dimethyl-1-pyrroline N-oxide (DMPO) as a spin trapping agent for •OH. With 80 μl of DMPO buffer solution (100 mM) in a dark EP tube, the subsequent reaction groups included the following additions respectively: 40 μl H_2O_2 (2 mM), 40 μl H_2O_2 (2 mM) + 1 mM Fe^{2+}, 40 μl H_2O_2 (2 mM) + 1 mM Fe^{2+} with several seconds heating using 320 K water for several seconds. Immediately, the mixture was transferred into a quartz capillary using capillarity, X-band EPR spectra were then measured at room temperature in perpendicular mode on a Bruker EMX-8/2.7 spectrometer and recorded with the following settings: microwave frequency=9.872 GHz, microwave power=6.375 mW, modulation frequency=100.00 kHz and modulation amplitude =1.00 G.

Cell culture.

MDA-MB-231 and MCF-7 human breast adenocarcinoma cell line, Hela cervical cancer cell line, DU-145 prostate cancer cell line were cultured in Dulbecco's modified Eagle's medium (DMEM). Each media contained 10% fetal bovine serum (FBS, Hyclone), 100 U/ml penicillin, and 100 μg/ml streptomycin and incubated at 37 ºC in 5 % CO2 humidified incubator for general 2-dimensional cell culture.

Cell viability test

Cytotoxicity of the samples was evaluated under various concentration. MDA-MB-231 cells, Hela cells, and DU-145 cells were seeded on 96 well plates at an initial density of 1.0 x 104 cells/well and incubated for overnight. A solution of free DOX, Fe_3O_4-C@MnO_2 NPs, Fe_3O_4-C@MnO_2 -NIR (808 nm, 1.5 W cm-2, 5 min), Fe_3O_4-C@MnO_2 -DOX, Fe_3O_4-

C@MnO_2 -DOX-NIR (808 nm, 1.5 W cm-2, 5 min) at various concentrations was treated with fresh medium and incubated for further 48 h. After incubation, cells were washed with DPBS and medium was replaced by 100 μl of a Prestoblue solution containing a medium. After incubation for 30 min, the fluorescence at 590 nm (excited at 560 nm) was measured by a microplate reader.

The half maximal inhibitory concentration (IC_{50}) was conducted under various DOX concentration (0.1, 0.5 1.0, 5.0, 10, 20, 30, 50 μM) and pretreated with fresh medium (control), Fe_3O_4-C@MnO_2 NPs (50 μg ml-1), and Fe_3O_4-C@MnO_2 NPs under laser irradiation (50 μg ml-1, 808 nm, 1.5 W cm-2, 5 min) and incubated for another 24 and 48 h. The cell viability was determined as mentioned.

Intracellular ROS detection

MDA-MB-231 cells were seeded in 24-well plates at an amount of 2×104 for 24 h and incubated with the following additions respectively: i) cells without any treatment; ii) cells incubated with Fe3O4; iii) cells incubated with MnO2; iv) cells incubated with Fe_3O_4-C@MnO_2 for another 24 h. After incubation with 1 ml DCFH-DA (10 μM in FBS-free DMEM) at 37 °C in 5% CO2 for 20 min, cells were washed with PBS three times. The level of intracellular ROS was evaluated by detecting the fluorescence of DCF (λex = 488 nm, λem = 525 nm) with a fluorescence microscope.

Live/dead staining

The cell apoptosis evaluation after CDT, PTT, chemotherapy and synergistic therapy was further confirmed by live/dead staining. After 24 h incubation, the live and dead cells were stained by calcein-AM (100 μl, 20 μM) and PI (100 μl, 20 μM), respectively. After 15 min

of incubation, staining solution were removed and rinsed by PBS twice and the samples could be subsequently visualized by fluorescence microscope.

In vitro photothermal effects

MDA-MB-231 cells were seeded in 96-well plates at an amount of 1.0×104 for 24 h and incubated with and without Fe_3O_4-C@MnO_2 NPs (10, 20, 50, 100 μg ml-1) for another 24 h. Subsequently, the cells were cultured with fresh complete medium and irradiated with an 808 nm laser at a power density of 1.5 w cm-2 for 5 min. After 24 h of incubation, the cell viabilities were determined with the similar approach described.

In vitro cellular DOX accumulation detection.

To investigate the cellular accumulation of DOX, MDA-MB-231 cells were seeded in a 48-well plate (2.0 x 104 cells/well) and incubated overnight. Fe_3O_4-C@MnO_2-DOX NPs were incubated with cells with/without laser exposure (808 nm, 1.5 w cm-2, 5 min) at a final concentration of 50 μg ml-1. After 6 h, 12 h, 24 h incubation, cells were fixed and stained with DAPI for observation by fluorescence microscopy and the mean fluorescence intensity (MFI) per cell was further measured.

In vitro cellular targeting assays.

The in vitro cellular targeting effect of Fe_3O_4-C@MnO_2 NPs was investigated by confocal laser scanning microscopy (CLSM). Briefly, MDA-MB-231 cells and MCF-7 cells were incubated with Fe3O4-C@MnO2 -DOX-iRGD (50 μg ml-1) at 37 ºC for six h, 12 h, 24 h, respectively. After fixing and staining with DAPI, the cells were observed by CLSM and the mean fluorescence intensity (MFI) per cell was further measured.

In Vitro Gene expression analysis.

To determine the influence of laser irradiation on gene expression, quantitative RT-PCR was performed. After 24 h uptake of Fe_3O_4-C@MnO_2 (50 μg ml-1), MDA-MB-231 cells were collected after six h post-irradiation (1.5 W cm-2, 5 min). Untreated MDA-MB-231 cells (control), those containing Fe_3O_4-C@MnO_2 NPs (50 μg ml-1) without laser irradiation were processed in the same way.

The total RNA was isolated using TRIzol Reagent (Life Technologies, MA). The conversion of total RNA to cDNA was accomplished using Superscript III First-Strand Synthesis System (Life Technologies, MA). The mRNA expression level of genes of interest was analyzed using quantitative PCR (qPCR) and reported in fold change values relative to control as described previously.

In vivo Fluorescence (FL) imaging

For in vivo FL imaging, MDA-MB-231 tumor-bearing female mice were intravenously injected of FITC labeled Fe_3O_4-C@MnO_2 NPs at a dose of 10 mg kg-1 via the tail vein. The mice were imaged using in vivo imaging system (IVIS) spectrum (PerkinElmer, Waltham, MA) at 1, 2, three h post-injection. Moreover, major organs and tumor were collected and washed with PBS for ex vivo imaging.

In vitro and in vivo MR imaging

The magnetic resonance (MR) imaging was conducted under anesthesia on a 3T MRI scanner with the following parameters: field of view = 5×3cm2 matrix size = 256 ×256, slice thickness = 1 mm, echo time (TE) = 10 ms, and repetition time (TR) = 350 ms. To test the MR imaging performance, different concentration of Fe_3O_4-C@MnO_2 NPs were incubated with 10 mM GSH for 20 min, and the supernatant were collected and placed in 96 well strips for MRI scanning.

For in vivo MR imaging, Fe_3O_4-C@MnO_2 NPs were intratumor injected and monitored its performance after 0, 1, 2, 3, 5, 24, 96 h, respectively.

Distribution characteristic of Mn and Fe in mice

MDA-MB-231 xenograft-bearing female nude mice (n=3) were injected with Fe_3O_4-C@MnO_2 NPs, at a dose of 10 mg kg-1. At 48 h post-injection, mice were euthanized, and major organs were collected and weighed. The organs were digested with ultra-pure nitric acid, and the obtained solutions were diluted to 5 ml by adding DI water. The Mn and Fe content in these solutions and the original injectate was measured by ICP-MS. The percentage of injected dose per gram of organ (%ID/g) was calculated by comparing the concentrations in samples with that of the ID.

In vivo antitumor efficacy

All animal work was conducted following the regulation of the Institutional Animal Care and Use Committee (IACUC) at Rutgers University. Six-week-old BALB/c nude mice were used in this study. To develop the tumor model, MDA-MB-231 (5.0X106) were mixed with Matrigel (BD, Biosciences, CA) and were transplanted in the flanks via subcutaneous (SC) injection. For in vivo therapeutic evaluation, nude mice were randomly assigned (n=3) into four groups. The anti-cancer experiments were performed until the volume of tumors reached 100 mm3. Four groups for different treatment contained the following conditions: i) the first group as the control (injected with the dose of 50 μl of PBS); ii) the second group were injected with 50 μl of DOX (28 μM); iii) the third group were injected with 50 μl of DOX-loaded Fe_3O_4-C@MnO_2 NPs (with concentration of 300 μg ml-1); iv) the fourth group were injected with 50 μl of DOX-loaded Fe_3O_4-C@MnO_2 NPs (with concentration of 300 μg ml-1) and irradiated under a 1.5 W cm-2 NIR laser for

5 minutes. Using a digital caliper to monitor the volume of the tumors every 3-4 day lasting 28 days after the corresponding experiments. The tumor volumes were calculated according to the following equation: V=length x width x hight x 3.14/6. The normalized tumor volume was defined as VR=V V0-1 X 100%. The body weights were measured every 3-4 day to evaluate the in vivo biosafety.

The pathological tissue sections of tumor and major organs (i.e., heart, liver, spleen, kidney, lung) were collected for hematoxylin and eosin (H&E) staining assay. The TUNEL analysis was performed on the tumor slides.

The fresh tumors were washed with PBS and transferred into liquid nitrogen for in vivo PCR analysis. After crushing, the total RNA was isolated using TRIzol Reagent and analyzed as previous mentioned.

2.3.3 Results and Discussion

Synthesis and characterization of core-shell and porous RHACK nanoparticles.

Our hierarchical multifunctional nanoparticle-based DDS was constructed via two sequential redox reactions (Figure 2-13). By first generating an ultrasmall iron oxide NPs doped porous carbon matrix based on a ferrocene-based hydrothermal reaction, we are aimed to achieve fast intracellular leaching of iron ions for efficient Fenton reaction. By performing HRTEM and EDS mapping, we can further observe a desired hollow nanostructure composed of amorphous carbon matrix doped with ultrasmall Fe_3O_4 NPs (average size of 5 nm). Based on this iron oxide-carbon NPs, a MnO_2 nanoshell was then uniformly coated by an interfacial redox reaction between carbon and $KMnO_4$. In our synthesis, the sizes of core and thicknesses of shells can be effectively controlled by

modulating the ratio of ferrocene and H_2O_2 and the concentrations of $KMnO_4$, respectively, thereby meeting the needs for versatile applications. From the SEM and TEM, the core and core-shell RHACK NPs show a spherical hollow morphology and have an average size of 167 nm and 197 nm, respectively. Such hollow and highly porous structures with high specific surface area could enhance the anti-drug loading capacity (50%) and drug loading efficiency (79%), and we demonstrated this using doxorubicin (DOX) as an exemplary drug. Moreover, iRGD is covalently conjugated onto the NPs to endue specific targeting and penetration. The serial changes on the zeta potential of each step further indicated a successive loading of DOX and conjugation of iRGD. Additionally, with a MnO_2 shell, the high payload of the drug can be effectively released in response to cancer-specific redox stimuli. More specifically, when we incubated the RHACK NPs with ten mM GSH, which represents the pro-reductive cytoplasmic microenvironment in breast cancer cells, a dramatic (5.46 fold) increase on the drug releasing amount was observed compared to the control (2 μM GSH). And the degradation of MnO_2 shells was further confirmed by EDS data. Considering the big disparity of GSH concentration between physiological conditions and cancer cell, the distinctive stimuli-responsive drug release indicates its good potential as a drug delivery platform to reduce side effects caused by leaked drugs.

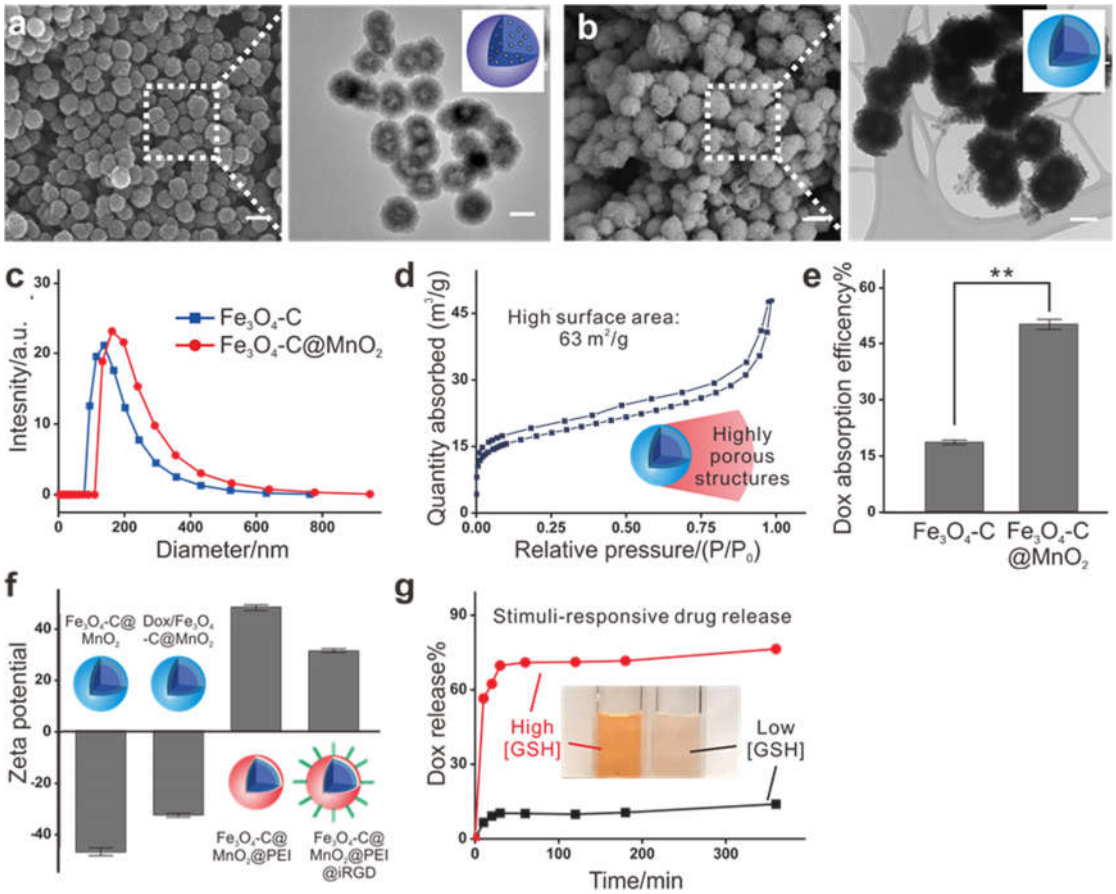

Figure 2-13. Synthesis and characterization of core-shell and porous RHACK nanoparticles. a-b, RHACK nanoparticle before (a) and after (b) MnO_2 shell coating. Scale bars: 200 nm, 100 nm, 200 nm, 100 nm, from left to right. c-g, Hydrodynamic size (c), BET surface area characterization (d), anti-cancer drug loading (e), surface charge (f) and anti-cancer drug release (g) of RHACK nanoparticles and the comparison to the control nanoparticles.

RHACK induced GSH reduction and ROS generation

Tailored to the fact that cancer cells are under oxidative stress associated with the overproduction of ROS mainly H_2O_2 and are susceptible to further ROS insults, our hybrid RHACK NPs show desired step-wise biodegradability under endogenous bio-stimuli and simultaneous produce theragnostic ion species (e.g., Mn^{2+} and Fe^{2+}) for enhanced CDT could be highly advantageous and unique (Figure 2-14). More specifically, the MnO_2 shell underwent a redox reaction with endogenously overexpressed GSH to yield Mn^{2+} and glutathione disulfide (GSSH). Then the iron oxide-carbon core would be exposed to GSH that had been ascribed to the acceleration of iron leaching from the interior ultra-small Fe_3O_4 nanocrystals, which would disrupt the integrity of iron oxide-carbon core and triggered dissociation of the carbon matrix into ultrasmall graphitic segments and soluble iron ions (Fe^{2+}/Fe^{3+}). Meanwhile, the synchronously released Fe^{2+}/Fe^{3+} with excellent Fenton-reaction activity to transform intracellular H_2O_2 induced by mitochondria and anticancer drug (doxorubicin, termed as "DOX") to highly lethal ×OH and consume antioxidant GSH to avoid ×OH scavenging. Interestingly, such biodegradation of our RHACK NPs could be readily achieved by treating GSH and we monitored the degradation by the disappearance of their characteristic UV-Vis absorption peaks as well as the time-dependent decrease of particle size in DLS and TEM. More importantly, by collecting and performing ICP-MS analysis on the supernatants during the degradation of RHACK NPs, we found a time-dependent increase of manganese and iron ions release, concurred with our hypothesis. To demonstrate the ability of RHACK for the redox manipulation, we have investigated both GSH reduction and ROS generation individually. The scavenging of ROS (e.g., H_2O_2) by the varied concentration of GSH was firstly confirmed using 2,7-

dichlorodihydrofluorescein diacetate (DCFH-DA) as a ROS probe. To detect changes in intracellular GSH concentrations, Ellman's reagent was used as reported. From the results, after the addition of RHACK NPs, a clear decrease on the GSH levels was observed in a concentration-dependent manner. To show the potential of RHACK NPS for inducing ROS, we also delivered one of the degradation product, iron ions to the H_2O_2 solution and we monitored the Fenton reaction by a methylene blue (MB) dye. A significant decrease in absorbance was observed when MB was incubated with H_2O_2 and Fe^{2+}, whereas no apparent change after treating with H_2O_2 and Fe^{2+} alone. Using ROS probe, we delivered RHACK NPs into cancer cells and monitored the redox changes intracellularly. As a control, we delivered an equivalent amount of MnO_2 nanostructures and iron oxides. By quantifying the ROS level, significant higher ROS levels were observed in our experimental condition compared to MnO_2 control and iron control, respectively. This result suggests a synergistic induction of ROS by the MnO_2 nanostructures and iron ion-based Fenton reaction. A detailed mechanistic study on the molecular biology pathways further revealed the synergy originate from the regulation over several important cell apoptosis genes including BCL-2, BAX, Caspase 3, which are mitochondria-related and closely regulated pathways of cytoplasmic redox.

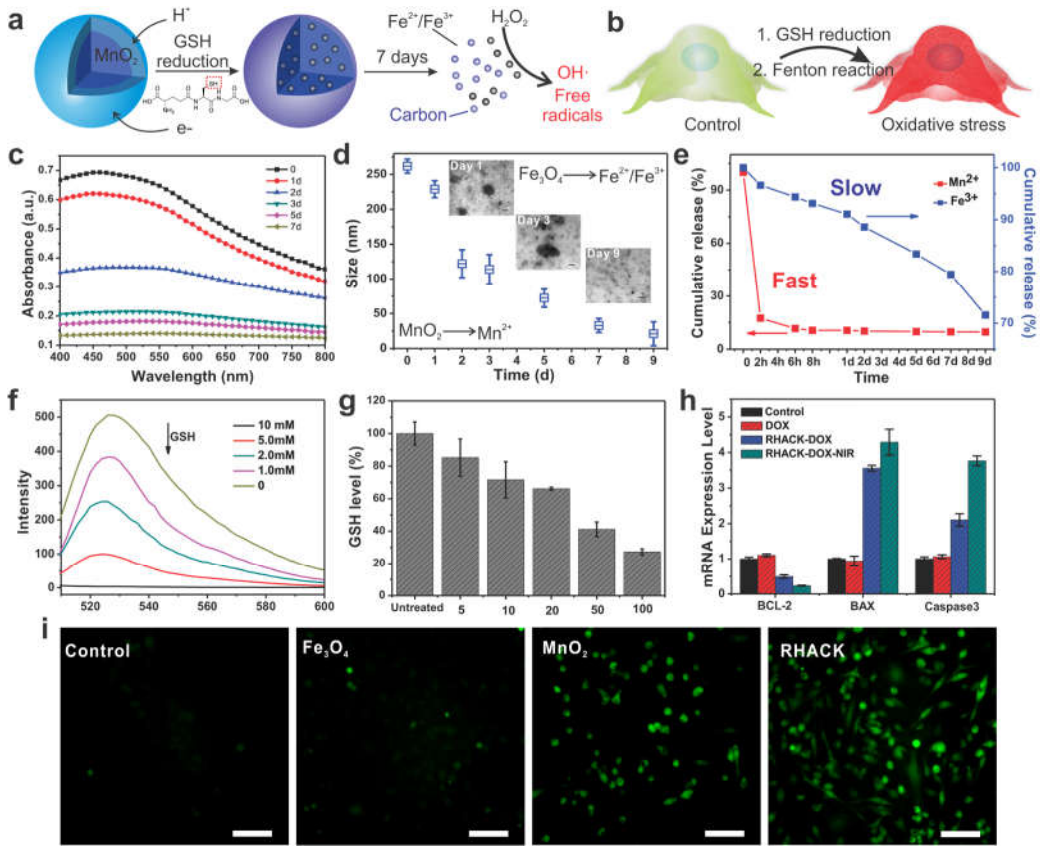

Figure 2-14. RHACK induced GSH reduction and ROS generation. a, Schematic diagram illustrating the mechanism of RHACK-based ROS induction. b, The combined GSH reduction and Fenton reaction lead to enhanced oxidative stress for cancer killing. c-e, The color change (c), size reduction (d) and release of Mn and Fe (e) during degradation of RHACK. f-h, The degradation-associated reduction of GSH concentrations (g), which lead to the increase of pro-apoptosis pathways in cancer cells based on qRT-PCR (h). i, The combined Fenton reaction by Fe3O4 nanoparticles and reduction of GSH by MnO_2 shell in a single platform lead to synergistic ROS generation. Scale bars: 100 μm.

RHACK nanoparticle-based photothermal hyperthermia

The biodegradable RHACK NPs not only delivers chemotherapeutics effectively in a stimuli-responsive manner, reduces GSH and induces ROS by a Fenton reaction, but also provides strong NIR responsive photothermal heating (Figure 2-15). For the NIR responsive photothermal conversion performance, we focused on an 808 nm wavelength laser considering their minimal absorption by water and a good penetration depth[6,7,148]. Under a laser power of 1.5 W/cm^2, we identified a significant temperature increase within 5 minutes. As a control, water alone under this laser power doesn't show any noticeable heating effect. Additionally, the photothermal conversion efficiency was calculated to be 30.6 %, which is consistent with the strong NIR absorption spectrum of our RHACK NPs and are comparable to the most efficient NIR photothermal reagents (e.g., carbon nanotube, Au nanorod). By comparing the NIR heating effects between the iron oxide-carbon core and the RHACK core-shell NPs; the former contribute more than 91% temperature increase compared to the latter, further confirmed the photothermal effect mainly come from the carbon nanostructure in the core. Equal importantly, the photothermal effect of the RHACK NPs can be readily controlled spatiotemporally for different purposes by directly modulating the NIR laser. For example, by varying the laser power intensity, we can realize temperature change from 40-45 °C, which is desired for inducing cancer apoptosis and sensitize cancer cells to chemotherapy without damaging surrounding normal tissues. Also, four heating/cooling cycles were valuated and no obvious temperature decrease was observed, indicating the RHACK NPs possessed high photothermal stability. Moreover, electron paramagnetic resonance (EPR) was used to detect the in situ ·OH to investigate whether localized heat could influence the CDT performance of our NPs. Assessment at

318k showed the much higher intensity of the EPR, which indicated the heat generated from photothermal could accelerate and improve the quantity of ·OH. Furthermore, our RHACK NPs not only improve CDT performance but also reduce drug efflux and enhance intracellular accumulation of drug. By delivering the Dox-loaded RHACK NPs into cancer cells, a mild treatment of NIR laser directly leads to higher accumulation (1.93 fold increase) of anti-cancer drugs inside cancer cells based on the distinctive DOX fluorescence. The related molecular biology pathways were further conducted. Through the localized hyperthermia, several MDR pathways including MDR-1 and TP53 are effectively suppressed, leading to a dramatically reduced drug efflux and enhanced apoptosis, which is consistent with previous reports. Therefore, combining with the GSH-responsive and strong photothermal properties of RHACK NPs, make our DDS a particularly smart platform in selectively killing cancer cells.

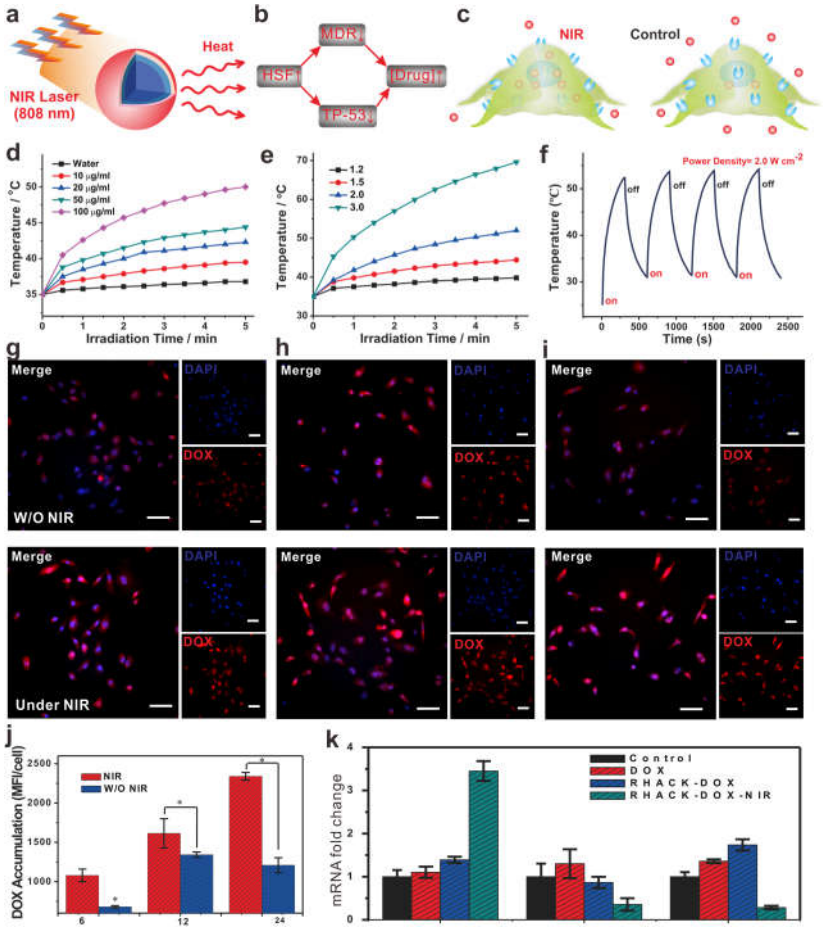

Figure 2-15. RHACK nanoparticle-based photothermal hyperthermia. a-c, Schematic diagram illustrating RHACK-based photothermal effect (a) and the suppression of chemoresistant pathways, which lead to the reduced drug efflux in cancer. d-f, Concentration (d) and laser power (e) and laser cycle controllable photothermal effect of RHACK nanoparticles. g-i, Drug accumulation in cancer cells under or without NIR laser of RHACK nanoparticle-delivered doxorubicin at different time points of 6 (g), 12 (h) and 24 hours (i). Scale bars: 50 μm. j-k, Statisctical summary of Dox accumulation at different time points (j) and gene fold-change under diferent treatment.

Synergistic induction of cancer apoptosis based on ROS generation and photothermal therapy

By demonstrating redox manipulation and robust photothermal effect separately, we hypothesized that these two modalities would synergistically co-sensitize cancer cells towards chemotherapy by orthogonally targeting the heterogenous pathways in cancer (Figure 2-16). To test our hypothesis, we first performed a comprehensive cancer apoptosis assay in vitro. In our experimental condition (RHACK-NIR-DOX), DOX-loaded RHACK NPs was delivered to cancer cells for 24 hours, followed by an 808 nm NIR laser exposure. As controls, four additional groups were included: i) RHACK NPs alone; ii) DOX alone; ii) RHACK NPs with NIR (RHACK-NIR); and iv) DOX-loaded RHACK NPs without NIR were included (RHACK-NIR-DOX). To obtain IC50 of DOX and validate the improved chemotherapeutic effects, and anti-cancer effects from NPs with varying concentrations were further studied. From the results of cancer apoptosis assay, while RHACK NPs show high biocompatibility (>90%), RHACK-NIR and RHACK-Dox groups induce significant apoptosis of cancer cells at all concentrations, and such apoptosis presents a clear dosage-dependent manner. Based on our calculation and considering a drug loading capacity of 50%, we identified a significant improvement on the IC50 of anti-drug that we used in both the RHACK-NIR (17.2% decrease) and RHACK-Dox (80.56% decrease) groups. Remarkably, by combining the NIR treatment and the DOX treatment, a further lowered IC50 at 0.38 μm (80 times decrease) was achieved, which is more than a combinatorial effect. More specifically, at concentrations of 100 μg/ml, the RHACK-NIR-Dox group can almost kill 100% of cancer cells, while there are 23% and 11% cancer cells remaining in the RHACK-NIR and RHACK-DOX groups, respectively. However, such

highly potent anti-cancer drug delivery platform may also induce undesired cytotoxic effects once they circulated into normal cells, despite the passive targeting effect and spatiotemporal controlled drug delivery provided by RHACK. As such, we used iRGD, a cell targeting and tissue-penetrating peptide, to impact tumor targeting-mobilities. The iRGD peptide can bind to $\alpha_v\beta3$ integrin, which is overexpressed on some cancer cells (e.g., MDA-MB-231). To achieve this, we decorated the outer PEI layer of our RHACK NPs with a combination of polyethylene glycol (PEG), namely PEI-PEG-iRGD, to form Fe_3O_4-C@MnO_2-iRGD constructs. To demonstrate this, we delivered the DOX-loaded constructs into two breast cancer cell lines in vitro: MCF-7 cells, which have low integrin levels, and MDA-MB-231, which are more invasive and highly express integrin. By visualizing DOX using confocal microscopy, a nearly 2-fold increase in the MDA-MB-231 cell uptake was observed when comparing the MCF-7 cells. This indicates not only successful conjugation of functional iRGD to the particle but also the suitability of this targeting strategy for specific targeting.

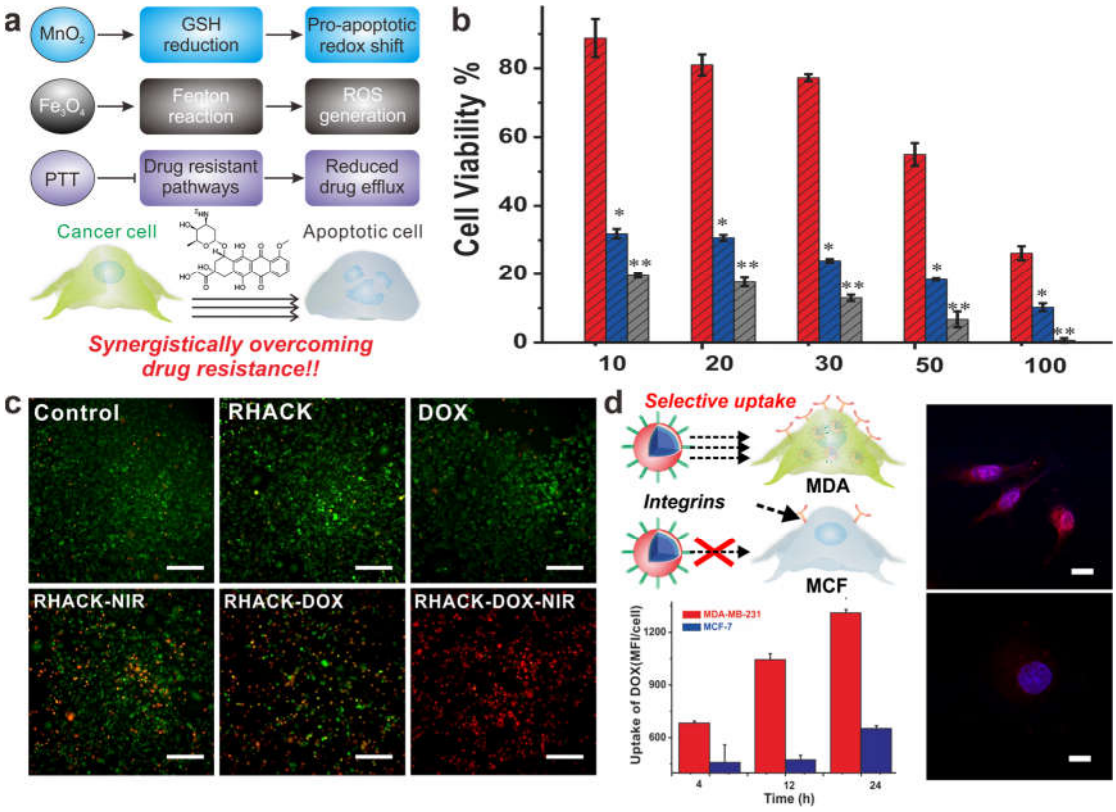

Figure 2-16. Synergistic induction of cancer apoptosis based on ROS generation and photothermal therapy. a, Schematic diagram showing the pathways leading to synergistic induction of cancer apoptosis. b-c, MTT assay (b) and live-dead staining-based confirmation of synergistic induction of cancer apoptosis from NIR treatment alone (red), without MnO2 shell (blue) and the RHACk nanoparticles with NIR treatment (grey). Scale bars in c: 200 μm. d, Schematic and experimental results showing the targeted delivery of anticancer drugs (shown in red fluorescence) into malignant cancer cells by RGD-conjugated RHACK nanoparticles. Scale bars: 50 μm.

Significant suppression of tumor growth induced by RHACK nanoparticles

Following the promising in vitro findings, we explored whether the iRGD conjugated NPs also improve targeting and penetration in solid tumors in vivo (Figure 2-17). For this purpose, we labeled the NPs with FITC via amine-isothiocyanate conjugation. The FITC labeled NPs were administered intravenously into mice bearing orthotopic MDA-MB-231 tumors, and whole body fluorescence imaging was performed at different time points. A strong fluorescence signal was detected in the tumor as early as 1h after injection. The tumor accumulation improved with increased time, suggesting the NPs remained in circulation and could accumulate in the tumor effectively. Following animal sacrifice, the tumors and other organs were extracted for ex vivo fluorescence imaging. We indeed found significantly higher fluorescence in tumors compared to other organs. We further investigated the biodistribution of the NPs. After 48 h, the vast majority of the injected NPs were accumulated in tumors and reticuloendothelial system, including the liver and spleen, while the Mn^{2+} was almost cleared from the whole body. The enhanced tumor accumulation was assumed to improve the eventual performance in antitumor therapy.

While specific tumor targeting is the primary task for cancer treatment, monitoring tumor progression under more clinic relevant settings is also critical to diagnose the stage of cancer and provide invaluable information for doctors. To this end, RHACK NPs not only serve as a distinctive and efficient anti-cancer drug delivery platform but also provides self-enhanced MRI imaging modalities based on the release of T1 MRI positive probes (Mn^{2+}) after entering cancer cells. To demonstrate this unique imaging ability, we further treated varying concentration of RHACK NPs with ten mM GSH and collected the supernatant for MRI. From our results, there is a clear concentration-dependent increase of MRI signals

compared with PBS control group and directly supported our hypothesis. Following this, we further performed time dependent in vivo MRI imaging. We found that while an initial NPs injection doesn't yield noticeable MRI signals, a constant increase of MRI intensities can be found throughout the time course between 1 hour to 3 hours, then remained stable between 5 to 24 hours followed by a signal decrease until 96 hours. Compared to other NPs-based imaging tools, these results are particularly interesting, as the onset of T1 MRI signals directly corresponds to the degradation of the RHACK nanomaterials and release of drugs. In another word, we confirmed an MRI monitorable degradation and drug release in vivo in a tumor model. More importantly, the MRI imaging enhanced by the Mn^{2+} has high contrast and signal-to-noise ratio, especially at the time point of 3 hours. Such high quality and glutathione responsive MRI imaging can better identify the tumor region, the progression of cancer in vivo and better guide the treatment strategy for the doctors in clinical cancer treatment.

With the promising results from highly efficient (almost 100%) in vitro cancer killing, excellent specific targeting and self-enhance MRI monitoring both in vitro and in vivo, we then further evaluated the in vivo performance of RHACK nanoparticle-based anti-drug delivery for tumor suppression. By performing a standard in vivo breast tumor assay, we injected DOX-loaded RHACK NPs, treated with 808 nm NIR laser and analyzed the time-dependent progression of tumor volumes. Consistent with our in vitro studies, we also injected DOX-loaded RHACK NPs without additional NIR treatment. Also, two controls with saline treatment only and DOX injection only were included. By time-dependent body weight curve and H&E histological staining of the main organs, no detectable damage could be observed, except the DOX group showed some defect in heart resulted from the

side effect of free circulating DOX. For the therapeutical results, as expected, the group treated with saline only showed an exponential increase of tumor volume and the growth of tumor with DOX injection start to slow down due to its cancer-killing effects. However, when the DOX was delivered by RHACK NPs under identical concentrations, tumor growth further decreased significantly compared to both control groups. Most importantly, the delivery of doxorubicin by RHACK NPs and combing NIR laser exposure almost completely stopped the tumor growth throughout the 1-month observation. Additionally, 1-month after NPs treatment, by dissecting the tumor from each group, we found a similar trend in tumor weights, with 10.3-151.2 fold decrease in the experimental group compared to the other controls. By further performing in vivo gene analysis in the dissected tumor tissue, we confirmed the suppression of HSF-1, MDR-1, and TP-53, BCL2 and upregulation of BAX, Caspase 3 in the tumor site, compared to the controls, further supporting our strategy that has been proven in vitro pathway analysis. Moreover, TUNEL and H&E staining of the tumor sections were investigated to confirm the enhanced cell apoptosis. These results are reflective of the in vitro experiments and collectively suggest a high potential of RHACK nanoparticle-based DDS for in vivo and clinical applications of breast tumor suppression.

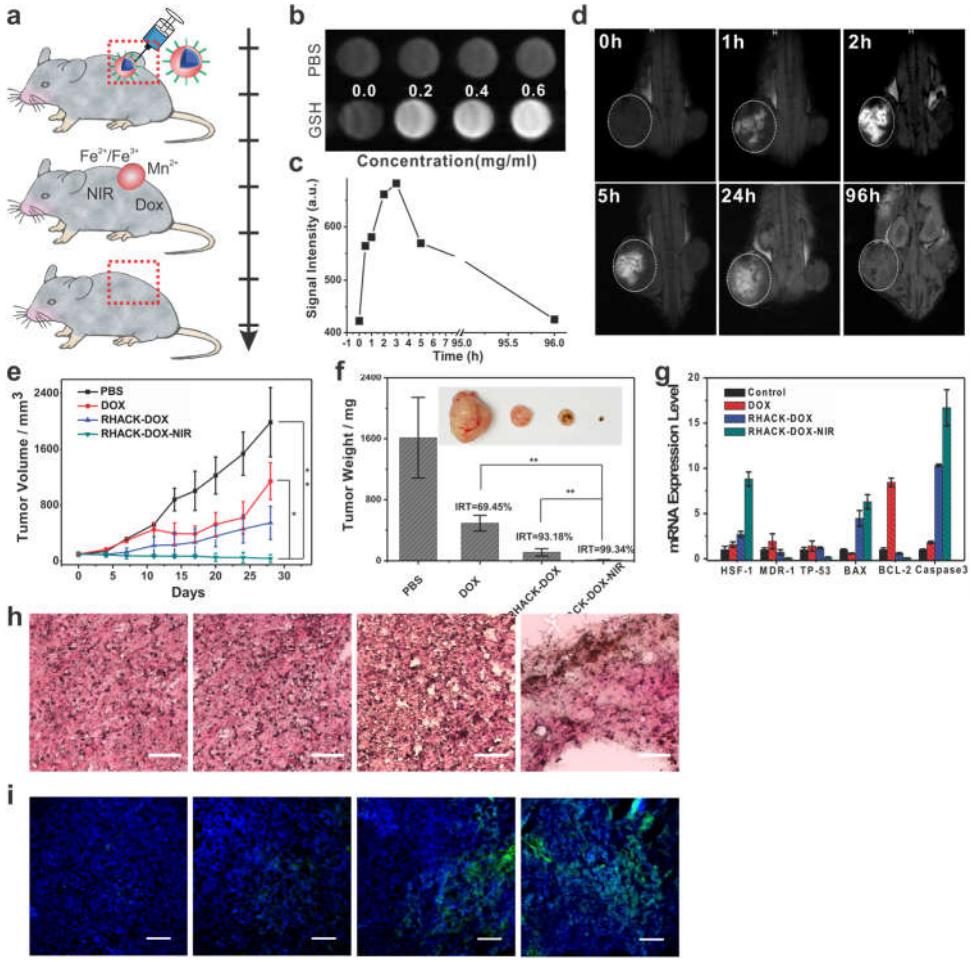

Figure 2-17. Significant suppression of tumor growth induced by RHACK nanoparticles. a, Schematic diagram of the treatment method. b, MRI imaging enabled by the released of Mn(II) during in vivo degradation of RHACK nanoparticles. c-d, Time dependent accumulation of Mn(II) detected by MRI. e-f, Time depedent tumor growth (e) and the final tumor volume comparsion (f) revealed the strong anti-tumor effect of RHACK nanoparticles in vivo. g-i, In vivo mRNA expression (g), H&E staining (h) and immunostaining (i) further support the enhanced treatment of tumor by RHACK nanoparticles in the genetic, histological and protein level.

2.3.4 Conclusion and Outlook

In summary, as a proof of concept, we developed a novel multifunctional nanoparticle with unique hollow structure, step-wised biodegradability, specific targeting, self-enhanced MRI monitoring and synergetic CDT/PTT/Chemo "weapon" for synergistically enhanced treatment of cancer in vitro and in vivo. More specifically, our hybrid nanoparticle-based DDS not only achieves a high drug loading efficiency and stimuli-triggered drug release but also endues a self-reinforced CDT nanoagent that possesses both GSH depletion and $Fe^{2+}/Fe^{3}+$ induced Fenton reaction to interfere with redox homeostasis and down-regulate several vital anti-apoptotic pathways. Moreover, the localized heat generated by PTT could simultaneously elicit clinically used anti-cancer drugs outcome by down-regulating pivotal MDR-related genes and accelerate the intratumoral Fenton process. To the best of our knowledge, this is the first study to construct activable theranostic nanosystem for MRI-monitored CDT/PTT/Chemo combination cancer therapy. Our approach demonstrates a new avenue for the development of nanomedicine with maximized treatment outcome while minimized adverse side effects and shows great promise for the efficient clinical tumor treatment and imaging.

Chapter 3: 2D-hybrid nanomaterials for advanced stem cell therapy

3.1 A Biodegradable Hybrid Inorganic Nanoscaffold for Advanced Stem Cell Therapy

Note: This section is modified from a published work in Nature Communications[452].

3.1.1 Introduction

Developing reliable therapeutic methods to treat central nervous system (CNS) diseases (e.g. Alzheimer's and Parkinson's diseases), degeneration in the aging brain, and CNS injuries [e.g. spinal cord injury (SCI) and traumatic brain injuries] has been a major challenge due to the complex and dynamic cellular microenvironment during the disease progression[453,454]. Several current therapeutic approaches have aimed to restore neural signaling, reduce neuroinflammation, and prevent subsequent damage to the injured area using stem cell transplantations[455-458]. Given the intrinsically limited regenerative abilities of the CNS and the highly complex inhibitory environment of the damaged tissues, stem cell transplantation has great potential to regenerate a robust population of functional neural cells such as neurons and oligodendrocytes, thereby re-establishing disrupted neural circuits in the damaged CNS areas[456,459-462]. However, several pertinent obstacles hinder advances in stem cell transplantation. First, due to the inflammatory nature of the injured regions, many transplanted cells perish soon after transplantation[463]. Second, the extracellular matrix (ECM) of the damaged areas is not conducive to stem cell survival and differentiation[454,464]. Therefore, to address the aforementioned issues and facilitate the progress of stem cell therapies, there is a clear need to develop an innovative approach to increase the survival rate of transplanted stem cells and to better control stem cell fate in

vivo, which can lead to the recovery of the damaged neural functions and the repair of neuronal connections in a more effective manner.

To this end, we report a biodegradable hybrid inorganic (BHI) nanoscaffold-based method to improve the transplantation of human patient-derived neural stem cells (NSCs) and to control the differentiation of transplanted NSCs in a highly selective and efficient way. Further, as a proof-of-concept demonstration, we combined the spatiotemporal delivery of therapeutic molecules with enhanced stem cell survival and differentiation using BHI-nanoscaffold in a mouse model of SCI. Specifically, our developed three-dimensional (3D) BHI-nanoscaffolds (Figure 3-1) have unique benefits for advanced stem cell therapies: i) wide-range tunable biodegradation; ii) upregulated ECM-protein binding affinity; iii) highly efficient drug loading with sustained drug delivery capability; and iv) innovative magnetic resonance imaging (MRI)-based drug release monitoring (Figure 3-1a-c). Hybrid biomaterial scaffolds have been demonstrated to mimic the natural microenvironment for stem cell-based tissue engineering[45,465-473]. In this regard, scientists including our group, have recently reported that low-dimensional (0D, 1D, and 2D) inorganic and carbon nanomaterial (e.g. TiO_2 nanotubes, carbon nanotubes, and graphene)-based scaffolds, having unique biological and physiochemical properties, and nanotopographies, can effectively control stem cell behaviors in vitro as well as in vivo[35,243,276,474-479]. However, these inorganic and carbon-based nanoscaffolds are intrinsically limited by their non-biodegradability and restricted biocompatibility, thereby delaying their wide clinical applications. On the contrary, MnO_2 nanomaterials have proven to be biodegradable in other bioapplications such as cancer therapies, with MRI active Mn^{2+} ions as a degradation product[171,193,207]. Taking advantage of their biodegradability, and incorporating their

unique physiochemical properties into stem cell-based tissue engineering, we have developed MnO_2 nanomaterials-based 3D hybrid nanoscaffolds to better regulate stem cell adhesion, differentiation into neurons, and neurite outgrowth in vitro and for enhanced stem cell transplantation in vivo (Figure 3-1d-e). Considering the difficulties of generating a robust population of functional neurons and enhancing neuronal behaviors (neurite outgrowth and axon regeneration), our biodegradable MnO_2 nanoscaffold can potentially serve as a powerful tool for improving stem cell transplantation and advancing stem cell therapy.

3.1.2 Methods

Synthesis and characterization of MnO_2 nanosheet and GO

MnO_2 nanosheets were synthesized based on a previous protocol with minor modifications [480]. Briefly, 2.2 g Tetramethyl ammonium pentahydrate ($TMAOH \cdot 5H_2O$, Alfa Aesar) was first dissolved in 20 ml 3% wt. H_2O_2 (Sigma-Aldrich) by vortexing (concentration of TMAOH is 0.6 M). In parallel, 0.594 g $MnCl_2 \cdot 4H_2O$ (Sigma-Aldrich) was dissolved in 10 ml de-ionized water (Concentration of $MnCl_2$ is 0.3 M) through sonication. Then the TMAOH dissolved in H_2O_2 solution was rapidly added into $MnCl_2$ solution within 10 seconds with fast stirring at 1200 rpm (round per minute). Please note that gas will be generated and rapid increase of solution volume will be observed. The solution was continued to be stirred at 600 rpm overnight and centrifuged at 2000 g for 5 minutes to obtain the bulk δ-MnO_2. After washing with water for 3 times and ethanol 2 times through shaking and centrifuge, bulk MnO_2 was dried in the oven under ambient conditions for 12 hours. After adding 100 mg into 10 ml de-ionized water, the solution was extensively

sonicated in the Sonics bath sonicator for 10 hours. Lastly, the solutions were centrifuged at 8801 g for 10 minutes to get rid of the aggregations and un-exfoliated products. The black solution was measured with concentration by evaporating water in the solution. MnO_2 nanosheet was diluted to 10 μg per ml for TEM (80Kv on a Philips CM12 with an AMT digital camera model XR111) and Ultra-Stem imaging. For X-ray photoluminescence spectroscopy (Thermo Scientific ESCALAB 250 Xi with a base pressure $<1*10^{-9}$), MnO_2 nanosheet solution (100 μg per ml) was drop-casted onto a silicon substrate and dried in the vacuum. An Al-Kα monochromated X-ray source was used to obtain the core level spectra, and the instrumental broadening was around 0.5 eV. The hydrodynamic size and zeta potential of MnO_2 nanosheets in aqueous solution were measured by a ZS (Nano Zetasizer) dynamic light scattering instrument (Malvern Instruments, Malvern, UK), with the temperature set at 25 °C and a detection angle of 90 degrees. UV-Vis absorption spectrum of MnO_2 nanosheet solution was measured by a Varian Cary 50 spectrophotometer using a quartz cuvette.

Graphene oxide was synthesized based on our previous publications [47,52]. 1.0 gram of Graphite (Bay Carbon) was preoxidized in the mixture of sulfuric acid (Sigma-Aldrich, 98%), phosphor oxide (Sigma-Aldrich) and potassium persulfate (Sigma-Aldrich) at 80 degrees for overnight. Then the pre-oxidized graphite was washed with water, dried and reacted with sulfuric acid and potassium permanganate through a 3-step process. After quenching with H_2O_2, a shining gold solution appear, and the graphite oxide was purified with 10% HCl solution (Sigma-Aldrich) and water extensively. Lastly, graphite oxide was exfoliated into graphene oxide by tip sonication (Branson). Multi-layered graphene oxide

was centrifuged down at 16639 g for 45 minutes, and the final suspension of single or few layered graphene oxides was obtained.

Measurement of protein absorption by MnO_2 nanosheet

Into the solutions of ECM protein (laminin protein from Sigma-Aldrich, stock concentration of 200 μg per ml, 0.5 ml, PBS is from Thermo Fisher), 10 μl of MnO_2 nanosheet aqueous solution (3 mg per ml) was added, or a piece of etched glass [first treated by pirahana solution for 1 hour, then oxygen plasma treated for 1 minute, followed by polylysine (1 mg per ml) coating for 4 hours] and polymer scaffold (Polycaprolactone nanofiber scaffold[276], 1 mg) was inserted. The solutions turned brown immediately, and then they were continued to incubate under 37 °C for 1 hour. To remove the MnO_2 nanosheet with absorbed proteins, the solution was centrifuged 3 times at 8801 g for 10 minutes, and precipitates were removed each time until there are no visible precipitates anymore. The solution should be transparent at this moment. 0.1 ml supernatant solution was transferred into a 96-well plate, and BCA (bicinchoninic acid assay, Thermo Fisher, A53226) was used to quantify the percentage of protein absorbed on nanosheets by subtracting the total amount of proteins remaining in the control group to the protein remained in the experimental groups. The assay was conducted strictly following the protocols from Thermo Fisher and absorption at 570 nm was used to quantify the protein amount for each group. These experiments were replicated 3 times, and the values were normalized to the glass control. The amount of laminin absorbed on MnO_2 nanosheet was calculated by subtracting the laminin concentration after MnO_2 nanosheet absorption from the original concentration. The percentage of laminin absorption was calculated by dividing the amount of laminin absorbed by the original laminin concentration. BCA

protein assay was repeated 3 times experimentally to get error bars shown in Figure 3-1. Data are mean±s.d., n=3, **P<0.01 by one-way ANOVA with Tukey post-hoc test.

In vitro biodegradation of MnO_2 hybrid nanoscaffold

We first studied the in vitro degradation of MnO_2 nanosheet in physiological conditions, different PBS solutions with varying concentrations of vitamin C (10 μg per ml, 50 μg per ml, 100 μg per ml, 200 μg per ml, 500 μg per ml) were prepared. Then 10 μl of 3 mg per ml MnO_2 nanosheet solution was added to 3 ml of vitamin C solution, and the UV-Vis spectrum of the solution was recorded every two minutes. The percentage of nanosheet remaining was normalized to the absorption (at 385 nm) of a control group without any vitamin C added. To study the degradation of thinly layered nanoscaffold, we drop-casted 100 μL of MnO_2 nanosheet solution (1.0 g per ml) into the wells of 24 well plate treated with oxygen plasma. After vacuum drying for 3 hours, a homogeneous, yellow and transparent film formed. Then the wells were coated with laminin (Thermo Fisher, Catalog No.: 23017015) and seeded with human neural stem cells at a cell density of 80k per well. The cells were cultured in standard differentiation media (w/o bFGF and no exogenous compounds) for different periods (1 day, 3 days, 7 day, 12 day, 17 day, and 22 day). The cells were then fully detached using acutase for 10 minutes at 37 °C. Followed by washing with PBS and de-ionized water, 24-well plate was vacuum dried. Based on the absorption of MnO_2 nanosheet at 385 nm, the degradation percentage was quantified by subtracting background (empty well) and normalize to the well without culturing the cells.

To study the degradation of thick layered nanoscaffold, a 3-layer, cell-MnO_2 nanoscaffold-cell sandwiched structure that mimic tissue structures was formed through centrifugation at 130 g in a 15 mL Eppendorf centrifuge tubes. A similar structure of GO nanoscaffold-

cell construct was formed using the same protocols as a control. The first layer contains 1 million iPSC-NSCs. The second layer is composed of 1.0 mg of MnO_2 nanosheet or graphene oxide. The third layer (Top layer) was centrifuged down from another 1 million iPSC-NSCs. Degradation of the scaffolds was monitored by the volume change and thickness change of scaffold on a weekly base. Based on the assumption that the scaffold has identical radius and areas, the percentage of scaffold volume was normalized to the thickness that was measured on Day 1.

To demonstrate cell-seeded nanoscaffold can fast degrade under biocompatible redox conditions, an aqueous solution of 0.3 mg per ml MnO_2 nanosheet was filtered through a cellulose membrane, then a layer of dye-labeled (food dye) cells were formed on the MnO_2 nanosheet assembled substrate using a tri-circular PDMS (Polydimethylsiloxane, Dow Corning®) chamber. After the addition of 20 mg per ml ascorbic acid (Sigma-Aldrich) for 5 minutes, most of the dark color of MnO_2 nanosheet disappeared, and a layer pink colored cell layer was formed.

Tunable biodegradation of MnO_2 nanoscaffolds

To show the tunable biodegradability of MnO_2 nanoscaffolds, we controlled the geometrical and chemical structures of MnO_2 nanoscaffold (Figure 3-18) which includes: i) thickness [0.2 H versus 1 H (H=0.4 mm), shown in a and b, respectively, which is achieved by filtrating different concentrations (0.6 mg per ml and 3.0 mg per ml, respectively) of MnO_2 nanosheet solution while keeping solution volume (1.0 ml) and filtrating area (1075 mm^2) constant]; ii) Height to surface area ratio (from 0.4 mm:1075 mm_2 in Figure 3-18b to 4 mm:107.5 mm^2 in Figure 3-18c), which was achieved by filtrating same amount of MnO_2 nanosheets (1.0 ml of 3.0 mg per ml) but reduced the filtrating area

by 10 times ; iii) protein amount in the scaffold (MnO_2 nanosheets absorbed with 1.0 mg per ml vs with 10 mg per ml bovine serum protein and then vacuum filtered). Degradation profile of different scaffolds obtained by measuring time-dependent manganese concentrations in the solution using Inductively coupled plasma mass spectrometry (ICP-MS, Fisons Instruments PlasmaQuad 2+). Each sample was measured 3 times to obtain error bars and standard deviation. To control scaffold degradation without any additional bioreductants, different cell densities (0, 0.1, 0.5, 1 and 5 million cells per well in a 24 well plate) were seeded onto MnO_2 nanoscaffold, and the complete degradation time was monitored by the full disappearance of dark color. 0.5 ml media was changed every two days. Each experiment was repeated twice. Results are summarized in Figure 3-18m.

Fabrication and characterization of MnO_2 hybrid nanoscaffold

To fabricate the MnO_2 hybrid nanoscaffolds, 10 ml of MnO_2 nanosheet solution at a specific concentration was filtered through a cellulose filter paper (pore size=20 nm) under the vacuum condition. Then the filter paper was taken out and cut into sizes and shapes of choice. To transfer into a transparent glass substrate, cleaned glass was first treated with oxygen plasma, then the MnO_2 nanosheet deposited on filter paper was wetted with de-ionized water and pressed against the glass. A 2.0 kg per cm^2 pressure was placed on top of the filter paper for 8-12 hours, and glass attached with MnO_2 nanosheet was detached from the weight. To remove the cellulose attached with nanoscaffold, the substrate was incubated in acetone for 0.5 hours and then briefly washed in methanol for 1 hour. The transparency of nanoscaffold can be easily tuned by using different concentrations of MnO_2 nanosheet solution. The 3 concentrations used in Figure 3-11 are 50 μg per ml, 100 μg per ml and 200 μg per ml. For cellular studies, the concentration of 200 μg per ml MnO_2

nanosheet solution was used throughout the study. Graphene oxide assembled scaffold was fabricated using an identical protocol with a graphene oxide aqueous solution of 200 μg per ml. FESEM (Field Emission Scanning Electron Microscopy, Zeiss with Oxford EDS) was used to characterize the nanoscaffold.

To form MnO_2 laminin hybrid nanoscaffold, 400 μL of MnO_2 nanosheet aqueous solution (2 mg per ml) was quickly added to 100 μL of laminin solution (1.0 mg per ml, PBS, PH=7.4). Then the laminin conjugated MnO_2 nanosheet was centrifuged and re-suspended in 10 ml de-ionized water (MnO_2 nanosheet concentration was 80 μg per ml). After vacuum filtration, the cellulose filter paper was cut into size and shape of interest for the following cell culture studies.

HiPSC-NSC culture

Human iPSC-NPCs were derived from human iPSCs (WT126 clone 8; and WT33 clone 1) as described and validated by publication of Marhetto et al. [481]. iPSC-NPCs were expanded in a proliferation media containing DMEM/F12 with Glutamax (Invitrogen), B27-supplement (Invitrogen), N2 (Stem Cells), and 20 ng per mL FGF2 (Invitrogen). Tissue culture vessels were treated with Matrigel (Corning) 1:200 dilution with DMEM (Invitrogen) at 37 °C for 1hr. To initiate the neuronal differentiation process, bFGF was removed. Fresh media was exchanged every other day. iPSC-NSCs with passage 8-11 were used in all our transplantation and in vitro studies.

Differentiation of iPSC-NSC on MnO_2 nanoscaffold

The viabilities of iPSC-NSCs and human neural progenitor cells (hNPC) cultured on MnO_2 nanoscaffold were measured by presto blue cell viability assay (Thermo Fisher, Catalog No.: A13261, 10% volume ratio as compared to cell media). Into 24-well plates, laminin

(10 μg/ml) was first coated onto the glass (control), graphene oxide assembled scaffold (positive control) and MnO_2 nanoscaffold at a concentration of 20 μg per ml (media volume: 1.0 ml per well), for 4 hours. Then the iPSC-NSC was seeded into each well at a cell density of 20k in growth media (bFGF added, 20 ng per ml). After the cells were cultured for 48 hours, cell viabilities cultured on different substrates were quantified using fluorescence (excitation at 570 nm and emission at 590 nm) presto blue assay and normalized to the control group (glass). For the neurite length analysis, neurites on each substrate were first automatically traced and the lengths were automatically measured by NeuronJ in ImageJ software. The values are all averaged from 9-12 measurements in the representative immunostaining images [482]. Here is a summary of the average neurite lengths with standard deviation obtained from software: Glass control, 5.2±2.3 μm; MnO_2 nanoscaffold, 59.3±19.8 μm; MnO_2 laminin nanoscaffold, 84.5±26.5 μm.

For the differentiation of iPSC-NSC on glass substrates, MnO_2 nanoscaffold, graphene oxide assembled scaffold (GO nanoscaffold) and glass were first sterilized in the UV lamp for 5 minutes and then coated with laminin solution (20ug per ml) for 4 hours. The substrates were placed in 24-well plates, and iPSC-NSCs were seeded into the wells at a cell density of 60,000 cells per well. The cells proliferated for 24 hours, and the media was changed to differentiation media without bFGF. To observe the stem cell proliferation and attachment onto the substrate, the cells were imaged in the optical microscope (Nikon Eclipse Ti-E microscope). After 6-days' differentiation, the cells were fixed and immunostained with nuclei (Hoechst, Thermo Fisher, catalog number: 33346, 1:100 dilution, 0.2 mM) and neuronal marker (TuJ1, Cell Signaling, catalog number: 4466, 1:500

dilution). To quantify the neuronal markers (TuJ1) and astrocyte markers (GFAP), qRT-PCR was conducted by using GAPDH mRNA as a control.

Fabrication of MnO_2 laminin hybrid nanoscaffold

MnO_2 laminin hybrid nanoscaffold can be facilely fabricated by adding 10 μL of MnO_2 nanosheet aqueous solution (3 mg per ml) into 100 μL laminin solution (1 mg per ml), and the MnO_2 nanosheet will be assembled within 5 seconds. To fabricate larger scale MnO_2 laminin hybrid nanoscaffold, 100 μL of MnO_2 nanosheet aqueous solution (3 mg per ml) was added into 500 μL laminin solution (1 mg per ml) and then vacuum filtered on a cellulose paper as described above. The structure of MnO_2 laminin hybrid nanoscaffold was then analyzed in FESEM. To fabricate cell encapsulated MnO_2 laminin-nanoscaffold, 1 million iPSC-NSCs were centrifuged down and re-dispersed in 25 μL laminin PBS solution. Different amount (0, 0.3 μL, 1.5 μL, 3 μL, 15 μL and 30 μL) of MnO_2 nanosheet solution (3 mg per ml) was injected into the cell laminin solution, and a iPSC-NSC encapsulated pellet was spontaneously formed after one hour. To investigate the interaction between MnO_2 and encapsulated iPSC-NSCs, the medium was removed and the neurons were fixed in Formalin solution (Sigma-Aldrich) followed by two PBS washes. The biological samples were then dehydrated to eliminate water through a series of ethanol dehydration process by replacing PBS with 50% ethanol/water, 70% ethanol/water, 85% ethanol/water, 95% ethanol/water, and absolute ethanol twice for 10 minutes each in succession. The biological samples were then stored in absolute ethanol before transferring to critical point dryer to eliminate traces of ethanol. Then 20 nm of gold was sputter coated onto the surface of biological samples after drying. FESEM was then used for micrograph acquisition.

For the differentiation of iPSC-NSC on substrates, glass, MnO_2 nanoscaffold and MnO_2 laminin hybrid nanoscaffold were first sterilized in the UV lamp for 5 minutes and then coated with laminin solution (10 μg per ml) for 4 hours. The substrates were placed in 24-well plates, and iPSC-NSCs were seeded into the wells at a cell density of 60,000 per well. After 6 days' differentiation, the cells were fixed, and immunostaining on nuclei (DAPI) and neuronal marker (TuJ1) was conducted. Stem cell assays were repeated 3 times to obtain statistical information unless mentioned otherwise. Student t-test was used for two group analysis and ANOVA with Tukey post hoc test was used for multi-group (more than 3 groups) analysis. For the long-term (1 month, 30 days) stem cell differentiation assay, identical protocol was used with twice media change per week. Mature neuronal marker (MAP2) was used for identifying neurons differentiated from iSPC-NSCs on MnO_2 nanoscaffold.

Calcium imaging of neurons differentiated from iPSC-NSCs on MnO_2 laminin hybrid nanoscaffold in 12 well-plates. iPSC-NSCs were differentiated on MnO_2 laminin hybrid nanoscaffold using an identical protocol mentioned above for 6 days, then the cells were incubated with 1 ml of Fura-2 AM (Life Technologies, Catalog Number: F1201, 1:200 dilution, 5 μg per ml) in cell media for 1 hour. Afterwards, cell media was changed to PBS. Under the movie mode of a fluorescence microscope, concentrated KCl solution in PBS (50 mM, 0.1 ml) was added to the cells, and the movie was taken for 10 minutes with 60 frames per seconds. The movies were pseudocolored, with red indicating strong calcium flux and green indicating weak calcium flux. An identical procedure was also applied for collecting calcium imaging of neurons differentiated from hNPCs. A summary of time

dependent calcium intensity peaks can be found in Figure 3-4, which was automatically obtained from the Nikon ND2 software.

Dye loading on MnO_2 nanoscaffold and MRI studies

To study drug loading and release on MnO_2 nanoscaffold, rhodamine B was used a model drug. Briefly, 0.3 mg rhodamine B (Alfa Aesar, Catalog Number: A13572) was added into 3.0 ml of MnO_2 nanosheet solution. After incubation at room temperature for 12 hours, 5.0 ml PBS (PH=7.4) was gradually added into the solution and RhB loaded MnO_2 nanosheet was centrifuged down at 3431 g for 5 minutes and extensively washed with PBS for 6 times to remove the residual RhB solution. Then the RhB-loaded MnO_2 nanosheet was re-suspended in 10 ml solution and re-assembled with laminin using the identical conditions for fabricating MnO_2 laminin hybrid nanoscaffolds. To monitor the dye hold-up, RhB-nanoscaffold was incubated with PBS for 12 hours, then the fluorescence of the supernatant was detected by a fluorescence spectra (Varian Cary Eclipse). The dye loading was confirmed by degrading the RhB-nanoscaffold using 1.0 mg/ml ascorbic acid PBS solution. Instant appearance of pink color from RhB proves the loading of RhB inside nanoscaffold. RhB-nanoscaffold before and after degradation was also spotted in a glass slide in a close-proximity and then imaged in the fluorescent microscope. To test the correlation between MRI signals and RhB released, different amount of RhB-nanoscaffold [5, 2.5, 1, 0.5, 0.1 mg (from left to right in Figure 3-5c)] were degraded with ascorbic acid (1.0 mg per ml) to form a homogeneous solution. Then the same solution in 96-well plates was used for MRI (Aspect's M2^{TM} Compact High-Performance MRI, 1T) measurement and fluorescence measurement under Nikon fluorescent microscope.

To study the day-dependent drug (RhB) release from our MnO_2-laminin hybrid nanoscaffold, PBS with 10 μg per ml vitamin C was used to incubate the RhB loaded nanoscaffold, and was changed regularly every day. Fluorescence images (Nikon fluorescent microscope) were taken at Day1, Day2, and Day7, and the intensities from 3 different experiments were used to quantify the amount of RhB released. As a control, PCL polymer was dissolved with RhB and then formed a scaffold by drying at room temperature. Then the dye release was measured at the same time points as RhB loaded nanoscaffolds. The percentage of dye release was all normalized to the fluorescence intensity obtained at Day1.

To load neurogenic drugs into MnO_2 laminin hybrid nanoscaffold, DAPT (N-[(3,5-Difluorophenyl)acetyl]-L-alanyl-2-phenyl]glycine-1,1-dimethylethyl ester, Tocris, Catalog Number: 2634) was first dissolved in a PBS: DMF=9:1 solution (dimethylformamide, Sigma-Aldrich) at a concentration of 0.1 mg per ml. Then 1.0 ml of DAPT solution was quickly mixed with 100 μL of 3 mg per ml MnO_2 nanosheet aqueous solution. After incubating for 12 hours, the solution was centrifuged down and washed with de-ionized water for 3 times. The successful loading of DAPT onto MnO_2 nanosheet was confirmed by MALDI-TOF (Bruker, Ultraflex) based on the Na^+-DAPT peak at 455 (molecular weight to charge ratio). Briefly, 50 μL MnO_2 nanosheet loaded with DAPT solution was mixed with 50 μL gold nanoparticle solution (Ted Pella, 10 nm, $5.7*10^{12}$ particles per ml). Then 1 μL of the mixed solution was drop-cast onto ITO glass and baked at 50 °C for 1 minute to fully evaporate water. The DAPT solution was drop-cast on the same ITO glass as a reference. ITO glass was placed into the MALDI-TOF and exposed with a laser for the analysis.

To measure the DAPT loading and releasing profile on DAPT MnO_2 nanoscaffold, 3.0 mg MnO_2 nanosheets were first loaded with DAPT using the previous protocol and then assembled into MnO_2 laminin hybrid nanoscaffolds. Using UV-Vis spectroscopy, we first identified the characteristic absorption peak of DAPT (20 μM in water with 1% DMF) at 264 nm. Then the drug loading amount was determined by the full disappearance of the 264 nm peak after incubated with nanosheets (2.0 ml PBS, 1.5 mg per ml). This corresponds to a loading efficiency of 110 μg per 3.0 mg nanosheets and a molar ratio between DAPT and manganese atom=1:134 (Figure 3-21). After that, to quantify the release of DAPT, degradation and DAPT release from the nanoscaffold was initiated by incubating it in a solution containing 10 μg per ml ascorbic acid. As DAPT form strong binding complex with MnO_2 nanosheets (Binding Energy=-18.43 kcal per mol), we monitored DAPT release through quantifying the amount of manganese amount at different time points, and estimated the drug release based on the constant molar ratio between DAPT and manganese (1:134) in the MnO_2-DAPT complex. The average daily release was quantified through dividing the total amount of manganese released by the length of degradation. The summarized DAPT release profile can be found in Figure 3-22.

DFT simulations on small molecule and MnO_2 binding

DFT calculations were carried out using the Quantum ESPRESSO software package. For the geometry optimization Perdew–Burke–Ernzerhof (PBE) functional along with D2 dispersion corrections were used [483,484]. The MnO_2 surface and the MnO_2 bound complexes were treated with DFT+U method. This is because conventional DFT functionals are unable to describe the strong correlation effect among the partially filled d states in Mn [485]. The Hubbard parameter 'U', is introduced for the Mn 3d electrons to describe the on-site

Coulomb interaction, as given in the well-known GGA +U method [486]. The values of U = 4 eV and J = 0 eV for MnO_2 were adopted [487]. Spin-polarized calculations were performed since bulk MnO_2 has an antiferromagnetic ground state. The electron cores were defined using ultrasoft pseudopotential for all the elements and were extracted from the Quantum ESPRESSO main website (http://theossrv1.epfl.ch/Main/Pseudopotentials). For the k-point mesh, a γ-center was used. The wave function cutoff of 60 Ry and kinetic energy cutoff of 240 Ry were used in all the cases studied. The Gaussian smearing was turned so that the difference between the free energy and the total energy is less than 0.005 Ry per atom. The energy convergence was set to 1×10^{-6} a.u. And the force convergence threshold for the ionic minimization was set at 1×10^{-4} a.u.

The binding energies on the MnO_2 surface were calculated for a series of small molecules (Table 1) and the DAPT drug molecule. The size of the cell was taken equivalent to the size of the MnO_2 surface that has 8x8 oxygen atoms at the periphery. The box size for the simulated system is 23x23x40 Å, and periodic boundary conditions are used. This condition was chosen to mimic the 2D MnO_2 surface. We first performed geometry optimizations for the bound complexes, with the resulting energy referred to as $C_{complex}$. We then optimized the structures of isolated MnO_2 surface and the molecule of interest, obtaining their energies E_{MnO2} and E_{mol}, respectively. The binding energy is defined as $E_b = E_{complex} - E_{MnO_2} - E_{mol}$. Negative E_b indicates binding while positive E_b indicates repulsion to the surface.

Degradation of micro-contact patterned MnO_2 nanoscaffolds: We first generated Photoresist (PR) micropatterns on Silicon wafer based on photolithographic technique. Then silicon coated with photoresist micropattern was deposited with a layer of

(heptadecafluoro-1,1,2,2-tetrahydrocecyl)trichlorosilane for 2 h in a desiccator. PDMS (Sylgard 184 silicone elastomer base and curing reagent) was then poured into pre-coated photoresist patterns and kept in a 60 °C oven for curing. The PDMS mold with micro-patterns was then detached from photoresist and treated with oxygen plasma ($1.5*10^{-1}$ Torr, 25 seconds). MnO_2 nanosheet solution at 2.0 mg per ml was drop-casted on PDMS stamp and spin coated at 500 rpm for 10 seconds, 1500 rpm for 20 seconds and 3000 rpm for 30 seconds. At the same time, a glass substrate (please note that gold and silicon also work under the same parameters) was treated with oxygen plasma (Femto Science, Cute series) for 1 minute. Then the PDMS stamp coated with the MnO_2 solution was tilted and pressed on the glass substrate. After 1 minute, a pressure of 75 g per cm^2 was mounted on PDMS stamps for 20 minutes. The MnO_2 nanosheet patterned glass was finally washed with ethanol and water and imaged under an optical microscope. To monitor the degradation of MnO_2 nanosheet micropatterns on the glass, the substrate was incubated with ascorbic acid (50 g per ml) solution and images were taken before and after solution treatment. Field Emission Scanning Electron Microscopy (FESEM, Zeiss Sigma) was used for micrograph acquisition, and Electron Dispersive X-ray (EDX) was also used to surface changes of the substrate before and after ascorbic acid treatment under identical parameters.

Human Neural Progenitor Cell (hNPC) Culture: The human neural progenitor cell (hNPC) line was purchased from Millipore (SCC008) and cultured according to the manufacturer's protocol. Cell line was authenticated by ReNeuron Group plc and validated by high expression of Sox2 and Nestin. Tissue culture vessel were treated with 20µg per cm^2 of Poly-L-Lysine (Sigma-Aldrich) and 7 µg per cm^2 laminin (Life Technologies) for 6hrs at room temperature and 4hrs at 37°C respectively. All cells were maintained at 37°C in a

humidified incubator with 5% CO_2. All experiments were conducted on passage number 3 and 5 cells. The hNSCs were seeded at 33K cells per cm^2 in hNSC specific media (from Millipore) supplemented with basic fibroblast growth factor (bFGF, 20 ng per mL) and epidermal growth factor (EGF, 20 ng per mL) with media exchanges occurring every other day. Neural differentiation of hNPC is done with the withdrawal of bFGF and EGF. Through qPCR, TuJ1 gene is checked for successful neuronal differentiation.

HiPSC-NSC culture: Human iPSC-NPCs were derived from human iPSCs (WT126 clone 8; and WT33 clone 1) as described and validated by publication of Marhetto et al [481]. iPSC-NPCs were expanded in a proliferation media containing DMEM/F12 with Glutamax (Invitrogen), B27-supplement (Invitrogen), N2 (Stem Cells), and 20 ng per mL FGF2 (Invitrogen). Tissue culture vessels were treated with Matrigel (Corning) 1:200 dilution with DMEM (Invitrogen) at 37 °C for 1hr. To initiate the neuronal differentiation process, bFGF was removed. Fresh media was exchanged every other day. iPSC-NSCs with passage 8-11 were used in all our transplantation and in vitro studies.

Immunocytochemistry: To confirm neuronal differentiation, we conducted immunocytochemistry study. All fluorescence images were obtained using a Nikon Eclipse Ti-E inverted fluorescence microscope. Following the generation of mature neurons, media was removed, and the cells were fixed for 15 minutes in formalin (Sigma) followed by two washes with D-PBS. The nucleus was stained with DAPI (Life Technologies, Catalog Number: D1306, 1:100 dilution) for 30 minutes and then washed with PBS three times. Cells were then permeabilized with 0.1% Triton X-100 in PBS for 10 minutes, and non-specific binding was blocked with 5% normal goat serum (NGS, Life Technologies) in D-PBS for 1 hr at room temperature. Neuronal marker TuJ1 was stained using the mouse

monoclonal antibody against TuJ1 (Biolegend, catalog number: 801202, 1:500 dilution). Mature neuronal markers MAP2 (mouse monoclonal, Cell Signaling, catalog number: 8707S, dilution factor: 1:500), and Synapsin 1 (rabbit monoclonal, Sigma Aldrich Millipore, catalog number: AB1543P, 1:500 dilution) were also used for the immunostaining analysis (Figure 3-15). Following the manufacturer's protocol, the fixed samples were incubated overnight at 4°C in a solution of these antibodies in PBS containing 10% NGS. After washing three times with PBS, the samples were incubated for 1 hr at room temperature in a solution of Alexa 594 anti-mouse secondary antibody (Biolegend, catalog number: 8890, 1:300 dilution) and Alexa 488 anti-rabit secondary antibody (Biolengend, Catalog Number:406416, 1:300 dilution), in PBS containing 10% NGS, and washed with D-PBS three times thereafter. For tissue and cell culture analysis, all GFP+, TuJ1+, MAP2+ cells were identified by automatic function in the Nikon NIS element software and then amounts of cells were recorded.

Focal adhesion kinase studies: To study the effect of laminin density on the adhesion of iPSC-NSC, MnO_2 nanoscaffold, GO nanoscaffold and glass were coated with laminin under identical conditions except for the concentrations (5 μg per ml, 10 μg per ml, 20 μg per ml) during laminin solution coating. After 3 days' differentiation process, the morphology and attachment of cells were imaged under an optical microscope. To further quantify focal adhesion kinase that is directly involved in the cell adherence, cells cultured on different substrates and different laminin concentrations were trizoled. FAK mRNAs and GAP43 mRNAs were then quantified and normalized to GAPDH mRNAs in the qRT-PCR analysis.

Gene Expression Analysis: Total RNA was extracted using TRIzol Reagent (Life Technologies) and transcribed to cDNA for quantitative PCR (qPCR) analysis. Specifically, cDNA was generated from 1 μg of total RNA using the Superscript III First-Strand Synthesis System (Life Technologies). The qPCR reactions were performed using Power SYBR Green PCR Master Mix (Applied Biosystems) on a StepOnePlus Real-Time PCR System (Applied Biosystems) with the primers specific to each of the target mRNAs. The resulting Ct values were normalized to GAPDH. Standard cycling conditions were used for all reactions with a melting temperature of 60 C. All primers were obtained from the PrimerBank database, purchased from IDT Technologies and listed in Table 2.

Immunohistochemistry: Frozen spinal cord tissue was sectioned transversely or sagittally (10-12 μm in thickness) using a cryostat (ThermoScientific) and air dried. Sections were blocked and permeablized for 1 hr in blocking buffer containing 10% donkey serum, 0.1% TritonX, and 0.1% Tween® 20 at room temperature. Afterwards, they were incubated with primary antibodies overnight at 4ºC. Following three 10-min washes in PBS, sections were incubated in the blocking buffer containing corresponding fluorophore-conjugated secondary antibodies for 1 hour at room temperature. Slides were then washed for three times with PBS (10-min each), stained with DAPI and then incubated with 4 mM $CuSO_4$ in 50 mM ammonium acetate buffer for 10 min to reduce autofluorescence. Sides were then mounted with mounting media (Vector Laboratories) right away, and images were taken within a week. The following primary antibodies were used: PH3 (1:100, rabbit polyclonal, sc-8656-R) from Santa Cruz Biotechnology, TuJ1, cleaved Caspase 3 (Cell Signalling, Catalog number: 9661T, 1:500 dilution), GFAP (1:1000 dilution, mouse monoclonal, G3893) from Sigma Aldrich and F4/80 (1:500 dilution, ab16911) from

Abcam. Alexa 488 conjugated anti-rabbit and Alexa 594 conjugated anti-mouse antibody from Biolegend were used at 1:500 dilutions. Images were captured and analyzed using a Zeiss Axio Imager M1 fluorescence microscope and visualized with AxioVision 4.8 and Nikon Eclipse Ti-E microscope.

In vivo transplantation of hiPSC-NSCs

Spinal cord injury, transplantation of nanoscaffold and tissue harvest: All animal work was conducted following the regulation of the Institutional Animal Care and Use Committee (IACUC) at Rutgers University. The Notch1CR2-GFP transgenic mouse (Mus musculus) (Tzatzalos et al., 2012) was used in this study. Adult mice that are 5-6 months old were picked for the spinal cord injury experiments. No difference was observed between male or female animals, and thus the gender was not specified. Animals are randomized without pre-knowledge of their behaviors and then assigned to different experimental groups without selection. Three mice were used for each group. Animals were randomized and observers were blind to animal groups when performing experiments and analysis. During the surgery, initial anesthetization was performed with 5% isoflurane and then maintained at 2% Isoflurane. For hemisection, a laminectomy at T10~11 lateral section of spinal cord (length of gap ≈ 1mm) was first performed. Then the dorsal blood vessel was burned with a cauterizer, and the spinal cord was cut from middle line toward the left using a #10 scalpel. Following induction of injury, bio-materials with iPSC-NSCs, laminin-coated and DAPT-treated PCL (Shah et al., 2014), or surgifoam was inserted into the wound site, and the muscle around surgical wound was sutured and skin is stapled using wound clips. A cell density of 1 million cells/cm^2 was used for transplantation and mice were sacrificed 7-week after injury. For harvest, the spinal cords from the injured animals were obtained via

microsurgical dissection. They were washed in 1x PBS and fixed with 4% (w/v) paraformaldehyde (PFA) for 24 hrs. Fixed tissues were washed again and then cryopreserved in 30% (w/v) sucrose for 48 hrs. Afterwards, the spinal cord tissue was embedded in cryo-preserving media (Tissue Tek® OCT compound) and kept frozen at -80ºC. Spinal cord sections were stained with PH3, GFAP and F4/80 antibodies to analyze the long-term effect of nanoscaffold on SCI (Figure 3-8). One-way ANOVA was used for multi-group analysis. Data represents mean±s.d., n=3, *P<0.05, **P<0.01 with Tukey's post-hoc analysis. All tissue sections are in the center of the scaffold implants and then identified nearby the transplanted sites. Related antibody information and staining protocol can be found in A.19.

In vivo hiPSC-NSC-GFP transplantation assay

This corresponds to Figure 3-28-32 and manuscript Figure 3-7. To study enhanced transplantation of iPSC-NSCs using our nanoscaffold, we further transplanted GFP labeled iPSC-NSC cells (iPSC-NSC-GFP) into a non GFP wild type C57BL/6 mouse strain [488]. To obtain GFP labeled cells, we transduced iPSC-NSCs with lentiviral vectors expressing GFP using previously reported protocol (Figure 3-27) [456]. We confirmed the high transfection efficiency (>90%) and strong green fluorescence from iPSC-NSCs before seeded to the scaffold for in vivo cell transplantation using fluorescent microscope (Figure 3-27b). The surgical procedures for transplantation of iPSC-NSC-GFP into C57BL/6 were kept identical as the experiments on Notch1CR2-GFP mice and we repeated the immuno staining on tissue sections 1-week post transplantation and 1-month (30 days) post transplantation. In addition to the 3 groups [injury only (surgifoam insertion), 3D BHI nanoscaffold, and PCL cell group] evaluated in Notch1CR2 mice, we added 3 other

important control groups to better support the therapeutic potential of our developed scaffold system: MnO_2 scaffold without laminin or DAPT but with cell transplantation (MnO_2 cell group), MnO_2 nanoscaffold with laminin and DAPT but without cell transplantation (MnO_2 DAPT group), and direct injection of GFP iPSC-NSCs with laminin (laminin cell group). All other conditions were kept identical to the experimental group (3D BHI nanoscaffold). Each group includes 3 animals (n=3) to check reproducibility. We summarized the animal groups in Figure 3-28, and all the tissue analysis results were summarized in Figure 3-7 and Figure 3-29-31. GFP, TuJ1 and MAP2 positive cells were first identified by automatic detection function in the NIS Nikon software (NIS element AR) then the amount of cells were recorded for making the graphs. Percentage of Syn positive cells are quantified by first identify GFP+Syn+ cells then divided by amount of GFP+ cells in each section. Unpaired student t-test was used for two group significance analysis and one-way ANOVA was used for multi-group analysis. Data represents mean$\pm$s.d., n=3 unless described otherwise, *$P<0.05$, **$P<0.01$, ***$P<0.001$. In Figure 3-28, when we count GFP+cells, we used the automatic detection function in the NIS Nikon software to identify GFP+ cells shown in Figure 3-28e, then summarized the amount of GFP+ cells at specific distance intervals (100 μm) in the sagittal sections. All tissue sections are in the center of the scaffold implants and then identified nearby the transplanted sites.

3.1.3 Results and Discussion

Enhanced stem cell differentiation on MnO_2 nanoscaffolds

Recently, hybrid inorganic 2D nanomaterial-based scaffolds have been demonstrated to control stem cell differentiation by providing controlled physical, chemical, and biological properties that can be utilized to regulate cell-matrix interactions[276,475,489,490]. To investigate whether our biodegradable MnO_2 hybrid nanoscaffolds have an enhanced binding affinity toward ECM proteins to promote cell adhesion, neuronal differentiation of stem cells, and neurite outgrowth through the ECM-mediated integrin signaling pathway, we first investigated the interaction between 2D MnO_2 nanosheets and laminin proteins (Figure 3-2a-b, Figure 3-9). Using a bicinchoninic acid (BCA) assay, we observed significantly increased laminin adsorption on MnO_2 nanosheets (7.5-fold increase) compared to its binding toward control glass and polymer substrates (Figure 3-2c). To better understand the origin of such strong binding interactions between ECM proteins and MnO_2-nanosheets, we used the density functional theory (DFT) method to calculate the binding energies between the MnO_2-nanosheets and a series of functional groups commonly exhibited in ECM proteins (Figure 3-2b and d-e). The calculation results showed that electrostatic and polar-π interactions are the main contributors to the strong binding interactions of the biomolecules onto the MnO_2-nanosheets. For example, the binding energies for methylamine and methylbenzene are about 3-fold higher than that of water (Figure 3-2e, Figure 10, Table 1). Considering laminin proteins are rich in amino and aromatic functional groups, the DFT calculation results indicated that these interactions are critical for the strong binding of ECM proteins onto the MnO_2-nanosheet. Given the extraordinarily high crystal surface of 2D MnO_2 nanosheets, we speculated that the nanoscaffolds would also have strong binding interactions toward small molecule drugs that contain aromatic and amine structures. Our DFT calculation approach was thus further utilized to provide insight

into the laminin-induced formation of 3D MnO_2 hybrid nanoscaffolds and acted as a screening method to identify neurogenic or anti-inflammatory drugs that can enhance survival and neuronal differentiation of NSCs in vitro and in vivo.

To study neuronal differentiation of stem cells using our MnO_2 hybrid nanoscaffolds, we synthesized layer-by-layer MnO_2 nanoscaffold assembly (3D-MnO_2 nanoscaffolds) using a vacuum filtration method that enabled us to generate highly homogeneous and reproducible 3D-MnO_2 nanoscaffolds (Figure 3-2f). Compared to conventional 3D nanoscaffold-fabrication methods such as spraying, drop-casting, and electrochemical deposition, our applied vacuum filtration method can produce large-scale, homogeneous, free-standing, and mechanically robust 3D nanoscaffolds in a highly controllable way (Figure 3-11-12). To perform the 3D-MnO_2 nanoscaffold-based stem cell assay, we chose human induced pluripotent stem cell (hiPSC)-derived NSCs as a model system since hiPSC-derived NSCs can be effectively translated into clinical applications for neuro-degenerative diseases and injuries[491].

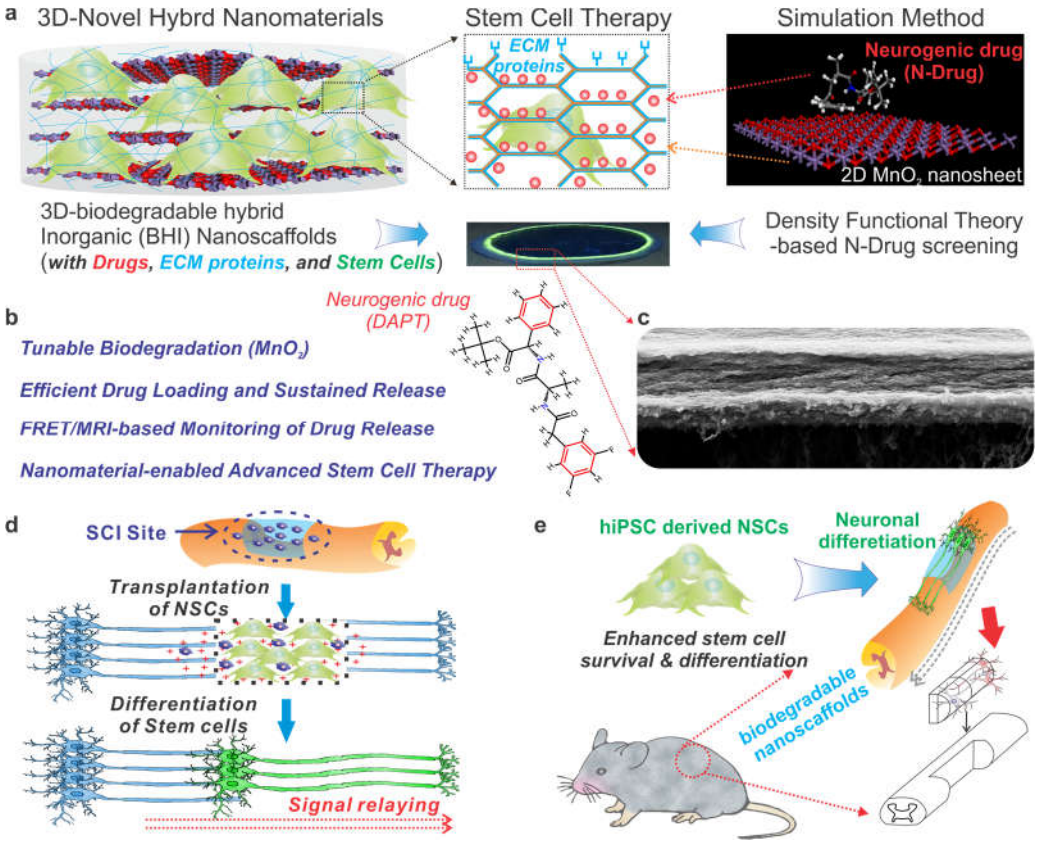

Figure 3-1. BHI nanoscaffolds for advanced stem cell therapy. a, BHI nanoscaffolds that simultaneously integrate 3D-hybrid nanomaterials and DFT simulation for stem cell therapy. b, Advantages of BHI nanoscaffolds. c, A representative SEM image of BHI nanoscaffolds. d-e, Improved stem cell transplantation under CNS diseased microenvironments, which typically have highly inflammatory and inhibitory microenvironments at the injury site (d). A murine hemisection SCI model was used to evaluate the *in vivo* survival and differentiation of BHI nanoscaffold-transplanted iPSC-NSCs (e).

By seeding hiPSC-NSCs on laminin-coated 3D-MnO_2 nanoscaffolds, we observed a significant enhancement of neuronal differentiation (43% increase) and neurite outgrowth (11-fold increase) compared to the control conditions by measuring the biomarker protein and gene expression levels (Figure 3-2g-i, Figure 3-13-14). To understand the underlying mechanism of the 3D-MnO_2 nanoscaffold-based enhanced neuronal differentiation and neurite outgrowth, we investigated the relevant laminin-mediated focal adhesion-dependent signaling pathways using a qRT-PCR (quantitative reverse transcription-polymerase chain reaction) technique. Indeed, a substantial increase of focal adhesion kinase (FAK) gene (4.7-fold) and an upregulation of a neuronal growth cone-associated GAP43 gene (36%) were observed from hiPSC-NSC-derived neurons on 3D MnO_2 nanoscaffolds, compared to those cultured on a glass substrate (Figure 3-2g, Figure 3-14, 16). In short, these results strongly suggested that our 3D-MnO_2 nanoscaffolds can improve neuronal differentiation and neurite outgrowth, through the enhanced laminin binding and focal adhesion-related pathways.

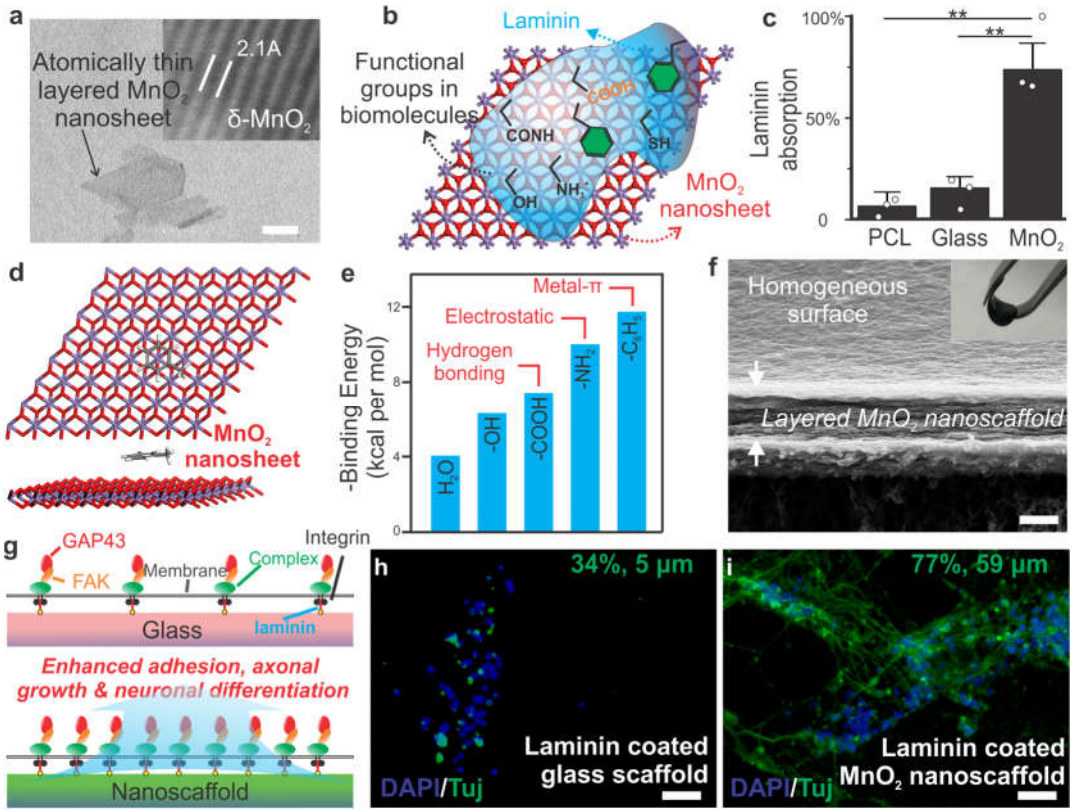

Figure 3-2. Enhanced stem cell differentiation using biodegradable MnO2 hybrid nanoscaffolds. a, Representative TEM and HRTEM images of MnO2 nanosheets. b-e, Schematic diagram describing the intermolecular binding (b), experimental validation of strong laminin binding (c), computation model (d) and binding energy calculation (e) between MnO2 nanosheets and selected functional groups that are commonly existent in ECM proteins and biomolecules. f, A SEM image showing the layered structure and homogeneous surface of MnO2 hybrid nanoscaffolds g-i, A schematic diagram illustrating the proposed mechanism and immunostaining results for showing the enhanced neuronal differentiation on MnO2 hybrid nanoscaffolds. Scale bars: a, 25 nm; f, 500 nm; h-i, 100 μm.

Controllable biodegradation of MnO_2 hybrid nanoscaffolds

While low-dimensional inorganic nanomaterials have shown great potential in stem cell-based regenerative medicine, in vivo biocompatibility and biodegradation of these nanomaterials are the most critical issues to be addressed before inorganic nanomaterial-based stem cell applications can be fully realized. To demonstrate the tunable biodegradation study of MnO_2 nanoscaffolds in extracellular microenvironments, we first investigated the degradation of 2D-MnO_2 nanosheets using aqueous solution of ascorbic acid (vitamin C, Figure 3-3a, Figure3-17). UV-Vis absorption spectrum data confirmed that 2D-MnO_2 nanosheets were degraded by ascorbic acid in a dose-dependent manner. Similarly, a controllable degradation rate of MnO_2 nanosheets by ascorbic acid was observed using micropatterned-MnO_2 nanoscaffolds, by directly monitoring the disappearance of the micropatterned-MnO_2 nanoscaffolds and by analyzing the x-ray energy dispersive spectroscopy (EDS) data (Figure 3-3c-d). In addition, the tunability of biodegradation rate can be effectively achieved by changing the number of assembled layers (Figure 3-18). Furthermore, we investigated the redox properties of MnO_2 nanoscaffolds in PBS using cyclic voltammetry (CV) to study the degradation without exogeneous bioreductants. We could detect a clear reduction voltage peak at -700 mV from the CV curves, at which MnO_2 nanoscaffolds (Figure 3-3b) degrade. From these electrochemical experiments, we confirmed our hypothesis that our synthesized MnO_2 nanoscaffolds could be degraded via an unconventional redox-mechanism. In parallel, we inserted MnO_2 nanoscaffolds in between two layers of cells, which can mimic in vivo transplantation conditions, to study the nanoscaffold degradation profiles as well as to investigate whether such redox-mediated biodegradation of MnO_2 nanoscaffolds was

possible in tissue-mimicking conditions without adding any exogenous bioreductants or electrical stimuli. As a negative control experiment, graphene oxide (GO) nanoscaffolds were also inserted in between two layers of cells. The biodegradation of both nanoscaffolds (MnO_2 VS. GO) was examined daily by measuring the thickness of the dark-colored nanoscaffold layers. Consistent with previous reports, we did not observe any noticeable degradation of GO nanoscaffolds throughout a month-long observation (Figure 3-3e) [492]. In contrast, MnO_2 nanoscaffolds rapidly degraded with over 30% of the MnO_2 nanoscaffolds degraded within one week, and a half-degradation time was around 2 weeks (Figure 3-17). This result proved that the biodegradability of MnO_2 nanoscaffolds could be induced by cells without delivery of exogenous reductants. Moreover, we could control the degradation rate of MnO_2 nanoscaffolds by showing a tunable half-degradation period from a few minutes to one month. This tunability of a biodegradation rate was achieved by changing the assembled layered-structures of MnO_2 nanosheets and by controlling concentrations of reductants (Figure 3-3f, Figure 3-18). In short, our developed MnO_2 nanoscaffolds represent an innovative inorganic hybrid nanoscaffold system that can be biodegraded in vitro. Given that CNS microenvironment contains highly concentrated bioreductants and different degradation speeds would be needed for different applications, the controllable biodegradation properties of MnO_2 nanoscaffolds could be more appealing and important in the field of neural tissue engineering[493].

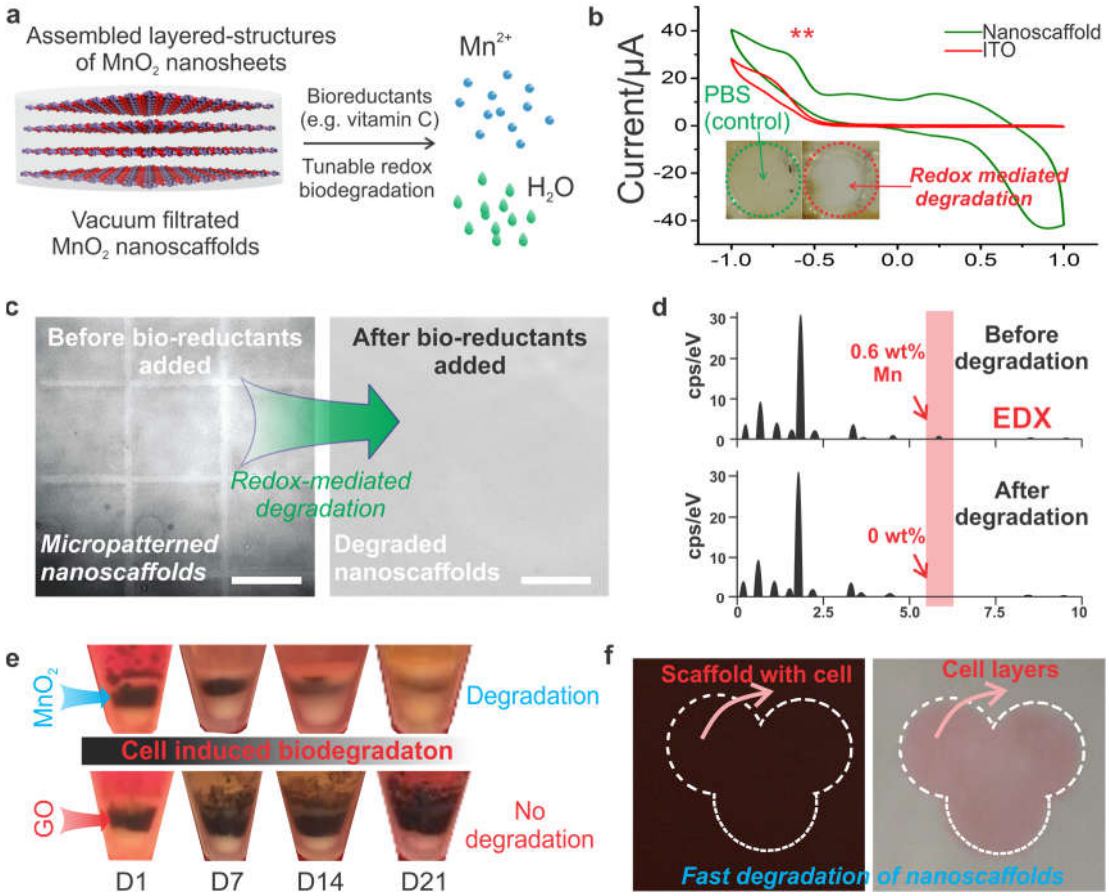

Figure 3-3. Controllable biodegradation of MnO2 hybrid nanoscaffolds. a, A schematic diagram explaining an unconventional redox biodegradation mechanism of MnO2 hybrid nanoscaffolds. b, Controllable redox biodegradation of MnO2 hybrid nanoscaffolds demonstrated through cyclic voltammetry. c-d, Degradation of nanoscaffold by vitamin C, indicated by the decay of micropatterns (c) and the EDS analysis (d, Mn peak: 6.8 eV). e, Time dependent biodegradation of MnO2 hybrid nanoscaffolds in cell culture. f, Controllable fast-biodegradation of MnO2 hybrid nanoscaffolds at high vitamin C concentrations. Scale bar: c, 100 μm.

3D MnO_2 hybrid nanoscaffolds self-assembled with ECM protein

One of the critical issues of conventional degradable bioscaffolds is degradation-mediated disruption of cellular microenvironments, which can interrupt continuous neuronal differentiation and neurite outgrowth of transplanted NSCs[467,494]. To this end, biocompatible 3D bioscaffolds complexed with ECM proteins or peptides, such as laminin, fibronectin and Arginylglycylaspartic acid (RGD), that enhance neuronal differentiation of stem cells and neurite outgrowth continuously, have provided a promising solution for advanced stem cell-based tissue engineering[275,489,495]. As such, inspired by a recent report on the non-covalent preparation of hydrogels[496], we developed a method to generate biocompatible 3D-MnO_2 hybrid nanoscaffolds complexed with laminin-protein, termed, 3D-MnO_2-laminin hybrid nanoscaffolds. Interestingly, MnO_2-laminin hybrid nanoscaffold, an innovative 3D-inorganic scaffold self-assembled from laminin, was successfully synthesized by mixing 2D-MnO_2 nanosheets with laminin solutions (Figure 3-4a-e, Figure 3-19). The self-assembly process could be achieved by the strong interactions of laminin toward 2D-MnO_2 nanosheets, where laminin can function as adhesive layers (binder) for individual MnO_2 nanosheets. To investigate whether 3D-MnO_2-laminin hybrid nanoscaffolds promote the neuronal differentiation of NSCs and the following neuronal behaviors including neurite outgrowth, we performed stem cell assays using three different substrates/scaffolds (glass, MnO_2 nanoscaffolds, and 3D-MnO_2-laminin hybrid nanoscaffolds) under the same culture conditions. After 6 days of stem cell differentiation assays, we found dramatically higher cell counts from our 3D-MnO_2-laminin hybrid nanoscaffolds compared to glass (740% higher) and MnO_2 nanoscaffolds (270% higher) controls (Figure 3-4b and f-h, Figure 3-19). Furthermore, through a neuronal marker, beta-

III tubulin (TuJ1) immunostaining, we confirmed even more significant improvement of neuronal differentiation and neurite outgrowth from our 3D-MnO_2-laminin hybrid nanoscaffolds compared to the other control substrates, showing 11 times longer average neurite lengths compared to laminin-coated glass and 1.4 times longer than laminin-coated MnO_2 nanoscaffold (Figure 3-4f, Figure 3-14). Meanwhile, we have also verified the neurons formed on our hybrid nanoscaffolds are mature through time-dependent calcium imaging technique and immunostaining with mature neuronal markers such as Microtubule-associated protein 2 (MAP2) and Synapsin (Syn1) (Figure 3-4i-k, Figure 3-15). These results support our hypothesis that 3D-MnO_2-laminin hybrid nanoscaffolds can effectively and steadily promote neuronal differentiation of stem cells and neuronal behaviors for versatile stem cell therapies.

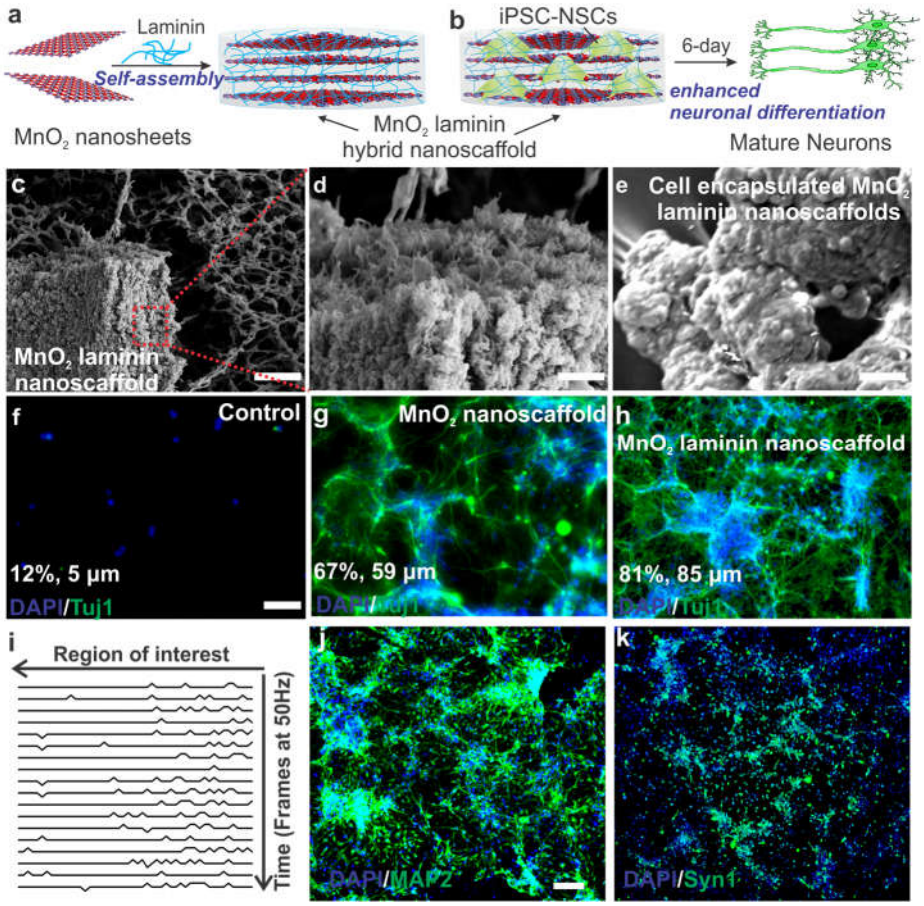

Figure 3-4. 3D MnO_2 hybrid nanoscaffolds self-assembled with ECM proteins. a-b, Proposed mechanism for the scaffold formation and differentiation of iPSC-NSCs cultured on MnO_2-laminin hybrid nanoscaffolds (b). c-e, Representative SEM images of MnO_2 laminin hybrid nanoscaffolds (c, d), and cell encapsulated nanoscaffolds (e). f-h, Immunostaining on neuronal markers demonstrate enhanced cell adhesion and neuronal differentiation of iPSC-NSCs on MnO_2 laminin hybrid nanoscaffolds (h) compared to control (f) substrates and MnO_2 hybrid nanoscaffolds (g). i, Calcium imaging results (i) of iPSC-NSC differentiated neurons on MnO_2 laminin hybrid nanoscaffolds. j-k, Immunostaining images on mature neuronal markers (MAP2 and Synapsin 1, labelled with green). Scale bars: c, 10 μm; d, 500 nm; e, 100 μm; j-k, 100 μm.

Spatiotemporal controlled delivery and monitoring of drugs

While some conventional biodegradable and biocompatible 3D-hybrid scaffolds have shown their potential to promote stem cell neuronal differentiation and neurite outgrowth, there is still a lot of room for improvement to control stem cell differentiation and neuronal behaviors in a more selective and temporally controlled manner in vivo[497-500]. These requirements would be essential to achieve the full therapeutic potential of transplanted stem cells for SCI treatment. Addressing this challenge, spatiotemporal controlled delivery of soluble cues such as small organic molecules (e.g. neurogenic drugs to selectively induce stem cell neuronal differentiation) using our 3D-hybrid inorganic nanoscaffolds provides a promising solution[497,499,500]. Conventional scaffolds that typically use physical encapsulation to load drugs normally suffer from rapid diffusion of drugs, which leads to undesired damage to the transplanted cells as well as the surrounding tissues because of the high drug concentration initially, and limited neurogenic effect later on due to an insufficient remaining drug concentration[498-500]. To this end, our developed 3D-MnO_2-laminin hybrid nanoscaffolds showed improved drug-loading capability and minimized burst-release owing to strong drug-binding affinity to the nanoscaffolds. For a comprehensive study of drug loading and monitoring of drug release using our nanoscaffolds, we first used a fluorescent aromatic ring-containing small molecule, Rhodamine B (RhB), as a model drug system. To optimize the loading and binding of drug molecules, RhB was first loaded onto 2D-MnO_2-nanosheets. Then, the RhB-loaded MnO_2-nanosheets self-assembled with laminin to generate 3D-MnO_2-laminin hybrid nanoscaffolds (Figure 3-5a). We adapted a quantitative fluorescence resonance energy transfer (FRET)-based approach to monitoring released or non-binding RhB molecules[171].

Our FRET-based method allowed us to assay the drug loading and release process (Figure 3-5a). Based on this FRET-based drug monitoring method, we observed an excellent drug-binding affinity onto the 3D-MnO_2-laminin hybrid nanoscaffolds, wherein minimal RhB release from the nanoscaffolds was detected over 7 days. However, as soon as we introduced bioreductant (vitamin C) to the RhB-loaded 3D-MnO_2-laminin hybrid nanoscaffolds, the fluorescence signal of RhB release was observed with an over 500-fold increase with a sustainable delivery profile (Figure 3-5b, Figure 3-20-21). This experimental result strongly supports that our 3D-hybrid inorganic nanoscaffold-based drug delivery platform can control drug release kinetics over a few weeks through degradation of nanoscaffolds. Additionally, the stoichiometrically equivalent Mn^{2+} ion release and the MnO_2 degradation (1:1 ratio) encouraged us to hypothesize that MRI signals from Mn^{2+} can be utilized to quantify the degradation rate of our hybrid nanoscaffolds and to correlate the intensity of MRI signal with the amount of drug released (Figure 3-5a, c). Indeed, by inducing the nanoscaffold degradation by bioreductants, we found that the amount of released drug, measured by the fluorescence intensity of RhB was closely correlated with the intensity of MRI signal (Figure 3-5c). This "on/off" MRI-based monitoring of drug release has not yet been demonstrated in conventional scaffolds, thereby offering a tool that can provide a much-improved investigation of drug delivery and in vivo release[446].

The optimized condition regarding drug loading and release, based on the fluorescent RhB molecule as a model drug, was used to load and deliver neurogenic drugs for enhanced neuronal differentiation. To screen the optimal neurogenic drug, we applied the DFT calculations (Figure 3-2d, Table 1) and selected a neurogenic drug (DAPT: N-[N-(3,5-

Difluorophenacetyl)-L-alanyl]-S-phenylglycine t-butyl ester) based upon its high binding energy to 2D-MnO_2 nanosheet (Figure 3-5d, Figure 3-21-22). DAPT is a γ-secretase and Notch inhibitor that simultaneously promotes neuronal differentiation and neurite outgrowth while suppressing astrocyte differentiation[501,502]. The calculated binding energy between DAPT and the 2D-MnO_2 nanosheet is -18.3 kcal mol^{-1}, an over 4-fold increase compared to the binding of solvent (water) to nanoscaffolds, indicating that DAPT drugs can be strongly adsorbed to the MnO_2 surface. Indeed, by forming DAPT-loaded 3D-MnO_2-laminin hybrid nanoscaffolds, the spectrums from matrix-assisted laser desorption/ionization (MALDI) time-of-flight (TOF) mass spectrometer showed a high amount of DAPT loaded onto the nanoscaffolds, while control scaffolds (glass and polymer substrate) did not show any noticeable peaks (Figure 3-22). To investigate the effect of DAPT-loaded 3D-MnO_2-laminin hybrid nanoscaffolds on stem cell neuronal differentiation and neuronal behaviors, we tested hiPSC-NSC-based neuronal differentiation assays using DAPT-loaded 3D-MnO_2-laminin nanoscaffolds and related controlled conditions for one week. We found a strong enhancement of neuronal differentiation from the DAPT-loaded 3D-MnO_2-laminin nanoscaffold condition (a 1.4-fold enhancement of Tuj1 mRNAs and a 1.7-fold enhancement of neurite outgrowth compared to 3D-MnO_2 laminin hybrid nanoscaffolds), as well as suppressed GFAP (Glial fibrillary acidic protein) mRNA expression (Figure 3-5e, Figure 3-23-24). Remarkably, in the boundary of DAPT-loaded 3D-MnO_2-laminin hybrid nanoscaffold and glass, NSC-derived neurons across the boundary, cultured under the same condition, had a dramatic change in morphology and neurite outgrowth (Figure 3-5e). This result provided a direct comparison between our 3D-MnO_2-laminin hybrid nanoscaffolds and conventional

scaffolds and indicated the ability of spatiotemporal control of hiPSC-NSC differentiation using our drug-loaded 3D-hybrid inorganic nanoscaffolds.

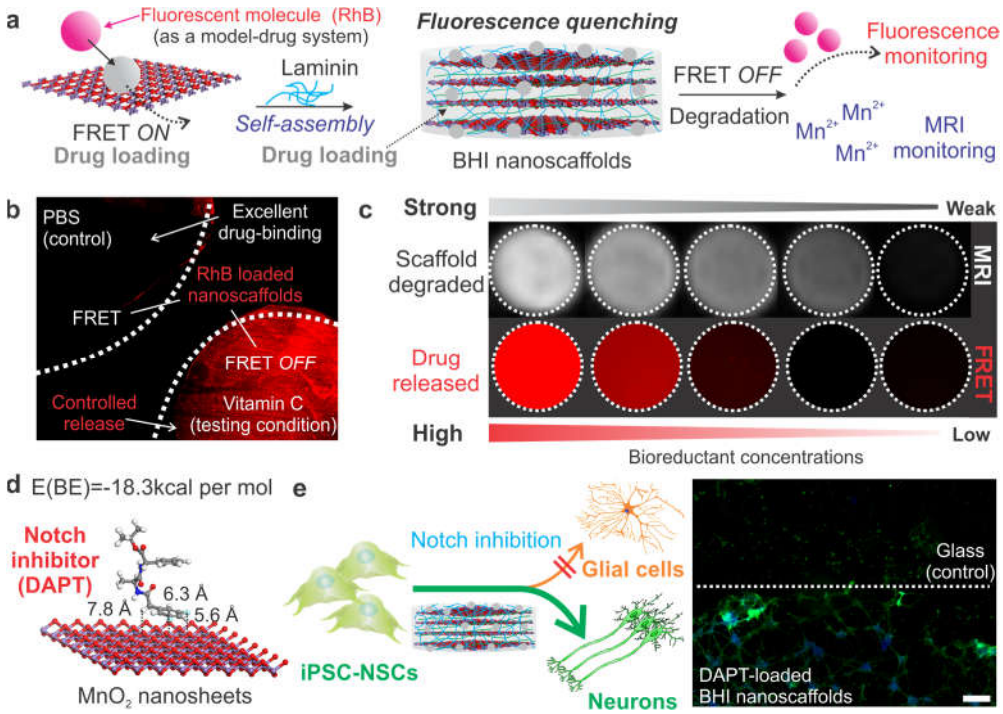

Figure 3-5. Spatiotemporal controlled delivery of soluble cues using 3D-hybrid inorganic nanoscaffolds. a, Diagram of drug loading, releasing, and monitoring on the MnO2 laminin hybrid nanoscaffolds. b, Excellent drug hold-up from drug-loaded hybrid nanoscaffolds, and controlled drug release by bioreductants. c, A MRI-based monitoring of drug release enabled by our hybrid nanoscaffold. d, An optimized binding geometry and binding energy of simulation-screened neurogenic drug (DAPT) toward nanosheets. e, Spatial control of neuronal differentiation and neurite outgrowth across the boundary between control substrates and DAPT-loaded MnO2 laminin hybrid nanoscaffolds. Scale bar: e, 100 μm.

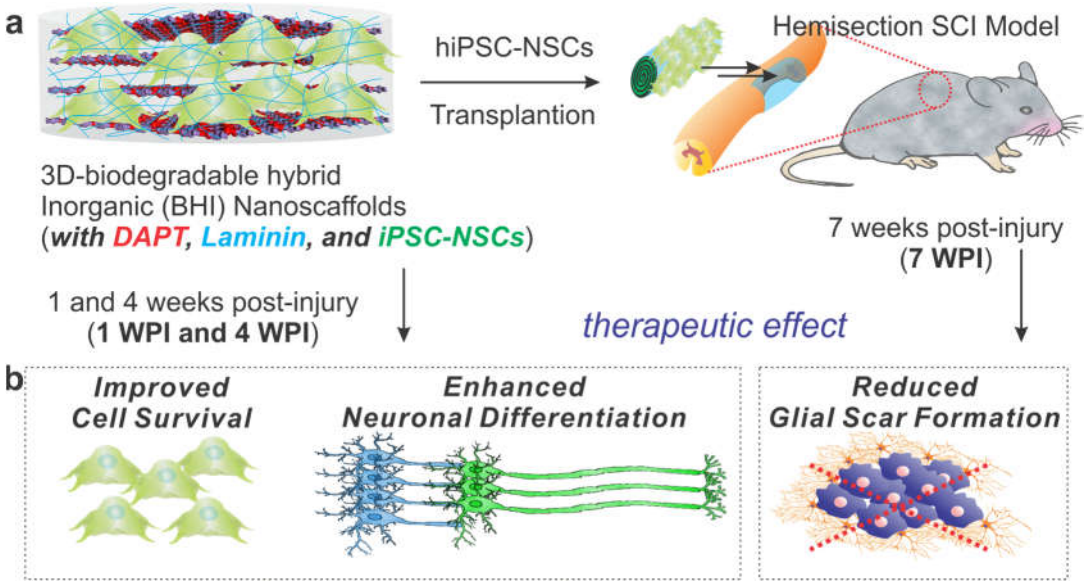

Figure 3-6. Pathways of enhanced stem cell transplantation into SCI sites by 3D-BHI nanoscaffolds. a-b, Schematic diagram (a) showing the enhanced transplantation of iPSC-NSC in a murine lateral hemisection SCI model by 3D BHI nanoscaffold and the proposed mechanisms (b) for the enhanced transplantation and potential beneficial effects on overcoming inhibitory microenvironments in the SCI sites.

Enhanced stem cell transplantation into spinal cord injury sites

With the prominent effects of the 3D-hybrid inorganic nanoscaffolds on improving the adhesion, neuronal differentiation of hiPSC-NSCs, and neurite outgrowth of differentiated neurons, we then further tested the effects of the nanoscaffold on enhanced stem cell transplantation in vivo (Figure 3-6). To transplant the stem cell-seeded nanoscaffolds, we first generated a T10 thoracic hemisection lesion to the spinal cord of an adult mouse, then

the hiPSC-NSC seeded-nanoscaffolds [as an experimental condition] and -polycaprolactone (PCL) polymer scaffolds [PCL-cell group, as a control condition] were rolled up and inserted into the hemisected SCI lesion (Figure 3-6a)[503]. To identify our transplanted cells, hiPSC-NSCs were genetically labelled with green fluorescent protein (GFP) (i.e., hiPSC-NSC-GFP). Surgifoam inserted mice with injuries were used as a control condition. After transplantation, we first evaluated nanoscaffold biodegradation in vivo by detecting the amount of degraded Mn (manganese) element in mouse urine samples using inductively coupled plasma mass spectrometry (ICP-MS) analysis (Figure 3-25). Consistent with our previous in vitro studies, we could observe rapid in vivo degradation of nanoscaffold. This degradation of transplanted nanoscaffolds was also detected by the color change (from black to brown) in a time-dependent manner throughout the first-week post-transplantation. After investigating the in vivo biodegradability, we then studied the effects of 3D-BHI nanoscaffold for enhanced stem cell transplantation. We hypothesized that our 3D-BHI nanoscaffold could robustly improve the survival of hiPSC-NSCs and the differentiation of hiPSC-NSCs into neurons in the early and intermediate stages [1-4 weeks post-injury (WPI)] (Figure 3-6, Figure 3-26-33). We also expected that the 3D-BHI nanoscaffold could reduce astroglial scar formation in the longer term (7 WPI) (Figure 3-6). To test our hypothesis, we first performed short-term (1-week) in vivo stem cell transplantation assay in the injured site and 3 different control conditions for stem cell transplantation were included as controls (Figure 3-7, Figure 3-28-31). From our immunostaining data, we observed significantly higher populations of GFP+ cells and TuJ1+ cells from our testing condition compared to the other 3 control conditions, which directly suggests an enhanced stem cell transplantation. This result is also consistent with

our Caspase 3 immunostaining data (Figure 3-7, Figure 3-31), where fewer hiPSC-NSC-GFP cells transplanted by 3D-BHI nanoscaffold showed apoptotic markers as compared to the polymer scaffold-transplanted cells. Additionally, hiPSC-NSC-GFP cells transplanted by 3D-BHI nanoscaffold showed more spreading, whereas GFP+ cells from two control conditions (Figure 3-7) showed less spreading. This could be due to the promoted cellular adhesion and could improve neuronal differentiation, based on our in vitro focal adhesion studies (Figure 3-14). This trend of enhanced cell survival and increased neuronal differentiation of stem cells from 3D-BHI nanoscaffold-treated condition continued until 4-WPI, as shown in Figure 3-32. Furthermore, the percentage of hiPSC-NSC-GFP with more mature neuronal markers (Syn1) is also significantly higher in 3D-BHI nanoscaffold-treated condition as compared to cell injection condition at this time point, indicating enhanced neuronal differentiation from our nanoscaffold-treated conditions (Figure 3-32). Equally importantly, the improved transplantation from our 3D-BHI treated conditions can mitigate inhibitory microenvironmental effects in the long-term (7-WPI) (Figure 3-8). For example, immunostaining on a proliferation marker (PH3), inflammation marker (F4/80) and an astroglial scar marker (GFAP) revealed higher proliferation, suppressed inflammation and reduced astroglial scar formation from our 3D-BHI nanoscaffold, which could be largely attributed to the neurotrophic factors secreted by hiPSC-NSC-GFP and DAPT released from nanoscaffold in the early stages[464]. Overcoming the highly inhibitory microenvironment such as inflammation and astroglial scars has been considered as an effective strategy to treat SCI[463]; and our results showed that 3D-BHI nanoscaffold could be utilized for the enhanced stem cell transplantation and for the treatment of CNS injuries. On the other hand, as future plans to apply our nanoscaffold for disease treatment, it would

be essential to analyze long-term cell fates of transplanted stem cells and is critical to evaluate animal behavioral recovery from 3D-BHI nanoscaffold treated conditions using larger animal sets[504,505]. Nevertheless, given its unique properties demonstrated in vitro, and the enhanced transplantation of hiPSC-NSCs in vivo compared to conventional cell transplantation methods, our developed 3D-BHI nanoscaffold could represent a promising candidate for stem cell therapy and for advanced stem cell transplantation.

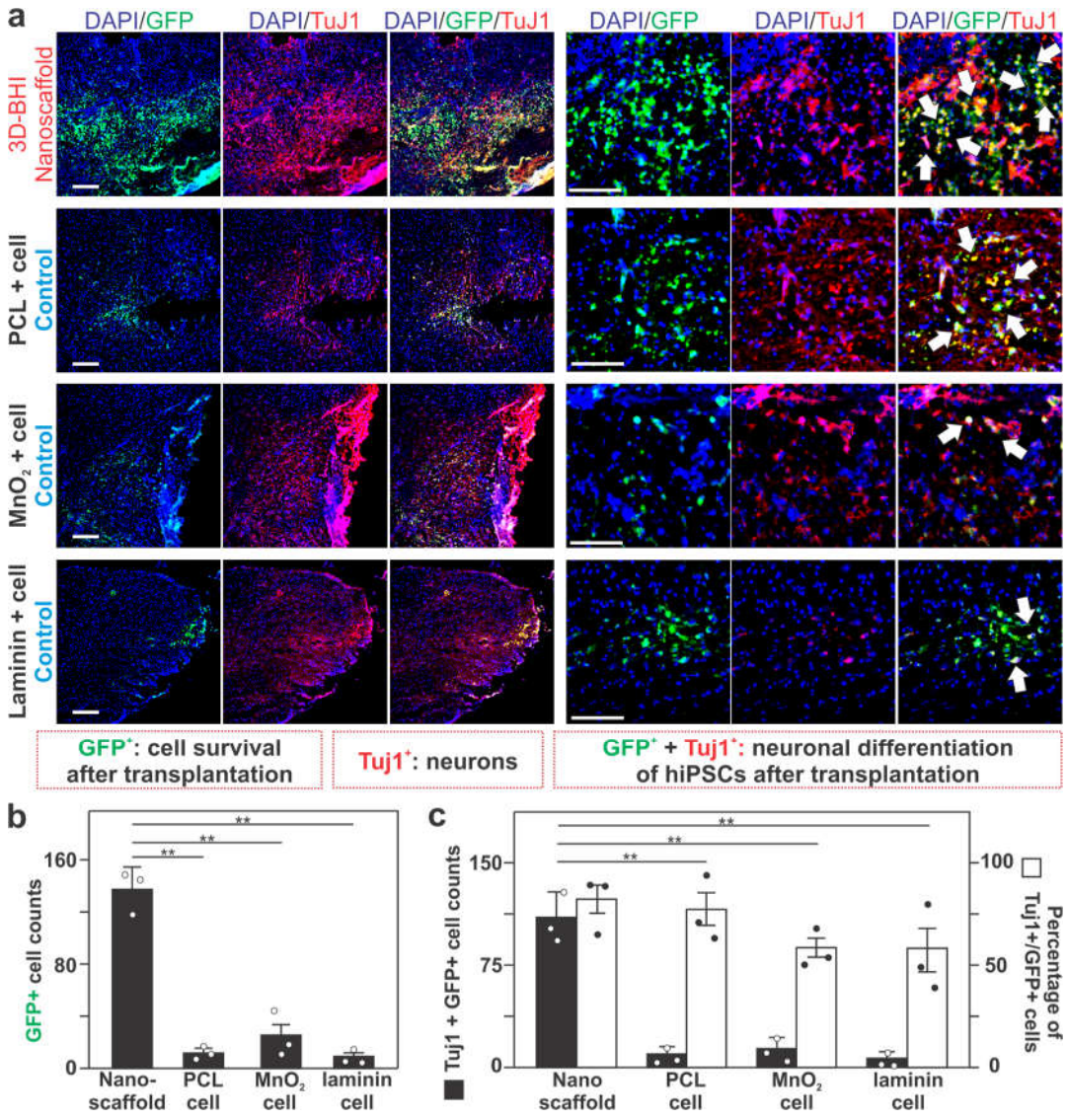

Figure 3-7. 3D-BHI nanoscaffold enhances survival and neuronal differentiation of hiPSC-NSC-GFP. a, Immunohistological staining analysis was performed on tissue slices from 4 different animal groups transplanted with hiPSC-NSC-GFP. b-c, Enhanced cell transplantation based on high cell retention (b) and neuronal cells in the SCI site in the nanoscaffold group. Scale bars: 100 μm. Error bars represent mean+s.d.; n=3, **P<0.01 by one-way ANOVA with Tukey post-hoc test.

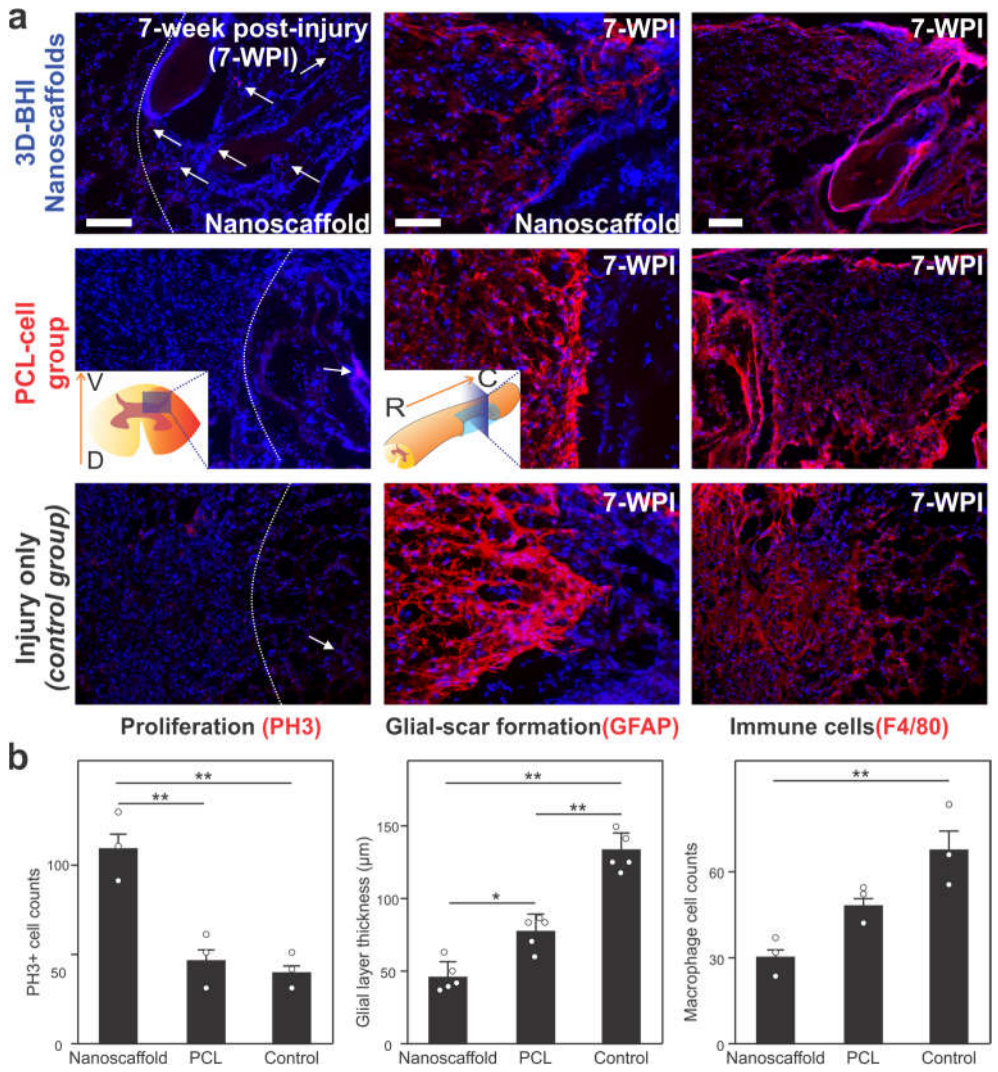

Figure 3-8. Improved long-term effects on SCI sites from 3D-BHI enhanced stem cell transplantation. a-b, Histological immunostainings images (a) and quantifications (b) of cell proliferation, astroglial markers and immune cell markers. Scale bars in a: left and middle column: 200 μm; right column: 100 μm. Error bars represent mean+s.d.; n=3 or 5, *P<0.05, **P<0.01 by one-way ANOVA with Tukey post-hoc test.

3.1.4 Conclusions and Outlook

The development and the use of biomaterials for stem cell-based tissue engineering to treat CNS diseases/injuries to date have focused on: i) providing favorable microenvironments for endogenous and exogenous cellular regeneration and ii) serving as a spatiotemporally controlled drug release platform to regulate pro-neuroregenerative signaling pathways. This work is based on the development of a biodegradable hybrid inorganic nanoscaffold and its utilization for the enhanced transplantation of stem cells into SCI sites. Our demonstrated nanoscaffold technology platform can be combined with other neurogenic drugs as well as stem cell therapeutic efforts currently in development. In the developed hybrid nanoscaffold, we can tune the 2D/3D structural properties of porous scaffolds and the unique physiochemical properties of MnO_2 nanoscaffold such as magnetic properties and degradation rate in a single platform. Recently, 2D/3D inorganic and carbon nanomaterials have attracted much attention, as they have the great potential to control stem cell neuronal differentiation and neuronal behaviors. However, several pertinent barriers including limited biodegradability and drug loading/release capability hinder their broad application toward stem cell-based tissue engineering. Thus, our developed biodegradable hybrid inorganic nanoscaffold-based stem cell therapeutic approach would be a useful tool for improving stem cell survival and inducing neuronal differentiation in vivo, and thus can provide insights into stem cell behaviors post-transplantation that may lead to novel therapies for the treatment of the neurodegenerative diseases. Collectively, our developed hybrid nanoscaffold-based approach to control stem cell differentiation into neurons and promote neurite outgrowth would provide an alternative to help overcome the critical barriers that limit cellular therapies for many devastating injuries and diseases.

3.1.5 Additional Figures

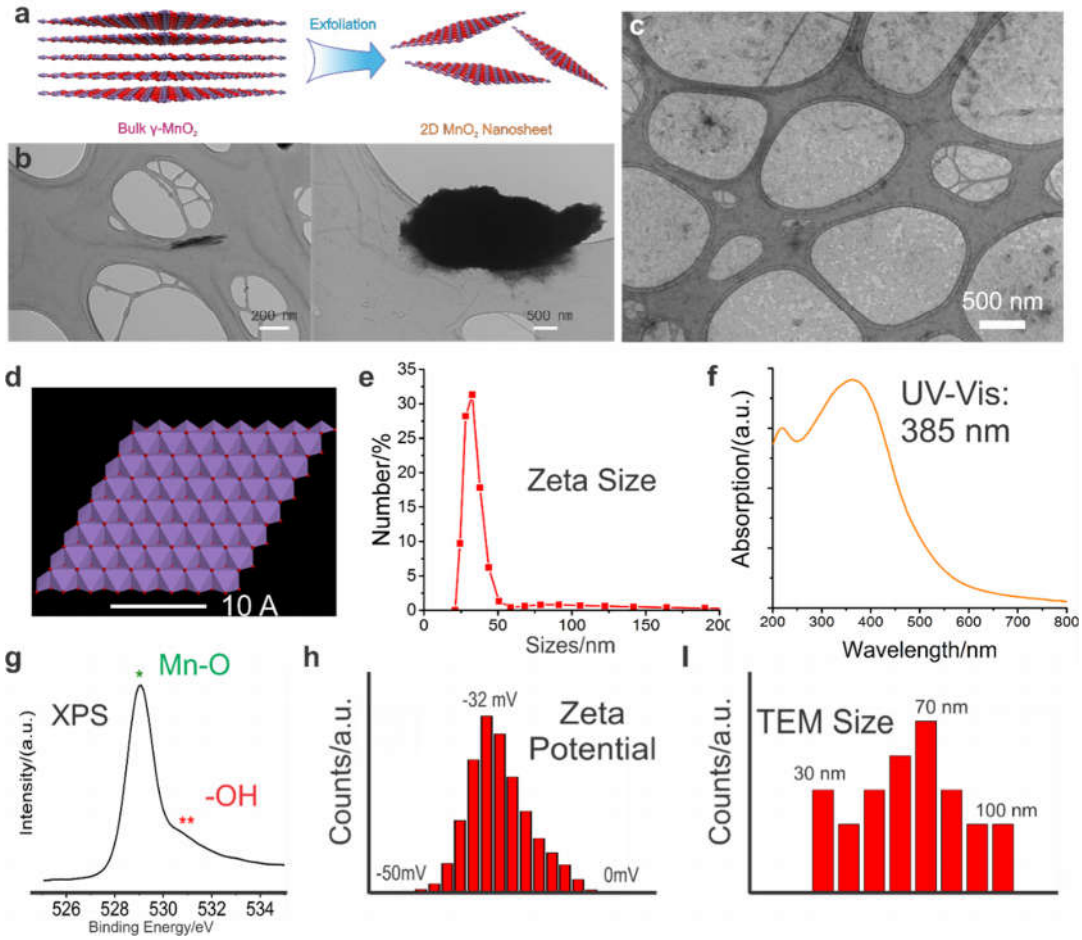

Figure 3-9. Characterizations of 2D MnO_2 nanosheets. a-b, Schematic diagram explaining the synthesis of 2D anisotropic MnO_2 nanosheet from birnessite-type of MnO_2 precursors, and representative TEM images of the precursor with a layered structure. Birnessite MnO_2 has a layered structure assembled from thin layered MnO_2 nanosheets. After exfoliation during ultrasonication, thin layered MnO_2 nanosheets can be obtained from the solution. c, Zoomed-out TEM images of MnO_2 nanosheets that assembled into a porous film. d, MnO_2 nanosheet structure created by DFT simulation. The simulated crystal lattice matched with experimental observations in HRTEM analysis. Blue refers to manganese atom, and red refers to oxygen. e-i, Zeta size, UV-Visible spectrum, XPS, Zeta potential, TEM sizes, of

MnO_2 nanosheets as-synthesized. The highly negative zeta potential around -30 mV could be originated from the hydroxyl groups existent in the defects of MnO_2 nanosheets. This high value of negative zeta potential also indicates good colloidal stability of MnO_2 nanosheets in solution. UV-Vis absorption spectrum of MnO_2 nanosheets shows the identical absorption of MnO_2 nanosheets in solution at 385 nm, which was used for quantifying remaining MnO_2 in biodegradation studies.

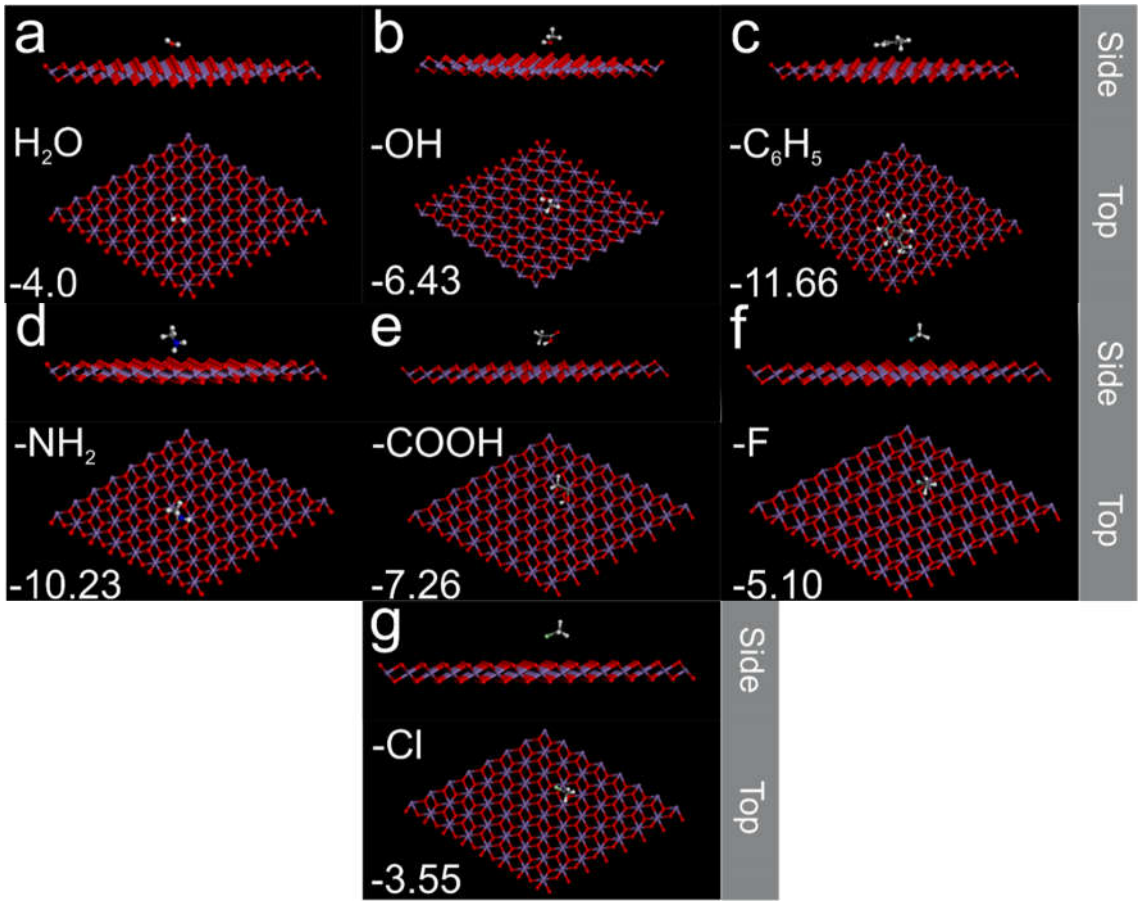

Figure 3-10. Modeling nanosheet-small molecule interactions using DFT calculation. a-g, Computational modeling result describing the optimized geometry (both top views and side views) of binding between MnO_2 nanosheets and water (a), hydroxyl group (b, hydrogen

bonding), aromatic benzene ring (c, metal-π polarization), amine group (d, electrostatic interaction), carboxylic group (e), fluoride (f) and chloride (g). The binding energies were calculated by the equation of E(BE)=E(A+B)-E(A)-E(B), and summarized in the left bottom of each figure (BE: Binding Energy; A: Single layer of MnO_2 nanosheet; B: Small molecules with assigned functional groups; Units: kCal/mol). In these simulation models, manganese atom is colored with blue, oxygen atom is colored with red, the carbon atom is colored gray, hydrogen is colored with white.

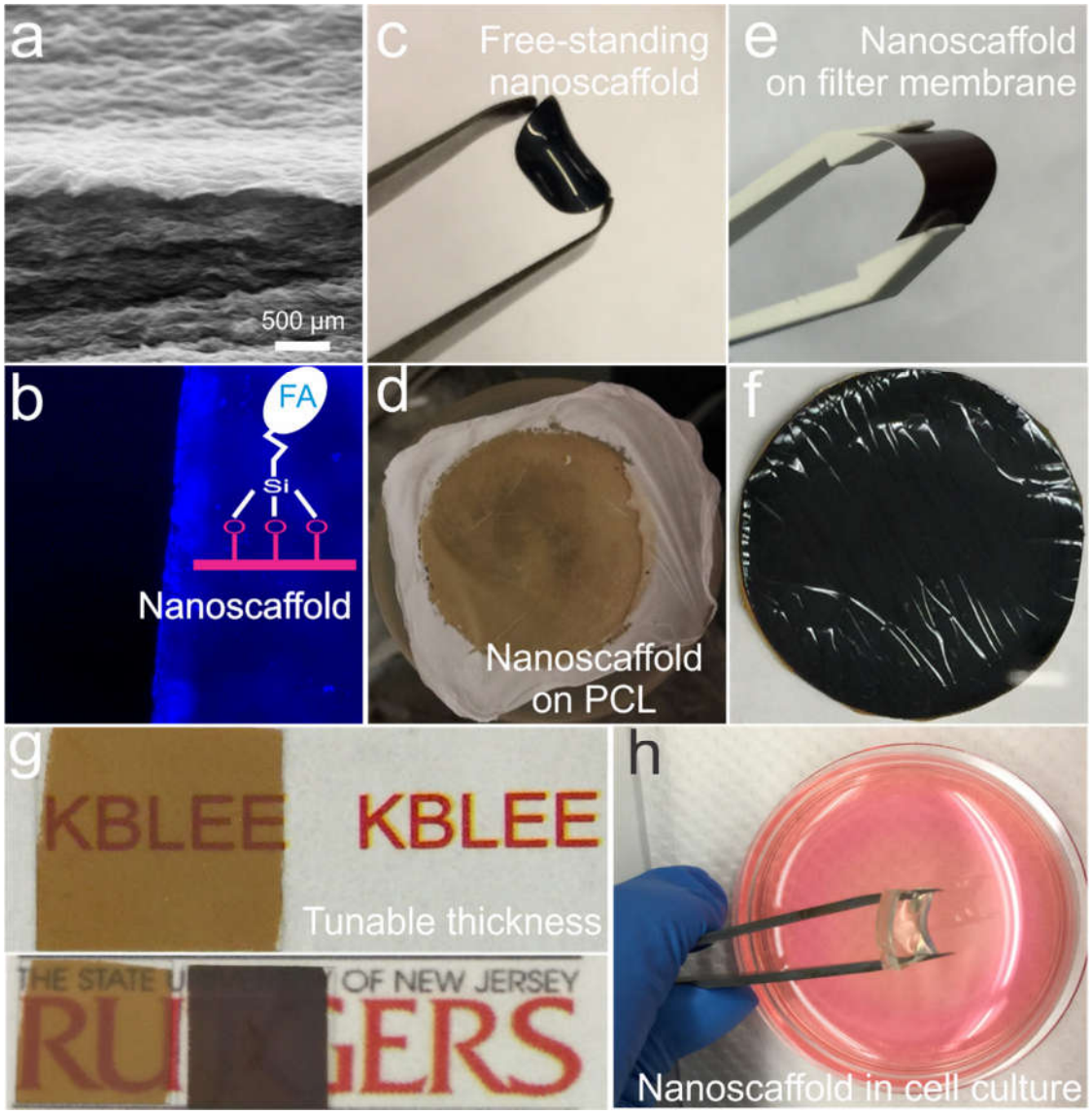

Figure 3-11. Characterizations of MnO_2 hybrid nanoscaffold fabricated by a vacuum filtration method. a, A zoomed-in SEM image of nanoscaffold from the side view showing the layered structure of MnO_2 nanoscaffold. b, Surface functionality of nanoscaffold. The existence of surface hydroxyl groups on MnO_2 nanosheet enabled the covalent functionality of the nanoscaffold By using APTES. Fluorescence from fluoresceinamine (FA, blue) conjugation was used to visualize the success of conjugation. c, Photograph showing a free-standing MnO_2 nanoscaffold. Nanoscaffold fabricated from vacuum filtration is mechanically robust and can be manipulated and held by tweezers. No cracks

were found on nanoscaffold during manipulation. d-e, A nanoscaffold placed on top of a biodegradable polymer (PCL nanofiber) or cellulose nano-porous membrane. The incorporation of polymer substrate can increase the flexibility of nanoscaffold during cell transplantation. f, A photograph showing MnO_2 hybrid nanoscaffold with the homogeneous surface in the large area. The size of the photograph is 25mmx25 mm. g, MnO_2 hybrid nanoscaffold with tunable thickness showing varying transparency. This is achieved by adjusting the concentrations of MnO_2 nanosheet solution used for vacuum filtration. h, A photograph showing MnO_2 hybrid nanoscaffold on PDMS seeded with cells.

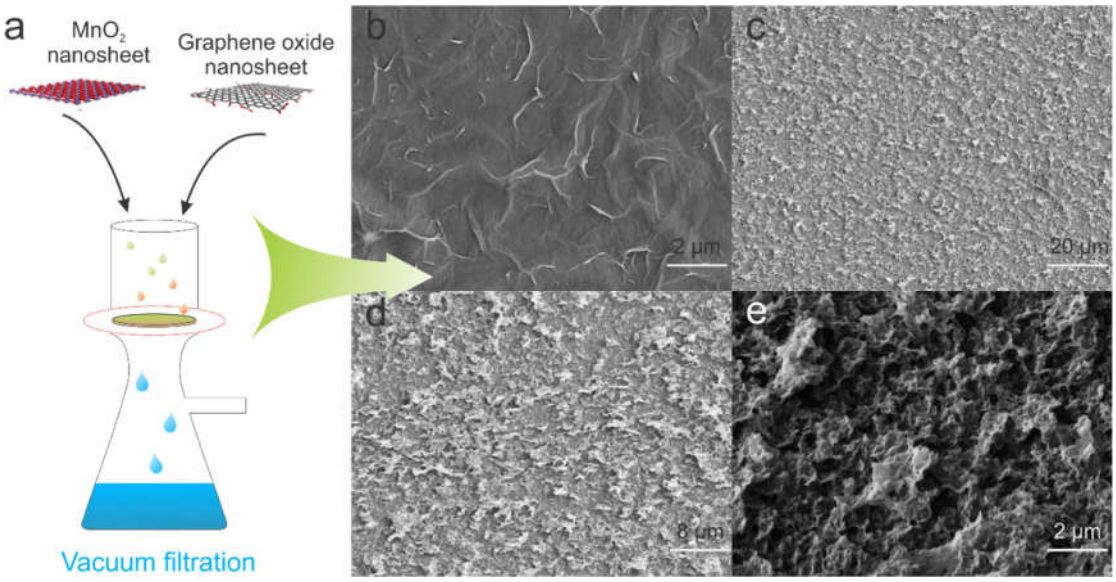

Figure 3-12. Vacuum filtration for fabricating MnO_2 and GO hybrid nanoscaffold. a, Schematic diagram for explaining the vacuum filtration approach for fabricating homogeneous GO nanoscaffold and MnO_2 hybrid nanoscaffold (a). b-e, FESEM of GO nanoscaffold (b) and MnO_2 nanoscaffold (c-e). Both nanoscaffolds were fabricated from vacuum filtration method and are highly homogeneous in the large scale. However, the

detailed nanotopographies of GO nanoscaffold and MnO_2 nanoscaffold are different. Whereas GO nanoscaffold has a relatively smooth surface, MnO_2 nanoscaffold has a much rougher surface with many ripple structures. This difference on substrate nanotopography could be originated from the more rigid bonding of Mn-O-Mn compared on nanoscaffold. Increased surface roughness could be one of the reason for nanoscaffold in promoting adhesion and differentiation of neural stem cells.

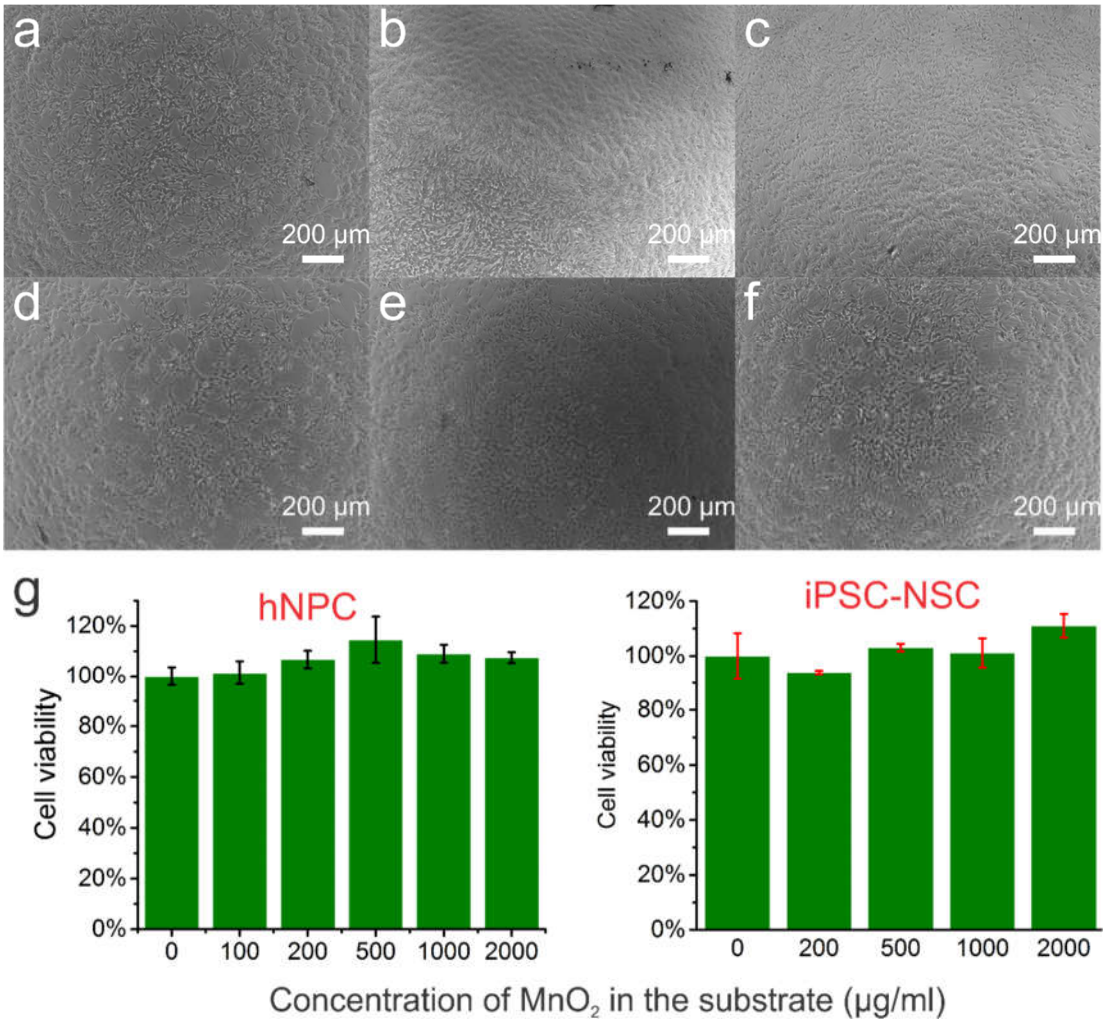

Figure 3-13. Biocompatibility of MnO_2 hybrid nanoscaffold. a-f, Representative images of NSCs adhesion and proliferation on different substrates (a,d: glass; b, e: graphene scaffold; c, f: MnO_2 nanoscaffold) one day after seeding. g, Viabilities of cells cultured on glass coated with laminin were used as controls. Cells were cultured on a laminin-coated glass substrate and nanoscaffold for 2 days, and then presto-blue assay was used for quantifying relative cell viability based on the absorption at 570 nm in plate-reader. The high cell viability of both hNPCs and iPSC-NSCs cultured on nanoscaffold indicates its excellent biocompatibilities. Due to the stronger protein absorption on graphene oxide assembled scaffold and nanoscaffold, higher numbers of NSCs were adhered and grown on graphene oxide assembled scaffold and nanoscaffold compared to glass substrates. Data represents mean$\pm$s.d., n=3, results are non-significant (*$P>0.05$) between different conditions by one-way ANOVA.

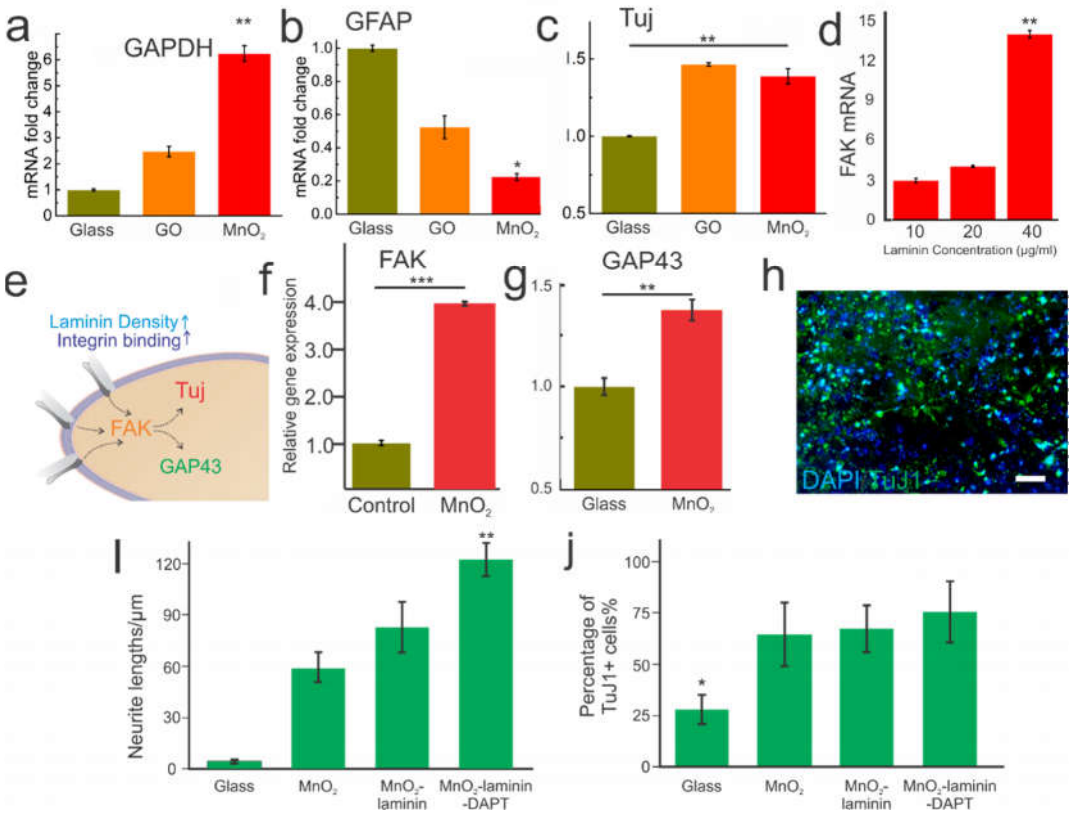

Figure 3-14. Enhanced Neuronal differentiation of iPSC-NSCs on MnO_2 hybrid nanoscaffold. a-g, mRNA levels of GAPDH (a), GFAP (astrocyte marker gene, b), TuJ1 (early neuron marker gene, c), laminin concentration dependent and substrate dependent FAK expression (5 μg/ml, 10 μg/ml, 20 μg/ml, from left to right) (d, f) and GAP43 (growth cone associated protein, g). e is a schematic diagram for proposed pathways summarizing the gene analysis. and comparison of axonal length for iPSC-NSCs differentiated on the different substrate for 6 days. This gene analysis result describes an obvious enhancement of neuronal differentiation on MnO_2 nanoscaffold compared to the control substrate, with a slight suppression of gliogenesis. h, Immunostaining of neuronal markers (green) and nuclei staining (blue) for iPSC-NSCs differentiated on GO nanoscaffold, which was used as a positive control comparing to MnO_2 nanoscaffold and the glass substrate in the main Figure 1. i-j, Quantified neurite growth of neurons (i) and percentage of neuronal cells.

Scale bar: 100 μm (j) differentiated from iPSC-NSCs cultured on a different substrate (glass, MnO_2 nanoscaffold, MnO_2 laminin nanoscaffold and 3D BHI nanoscaffold with DAPT loaded). Data are mean±s.d., n=3 for a-d and j; n=9-12 for i, **P<0.01 and ***P<0.001 by unpaired student t-test for f and g, *P<0.05 and **P<0.01 by one-way ANOVA with Tukey post-hoc analysis for a-d and i-j.

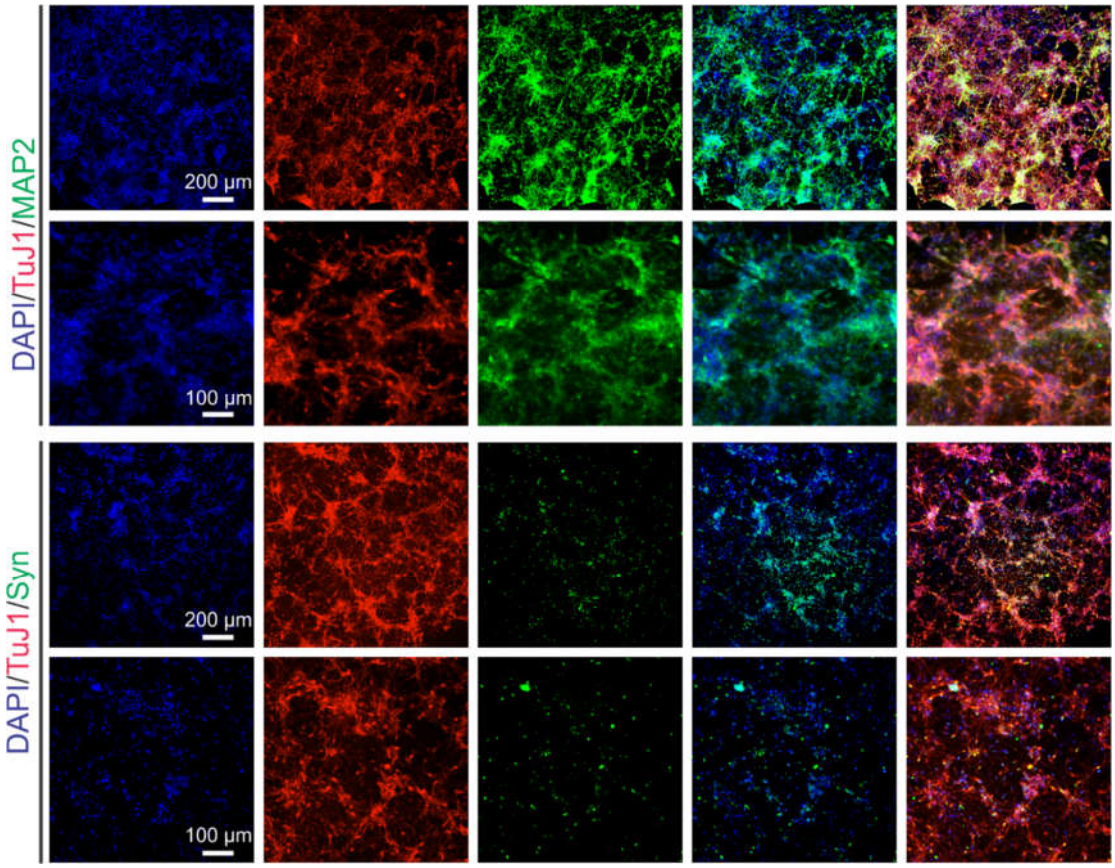

Figure 3-15. iPSC-NSCs differentiated on MnO_2 laminin nanoscaffolds expresses mature neuronal markers (MAP2 and Synapsin 1 (Syn)). Shown in this figure is immunostaining images of iPSC-NSCs differentiated after 6 days.

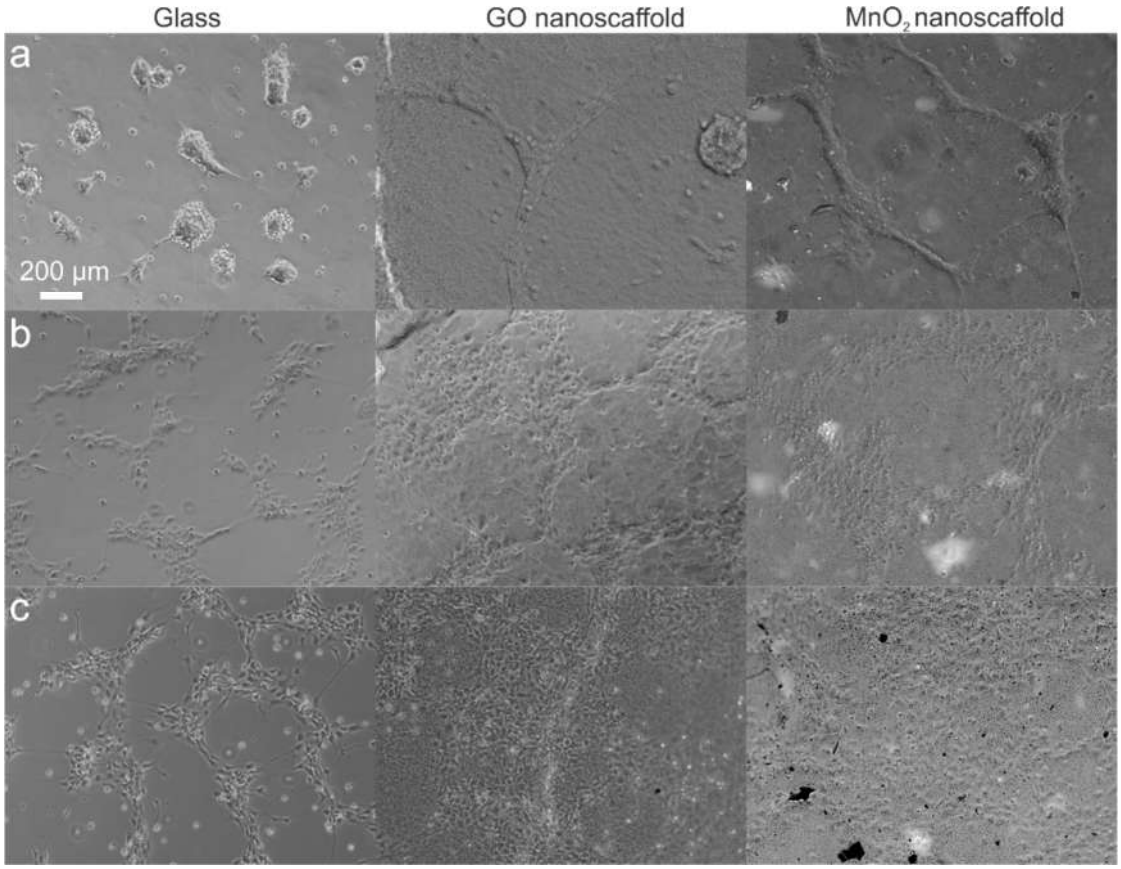

Figure 3-16. Laminin concentration-dependent adhesion of iPSC-NSCs in growth media on different scaffolds. a-c, Phase images of iPSC-NSCs cultured on a different substrate (glass, graphene oxide assembled scaffold, and nanoscaffold) under increasing concentrations of laminin (a: 5 μg/ml; b: 10 μg/ml; c: 20 μg/ml) during coating process. Varying laminin coating concentrations was found to significantly influence the adhesion of iPSC-NSC for all the 3 substrates. However, under low laminin coating concentrations (0.5x and 1x), cells seeded on MnO_2 nanoscaffold and GO nanoscaffold showed obviously improved cell spreading and adhesion. This enhanced adhesion on MnO_2 nanoscaffold and GO nanoscaffold was attributed to increased protein deposition on the surface of the substrates.

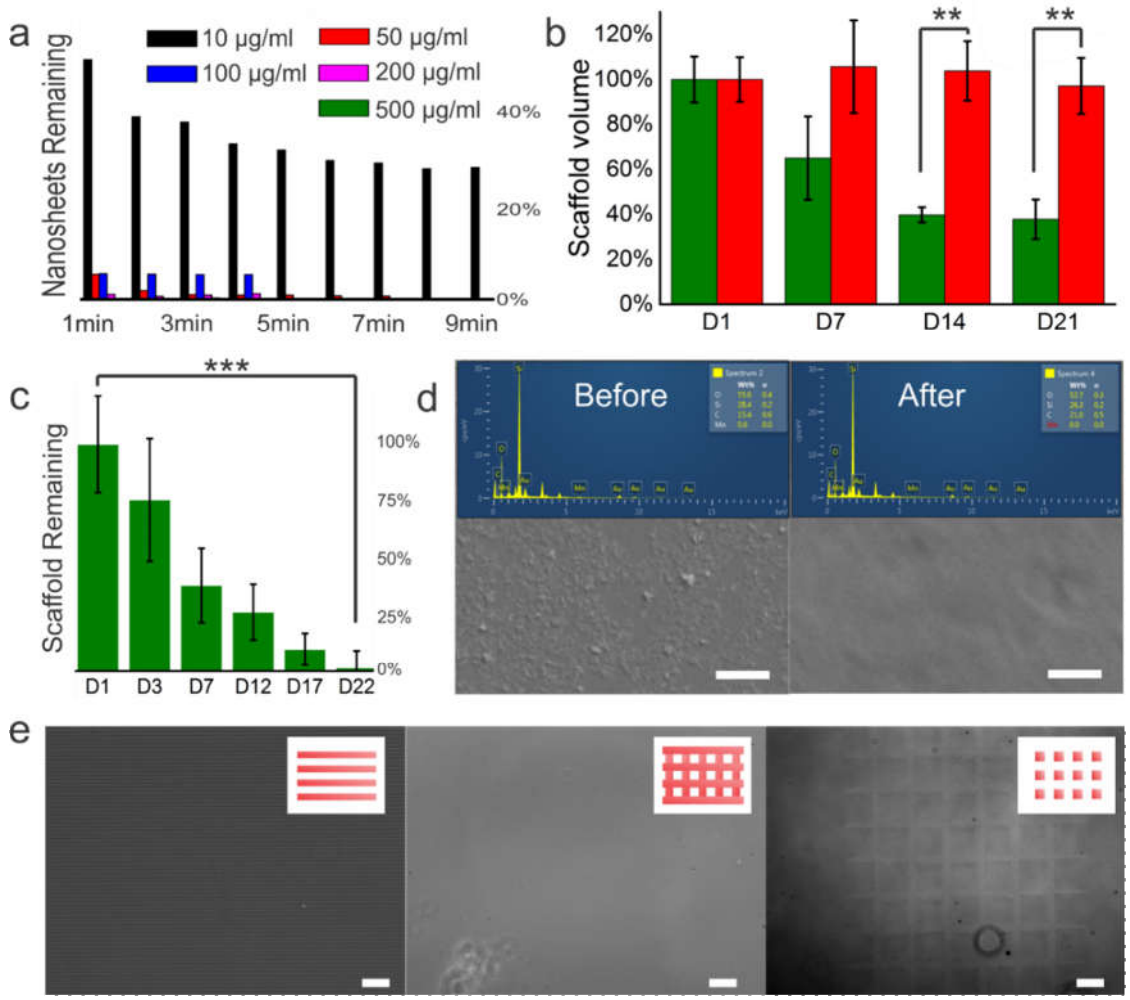

Figure 3-17. Tunable biodegradability of MnO_2 nanoscaffold through an unconventional redox-mechanism. a, Controlled biodegradation of 2D MnO_2 nanosheets by vitamin C in a dosage-dependent manner in physiological conditions. b, In the structure of thick layered (6 mm) nanoscaffold sandwiched by two cell layers, nanoscaffold has a half-degradation time around 2 weeks. This is achieved under regular cell culture conditions without the addition of any exogenous biochemical or vitamin C. Green bars (left bars) indicate MnO_2 condition and red bars (bars on the right) indicate GO condition. Data represents mean$\pm$s.d., n=3, *P<0.05 and **P<0.01 by unpaired student t test. c, When the thickness of

nanoscaffold was significantly reduced to a thin film (<1 mm), the half-degradation time was reduced to less than one week. Data represents mean±s.d., n=3, ***P<0.001 by one-way ANOVA with Tukey post-hoc analysis. d, The successful degradation of nanoscaffold thin film was confirmed with SEM and EDX based elemental analysis. e, Micropatterned nanoscaffold assembled from MnO_2 nanosheets using μ-contact printing. Based on the hydrophilic surfaces, nanoscaffold micropatterns with different shapes (line pattern, grid pattern and square pattern) were fabricated using micro-contact printing. These micropatterns were used to visualize the thin nanosheets film as a substrate, and for monitoring the degradation of the scaffold under an optical microscope. In addition, they can also be used as a substrate for controlling cellular geometries for controlled cell adhesion. Scale bars: d, 200 μm; e, 100 μm.

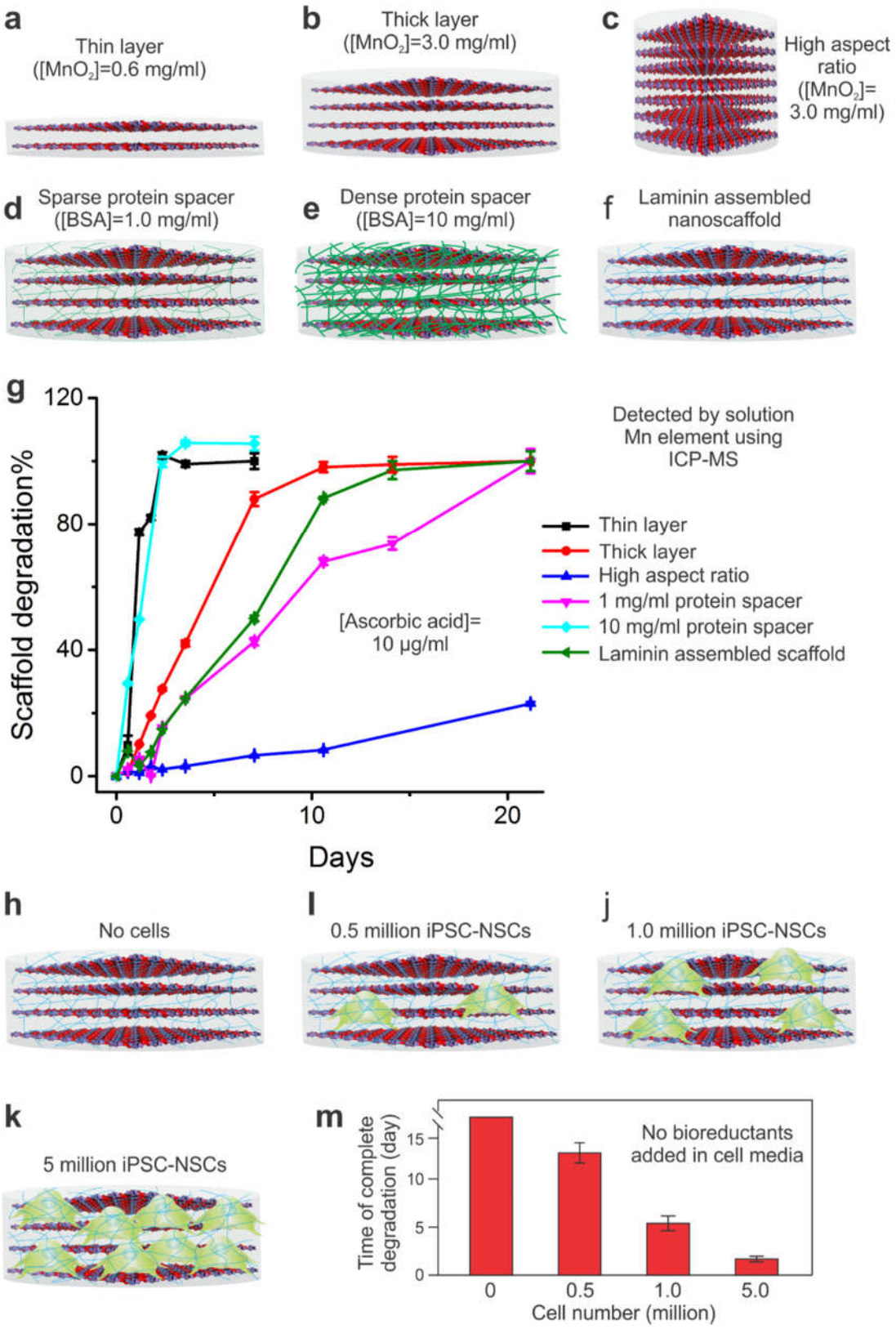
a
Thin layer
([MnO2]=0.6 mg/ml)
b
Thick layer
([MnO2]=3.0 mg/ml)
c
High aspect ratio
([MnO2]= 3.0 mg/ml)
d
Sparse protein spacer
([BSA]=1.0 mg/ml)
e
Dense protein spacer
([BSA]=10 mg/ml)
f
Laminin assembled nanoscaffold
g
Scaffold degradation%
Days
Detected by solution Mn element using ICP-MS
[Ascorbic acid]= 10 μg/ml
Thin layer
Thick layer
High aspect ratio
1 mg/ml protein spacer
10 mg/ml protein spacer
Laminin assembled scaffold
h
No cells
I
0.5 million iPSC-NSCs
j
1.0 million iPSC-NSCs
k
5 million iPSC-NSCs
m
Time of complete degradation (day)
Cell number (million)
No bioreductants added in cell media

Figure 3-18. Tunable biodegradability of MnO_2 nanoscaffolds by modulating scaffold structure and varying cell densities. a-f, 6 different methods to prepare scaffolds and for modulating scaffold degradation. Symbols were kept consistent with Scheme in manuscript. Green fibers in d and e represent bovine serum protein. b represents the control scaffold to show the tuning of biodegradability by comparing it to a, and c-f. g, Degradation profile of different scaffolds obtained from measuring time-dependent manganese concentrations in the solution using ICP-MS. h-m, Tuning scaffold degradation by controlling cell amount transplanted on the scaffold. h-k, Schematics showing scaffolds seeded with varying amount of iPSC-NSCs. m, A summary of full degradation time of scaffolds based on the complete disappearance of scaffold color. MnO2 laminin nanoscaffold was used for all the conditions, and regular iPSC-NSC differentiation media was used for maintaining cell viabilities with regular daily change. n=3, 2 in g and m, respectively. Error bars are standard error of the mean.

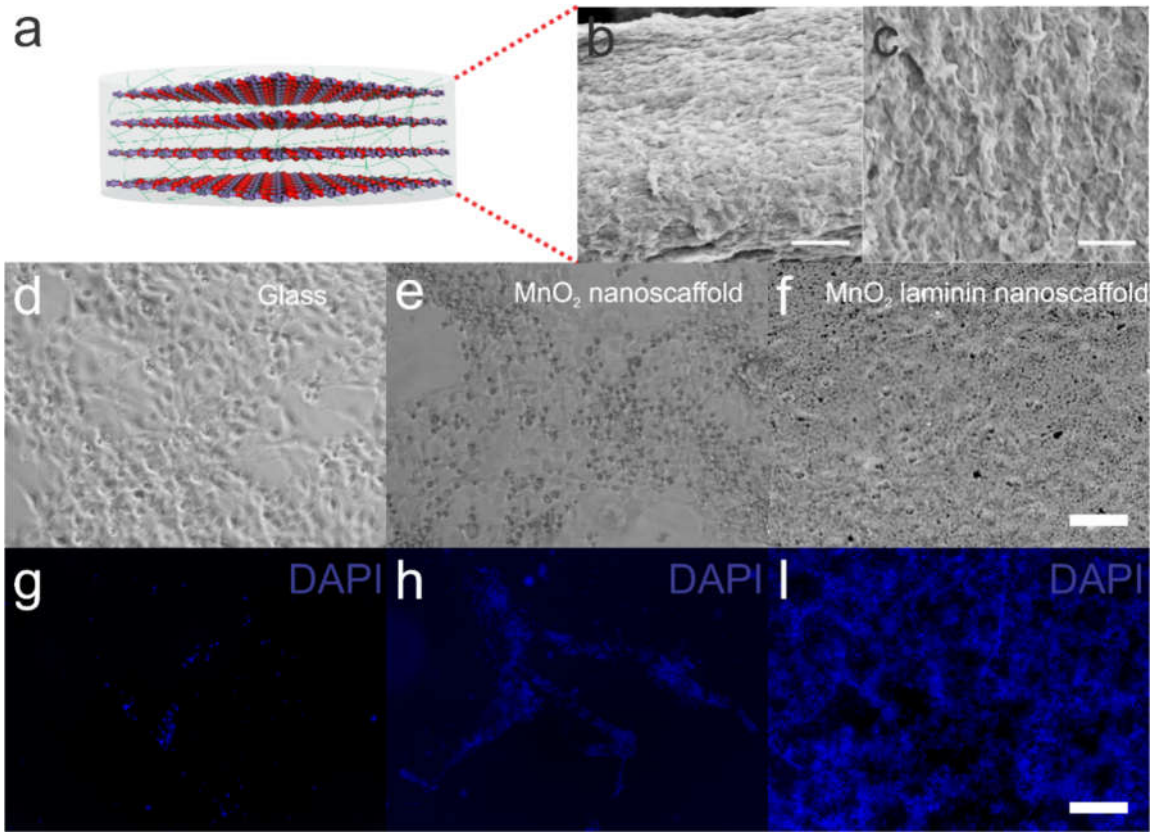

Figure 3-19. Cellular adhesion of iPSC-NSCs on MnO_2 laminin hybrid nanoscaffold during 6 days' differentiation of iPSC-NSC. a, Schematic diagram of MnO_2 nanosheet assembled into laminin-nanoscaffold. b, FESEM images of MnO_2 laminin hybrid nanoscaffold indicate it has a highly rough surface and the 2D MnO_2 nanosheet was spontaneously assembled into bulk substrates. d-f, Phase images of cells cultured on glass coated with laminin (d), nanoscaffold coated with laminin (e), and laminin-nanoscaffold (f) for one day. From the phase images, cell densities are similar between these 3 after seeding. g-i, Nuclei staining (blue) on cell adhesions of iPSC-NSCs differentiated for 6 days on glass coated with laminin (g), nanoscaffold coated with laminin (h), and laminin-nanoscaffold (i). These images clearly show that laminin-nanoscaffold significantly improved adhesion of iPSC-NSCs over the 6 days' differentiation, due to its uniformly distributed laminin adhesion proteins. Scale bars: b, 1 μm; c, 500 nm; d-f, 100 μm; g-i, 200 μm.

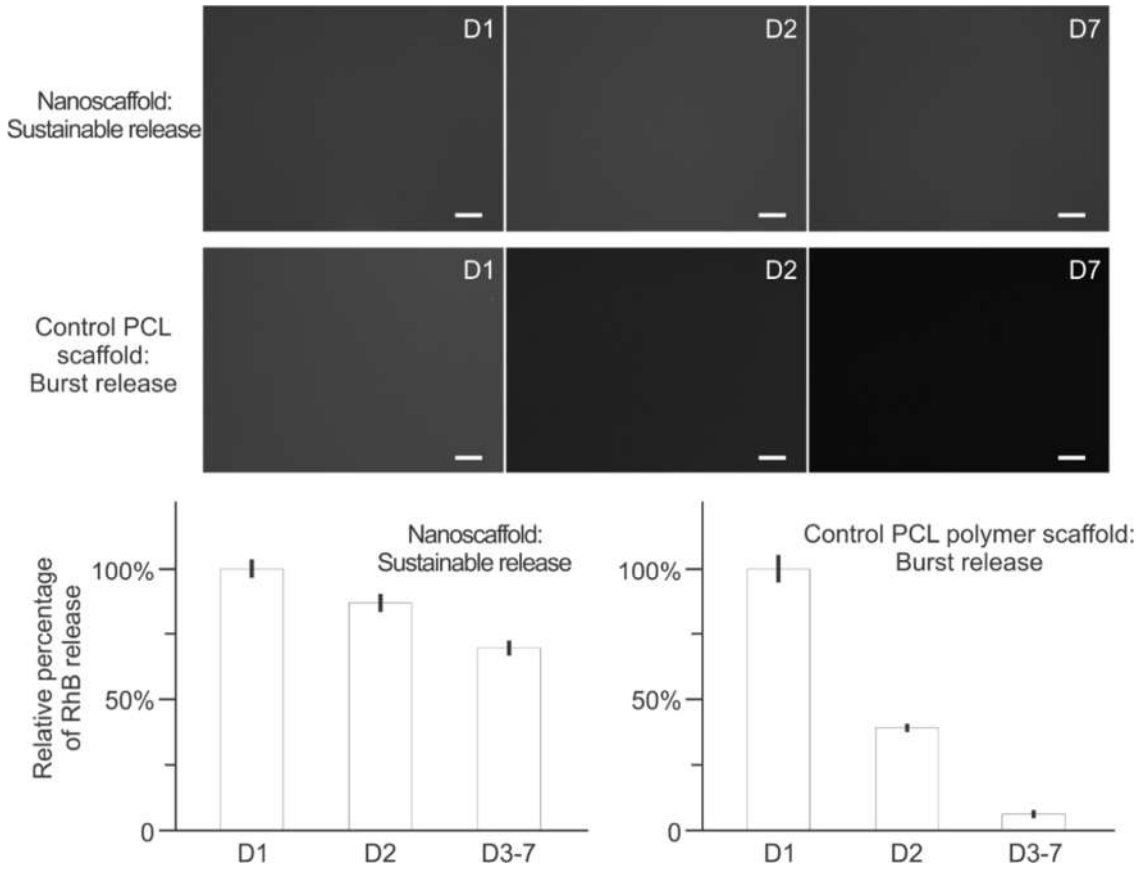

Figure 3-20. Drug (RhB) daily releasing profiles from MnO_2 laminin hybrid nanoscaffold and control polymer (PCL) scaffold. Compared to PCL scaffold, nanoscaffold has a more sustainable release profile through the one week's processes. RhB releasing was indicated by the brightness of monocolored images (top) and summarized in relative percentage compared to the amount of released at Day1.Scale bars: 200 μm. Error bars are the standard error of the mean (n=5).

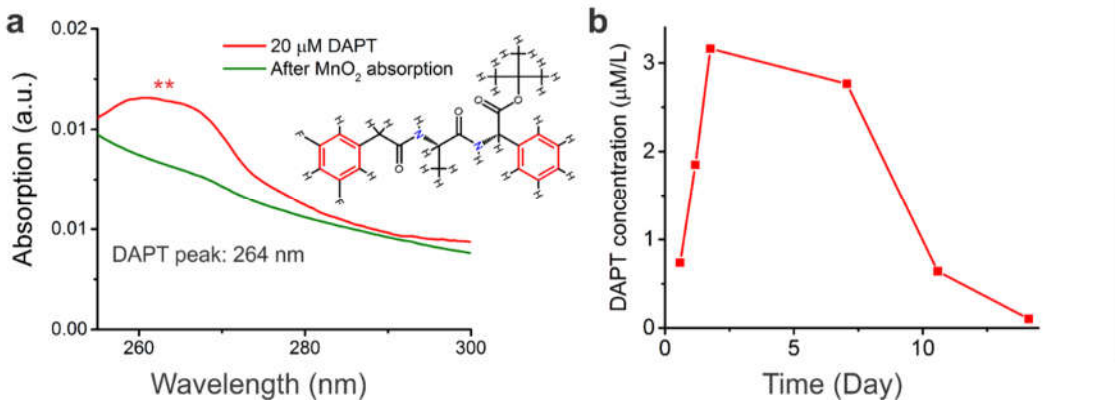

Figure 3-21. Efficient DAPT loading and sustainable release of DAPT on MnO_2 nanoscaffold. a, UV-Vis spectrum of DAPT solution before and after MnO_2 nanosheets absorption. Based on the disappearance of the characteristic peak of DAPT at 264 nm, we can quantify the excellent absorption of DAPT by nanosheets. Inset is a chemical structure of DAPT. b, Sustainable DAPT releasing from MnO_2 nanoscaffold. Daily DAPT release was averaged from the total DAPT released over the period of study. Between Day1 and Day10, DAPT concentrations are between 0.6 μM to 3.2 μM, which are within the therapeutic window of DAPT for guiding stem cell neurogenesis.

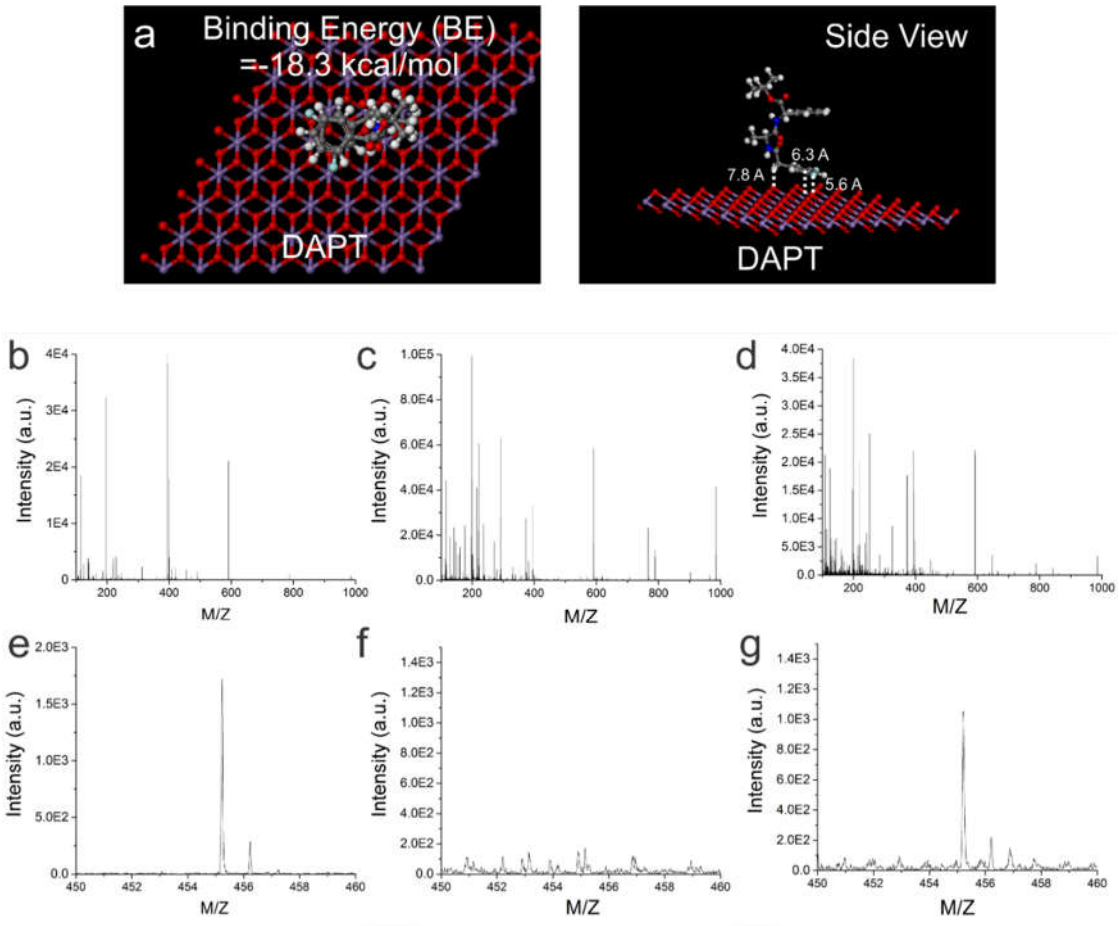

Figure 3-22. Neurogenic drug loading onto MnO_2 laminin hybrid nanoscaffolds. a, Computational modeling of drug-scaffold interactions based on highly precise DFT calculation. Computational modeling result describing the binding between 2D MnO_2 nanosheets and DAPT, a Notch inhibitor that known to selectively guide neural stem cell towards neuronal lineages. The binding energy was calculated by the equation of E(BE)=E(A+B)-E(A)-E(B), and was summarized in the unit of kCal/mol. Among the modeling result, a is the top view of optimized geometry; Image on the right is a side view of optimized geometry. The vertical distances of selected atoms to the surface of MnO_2 nanosheet were labeled in b. Modeling of MnO_2 binding with neurogenic or anti-

inflammatory drugs other than DAPT (e.g., retinoic acid and BET inhibitors) have been conducted, but results were not shown here. b-g, MALDI-TOF analysis of Notch inhibitor absorbed on different substrates. b, e, 1.0 mg/ml DMSO solution of DAPT deposited on ITO substrate. c, f, Polymer substrate (porous cellulose) absorbed with DAPT followed by washing. d, g, DAPT-nanoscaffold. DAPT was first loaded on individual MnO_2 nanosheets in PBS solution, then assembled into DAPT-nanoscaffold using vacuum filtration method.

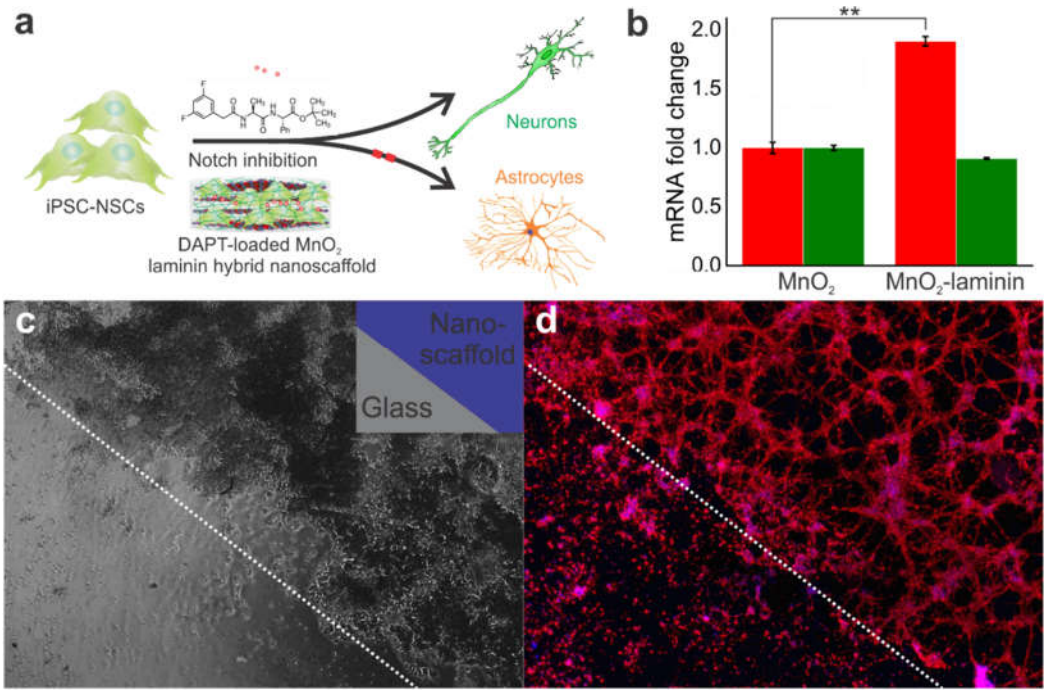

Figure 3-23. Enhanced neuronal differentiation of iPSC-NSCs from DAPT-loaded MnO_2 laminin hybrid nanoscaffold (short-term study). Immunostaining was performed 7-day post transplantation. a, Schematic diagram of guided and enhanced neurogenesis of iPSC-NSCs by Notch inhibition. b, Summarized gene (TuJ1 and GFAP) analysis and comparison of neurite outgrowth of neurons differentiated from iPSC-NSCs on MnO_2 hybrid nanoscaffold and MnO_2 hybrid. c, Phase image showing the boundary between DAPT-loaded MnO_2 laminin hybrid nanoscaffold (darker regions) and glasses (lighter regions), and their corresponding neuronal and nuclei marker staining (d). All the cells are cultured under identical media conditions in the same well of 24-well plate. This image directly proves the enhanced cellular adhesion and differentiation of iPSC-NSCs on DAPT-MnO_2 laminin hybrid nanoscaffold. e, Control group of iPSC-NSCs differentiated on MnO_2 hybrid nanoscaffold. f, A zoomed-in image of iPSC-NSCs differentiated on DAPT-loaded MnO_2-laminin hybrid nanoscaffolds. Scale bars: c-d, 250 μm; Data in b represents mean$\pm$s.d., n=3, **$P<0.01$ by unpaired student t-test.

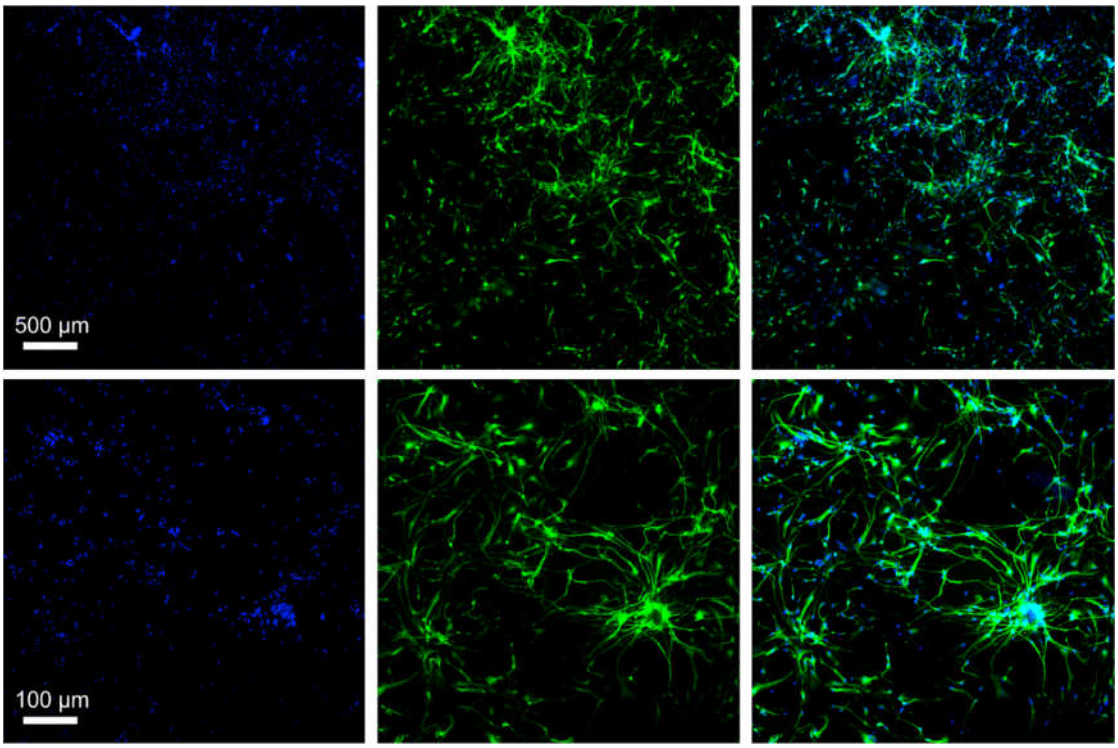

Figure 3-24. Long-term neuronal differentiation of iPSC-NSCs from DAPT-loaded MnO_2 laminin hybrid nanoscaffold. Immunostaining was performed 1 month (30 days) post transplantation. Blue indicates nuclei staining and green indicates mature neuronal marker MAP2. These results clearly support that large populations of differentiated cells and their neuronal fates remained after long-term (1-month) differentiation process on DAPT-loaded MnO_2 laminin hybrid nanoscaffold.

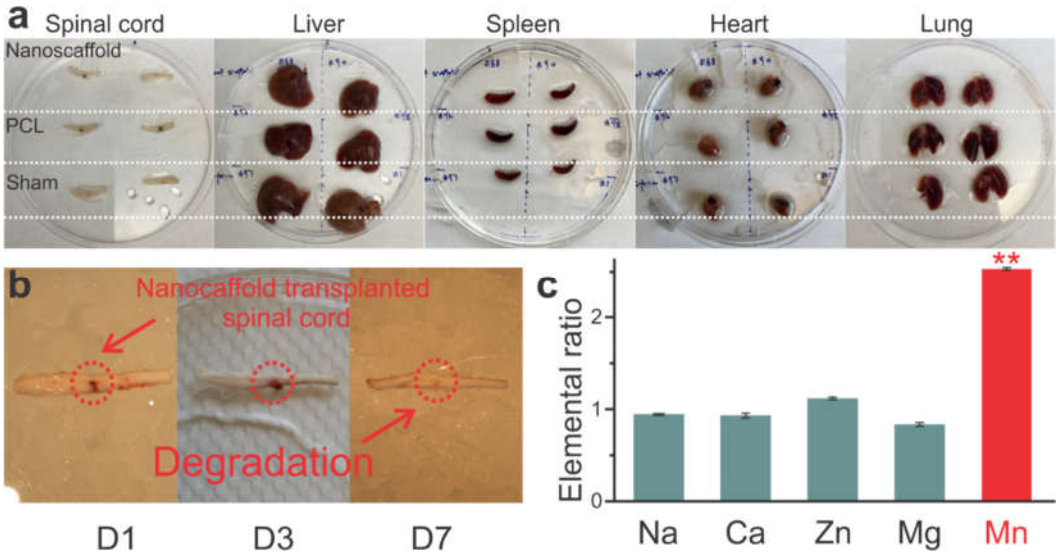

Figure 3-25. In vivo Biocompatibility and biodegradability of MnO_2 laminin hybrid nanoscaffolds. a, Photograph comparison on shapes of organs between mice transplanted with iPSC-NSC seeded MnO_2 nanoscaffold (top row), iPSC-NSC seeded polymer scaffold (middle row) and sham with surgifoam (no cells, bottom row). These images demonstrate that no obvious change in organ size, especially in liver and spleen, and minimal in vivo toxicity from the transplantation of nanoscaffold and polymer scaffold. b, Photographs of nanoscaffold transplanted mouse spinal cord at Day 1, Day 3, and Day 5 from left to right, respectively. These images suggest the time-dependent degradation of nanoscaffold (indicated by the disappearance of black color from nanoscaffolds), as well as a gradual healing of the wound on the hemisected spinal cord. c, Elemental analysis on urine samples of mouse 3 days after transplantation of nanoscaffold and polymer scaffolds using ICP-MS. Among the 6 common elements (Ca, Zn, Na, Fe, Mn, Mg) detected in the urine, only Mn level was significantly increased in nanoscaffold compared polymer control in the elemental analysis, which we attribute to the degradation of MnO_2 transplanted in the spinal cord region. Data are mean$\pm$s.d., n=3, *$P<0.05$ by one-way ANOVA with Tukey post-hoc test.

Figure 3-26. Representative photographs from SCI mice without any treatment (a) or transplanted with neural stem cell transplantation using polymer scaffold (b) or nanoscaffold (c) 3-week post injury.

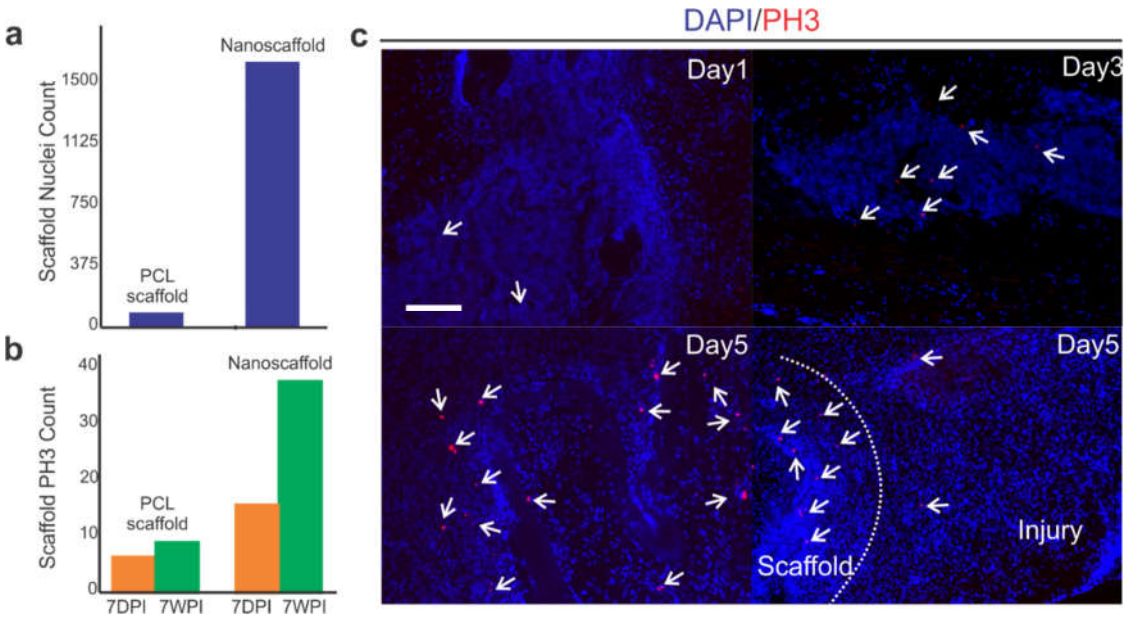

Figure 3-27. Cell proliferation in the MnO_2 laminin hybrid nanoscaffolds nanoscaffolds after transplanted into Notch1CR2 GFP mice. a-b, Graphs showing counts of transplanted cells and PH3 (proliferation marker) counts surrounding the nanoscaffold and PCL scaffold. The transplanted cells were distinguished from host cells by using GFP fluorescence-based approach described in Figure 3-18 b-c. A dramatic enhancement of cellular adhesion, survival, and proliferation can be found in our nanoscaffold-treated group. c, Day dependent (Day 1, Day 3 and Day5) proliferation marker staining for spinal cord injury after transplanted with iPSC-NSC seeded MnO_2 nanoscaffold. With increased days of transplantation, increased proliferation marker (PH3) was found surrounding the scaffold, while there is a minimum amount of PH3 markers found beyond the regions of transplanted scaffold and cells in the injury sites, indicating the growth factor loaded nanoscaffold can promote the survival and proliferation of cells surrounding the scaffold. Scale bars: 100 μm.

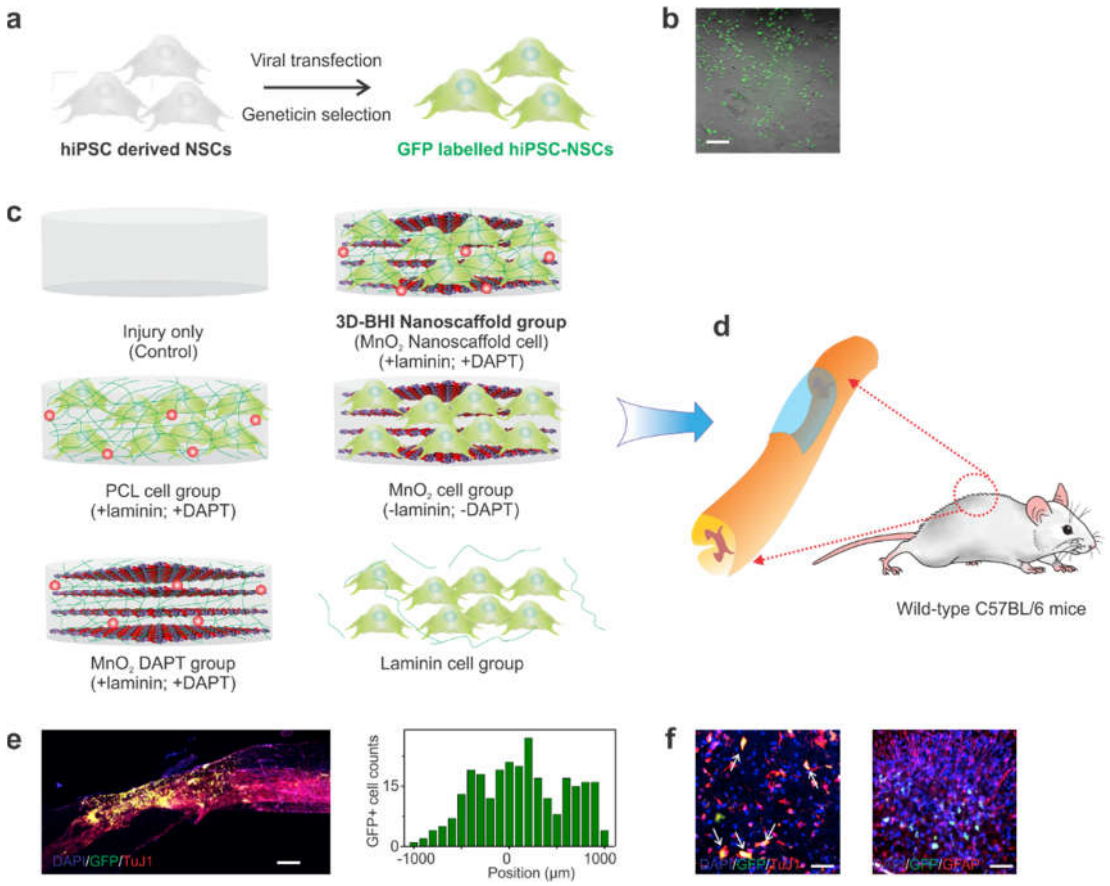

Figure 3-28. Animal groups for studying the effects of 3D-BHI nanoscaffold on the enhanced transplantation of iPSC-NSCs into the SCI sites. All tissue analysis was performed 7-week post transplantation. a, Schematic diagram illustrating the viral vector based transduction and anti-biotics (geneticin) based selection of GFP labelled iPSC-NSCs (GFP-iPSC-NSCs). By utilizing GFP-iPSC-NSCs, transplanted cells can be reliably tracked, and their in vivo differentiation can be accurately studied. b, Merged fluorescent and phase images of transfected iPSC-NSCs. Through the viral transduction and geneticin selection, a high percentage of the iPSC-NSCs (91%, 318 out of 349) showed bright GFP signals. c-d, Schematics of 6 experimental groups (c) and their transplantation into wild-type C57BL/6 mice (d). Indications of symbols in the schematics can be found in Figure 1 of the manuscript. e, Zoom-out images showing the distributions of GFP-iPSC-NSCs

transplanted by nanoscaffold. The graph on the right is a summary of the distance-dependent distribution of cells from the transplantation site. By utilizing GFP labeled cells, we can not only clearly track the transplanted cells that are diffuse into host spinal cord but also confirm the majority of transplanted cells showed early neuronal markers by identifying the GFP+TuJ1+ cells. f, Zoom-in images with DAPI-GFP-TuJ1 (image on the left) and DAPI-GFP-GFAP (image on the right) dual labeling. As shown in the pictures obtained from the nanoscaffold group, we can observe most (6 out of 7) GFP+ cells were TuJ1+, while only minor (1 out of 9 GFP+ cells were GFAP positive, indicating a successful induction of neurogenesis in vivo. More detailed co-labeling experiments and the comparison between nanoscaffold group to other groups will be shown in other additional Figures. Scale bars: b, 100 μm; e, 250 μm; f, 50 μm.

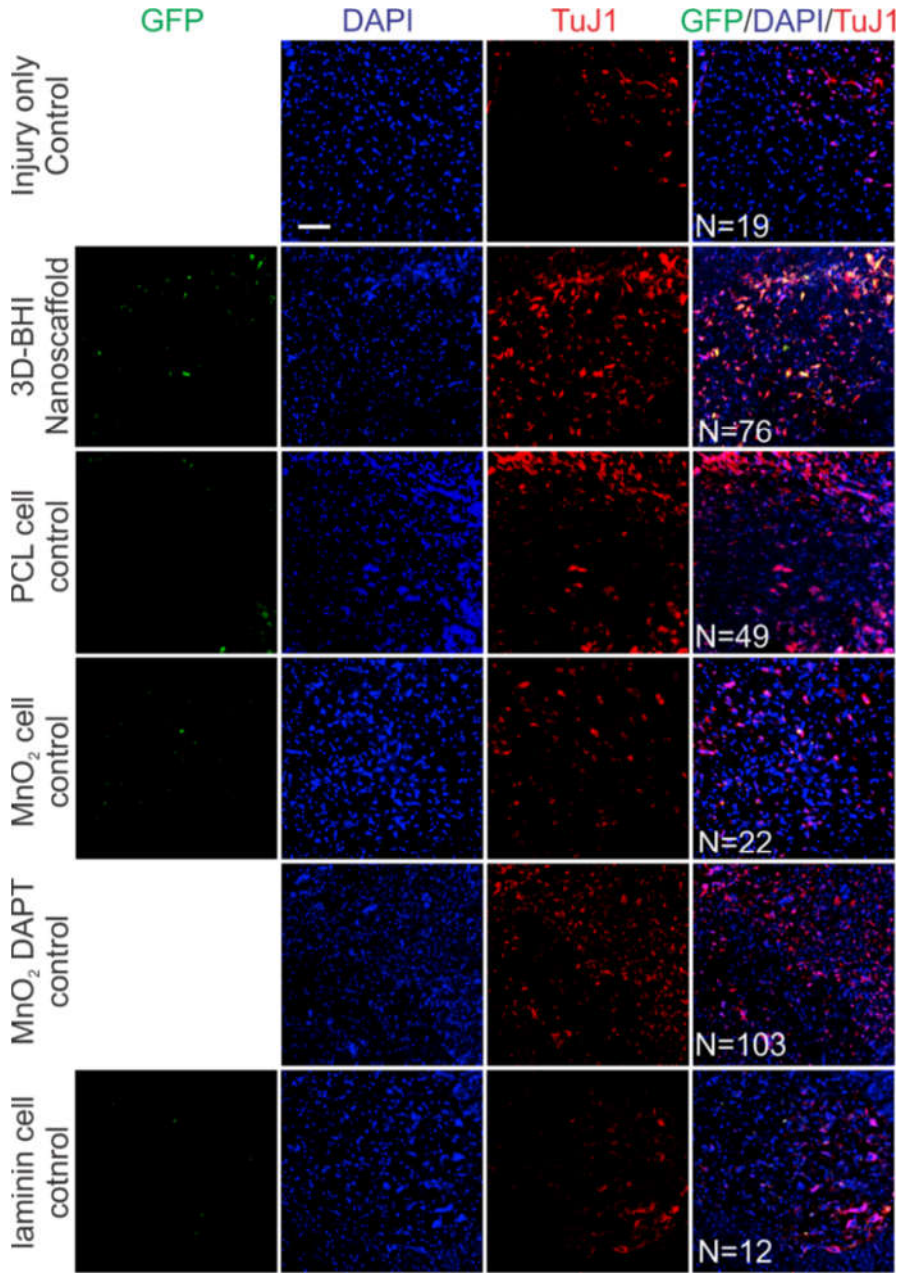

Figure 3-29. 3D-BHI nanoscaffold enhances neuronal differentiation. All tissue analysis was performed 7-week post transplantation and all tissue sections were from the center of spinal cord injury and nearby the transplantation sites. Immunohistological staining was performed to determine the effects on eNSC neurogenesis from different experimental treatments. A high number (N) of eNSC derived neuronal cells was observed in nanoscaffold group and MnO_2 DAPT group. Scale bar: 100 μm.

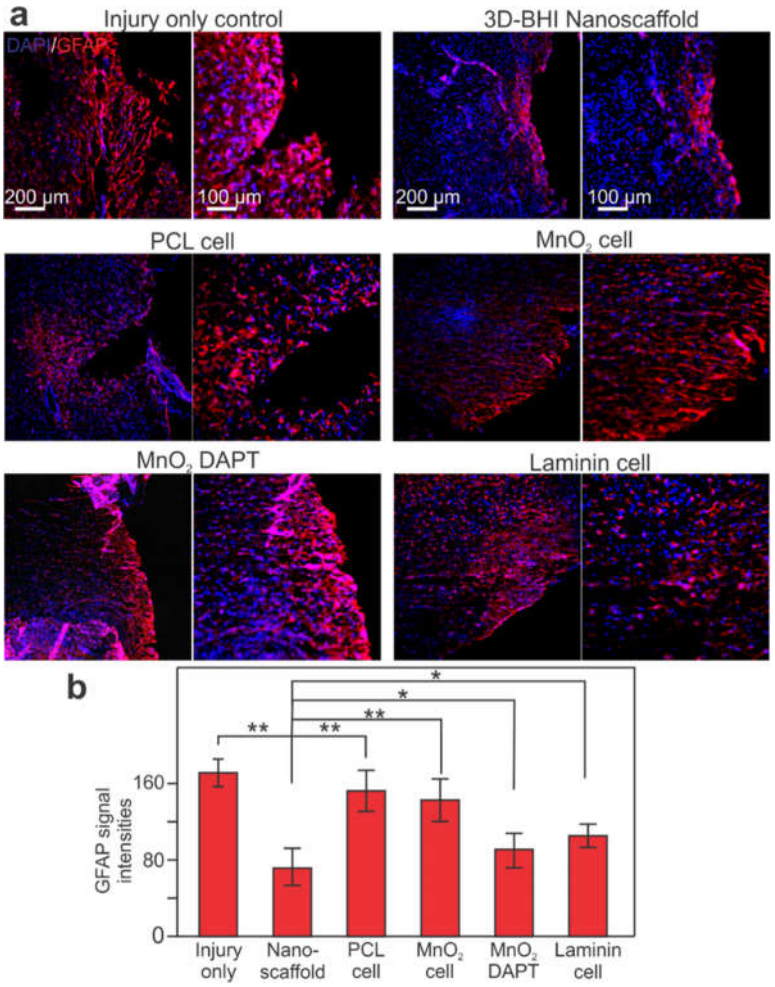

Figure 3-30. MnO_2 nanoscaffold suppresses astroglial activity. Immunohistological staining analysis on the effects of astroglial cell activities at the injured sites was performed 1-week post injury. All tissue sections were from the center of spinal cord injury and nearby the transplantation sites. a, Representative images from different groups of scaffold transplantation. Blue represents nucleus staining (DAPI); red indicates astroglial cells (GFAP). b, Quantification of GFAP signal intensities (area=132 μm^2, n=3). Exposure time was kept constant at 1 second for all sections from different experimental groups to obtain GFAP signal intensities. Automatic intensity detection modules in the ND2 Nikon software were used for measuring the signals. Data are mean$\pm$s.d. n=3, *P<0.05, **P<0.01 by one-way ANOVA with Tukey post-hoc test.

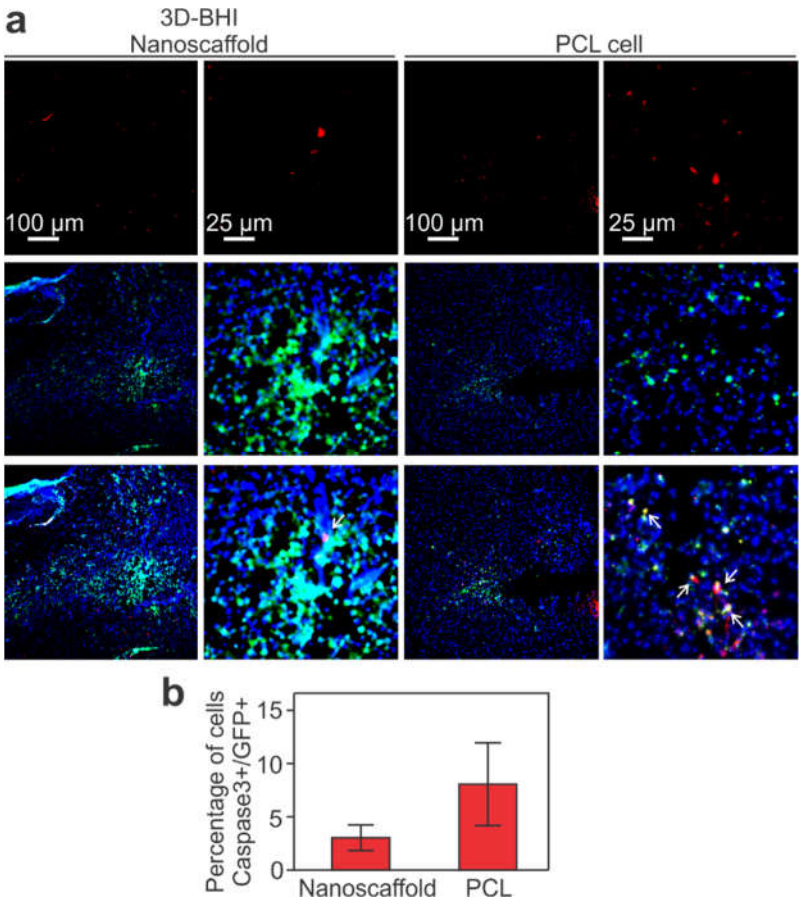

Figure 3-31. Enhanced cell survival of transplanted GFP-iPSC-NSCs on 3D-BHI nanoscaffolds compared to cells transplanted by PCL scaffolds. Tissue analysis was performed 7-day post injury. All tissue sections were from the center of spinal cord injury and nearby the transplantation sites. a, Immunohistological staining images of tissue sections from nanoscaffold group and PCL-cell group. Blue indicates cell nucleus (DAPI), green indicates GFP labeled iPSC-NSCs, and red stains cleaved Caspase 3. From the images, higher GFP+ cells and lower percentages of dead cells (Caspase 3 positive cells can be observed in our nanoscaffold group. b, Quantifications of Caspase3+/GFP+ cell percentages existent in GFP+ cells. Data represents mean$\pm$s.d., n=3, no significant statistical difference can be detected between the groups (P>0.05) by unpaired student t-test.

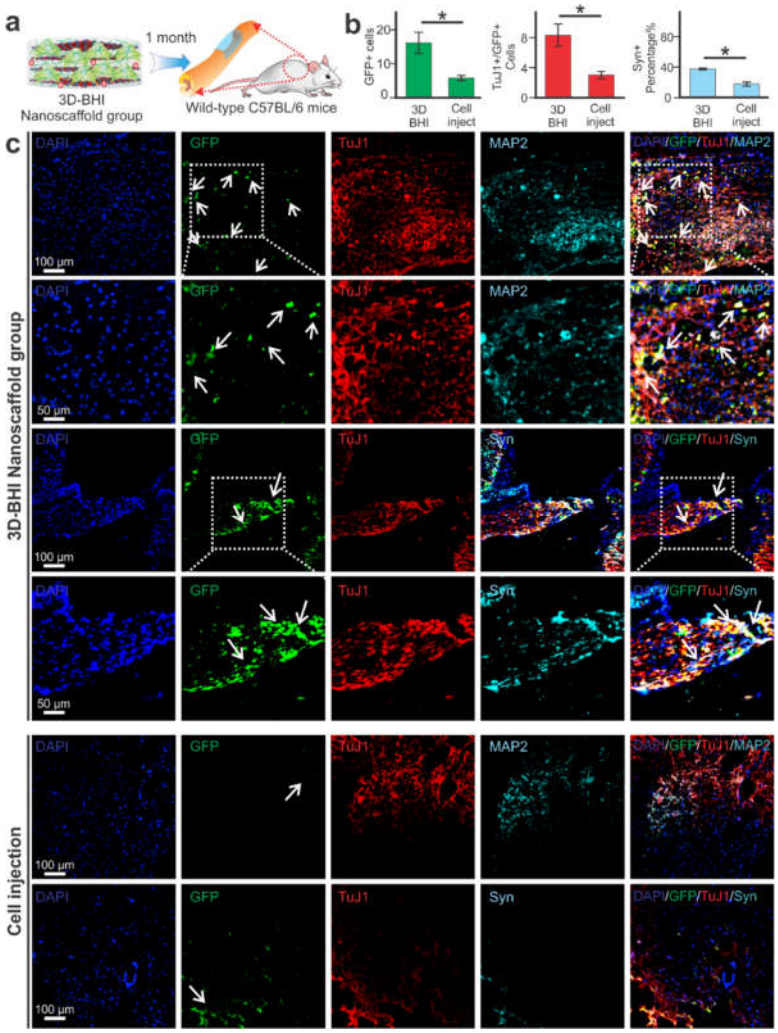

Figure 3-32. Enhanced transplantation and neuronal differentiation of iPSC-NSCs by 3D BHI nanoscaffold 1-month post injury. a, Schematic diagram illustrating the transplantation of iPSC-NSC-GFP into injured spinal cord for one month. b-c, Statistic summary (b) and corresponding immunostaining images (c) from 3D-BHI nanoscaffold group and cell injection group 1-month post-injury. All tissue sections in c were from the center of spinal cord injury and nearby the transplantation sites. GFP, TuJ1 and Syn positive cells were counted in individual sections (674 μm by 674 μm). Data in b are mean±s.d. n=3, *P<0.05 by one-way ANOVA with Tukey post-hoc test.

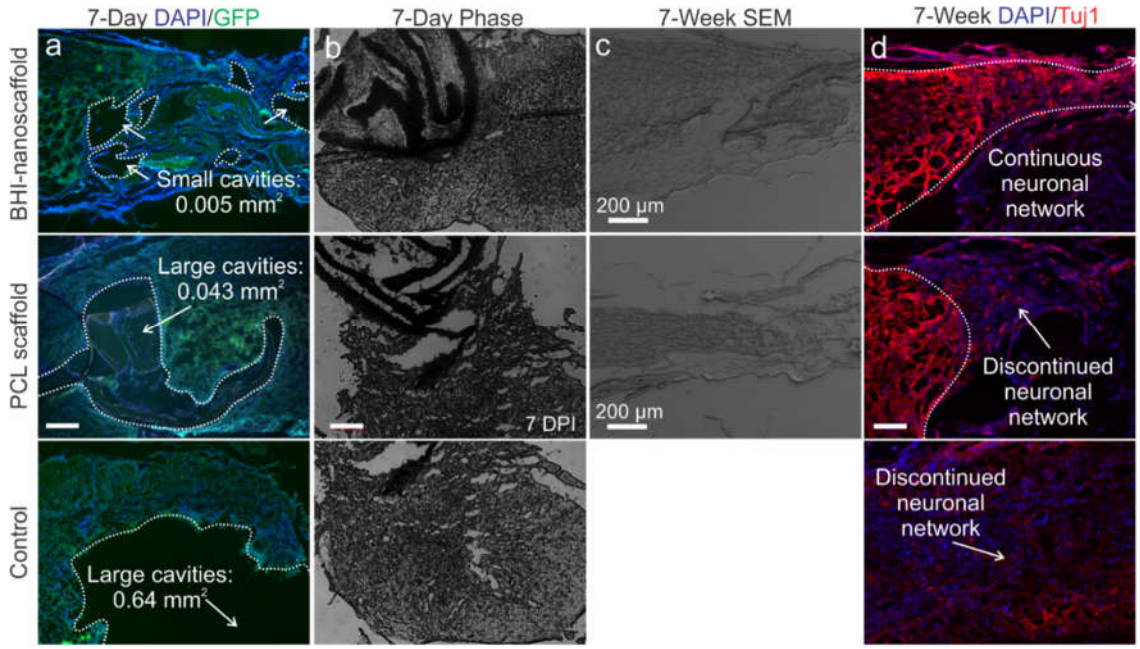

Figure 3-33. Supporting images describing beneficial effects on injured spinal cord from the 3D-BHI nanoscaffolds treated condition compared to the control conditions. a-d, Fluorescence imaging (in row a), phase imaging (in row b), electron microscopic imaging (in row c) and neuronal marker staining in the SCI sites 7 WPI, 7 DPI, 7 WPI and 7WPI, respectively. Different imaging techniques at different time points consistently reveal significantly higher cavities formation and less continuous neuronal networks in the PCL scaffold treated mice or the control groups compared to our nanoscaffold treated groups. Scale bars: a, b, d: 50 µm.

3.1.6 Additional Tables

Molecules	Functional group	Binding Energy (kcal/mol)	Intra-molecular Distance (Å)
CH_3Cl	-Cl	-3.55	3.16
H_2O	—	-4.0	3.45
CH_3F	-F	-5.10	2.96
CH_3OH	-OH	-6.43	2.54
CH_3COOH	-COOH	−7. 26	3. 01
CH_3NH_2	$-NH_2$	-10.23	2.98
Ph-CH_3	-Ph	−11. 66	3. 08
DAPT	Drug	-18.43	6.3

Table 1. Summary of binding energies (BE) between molecules with assigned functional groups and the 2D MnO_2 nanosheet as computed using DFT calculations. Red fonts indicate the strongest absorption on MnO_2 nanosheets.

Targets (species)	Forward Primer (5' to 3')	Reverse Primer (5' to 3')
GAPDH (Human)	CCGCATCTTCTTTTGCGTCG	GCCCAATACGACCAAATCCGT
TuJ1 (Human)	GGTGTCCGAGTACCAGCAGT	TTCGTACATCTCGCCCTCTT
GFAP (Human)	AGGAAGATTGAGTCGCTGGA	AACCTCCTCCTCGTGGATCT
GAP43 (Human)	AACCTGAGGCTGACCAAGAA	GGGACTTCAGAGTGGAGCTG
FAK (Human)	TGGTGCAATGGAGCGAGTATT	CAGTGAACCTCCTCTGACCG

Table 2. Summary of the primers used for quantitative PCR. All primers were obtained from the PrimerBank database.

3.2 A General Method for Assembling Cells into Macroscopic Scaffold-free Tissues

3.2.1 Introduction

An ultimate goal of biomedical research is to understand and cure human diseases. To this end, creating bioartificial tissues with controlled architecture that can model and replace diseased tissues provides a promising solution[506-520]. So far bioartificial tissues have been typically generated with bioscaffolds (e.g. Matrigel, macroporous scaffolds, hydrogel, 3D printed structures), which provide mechanical support to guide cell assemblies, providing biomimetic physical cues and can be used for drug delivery. However, the incorporation of scaffolds composed of exogenous materials unavoidably introduces biomaterial complexities which include immunogenicity, mechanical mismatches, an improper degradation rate and toxic degradation products after transplanted into the injured sites[521,522]. Assembling cells with biomaterials may also fail to represent natural cellular interactions in human tissues. One such example is the laminin based neural stem cell-astroglial co-culture to demonstrate astroglial-based regulation over stem cell neurogenesis, which do not mimic the process well in diseased and laminin-deficient microenvironments (e.g. spinal cord injuries). These complexities in tissue modeling and repair can be further compounded by the heterogenous scaffold dynamics and microenvironment during disease progression, leading to their impeded clinical applications. To this end, scaffold-free tissue engineering approaches have provided promising solutions (e.g. cell sheet engineering, cell spheroids-based 3D bioprinting, cell-laden microfibers). However, in the absence of scaffold support, these approaches frequently suffer from limited spatial controls over tissue structures, inadequate structural integrity for surgical implantation, limited choices of cell types, which significantly hurdle their clinical applications[229,523,524]. Also, these

methods can require a long (from a few days to a few weeks) fabrication processes, which could fail to provide timely treatment for acute diseases and increase the risks of infection at the injured sites. Considering the complicated disease progression in severe tissue injuries and diseases, and the critical role of tissue synthesis in next-generation precision and personalized regenerative medicine, an innovative method for creating bioartificial tissues on-demand without involving biomaterial complexities is in an urgent need.

Here we demonstrate the development of an ADcell (assembling and disassembling cell constructs) technology to timely create robust macroscopic tissues with precisely controlled cellular architectures on demand. This technology is achieved by inventing a chemically formulated and nanoengineered sacrificial membrane and combining it with a

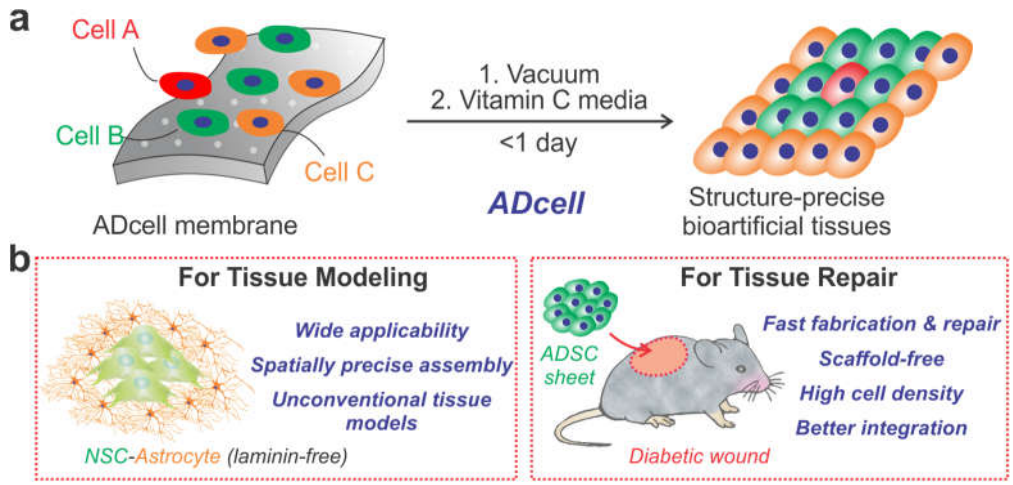

Figure 3-34. Schematic diagram illustrating principles of ADcell and its advantages for biomedical applications. a, Cells of different type were sequentially assembled into a spatially precise construct supported by a sacrificial and nanoporous ADcell membrane. b, Advantages of ADcell-generated tissues or cell assemblies for tissue modeling and tissue repair.

vacuum induced cell assembly in a single platform (Figure 3-34). Vacuum induced cell

assembly enables timely and precisely guided cell assembly from unlimited cell types and reinforces it into robust tissue-like structures; the sacrificial nanoporous membrane provides efficient vacuum flow, supports cellular adhesion and tissue genesis, and can be efficiently cleaved by cellular protective bioreductants. More specifically, under the external forces imposed by controlled vacuum field, the cell-assembly process is significantly faster than conventional approaches and the external force simultaneously reinforces the tissue-like structures with improved structural integrity and cell densities for injury treatment. Additionally, the initiation of vacuum-guided cell assembly process does not require specific cell-cell interactions or cell-ECM binding. Therefore, we can create unconventional bioartificial tissues with unlimited cell types and precisely controlled structures to represent better complex tissue models (e.g., laminin-free neural stem cell-astrocyte co-cultures) that have not yet been possible in previous tissue-engineering methods. By further cleaving the nanoporous membrane that supports the as-formed tissue, scaffold-free bioartificial tissue constructs can be then harvested for on-demand tissue transplantation and timely tissue repair. The implantation of scaffold-free ADSC sheets made by ADcell showed higher integration and successfully accelerated the wound healing of a diabetic wound in a murine model. Given the challenges of fabricating robust bioartificial tissues with well-defined structures on demand, and the wide clinical applications of scaffold-free bioartificial tissues, our novel ADcell method represents a unique and promising solution for understanding fundamental biology and to advance next-generation regenerative medicine.

3.2.2 Methods

Evaluation of cell biocompatibilities under different redox conditions: Cells were cultured in 96 well plates using their growth media until reaching 100% confluency, which mimics the cell densities of tissues formed on Adcell membranes. Then into the growth media, different amounts of varying reducing reagents (GSH, ascorbic acid and oxalic acid) were added to make final solution at different concentrations (0, 1 mg/ml, 2 mg/ml and 10 mg/ml). After incubating for 48 hours, cell media was changed and presto blue reagents (Thermo Fisher) was added based on protocols provided by vendor. Absorbance at 570 nm was used for quantifying the cell viabilities. All cell lines tested were repeated for 3-4 times to obtain statistical information of the cell viabilities. Cell viabilities after different bio reductant exposure were normalized to control (growth media only).

Room-temperature based synthesis of MnO_2 nanowires: 1.65 gram of TMAOH was first mixed and dissolved in 20 ml 3.0% (weight percent) cold (4 Celsius) H_2O_2. 0.594 gram of $MnCl_2$-$4H_2O$ was dissolved in 10 ml ultrapure water to make a 0.30 M solution. Under room temperature and vigorous stirring (1200 rpm), $MnCl_2$ solution was quickly added into the mixed H_2O_2 TMAOH solution. Clear solution turned dark immediately and the reaction was run for 1_2 hours to produce MnO_2 nanowires precursors. To purify MnO_2 nanowire precursors, the solution was centrifuged down for 10 minutes at 8000 rpm, and the pellet was washed with water and 190 proof ethanol for 3 times, respectively. The final product was dried overnight in a 65 Celsius oven. Afterward, 50 mg of the dried dark brown colored pellet was resuspended in 10 ml water and bath sonicated (Branson Sonifier, 6400) for 10 hours to resuspend the nanowires. The sonicated solution was left still for 1 hour, and then the large aggregates in the bottom of the solution were removed by selectively collecting the supernatants. The concentration of nanowires was measured by evaporating 1.0 ml of

solution in a 110 Celsius oven overnight and measure the mass of dried products. MnO_2 nanowires were dried and characterized by TEM, HRTEM and potential and XRD. MnO_2 nanowires in aqueous solution at a concentration of 50 ug/ml were characterized with zeta sizer and potential.

To rationalize the use of nanowires (1D nanostructures) over other nanostructures for constructing a vacuum-efficient nanoporous membrane, we also synthesized 2D (MnO_2 nanosheets) and 3D (MnO_2 microspheres) nanostructures and filtrated them onto a porous membrane under identical conditions and same concentrations. Then we measured the filtration speed on these structures by using 10.0 ml waster solution based on the following equation:

$$\text{Speed of filtration} = \text{Volume of water filtered}/(\text{Time of filtration} \cdot \text{Area of filtration})$$

To synthesize metal ion doped MnO_2 nanowires, different amount of monovalent (Li), divalent (Zn) and trivalent (Fe) chloride salts were added into 0.3 M $MnCl_2$ solution to form 3 different (3 mM, 15 mM and 30 mM) concentrations of dopants. Other procedures were kept identical to produce nine doped nanowires. These nanowires were characterized by TEM and XRD. To compare the degradability of different nanowires, we used 1.0 mg/ml ascorbic acid as a standard solution. To form a substrate from the nanowires from the solution, we vacuum filtrated the nanowires (1.0 ml, 200 ugs/ml) into identical shapes. The degradation time was recorded based on the complete disappearance of the black color. Based on the degradation, iron-doped nanowires demonstrate the fastest cleavage. Therefore, iron-doped MnO_2 nanowires were used throughout the project unless mentioned otherwise.

To functionalize nanowires with chitosan, a chitosan solution of 1mg/ml concentration was used. Into 100 ml chitosan solution under fast stirring, 100 ml MnO_2 nanowire aqueous solution with a concentration of 100 ug/ml was added drop by drop using an automatic syringe pump (0.3 ml/min). The electrostatic-based assembly was run for overnight; then the functionalized nanowires were centrifuged at 11000 rpm for 30 minutes then the pellets were resuspended in water. This purification was repeated for five times to remove free chitosan. Chitosan functionalized MnO_2 nanowires were then suspended in water at a concentration of 50 ug/ml and characterized by Zeta potential.

Fabrication of sacrificial nanoporous Adcell membrane by vacuum filtration: To form the nanoporous Adcell membrane, a vacuum pump (1*10-1 torr) was connected to a vacuum filtration set up. Onto the vacuum set-up, a nanoporous cellulose membrane (average pore size=100 nm) was attached and wetted by water. After placing a PDMS mold with a circular hole (diameter=1.0 cm), 200 ul solution of chitosan functionalized MnO_2 nanowires (1.0 mg/ml) was poured into the PDMS hole. Under the vacuum flow, the Adcell membrane with a circular shape can be formed in 5-10 minutes. To detach the Adcell membrane from the supporting cellulose substrate, we transferred them into 50 ml acetone, incubated for 12 hours, and then replaced action with 50 ml methanol. The white colored supporting membrane disappears and only dark colored Adcell membrane remains. By washing with methanol one more time, we can obtain the Adcell membrane free-of polymeric substrates. We also confirmed the removal of Adcell membrane under our previously tested biocompatible redox conditions (1.0 mg/ml ascorbic acid) by observing the fast disappearance of the membrane.

Vacuum guided cell assembly onto Adcell membrane: All steps that involve cells were carried out in certified biosafety cabinets. Onto the Adcell membrane, 20 μl of cell media with cell density at 20 million/ml was placed under no-vacuum conditions. Then the vacuum was turned on to initiate the cell filtration. This process was kept for 2-5 minutes until the liquid flow inside droplet was almost completely stopped. Cell media was constantly added on top of the cells when cells constructs were about to dry. After the vacuum induced-assembly was completed, Adcell membrane with cells was washed in PBS to remove any weakly attached cells and then cultured in the cell growth media. This process can apply to all cell types listed in Table 1. ADMSCs that were assembled onto Adcell membrane in a tightly packed structure were characterized using cell SEM.

Stem cell differentiation on Adcell membrane: To demonstrate that cells assembled on Adcell membrane can differentiate into functional tissues, we utilized iPSC derived neural stem cells. To induce the stem cell differentiation, we used cyclodextrin functionalized Adcell membrane to locally deliver retinoic acid, a well-known drug for guiding neuronal differentiation of neural stem cells. To synthesize cyclodextrin functionalized Adcell membrane, we centrifuged down 20 mg MnO_2 nanowires and resuspended them in 40 ml ethanolic APTES solution (APTES concentration: 1 mg/ml). After vigorously shaking overnight, APTES functionalized MnO_2 nanowires were washed by 200 proof ethanol three times and resuspended in 10 ml DMF. 20 mg of OTs functionalized cyclodextrin that was prepared based on previous literature was then added into the DMF solution followed by sonication and vigorous stir for overnight. The reaction product between APTES functionalized nanowires and OTs functionalized beta-cyclodextrin was then washed with DMF for one time, ethanol 3 times and water for 3 times. To load retinoic acid into the

cyclodextrin, cyclodextrin functionalized MnO_2 nanowires were suspended in 5 ml water at a concentration of 1.0 mg/ml. Then 100 ul of 100 mM retinoic acid solution was added and incubated overnight. Free retinoic acid was removed by centrifuge and the RA loaded nanowires were washed by water for one time. The nanowires were then assembled into Adcell membrane using the same protocol previously mentioned. After coating the RA loaded Adcell membrane with laminin (concentration: 20 ug/ml) for 4 hours, iPSC-NSCs were seeded and cultured in differentiation media for seven days. Laminin coated glass was used as a negative control. Immunostaining and qRT-PCR analysis on early neuronal markers (TuJ1) were performed once the differentiation process is finished. Even though direct addition of retinoic acid has also been shown to enhance neurogenesis, here we mainly demonstrate the functionalization and local delivery of soluble cues from Adcell membrane to control cell behaviors in situ.

Formation of scaffold-free cell assemblies and tissues: After the cells were assembled onto the Adcell membrane and maintained in growth media overnight, we then initiate the membrane removal process to obtain scaffold-free tissues. Briefly, Adcell membrane with cells assembled and attached was transferred into a 100 ml sterilized cell culture beaker together with 5 ml cell growth media. Then into the beaker, 50 ml growth media supplemented with 1.0 mg/ml ascorbic acid was added slowly. After incubating for 1 hour, the media was changed with fresh ascorbic acid supplemented media. Then media change was performed every 3 hours until the dark-colored Adcell membrane was completely disappeared which is usually accompanied by the formation of the semi-transparent tissue-like cell sheet structure. To test the viability of cells after forming scaffold-free tissue, we utilized hNPC as a model cell line, which is relatively fragile and sensitive to

environmental toxins. And we used commercialized live cell staining reagents (calcein-AM, thermos fisher) to identify cells alive. During the membrane removal process, depending on the robustness of cell-cell interactions, some tissue (e.g. monocytes) can break into smaller pieces. However, macroscopic scaffold-free tissues that can be facilely manipulated by surgical tools were successfully harvested for all cell lines (Table 1) tested. Detached scaffold-free hNPC tissues were characterized by cell SEM. Scaffold-free hNPC, ADSC, iPSC-NSC, THP-1 monocyte tissues were also stained and characterized by an optical and fluorescent microscope (Nikon Ti series).

Patterning single cell type tissues using the Adcell method: Shapes of cell assemblies was directly controlled by vacuum filed guided PDMS mask with pre-defined holes. To fabricate the PDMS masks, a milling machine was used to drill reversed pillar pattern on polyacrylamide substrates (dimensions given below). Into the designed and fabricated polyacrylamide molds, PDMS pre-mixed with sylgard (Dow Corning, 10:1 ratio) and de-bubbled under vacuum was poured in until reached half of the heights of polyacrylamide features. After curing at 75 C for 2 hours, PDMS membrane was carefully peeled off from the mold and hole patterns can be obtained. To guide the shape of the cell assembly, the PDMS membrane was attached to the porous Adcell membrane or supporting membrane, then was tightly adhered by finger pressing. Afterward, cell suspensions at a density of 20 million/ml were then added into the hole patterns. By turning on the vacuum, liquid flow follows the shape of the PDMS membrane, thereby forming the cell patterns. The vacuum process usually takes 2-10 minutes before the media flow was almost completely stopped. PBS was used to wash out unbound cells, and the membrane was then detached. Cells patterned on Adcell membrane can further form scaffold-free tissue constructs by cleaving

the membrane using protocols previously described. As tissue shapes are usually deformed in scaffold-free forms, most of the fluorescent images of patterned tissues were obtained before their detachment.

Forming tissues with multi-cellular patterns using Adcell: To form multi-cellular patterns using Adcell method, a "stitching" strategy by using the previously deposited cell as masks were used. By first establishing a design for multicellular distributions, a series of PDMS masks were created. For example, a circular hole pattern with a diameter of 3 mm was first used to generate the cell A (NSC-GFP) "core" pattern (100 ul of cell suspension), then a second mask with hole diameter of 5 mm was placed and aligned on top of the NSC core. By adding the cell B (ADMSC, 100 ul) into the hole and then turn on the vacuum, Cell B spontaneously filled in the empty spaces outside of cell A. After the media almost stopped filtration, free-floating cells in the remaining media were removed and the assembled cells were washed with PBS and cultured in rNSC media supplemented with 10% FBS. Briefly, two cell hybrid microarray was formed from i) microarrays of hole pattern with diameters of 75 um (U87-ERFP filling, red); ii) a second hole pattern with a diameter of 3 mm (U87-EGFP filling, green). The mosaic pattern is formed by ADMSCs (red) and NSC-GFP (green) in a 1:1 ratio and using a hole pattern with a diameter of 5 mm. Three cell pattern is formed by i) triangular pattern (U87-ERFP, red); ii) rectangular pattern (HDF, Hoechst stain, blue); iii) combined round and square patterns (for ADMSC filling, pre-stained with dextran rhodamine). 5 cell patterning is formed by i) circular pattern with diameter of 3 mm (ADMSC filling pre-stained with dextran rhodamine); ii) a second circular pattern with diameter of 2 mm (hNPC filling pre-stained with dextran rhodamine); iii) circular pattern with a diameter of 1 mm (iPSC-NSCs-GFP filling); iv) circular patterns that include i) and

ii) with diameters of 5 mm (U87-EGFP); v) a cross pattern with dimensions of 1 cm (HDF filling pre-stained with Hoechst). Seven cell pattern is formed by i) same procedure as five cell pattern; ii)

3.2.3 Results and Discussion

Creating a Sacrificial Nanoporous Membrane

To utilize our Adcell technology for creating advanced bioartificial tissues under vacuum, we designed a sacrificial nanoporous membrane to provide: i) efficient and homogenous vacuum flow for guiding cell assembly; ii) proper pore sizes to support cell adhesion; iii) high biocompatibility; and iv) fast biodegradability. Specifically, ADcell membrane was assembled from ion-doped 1D fast-degradable MnO_2 nanorods (Figure 3-35). These fast-degradable MnO_2 nanorods were synthesized using a facile room-temperature and water-based method, which could introduce defective sites and lead to high erosion rate during redox-based degradation. By further investigating a library of ion doped nanorods using our newly developed method, we identified multivalent ion doping such as iron (III) or zinc (II) could accelerate the cleavage significantly. These optimization processes make our ADcell membrane a unique sacrificial membrane that can be rapidly degraded in a controlled manner under highly biocompatible conditions. While several methods have been developed to fabricate biodegradable nanoporous polymer scaffolds (e.g., electrospinning, porogen embedding), these scaffolds either often form on top of non-porous solid supports, or cannot provide a continuous directional porosity, thereby leading to inefficient vacuum flow. On the other hand, using vacuum filtration, several 1D nanomaterials can form homogeneous layers with controlled directional

nanoporosities[223,255,525-527]. However, these inorganic or carbon-based nanomaterials cannot be cleaved or degraded by biocompatible reagents or under physiological conditions. Recently we demonstrated an unprecedented fast-biodegradability of unique MnO_2 (<10 minutes) based inorganic scaffolds by cells alone or through the addition of naturally existent bioreductants such as ascorbic acid, but these scaffolds are non-porous[42,44,48-51,53,169,447,452,528-530]. Herein, by vacuum filtrating aqueous suspensions of chemically formulated, metal ion doped 1D MnO_2 nanorods with fast bio-degradability, we successfully created our sacrificial nanoporous membrane with pore sizes from 50-200 nm, efficient vacuum filtration, and fast biodegradability (<10 minutes) under the incubation with oxalates or vitamin C, both of which have been tested for their biocompatibility with two cells of our primary interest (adipose-derived stem cells and neural stem cells).

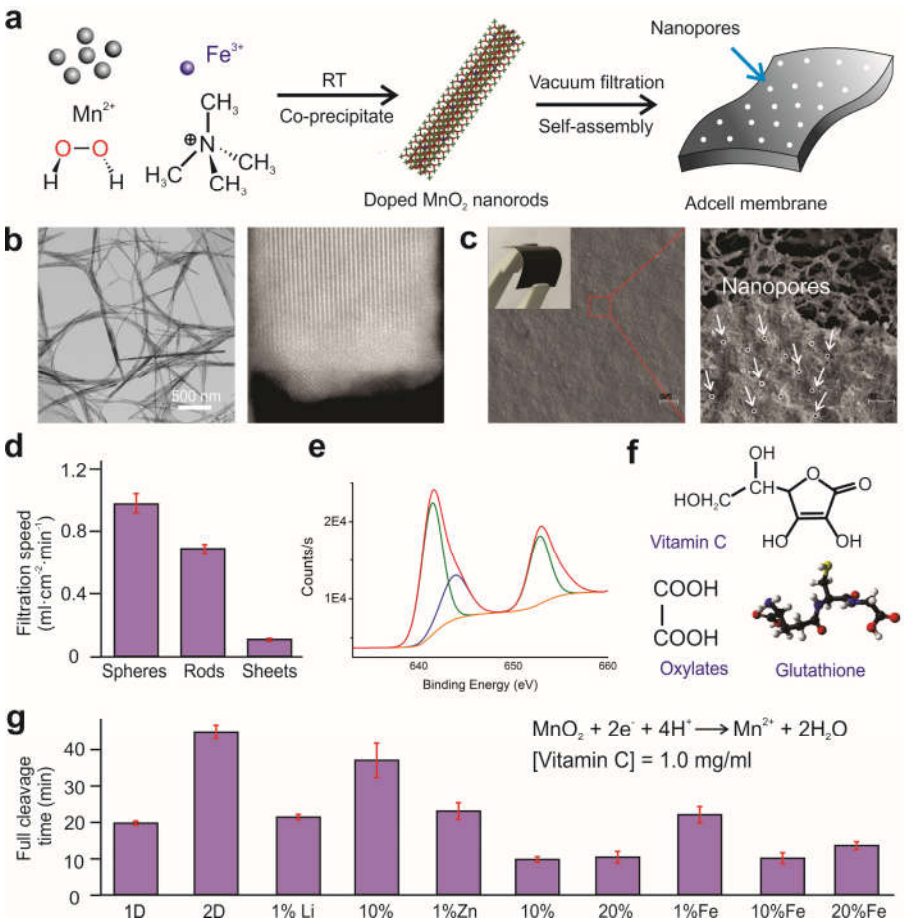

Figure 3-35. Developing a sacrificial nanoporous ADcell membrane. a-c, Schematic diagram (a) illustrating room temperature and water based synthesis of metal ion doped MnO2 nanorods (TEM images shown in b) and their assembly into large scale homogenous and nanoporous ADcell membrane using a filtration method. d, Comparison of filtration speeds for membranes assembled from different structures of MnO2 (Spheres: 0D; Rods: 1D; Sheets: 2D). e, XPS of synthesized nanorods. f-g, Fast biodegradability of ADcell membrane assembled from differentially doped MnO2 nanorods under biocompatible media conditions.

Generating a Library of Bioartificial Tissues

By applying controlled vacuum field on our ADcell membrane, we then demonstrate the wide applicability of our ADcell technology to generate varying bioartificial tissues, from single cell type to multiple cell type, from embryonic stem cells to different germ layers and from cell spheroid level to macroscopic tissue level with pre-defined shapes (Figure 3-36). Both scaffold-based (e.g., decellularized scaffolds, Matrigel, macroporous polymers) or scaffold-free approaches (e.g. cell spheroids, cell sheet engineering) have fabricated many bioartificial tissues assembled from single or multiple cell types. However, most of the current technologies rely on specific biological recognition in different levels to initiate cell assembly, either requiring strong cell-cell interactions (e.g., autologous cell assembly) or highly affinitive cell-protein interactions (e.g., extracellular matrix protein), thereby limiting their wide biomedical applications. More generalized methods include dielectrophoresis and DNA-programmed assembly, but they either only work at low ionic strength or involve extensive modifications of cell membranes for DNA recognition, which can lead to undesired abnormalities in cell behaviors[531]. Therefore, by demonstrating a generalized synthetic route to meet the needs for a full spectrum of disease modeling and tissue replacement, our ADcell method could represent a unique way to construct bioartificial tissues for biomedical applications.

We started our cell assembly with adipose-derived mesenchymal stem cell. Mesenchymal stem cell (MSC) is perhaps the most widely used and tested cell lines for clinical relevant regenerative medicine and immune modulation; utilizing adipose-derived MSCs as cell source can mitigate the donor's pain[532]. By extracting, purifying, expanding and then harvesting human ADMSCs in media suspensions at a high cell density (10 million cells

per milliliter), we then placed a drop (10 microliters) of suspension onto our optimized ADcell membrane. Cell suspension does not flow through the membrane due to its high surface tension and the nanosized pores; when a predefined and connected vacuum was turned on, due to the external forces provided by the vacuum underneath the cell suspension, cells can be rapidly seeded and assembled (<10 minutes) into a robust tissue-like structure on the nanoporous membrane. This cell assembly process can be directly monitored by the significantly impeded or stopped flow speed of media suspension as compared to the cell-free conditions we tested, where the nanosized pores on the membrane were blocked by cells. After washing with PBS to remove unbound cells, ADMSC layer formed on the ADcell membrane was cultured in growth media for one day to form cell junctions and then characterized by cell field emission scanning electron microscopy (FESEM). From the representative FESEM images, the rapidly assembled ADSCs are densely packed and start to form cell-cell connections after one day's culture. To confirm whether these highly packed ADSCs assembled using our ADcell method can upregulate cell-cell and cell-substrate interactions, we investigated gene expressions of focal adhesion kinase and Notch-related pathways using quantitative real-time polymerase chain reaction (qRT-PCR). Indeed, both gene expressions were upregulated in vacuum assembled ADMSCs, which suggest a higher level of surface receptor-mediated cell-cell interactions under the external forces and could lead to an increased structural integrity bioartificial tissues.

ADMSC constructs formed on ADcell membrane can be maintained, differentiated to specific cell lineages (e.g., transdifferentiate into myocytes) or directly transplanted by using surgical tools with standard protocols. While ADcell membrane could be applied as a novel yet advantageous scaffold for cell transplantation and tissue repair in these regards,

our ADcell method is unique to synthesize scaffold-free tissue structures following rapid cell assemblies. Compared to bioartificial tissues assembled by Matrigel or other biomaterials, scaffold-free bioartificial tissues have high cell density (almost 100%) for more efficient cell transplantation and reduced biomaterial complexities such as toxic degradation products, which provides distinctive advantages for next-generation biomedical applications. Using ADcell technology, scaffold-free ADMSC constructs were readily formed by incubating cell-membrane hybrids in growth media supplemented with ascorbate (vitamin C), leading to the removal of the sacrificial membrane through our tested bio-redox reaction, which can be seen by the disappearance of dark-color and non-transparent MnO_2 nanostructures and appearance of semi-transparent cell constructs. Vitamin C is an endogenous biomolecule that naturally exists in human, and has been commonly used as anti-oxidant supplements for the culture of cells. By utilizing optimized concentrations and exposure time of vitamin C supplemented media, we reliably harvest macroscopic ADMSC tissues within a day. Importantly, these tissue pieces composed of ADMSCs alone are robust, can be directly manipulated, transferred, and stacked by surgical tools such as tweezer, scissors as well as knives without requiring additional biomaterials or complicated procedures. This robustness may arise from the tissue-level high cell density and can significantly facilitate the transplantation process for the surgeon. Other methods such as 3D bioprinting based on cell assembled spheroids can also synthesize highly robust tissues with high cell densities, but cell spheroid formation templated by cell-repulsive microwells usually requires specific cell-cell interactions, and the 3D bioprinting process may take over a week[229]. In contrast, using the ADcell method,

ADMSC tissues free of the scaffold can be prepared within a day, which can be particularly valuable when timely tissue repaired is needed and we will discuss later.

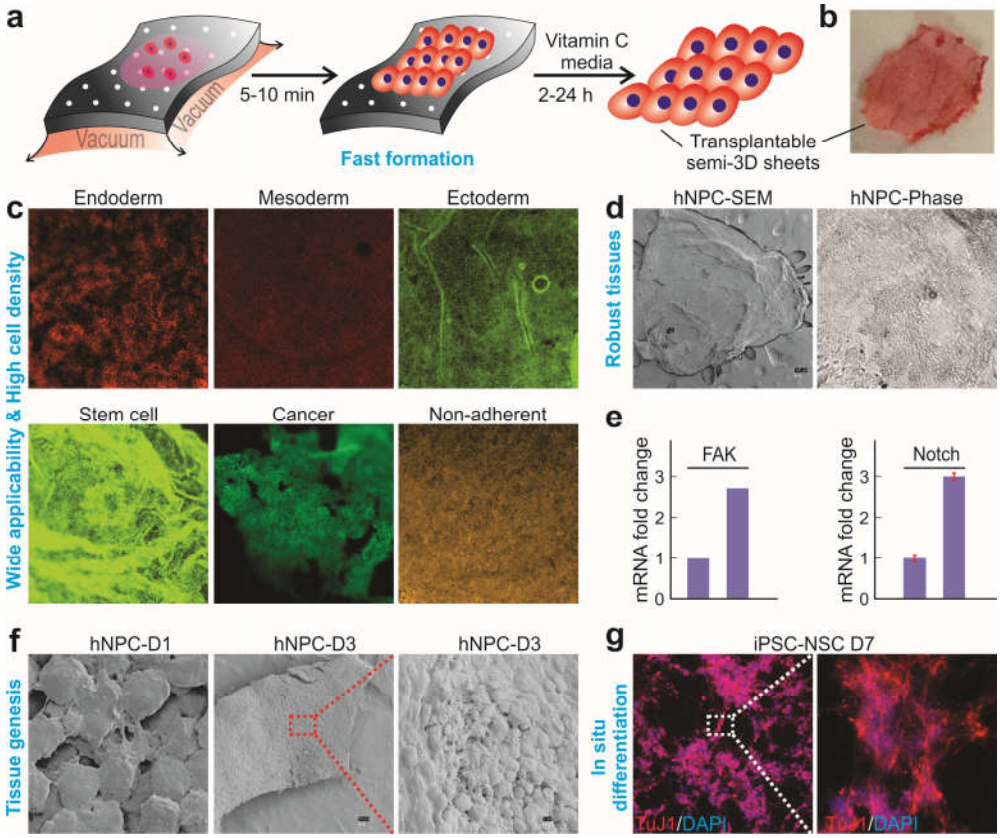

Figure 3-36. Generalized and rapid synthesis of cell-dense, robust and functional tissues from single cell types. a, Schematic diagram illustrating cell assembly. b, A photograph of scaffold-free macroscopic tissues. c, Wide applicability and densely packed cell assemblies. d, Cell SEM and opitical microscope images showing the robust tissue-like structures formed from hNPCs. e, Focal adhesion and cell-cell interaction related pathways were upregulated in the dense cell assembly. f-g, Day dependent cell SEM of hNPCs assembled by ADcell (f), and differentiated neuronal cells at D7 (g). Size of images in c: 665 by 665 μm^2.

While many synthetic strategies have been developed for fabricating a wide variety of bioartificial tissues, most of them start cell assembly from specific cell-cell or cell-protein binding and can only obtain limited types of bioartificial tissues, thereby failing to meet the needs of diverse disease treatment and disease modeling[229]. For example, while monocytes have been clinically used and spatially controlled transplantation of monocytes could lead to more localized therapeutic effects, fabrication of monocytes assembled tissue-like structures have not been possible due to the lack of cell-cell interactions. ADcell method initiates tissue synthesis through vacuum reinforced cell interactions and relied less on specific cell-cell or cell-ECM interactions. Therefore, our simple yet effective method can be well translated into the fabrication of many clinical relevant and unconventional bioartificial tissues constructed from other cell types. To demonstrate this, we generated bioartificial tissues assembled from: i) cells with different germ layer origins (endoderm cells: epithelium cells; mesoderm cells: muscle cells; and ectoderm cells: neural stem cells); ii) embryonic stem cells (induced pluripotent stem cell converted from fibroblasts); iii) cancer cells (breast cancer cells); iv) non-adherent cells (monocytes), either formed on ADcell membrane or detached into scaffold-free tissue structures. These bioartificial tissues of single cell origin are fabricated using similar protocols as for making ADMSC tissues with slight modifications regarding growth media composition, concentrations of vitamin C and the exposure time. Some bioartificial tissues such as monocyte assemblies we demonstrated in this library have not yet been reported, and could be challenging for conventional methods based on biological recognition where monocyte is inherently non-adherent and naturally weak in cell-cell interactions. Also, during removal of ADcell membrane, variations on robustness can be found on tissues of different cell origin, which

could largely depend on the strength of cell-cell interactions. For example, cell assemblies from monocytes and metastatic cancer cells broke more easily compared to those formed from iPSC origin. However, despite these variations on tissue robustness, all our experiments on synthesizing bioartificial tissues succeeded in rapidly creating macroscopic tissues with sizes above 1 mm that can be easily handled and transplanted by surgical tools. Also, other than Vitamin C based removal of the membrane, an alternative approach to obtain scaffold-free tissues can be an autologous detachment of tissues from the surface, which is mainly applicable for non-adhesive cells such as neural stem cells and monocytes. For example, after culturing for 3-7 days, neural stem cells assembled on ADcell membrane often (3 out of 7) spontaneously detach from the surface in an integrated tissue form by using regular cell growth media without Vitamin C or other bioreductants. Adhesion of neural stem cells on substrates is known to require specific extracellular matrix (ECM) protein such as laminin where cells can detach in the absence of such ECM proteins. This allows an alternative strategy when Vitamin C could have undesired effects on cell behaviors such as the induction of differentiation. On the other hand, when adhesion of NSCs on our ADcell membrane is required for further tissue genesis or to differentiate into neuronal cells in situ, ADcell membrane can be functionalized with laminin, cyclodextrin and further loaded with neurogenic drugs followed by Vitamin C treatment. It is not so practical to thoroughly study variations of cellular behaviors and biology for different cell origins, and for many of the bioartificial tissues, we are not clear about their immediate applications yet. However, the ability of ADcell to reliably and rapidly create a comprehensive library of bioartificial tissues that are robust, scaffold-free and

transplantable identifies our ADcell as a unique and generalized method for bioartificial tissue synthesis.

Structurally Defined Multi-cellular Bioartificial Tissues

Our ADcell method can synthesize more advanced bioartificial tissues from multiple cell types in a spatially controlled manner. Natural human tissues are heterogeneous and organized; to reconstitute or repair such heterogeneous tissues, multiple cell types with defined structure would be essential. Currently, most of the high-resolution heterogenous cell patterning has been demonstrated by spatially controlling distributions of cell-binding protein or peptides through soft or photo lithographies[533]. However, they're usually limited to specific cell types. Addressing this challenge, modifications of the cell membrane with biomolecules such as DNA provide promising solutions but requiring extensive modifications of the cell membrane with genetic biomolecules followed by DNAse treatment can cause strong concerns regarding their effects on cells to be assembled[534,535]. Other approaches that assemble cells using mechanical (e.g., ink-jet printing of cell spheroids) or magnetic forces can bypass specific cell-biomolecule recognitions and are usually more generalized for multicell patterning, but they either require a long fabrication time, having to modify cells with exogeneous materials or are limited in resolutions[229,536,537]. To this end, our generalized ADcell method that fabricates multicellular tissue patterns rapidly through vacuum forces, and does not require extensive modifications of cells gives us a unique tool for structurally controlled cell assembly and tissue generation.

As vacuum based method on controlling spatial distributions of bioartificial tissues has not yet been reported, we started synthesizing structure-defined multicellular tissue constructs from creating spatially precisely controlled assembly of single cell type (Figure 3-37). As a proof-of-concept, GFP labeled neural stem cells were selected, as it's directly related to the neural tissue co-culture model we are going to study and GFP labeling can facilitate the monitoring of cell patterning process. To achieve the spatial control, PDMS masks with pre-defined shapes were placed on the ADcell membrane, followed by the addition of cell suspensions on the PDMS mask. After vacuum was turned on, which is located underneath a supporting membrane, fields of vacuum force spontaneously follow the shape of PDMS holes, thereby guiding the media suspension flow and cell assembly precisely. A scaffold-free cell assembly with spatially defined structure can be further obtained by removal of ADcell membrane. Utilizing this vacuum guided cell assembly, we successfully synthesized bioartificial tissues from GFP-NSCs with macroscopic geometrical shapes as well as microscopic cell spheroids arrays with sub 100 μm sizes.

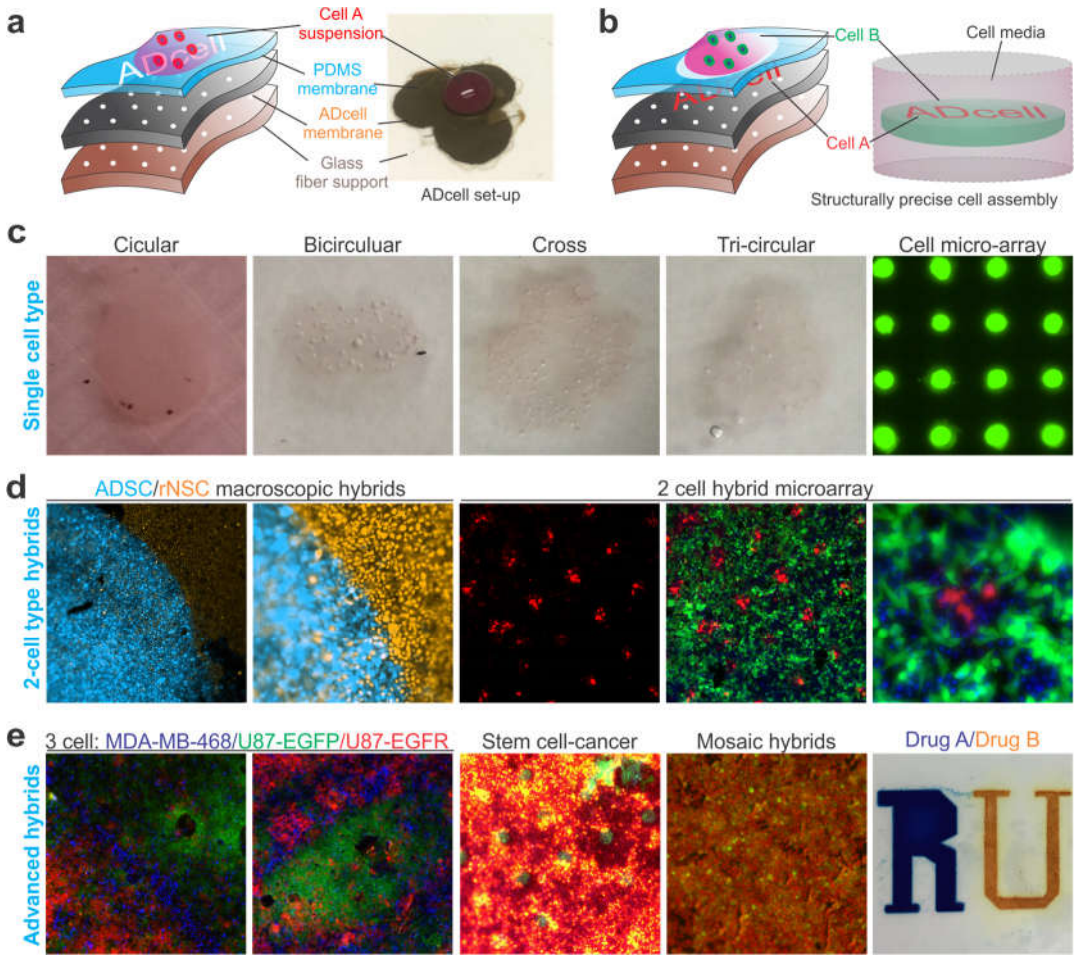

Figure 3-37. Spatially precise synthesis of multi-cellular tissues using ADcell. a-b, Schematic diagram illustrating spatially precise deposition of 1st and 2nd cell types. Similar approach that uses previously deposited cells as vacuum flow masks can also be extended to more than 2 cell types. c, Structure defined single cell types with high resolution. d, Spatially controlled assembly of 2 cell hybrid tissues. e, More advanced multi-cellular tissues that have been challenging based on conventional approaches.

Next, we went on to generate cell assemblies from multiple types, where we utilized a "stitching" strategy. Specifically, after the second cell suspension (Cell B) added to a second PDMS mask, Cell B will spontaneously fill into areas outside of the first cell layer (Cell A). This is due to that the first deposited cell layer blocks the vacuum flow and acts as a shape mask itself. To test our hypothesis, we used the two cells types that we have been focused on but from different species, GFP-NSCs (1st type, circle PDMS mask with diameter of 5 mm) from rat origin and ADMSCs (2nd type, circle PDMS mask) from human origin to form a macroscopic "core-shell" hybrid tissue-like structure on ADcell membrane as a proof-of-concept. After the assembly process, ADMSCs were stained using anti-human nuclei, whereas the GFP-NSCs were identified by its green fluorescence. As shown in Figure 3-37, we can see our designed "green core-red shell" hybrid structure formed with a highly distinctive boundary between these two cell types. By identifying all the red cells (ADMSCs, shell) that exist in the green cell region (GFP-NSCs, core), we found only 1.7% (17 out of 1000) false diffusion, which is improved as compared to the commonly used protein patterning approaches. We have further proved the ADcell based cell patterning can be a generalized approach and applicable for creating hybrid cell patterns with sub 100 μm microscopic features. These hybrid structures include ERFP-U87 (human glioblastoma) cell array surrounded by EGFP-U87 cells from the same cell origin; stem cells (GFP-NSCs) surrounded by cancer cells (U87-ERFP); and ADMSC and GFP-NSC hybrid mosaic patterns (single PDMS mask and the hybrid cell suspension were used). Additionally, by repeating the procedure for forming 2nd cell type onto our ADcell membrane, our stitching strategy has also been further extended to fabricating three hybrid cell patterns (metastatic breast cancer and two glioblastoma cancer with different colors)

with spatially controlled architecture. These multiple cell patterning in a single tissue structure has been challenging in conventional methods, and our cell assembling process is significantly faster as well as cost-effective. Furthermore, these multi-cellular tissues formed on our ADcell membrane can either be directly used for tissue modeling or can be detached from the surface for transplantation purposes. These experimental results collectively strongly support the ability of our ADcell method for generalized synthesis of heterogeneous multi-cellular bioartificial tissues with high resolutions, and we demonstrate two exemplary applications to indicate its great potential for advanced tissue modeling and regenerative medicine.

Neural tissue modeling using ADcell

While our ADcell method could create a broad range of complex tissues for tissue modeling and for studying fundamental biology, we're particularly interested in generating central nervous system (CNS) disease-relevant neural cell assemblies that have been challenging for current tissue-synthesis methods. Cells in CNS tissue mainly include neurons that are differentiated from neural stem cells as well as other supporting cells such as astrocytes. As a fundamental process for CNS development, neurogenesis from NSCs has been known to be heavily regulated by supporting cells[538-541]. Among supporting cells that could regulate neurogenesis, astrocyte is particularly important due to its prevalence in CNS tissue[542]. However, despite its importance and the extensive studies previously performed, the role of astrocyte on neurogenesis has not yet been fully elucidated[543]. For example, by using previous 2D or 3D culture models, people have concluded that supporting cells could independently regulate neural stem cell neurogenesis[544]. However,

laminin, a CNS ECM protein that regulates a wide variety of neural stem cell behaviors is required to form the astrocyte or fibroblast -neural stem cell co-culture in previous neural stem cell-based models. This not only introduces an additional variable to the intracellular interactions but also fail to represent important CNS diseases where laminin protein is not prevalent (e.g., neural stem cells transplanted or endogenous neural stem cells into the astroglial scar area of the injured spinal cord). To this end, ADcell that bypasses biomaterial complexities and applicable to unlimited cell types provides a unique platform to study unconventional cellular interactions in tissue level. Under the identical conditions, we successfully generated an array of shape and size-controlled multicellular assemblies using ADcell method: i) human astrocytes and neural stem cells (experimental group); ii) human neural stem cells alone (control group); iii) human fibroblasts neural stem cells (negative control) using ADcell technology; and iv) individual human neural stem cells without cell-cell contacts (negative control) (Figure 3-38). And we also created human neural stem cells cultured on laminin-coated nanoporous membrane as a positive control. As different supporting cells (e.g., astrocytes and fibroblasts) have been known to secret varying tropic factors that influence neural stem cell differentiation, we also spatially patterned these three co-cultures in a single porous membrane without any surface coating to make sure all cells are under identical microenvironment other than varying cell-cell interactions. To facilitate the observation of neural stem cell differentiation, we kept the membrane to provide physical support. After 7 days' culture in differentiation media, we performed immunocytochemistry on the co-cultured cells. As expected, individual neural stem cells cultured without laminin support do not show noticeable neuronal markers (TuJ1), and neural stem cells cultured with laminin supports successfully differentiate into

neurons with long axons. From the stem cell assay of NSCs based cocultures, however, we found large populations of NSCs still successfully differentiate into neurons with long axonal growth when NSCs were co-cultured with astrocytes. NSCs assemblies with high cell densities alone can also enhance neurogenesis significantly compared to NSCs with low cell densities or co-cultured with fibroblasts. These results strongly imply the individual role of astrocytes (even as significant as laminin) to support neurogenesis of neural stem cells and the axonal growth of differentiated neurons even under laminin-free conditions, which is consistent with recent reports on the benefits of astroglial scar for promoting axon growth post spinal cord injury. Both in vitro and in vivo models that utilizing laminin coated substrate or genetic modified mice have suggested the positive roles of astrocyte on enhancing neural stem cell neurogenesis[543,544]. However, the laminin coated substrate may not well represent disease conditions when laminin-rich ECM is replaced by scar tissues, and the in vivo models based on genetic modified mice have high levels of tissue heterogeneity with many variables, thereby failing to study astrocyte-neural stem cell interactions explicitly and selectively. Overall, our ADcell method with the ability to fabricate unconventional multicellular and structurally defined tissues can open the opportunities for studying or modeling complex tissue diseases and injuries.

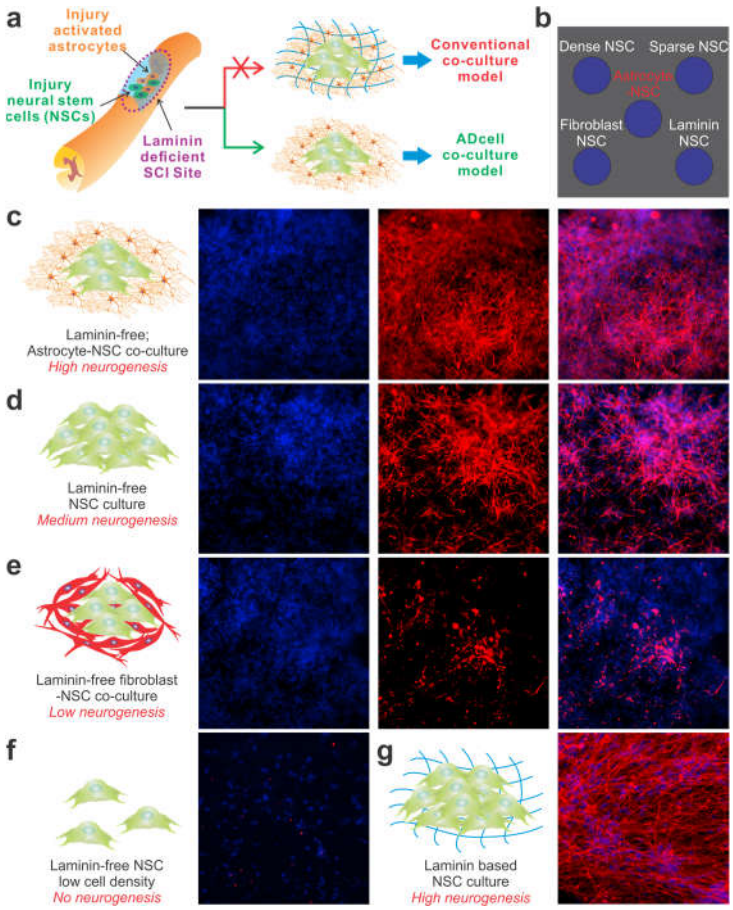

Figure 3-38. Independent role of astrocyte on regulating neural stem cell neurogenesis demonstrated by ADcell co-cultures. a, Comparison between NSC-astrocyte co-cultures formed by ADcell and conventional laminin based co-cultures and their relevance to central nervous system disease. b, Spatially patterned 5 co-cultures formed using ADcell. All soluble cues were identical, thereby cell interaction based neurogenesis regulation can be explicitly revealed. c-g, Immunostaining images (red, TuJ1) of NSCs differentiated for 7 days under different co-culture conditions. These results collectively reveal the beneficial role of astrocyte on NSC neurogenesis under laminin deficient microenvironment. Size of immunostaining images: 656 μm in width.

Scaffold-free bioartificial tissues for diabetic tissue repair

While tissue modeling provides insights for fundamental biology and disease treatment, successful bioartificial tissue transplantation can directly accelerate injured tissue repair and disease treatment. In this regard, our ADcell that is capable of fabricating scaffold-free tissues from wide variety of cells in a time efficient manner could provide a unique yet versatile route for timely tissue repair and to promote cell integration into the injured sites. As a proof-of-concept to demonstrate the application of our ADcell method for in vivo tissue repair, we created a well-established murine diabetic skin wound model generated by delivering streptozotocin into male mice followed by standardized excisional wound creation using biopsy punch on the mouse skin in the neck sites (Figure 3-39). While normal skin wound spontaneously heal, it can be significantly impeded in patients with diabetic diseases[545-547]. Additionally, as diabetic patients often have impaired immune responses, delayed treatment or wound closure could lead to severe infections. To this end, we generated ADMSC sheets using our ADcell technology using the aforementioned protocol as a treatment for diabetic wound healing. MSCs that secret growth factors stimulates proliferation and survival of cells as well as reduce inflammation locally have good clinical potential to treat skin wounds and other tissue injuries, thereby being widely studied in wound healing[548-551]. By transplanting the ADMSC sheets into the skin wound, we observed a daily closure of the wound, accompanied by an increase of cell sheet covered area. In contrast, minimal wound closure was observed in the control condition (no treatment). Remarkably, at Day 7, the ADMSC sheets transplanted wound achieved full (100%) wound closure, which is a significant enhancement compared to the control (25%). This results indicate the therapeutic potential of ADMSC sheets fabricated by our ADcell

technology. While thermoresponsive polymer based cell sheet fabrication and transplantation have also shown potential for skin wound healing, typically a few days are needed. The delayed transplantation of cell sheets for a few days was found to significantly influence the integration of transplanted cells into the injured areas, where scar-like tissue already started to form. By performing hematoxylin and eosin (H&E) staining and immunohistochemistry staining, we could further conclude better structural integrity of the injured tissue, and a higher proliferation marker expression in the wound from the same-day transplantation of ADMSC sheets comparing to delayed transplantation or non-treatment groups. In parallel, as our ADMSC sheets are free of exogenous bioscaffolds, they could provide better integration of cells into the injured area to achieve better therapeutic effects. As a control, we also transplanted ADMSCs using a biodegradable scaffold into the diabetic skin wounds. Over seven days' periods of observation, as expected, they also promoted significant wound closure, which is consistent with previous reports. However, through immunohistochemistry staining, the scaffold, indicated by the red fluorescence, still acts as a barrier between the ADMSCs and host tissue after seven days. This can ultimately limit the integration of ADMSCs, and lead to prolonged host responses to such foreign transplants. Therefore, our ADcell fabricated scaffold-free ADMSC sheets that can be timely formed and transplanted into the skin wound provide excellent solutions to conventional methods for severe tissue injuries. Considering the wide applications of scaffold-free bioartificial tissues for tissue repair and disease treatment, and the versatile tissue structures fabrication demonstrated, our method holds great potential to

treat many other human diseases and injuries other than our demonstrated wound healing model.

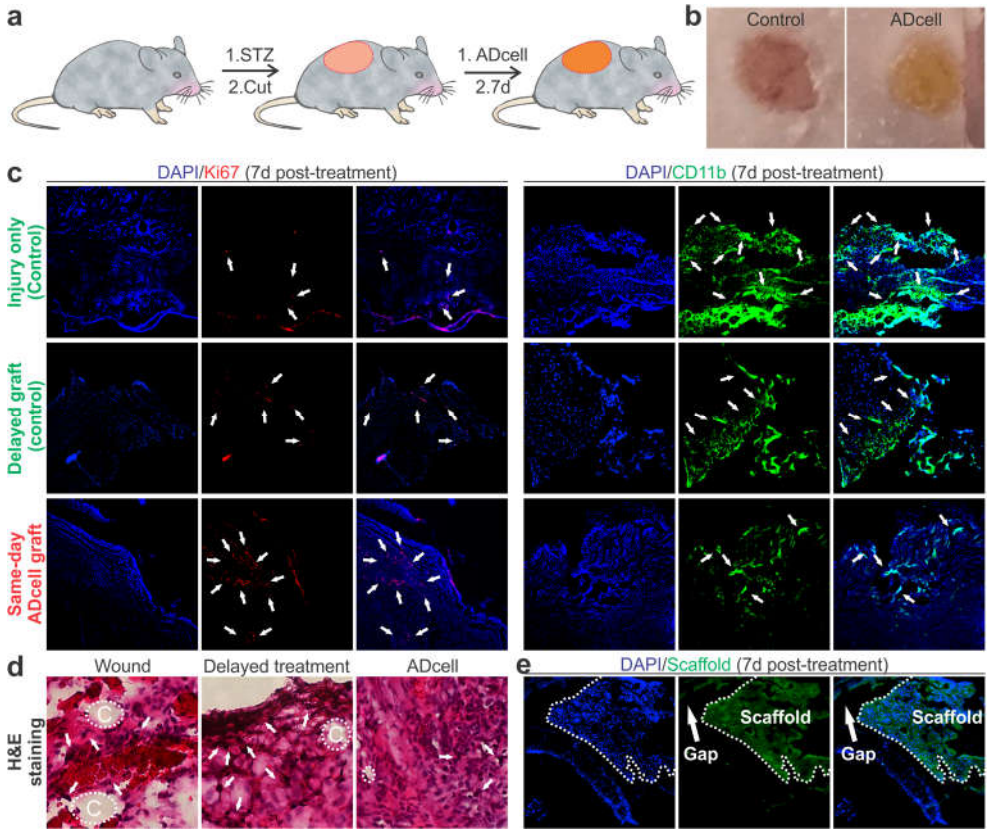

Figure 3-39. ADcell for fast tissue repair. a, Schematic diagram illustrating the induction of diabetic mice and the transplantation of ADSC sheets fabricated by ADcell. b, The rapid fabrication and timely transplantation of ADSC sheets into the diabetic wound successfully induced wound healing in 7 days. c-f, Enhanced wound healing, proliferation (PH3) and vascularization by the timely transplantation of ADSC sheets and representative H&E staining (d), optical images (e) and immunostaining (f) results as compared to control groups. g, Tissue staining images of diabetic wounds treated by ADSC polymer transplantation condition. Image sizes: 656 μm in width.

3.2.4 Conclusions and Outlook

Creating 2D and 3D bioartificial tissues or cell assemblies have wide applications for tissue engineering. Our ADcell technology that is based on vacuum guided assembly and a chemically formulated, nanoengineered membrane provides a unique route to create retrievable bioartificial tissues and cell assemblies of many kinds with precisely controlled architectures. Utilizing ADcell technology, we elucidated the independent role of astrocytes to promote large populations of neurogenesis, which is unexpected and have not been well understood in conventional tissue culture models. By successfully accelerating diabetic mouse wound repair, ADcell also demonstrated good potential for clinical based treatment of severe tissue injury. Scaffold-based approaches have been widely applied for tissue engineering, but some of the scaffold associated biomaterial complexities are undesired. Scaffold-free tissue engineering can bypass biomaterial complexities, but they are often limited by insufficient control over cell architectures, structural fragility, a relatively long period of fabrication and limited cell types available. Thus, our developed ADcell technology could be a useful method for controlling cell assemblies and its retrieval and to create bioartificial tissues with unconventional structures. Overall, our ADcell based method represents a unique route for next generation personalized and precision tissue engineering and would help overcome the critical hurdles for modeling and repairing many complex and devastating injuries and diseases.

Chapter 4: 2D-hybrid nanomaterials for biosensing applications

4.1 Graphene-gold hybrid nanoarray for SERS-based sensitive gene detection

4.1.1 Introduction

DNA/RNA sensor arrays play a fundamental role in investigating a variety of biological studies and applications, including gene profiling, disease diagnostics, and drug screening[552-565]. However, designing simple, sensitive, and specific sensors in arrayed systems has proven challenging. Recently, various DNA/RNA sensing techniques have been successfully developed into reliable arrayed systems based on fluorescence, electrical, and radioactive signals. Among these methods, surface enhanced Raman scattering (SERS) has arisen as a promising DNA/RNA sensing platform, owing to its high sensitivity and fingerprint improved specificity. While it is well known that Raman transition bands are highly specific to the chemical bond structure of molecules, due to their innate low signal strength highly sensitive signal detection is very difficult. To this end, it has been shown that Raman bands can be significantly amplified by surface-enhanced Raman scattering, through roughened noble-metal (e.g., Au, Ag, etc.) nanostructures[566,567]. In general, the enhancement of Raman signal on SERS platforms relies on two distinct phenomena known as the electromagnetic field mechanism (EM) and chemical enhancement (CE)[449]. When incident light is exposed to noble-metal nanostructures, the oscillating electric field causes an oscillation of the conducting electrons in the noble-metal nanostructures, which causes the EM. Separately, CE occurs when the noble-metal nanostructures transfer charges via holes or electrons to the adsorbed molecule, which increases the polarizability of the molecule as well[568,569].

While signal enhancement by SERS is a promising approach, heterogeneous distribution of the noble metal nanostructures, using standard techniques, creates an electromagnetic signal enhancement that is often irreproducible and not suitable for quantitative molecular analysis[570-573]. In the same vein, heterogeneous adsorption of molecules, both spatial and orientational, to different facets of the nanostructure hinder the practical application of the chemical enhancement for SERS-based sensors. To this end, it is essential to develop SERS-active nanoarrays that contain well-defined homogeneous noble-metal nanostructures with functional surfaces for chemical attachment. Creating well-designed, homogeneous, and uniform noble-metal nanostructures allows for high SERS signal enhancement through the EM effect with minimal variation in signal caused by irregularities in the substrate. Also, functionalization of the nanoarray surface with materials such as physiochemically-defined two-dimensional graphene can consistently enhance the Raman signal by CE through aligned adsorption of the specific molecules of interest[574-576].

Here, we propose a new DNA/RNA sensing platform consisting of a large-scale, homogenous SERS nanoarray that utilizes graphene encapsulated plasmonic metal (Au) features for both electromagnetic and chemical Raman enhancement (Figure 4-1). The graphene-Au hybrid array was generated by laser interference lithography (LIL) followed by gold deposition and electrostatic encapsulation with graphene oxide nanosheets. A highly reproducible SERS signal can be obtained using our substrate due to the homogeneous nanostructures generated by the LIL technique, providing a strong EM effect. Also, the graphene can also contribute to amplify Raman signals by CE through the tunable band Fermi level, and the aligned adsorption of specific molecules of interest via π-π and

electrostatic interactions, thus increasing the sensitivity and reproducibility of our system[574-576]. The impact of the chemical enhancement was also investigated based on the reduction rate of encapsulated graphene oxide nanosheets. As a result of the combinatorial effect of both the homogeneous Au array and the graphene nanosheets, our graphene-Au hybrid array could be utilized as a DNA/RNA sensing platform by adsorbing Raman dye-labeled synthetic probe DNA oligonucleotides (complementary DNA sequences). Moreover, real cell lysis sample will also be tested to prove not only the sensitivity and selectivity but also the stability of our graphene-Au hybrid SERS array in the complexed matrices of biological fluid. Specifically, neuronal differentiation of human neural stem cells (hNSCs) and TuJ1 mRNA gene expression levels were chosen as a proof of concept, to demonstrate the strong potential of our graphene Au hybrid SERS nanoarray as a DNA/RNA multiplex quantitative sensing platform.

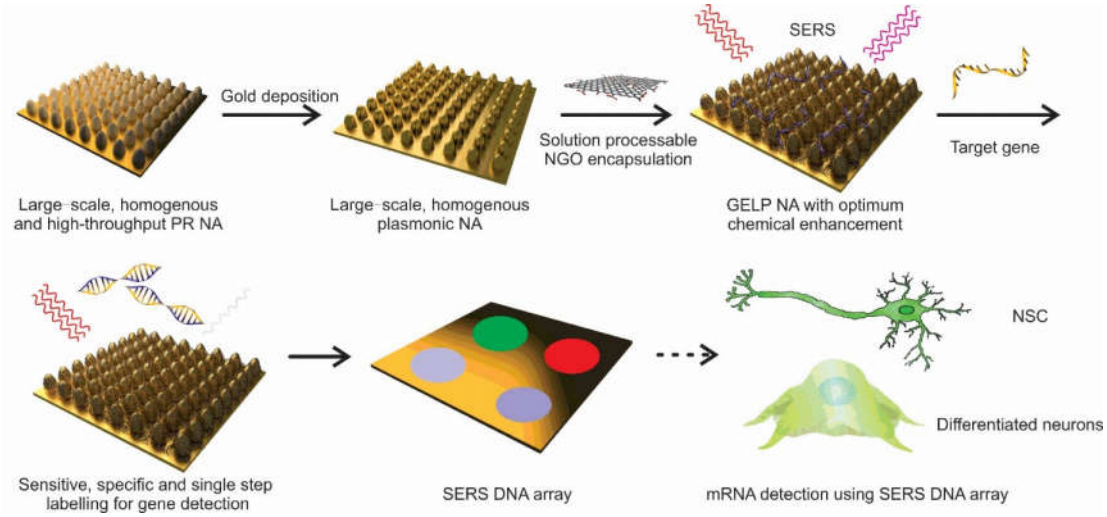

Figure 4-1. Schematic diagram illustrating the generation of gold-graphene hybrid nanoarray for SERS-based gene detection.

4.1.2 Methods

Materials and cells

ITO electrode was purchased from U.I.D., South Korea. Gold electrode, chromium (adhesion layer) and gold were deposited on the cover glass with a thickness of 2 nm and 50 nm using E-beam evaporator, respectively. All chemicals used in this study including gold (III) chloride hydrate, ammonium sulfate, potassium citrate tribasic monohydrate, dopamine, L-Dopa, 3,4-Dihydroxy-L-phenylalanine and Formalin solution (neutral buffered, 10%) were purchased from Sigma-Aldrich, USA. All the materials used for the photolithographic process including photoresist (AZ2020), solvent (AZ EBR Solvent), developer (AZ MIF3000) and stripper (AZ 400T) were obtained from AZ Electronic Materials, USA. SYLGARD 184 silicon elastomer kit (Polydimethylsiloxane, PDMS) was

purchased from Dow Corning, USA. For cell culture, Dulbecco's modified eagle's medium (DMEM), 0.05% trypsin, and Penicillin/Streptomycin (PS) were purchased from Life Technologies, USA. Phosphate buffered saline (PBS) was obtained from Sigma-Aldrich, USA. Heat-inactivated fetal bovine serum (FBS) was purchased from Gibco, USA.

Synthesis of graphene oxide nanosheets

Nano-sized graphene oxide was synthesized using our previous protocol with minor modifications. We first generated graphite oxide from graphite. Briefly, 0.5 gram 100 mesh-sized graphite was added into 6 ml 98% H_2SO_4, 1.3 g $K_2S_2O_8$ and 1.3 g P_2O_5 at 80 degrees for 8 hours. Then, 250 mL ultrapure water was slowly added and the mixed solution was vigorously stirred for 12 hours to get the preoxidized graphite. Afterward, the black colored mixture was centrifuged down and dried at room temperature overnight. To synthesize the graphite oxide, the dried and pre-oxidized graphite was slowly mixed with 10 ml concentrated (98%) H_2SO_4. Twenty minutes after the stirring, 8 g $KMnO_4$ was added into the mixture and stirred over one hour. All reaction was performed under the ice bath condition to keep the temperature of reaction below 15 degrees. Following the one-hour stirring, we increased the temperature of the reaction to 35 degrees using a hotplate and continuously stirred for 5 hours. Afterward, 150 ml de-ionized water was added to the mixture drop by drop (caution: temperature must not exceed 50 degree) as well as vigorous stirring for 6 hours. Lastly, 500 ml de-ionized water was slowly added to the reaction. Afterwards, to quench the reaction, 20 ml 30% H_2O_2 aqueous solution was injected. A shining yellow colored solution should appear at this stage, indicating the successful formation of graphite oxide. To purify the graphite oxide, the solution was centrifuged at 10000 rpm for 5 minutes and then washed with 12% HCl solution for three times followed

by five times washing by de-ionized water to remove the HCL. To obtain the graphene oxide, 10 hours of ultrasonication was performed. To remove the aggregated graphite oxide, the final solution was centrifuged at 10000 rpm for 30 minutes and the supernatant was collected. We measured the concentration of graphene oxide by drying 1.0 ml of the solution and weigh the solid after evaporation of water. The graphene oxide was then characterized by transmission electron microscope (TEM), zeta potential and zeta size (Nanosizer, Malvern Instruments).

Generation of Au nanoarray using LIL

To generate the homogeneous polymer nanoarray on a large scale as a template for the SERS substrate, we used laser interference lithography. Briefly, one by one-centimeter square silicone substrate was sequentially washed by 1% Triton-X aqueous solution, acetone solution and ultrapure water for one hour under bath sonication. Afterward, the substrates were dried under vacuum overnight. To increase the adhesion between the substrate and photoresist, a layer of Bis(trimethylsilyl)amine (HMDS) was first spin-coated for 15 seconds under 2000 rpm on a spin coater. Then the positive photoresist solution was spin-coated on the HMDS-coated substrate for 40 seconds at 4000 rpm. Soft baking was performed on the photoresist-coated substrate on a hot plate for 60 seconds at 120 degrees. After cooling down, the substrate was placed on a vacuum on a laser interference setup. To initiate the interference, a 325 nm Hd-Cd laser and a Lloyd's mirror was used. The exposure time was optimized for 25 seconds with a developing time of 30 seconds. Following the laser exposure, the substrate was washed in de-ionized water and dried using nitrogen gas. A hologram from the photoresist array should appear at this stage.

To generate the gold nanoarray, the polymer nanoarray was used as a template and gold was deposited onto the polymer substrate using a sputtering technique. To control the layer thickness of the gold, different deposition time of 120 s, 240 s, 480 s, 960 s and 1200 s were used for 10 nm, 20 nm, 40 nm, 80 nm and 100 nm, respectively. To characterize the substrates, field emission scanning electron microscope (FE-SEM, Zeiss) and atomic force microscope (AFM, Park systems, NX10) were used.

Generation of graphene Au hybrid SERS nanoarray

To fabricate the graphene Au hybrid SERS nanoarray, an electrostatic assembly strategy was used. Briefly, we functionalized the surface of Au nanoarray with a positive charge using cysteamine aqueous solution (concentration of 1.0 mg/ml) through the thiol-gold interactions overnight. After extensive washing in water to remove the residual cysteamine molecules, nano graphene oxide solution (concentration of 3.0 mg/ml) was added onto the Au nanoarray and incubated for 24 hours. Then the excessive amount of GO was washed away using de-ionized water. To perform the reduction of GO on the Au nanoarray, ascorbic acid and hydrazine-based reduction were used, respectively. For the ascorbic acid-based reduction, GO functionalized Au nanoarray was incubated with an ascorbic acid aqueous solution at a concentration of 1.0 mg/ml for a different period of 12 hours, 24 hours and 48 hours to modulate the reduction level and energy levels of RGO. To achieve the highest reduction level, hydrazine vapor-based reduction was used. In a sealed glass dish, the GO functionalized Au nanoarray was placed in proximity with a drop of hydrazine solution. Afterward, the dish was heated to 80 degrees for 24 hours. According to literature, such excess time of reduction of GO by hydrazine can generate a high reduction level similar to the pristine graphene with the working function of -4.5 eV. The graphene Au

nanoarray with different reduction levels was characterized using Raman spectrum using a laser at 780 nm with background subtracted using a polynomial function in the Labspec software. To confirm the high homogeneity of the SERS nanoarray, Raman mapping on a 100 μm by 100 μm scale.

To study the thickness-dependent SERS effects on the Au nanoarray based on the electromagnetic mechanism, we directly used GO as a Raman dye. GO was coated onto the Au nanoarray as well as control substrate of planar gold using identical procedure of electrostatic assembly described above. Afterwards, the GO coated nanoarrays with different thicknesses of gold were analyzed by Raman using a 780 nm laser. The intensities of the graphite peak at 1550 cm^{-1} were averaged from three individual measurements and then converted into a bar graph in Figure 4-2e.

Density Functional Theory (DFT) simulation

To calculate the energy levels of Cy5 Raman dye, the energy and frequency of C5 molecules were calculated using the B3LYP method with the 3-21G basis set in the Gaussian 09 software. The Cy5 dye has one positive charge and is in a triplet spin state. The total energy of Cy5 was calculated to be -1494.41172095 a.u. With RMS gradient norm of 0.00000198 a.u. The detailed atomic coordination of Cy5 was provided.

Similarly, to show the effect of reduction on a graphene-like structure, we also performed DFT simulation on a structure with nine fused benzene rings as well as its derivatives with four hydroxyl groups, four carboxylic groups, four epoxy groups or-or combination form. These functional groups are commonly seen in graphene oxide, and the coordination and calculation summaries can be found in the supporting information. The HOMO and LUMO of each compound listed were obtained from the molecular orbitals of the optimized form.

DNA Detection of by graphene Au hybrid SERS nanoarray

To detect target DNA, probe DNA with complimentary sequences and conjugated with Cy5 was designed and ordered from Integrated DNA Technologies. To immobilize the Cy5-labelled probe DNA to the graphene Au hybrid nanoarray, a concentrated probe DNA PBS solution (concentration of 1.0 mM) was placed on top of the nanoarray and incubated for four hours. Afterward, the solution was removed and washed with PBS three times until the unbound DNA was removed. The successful loading of probe DNA was confirmed by the distinctive Raman spectrum of Cy5 dye on the probe DNA. To detect the target DNA, the SERS nanoarray immobilized with probe DNA was incubated with target DNA sequence with different concentrations (0 pM, 1 pM, 10 pM, 100 pM, 1 nM, 10 nM,100 nM and 10 μM) or with single-mismatch DNA sequence at a concentration of 10 nM in the PBS. Then the Raman spectrum at three randomly chosen spots on each substrate was collected with background subtraction using the Labspec software with identical protocol aforementioned. The laser wavelength of 780 nm was used for all the measurements as well as Raman mapping for the single base pair mismatch experiment. To quantify the intensity change of the Raman spectrum, the identical Raman peak at 1120 cm-2 of the Cy5 dye was used as the standard peak.

To perform gene analysis for the neuronal differentiation of human neural stem cells, cell lysates from the stem cells or the differentiated cells were collected using Trizol. Then the mRNA in the lysates were converted into DNA. To increase the amount of DNA in the solution, we used a 10:1 ratio of forward and reverse primer to initiate the polymerase chain reaction for 40 cycles. Afterward, the amplified DNA solution was detected using Raman on the graphene Au SERS nanoarray using the identical protocol mentioned above.

Forward and reverse primer sequences were listed in Table 2. Three random chosen spots were used for the Raman analysis and obtain the statistical information.

Cell Culture and Differentiation

The Human neuro stem cells (hNSC) were maintained in mixture of neural basal medium (Gibco) and DMEM/F12 (Gibco) (50:50 ratio) supplemented with 0.5 % N2 (Gibco), 0.5 % B27, and 20 ng/mL FGF basic (Fibroblast growth factor-basic, PeproTech) respectively. All cells were maintained at 37°C in a humidified incubator with 5% CO_2. To differentiate cells, hiPSC-NPCs were seeded on matrigel (Life Technologies) pre-coated plates (300,000 cells/well for 6-well plate) 24 hr before experimentation. After one day of cultivation to promote cell attachment and spreading, the fresh hNSC media without FGF basic (differentiation media) was treated to stop proliferation and induce neuronal differentiation. The medium was changed with fresh differentiation media every 3~4 days during the differentiation. For consistency, all experiments were carried out on cells between 3 passage differences.

Immunocytochemistry

To study the extent of neuronal differentiation, cells are washed with DPBS (pH 7.4) and fixed with 4% formaldehyde solution for 10 min at room temperature (RT), followed by three times of washing with DPBS. Then, cells are permeabilized with 0.1% Triton X-100 in PBS for 10 minutes, and non-specific binding is blocked with 5% normal goat serum (NGS) (eLife Technologies) in PBS for 1 hour at room temperature. The primary rabbit antibody against Nestin (1:200 dilution, Invitrogen) and primary mouse antibody against TuJ1 (1: 200 dilution, Biolegend) are used. Following the manufacturer's protocol, the fixed samples are incubated overnight at 4°C in a solution of this antibody in PBS

containing 1% BSA and 0.3% Triton X-100. After washing three times with PBS, the samples are incubated for 1 hr at room temperature in a solution of anti-rabbit secondary antibody labeled Alexa Flour 488 (1:100, Life Technologies), anti-mouse secondary antibody labeled with Alexa Flour 647 (1:100, Life Technologies) and Hoechst (3 μg/mL, Life Technologies) to stain nucleus in PBS containing 1% NGS and 0.3% Triton X-100. After washing three times, all the samples are imaged using the Nikon T2500 inverted fluorescence microscope.

Gene Expression Analysis

Gene expression level was analyzed by quantitative reverse transcription PCR (RT-qPCR) from total RNA extracted from cells by a TRIzol reagent (Invitrogen, MA). The total RNA (1μg) was reverse transcribed to cDNA using the SuperScript III First-Strand Synthesis System (Invitrogen, MA) following the manufacturer's protocol. Subsequently, quantitative PCR was performed on a StepOnePlus Real-time PCR System (Applied Biosystems, MA) using an SYBR Green PCR Master Mix (Applied Biosystems, MA) with the gene-specific primers, listed in Table 2. The Standard cycling conditions were used for all PCR reactions with a melting temperature of 60°C. All the measurements were run in triplicate. The gene expression level was reported relative to the endogenous control gene, GAPDH.

4.1.3 Results and Discussion

Generation of homogeneous plasmonic Au nanoarrays via laser interference lithography for electromagnetic field enhancement

Obtaining reliable and reproducible SERS signals are essential for the precise quantitative analysis of bio/chemical molecules. It is well known that nanostructure homogeneity and oriented molecular adsorption are crucial for obtaining consistent enhancement of Raman signals. To this end, we generated a combinatorial graphene-Au hybrid SERS-active array as illustrated in Figure 4-2a. To do so, large-scale (1 x 1 cm^2) homogeneous photoresist (PR) nanodot arrays were generated using laser interference lithography (LIL) on a glass substrate. As shown in Figure 4-2b, a uniform hologram was obtained as a result of the homogeneously developed nanostructures over the surface of the glass. We then deposited gold (Au) to act as a plasmonic layer via physical vapor deposition (PVD) on the PR nanodot array, to obtain a homogenous Au nanodot array with controlled size and height parameters (Figure 4-2a and b). Both scanning electron microscopy (SEM) and atomic force microscopy (AFM) are utilized to characterize the surface of our nanoarray in detail. Both the width and gap of Au nanodot array were characterized to be ca. 300 nm and the height was ca. 80 nm Figure. 4-2c. As shown in Figure 4-2d, the enhancement of Raman signal was observed after deposition of a 10 nm thick layer of Au, and started to saturate between 20 to 40 nm; however, it diminished with 80 nm deposition, which is due to the connection of the Au layer forming a film instead of a nanodot array. To estimate, optimize, and better understand the optical amplification of Raman signals through our SERS-active graphene Au hybrid nanoarray, we also conducted electromagnetic (EM) simulations with three different incident light sources (514, 633 and 785 nm) (Figure 4-2e). The size and shape of Au nanoarray were fixed, with the average size obtained through SEM analysis (Figure 4-2c). In the EM simulation, local electric field enhancement ($|E|/|E0|$), the ratio of near-field ($|E|$) and the incident field ($|E0|$), is calculated. The EM field distribution images

indicate that when Au nanoarrays are exposed to incident light (514, 633 and 785 nm), the local electric field enhancement slightly increased for 514 nm, and significantly increased around the Au arrays for both the 633 and 785 nm wavelengths, owing to the unique arc structure of plasmonic noble-metal (here, Au). The increment, however, was strongest with 633 nm wavelength incident light. Thus, the 633 nm wavelength incident light was purposefully selected for further experiments.

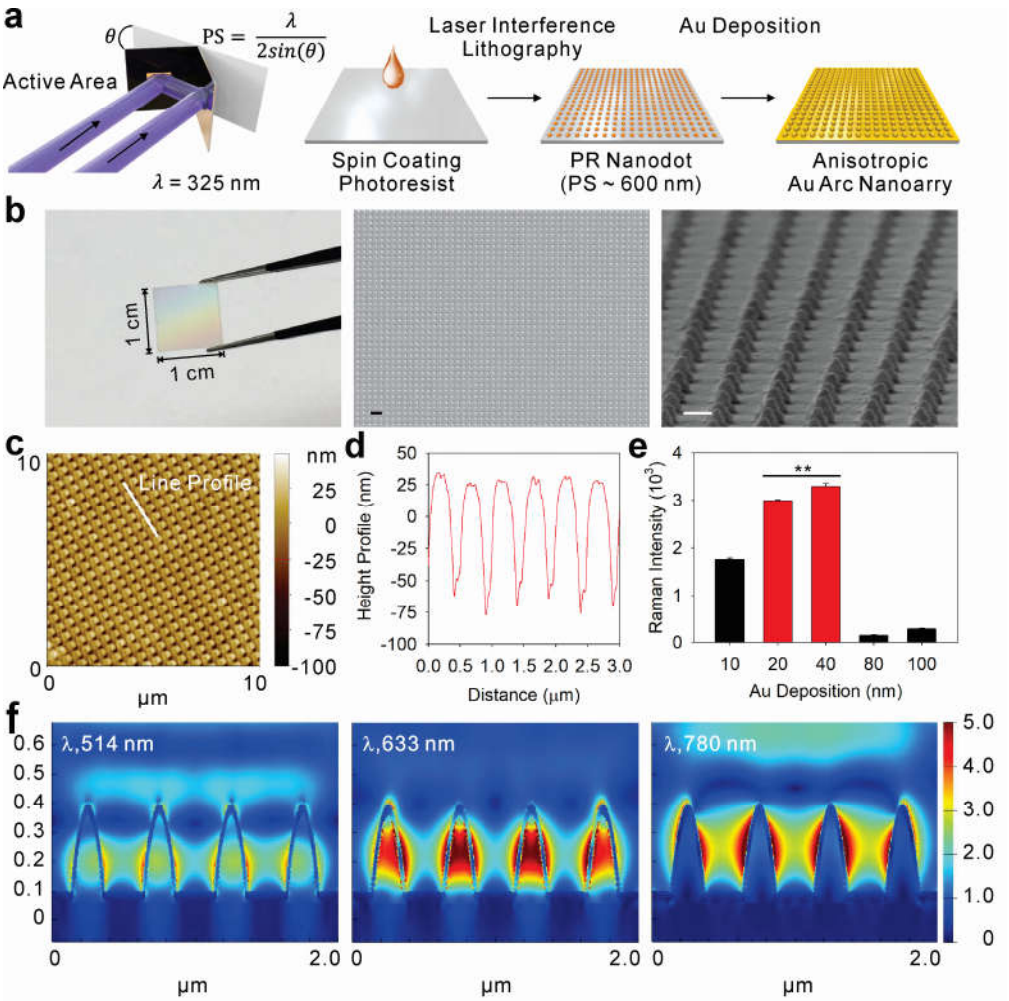

Figure 4-2. Generation and characterization of gold plasmonic nanoarray. a, Schematic illustration of sequential steps to generate gold hybrid nanoarray using laser interference lithography followed by gold deposition. b, Optical image (left) and SEM image (middle and left) of gold plasmonic nanoarrays. c-d, Corresponding AFM images (c) and height profile (d) of the nanoarray. e, Surface enhanced Raman spectroscopy based on gold nanoarray-enabled electromagnetic enhancement with different gold deposition time. f, FDTD optical simulations for the gold nanoarray under different wavelengths.

Surface functionalization with graphene for chemical enhancement

On the other hand, graphene oxide (GO) nanosheets were synthesized by a modified Hummers' method. The size of the GO sheets was carefully adjusted by utilizing an additional filtration process (pore size, 0.2 μm in diameter), to optimize the coverage of the Au nanoarray surface. As-prepared GO nanosheets were characterized through transmission electron microscopy (TEM) measurements [Figure. 3a]. The size distribution of the GO sheets ranged from 37.84 nm to 190.10 nm with an average size of 63.75 ± 24.63 nm analyzed by dynamic light scattering (DLS) analysis (Figure 4-3b). Furthermore, by utilizing a chemical linker, cysteamine hydrochloride (C_2H_7NS), as-prepared GO sheets were successfully functionalized onto the surface of the Au nanoarray through electrostatic interactions. Due to the unique physicochemical structure of atomically thin layered GO, Raman transition bands, of the distinct D (1,350 cm^{-1}) and G (1,600 cm^{-1}) bands of GO, were observed from both GO (functionalized on bare Au substrate) and graphene oxide-Au hybrid nanoarray as previously reported (Figure 4-3c).[18] Moreover, a remarkably strong and homogeneously distributed Raman transition band of GO (distinct G band, 1,600 cm-1, of rGO), was observed over a large scan area (100 × 100 spots per 100 × 100 μm2) [Figure. 3d] from the graphene-Au hybrid nanoarray, owing to the surface-enhanced Raman scattering effect caused by the homogeneous Au nanoarray.

To investigate the CE of Raman signal by the GO sheets on a Raman active reporter, GO was coated on a glass substrate and chemically reduced by ascorbic acid ($C_6H_8O_6$) solution. The reduction of GO to rGO was also validated by the comparison of Raman intensity ratio between D and G band (I_D/I_G) before and after the reduction process. As clearly shown in figure 3e, the I_D/I_G ratio increases from 0.90 to 1.22 as GO reduces to rGO (Figure 4-

3e).[19] As a proof of concept, Raman dye (Cyanine 5, Cy5) was carefully selected as a molecule of interest which would bind to GO. When the surface of GO was partially reduced, via the treatment of a weak reducing agent (ascorbic acid) for 12 h, a remarkable enhancement of the Cy5 signal was obtained compared to untreated GO. Also, when GO was fully reduced to go, either by longer treatment (24 h) or use of a strong reducing agent (hydrazine, N_2H_4 H_2O), Cy5 signal was diminished (Figure 4-3f). Both computational and experimental studies have reported that graphene-based SERS sensors can be directly modulated by altering the oxidation states of GO, thus changing the Fermi level of GO during the process of reduction. By using a mild and biocompatible reducing agent, we showcased the significant chemical enhancement that can be achieved by controlling the energy levels of graphene oxide. This technique can be easily translated into many other graphene-based SERS systems (Figure 4-3g). Based on our experimental results, we optimized and selected a reduction time of 12 hours to further combine with the electromagnetic enhancement of our Au nanoarray to create a sensitive, yet reproducible, SERS platform for multiplexed RNA detection.

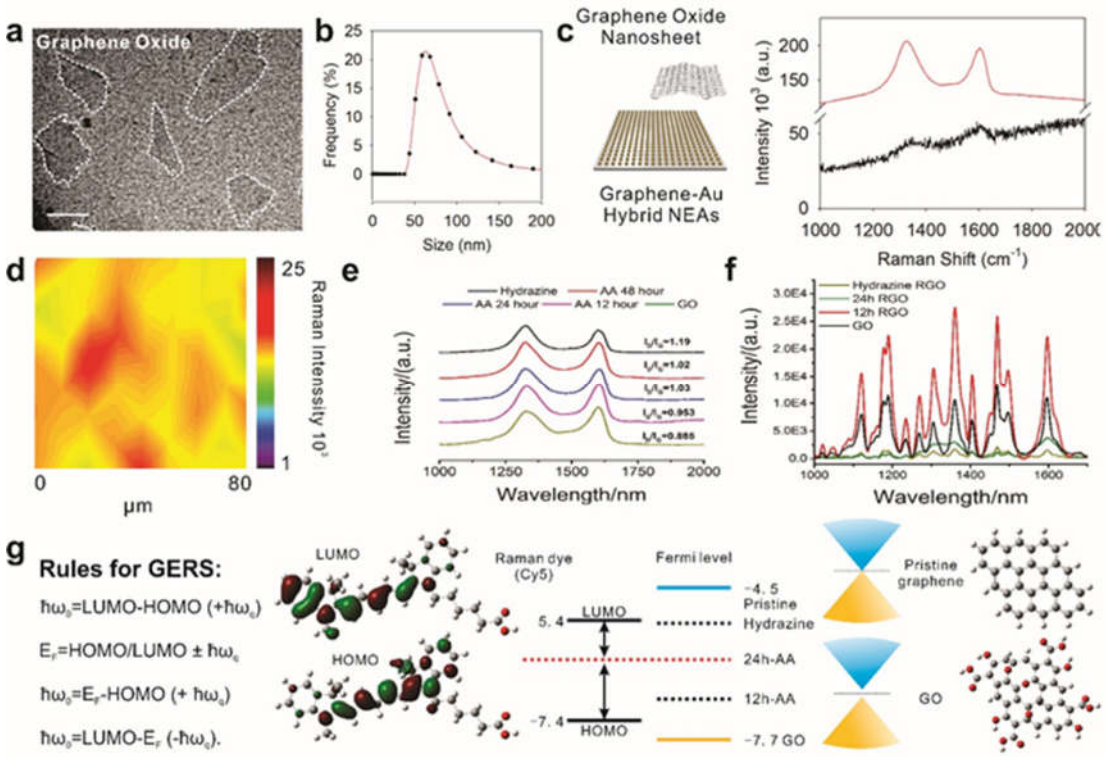

Figure 4-3. Chemical enhancement of Raman spectroscopy based on graphene-gold hybrid plasmonic nanoarray. a-b, Representative TEM images and Zeta Potential measurement of GO. c, Schematic diagram illustrating the mechanism of electrostatic-driven assembly of graphene oxide onto the positively charged gold nanoarray. d, Large-scale Raman mapping of the graphene-gold hybrid plasmonic nanoarray suggests the uniform and significantly enhanced EM field on the hybrid nanoarray. e, Controlled reduction of graphene oxide on the gold nanoarray using mild reductants. f, Reduction dependent chemical enhancement on the graphene-gold hybrid nanoarray. g, Proposed mechanisms for the reduction dependent chemical enhancement on the graphene surface.

Utilization of graphene-Au hybrid SERS nanoarray for quantitative DNA/RNA analysis

In order to create a system for RNA detection we functionalized the Raman dye, Cy5, onto DNA oligonucleotides to create a Raman reporter for specific DNA/RNA sequences. We then functionalized the surface of the graphene-Au hybrid SERS nanoarray with our reporter to create our highly sensitive oligonucleotide sensor. The probe DNA oligonucleotides were adsorbed on the surface of the graphene-Au hybrid SERS nanoarray through π-π stacking. The release of pre-adsorbed probe DNA from the GO surface was facilitated by its hybridization with its complementary sequence, which resulted in a significant decrease of SERS intensity, specific to the Cy5 Raman bands. Here, a probe oligonucleotide with 21 base pairs, that was complimentary to Tuj1 mRNA, was selected as a target molecule for a proof of concept study (Figure 4-4a). As seen in the figure 4b, the addition of the TuJ1 complementary DNA sequence (1 nM), led to a remarkable decrease in Cy5 Raman signal (Figure 4-4b), thus demonstrating the ability of our graphene-Au SERS nanoarray as an oligonucleotide sensor. After successful detection of the TuJ1 complementary DNA sequence on the graphene-Au hybrid SERS nanoarray, a quantitative assay was conducted. We confirmed that the observed Raman signal decrease correlated with the increase of TuJ1 complementary DNA, ranging from 1 pM to 100 nM. All three graphs at each specific Raman shift exhibited linear curves with correspondingly high R^2 value (above 0.96), demonstrating the system's potential for accurate and quantitative analysis (Figure 4-4c). Furthermore, the selectivity of our graphene-Au hybrid SERS nanoarray was also investigated by testing it with a single-base mismatched DNA target. For each measurement, 30 spots were randomly chosen to collect SERS spectra. Due to the specificity of DNA base paring, the Raman signal decrease from the TuJ1

complementary DNA sequence was significantly higher than the single-base mismatched DNA sequence (10 nM) (Figure 4-4d). To verify the sensitivity, selectivity and stability of our graphene-Au hybrid SERS array in the complexed matrices of biological fluid, cell lysis sample with extracted RNAs was also conducted after conversion into cDNA. As a proof of concept study we investigated the ability of our system to detect conversion of neuro-stem cells into neurons. Briefly, we induced neuronal differentiation of neuro-stem cells (NSC) (3.0×10^4 cells/cm^2) by removing growth factors (FGF basic) from the proliferation media. As shown in figure 4e, only cells that have undergone neuronal differentiation showed clear neuron-specific class III β-tubulin (TuJ1) messenger RNA (mRNA) gene expression, representative markers of neurons. Undifferentiated NSCs cells (D1) failed to show any significant TuJ1 expression. Furthermore, the results collected by our graphene-Au hybrid SERS nanoarray agreed with the results collected by immunostaining for characterizing neuronal differentiation (Figure 4-4f-g).. Also, to test the versatility of our graphene-Au hybrid SERS nanoarray, we also functionalized it with glial fibrillary acidic protein (GFAP) probe DNA oligonucleotides, a protein that is highly expressed by various cell types of the central nervous system (CNS) such as astrocytes. As expected, we also observed a slight decrease of SERS signal from differentiated stem cells compare to undifferentiated stem cells (Figure 4-4h-i).. These results agree with previously reported literature that show the plasticity of stem cells, where glial lineages, such as astrocytes, can arise during neuronal differentiation of NSCs (Palmer et al., 1997, Palmer et al., 2000, Steiner et al., 2004), thereby supporting the potential of our nanoarray-based platform for multiplexed gene detection in real biological samples.

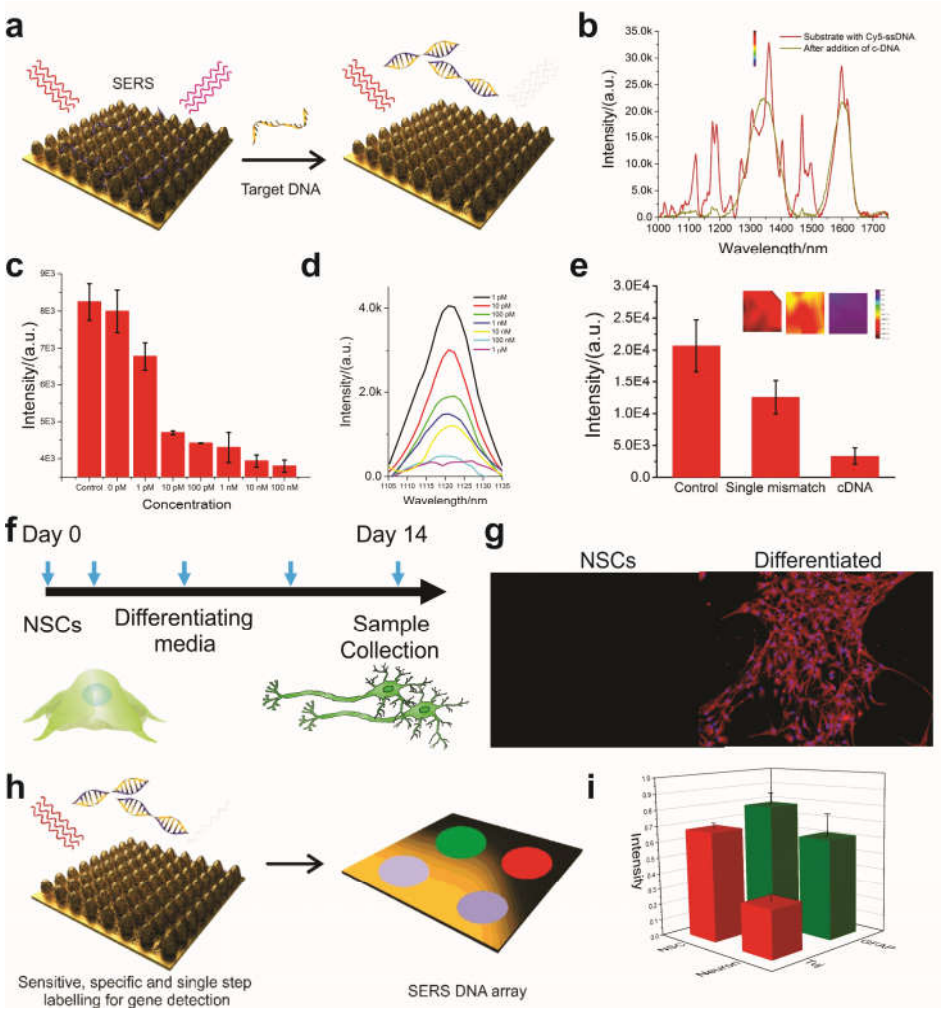

Figure 4-4. Hybrid nanoarray-based gene detection. a, Gene detection based on the reversible interaction between single-strand DNA on the hybrid nanoarray. b, SERS signals before and after the target DNA sequence was added. c-d, Quantitative measurement (c)and the corresponding peaks at 1120 cm^{-1} (d)of the concentration dependent gene detection. e, Specificity of the nanoarray-based SERS detection of target DNA sequences. f-g, Monitoring the neuronal differentiation of human neural stem cells using SERS. h-I, Mechanism (h) and SERS results (i) of nanoarray-based monitoring of stem cell differentiation.

4.1.4 Conclusions and Outlook

In conclusion, we have successfully developed a gene sensing platform by developing a large-scale, homogenous SERS platform based on combinatorial graphene encapsulated plasmonic metal (Au) hybrid nanoarray. Through the EM effect generated by homogeneous nanostructures developed by LIL technique, highly sensitive SERS signal was able to be obtained. Also, through aligned adsorption of specific molecules and the tunable band Fermi levels of the graphene coating, selective and reliable Raman signals were able to be obtained through CE effects. Taking combinatorial effect of both homogeneous Au array and graphene nanosheets, our graphene-Au hybrid array was successfully utilized as a highly sensitive and reproducible DNA/RNA sensing platform by incorporating Raman dye-labeled synthetic TuJ1 probe DNA oligonucleotides. The sensitivity, selectivity as well as stability of our graphene-Au hybrid SERS array in the complexed matrices of biological fluid was also verified with real cell lysate. The ease of sequence modification, the versatility of the graphene-Au hybrid SERS array was also tested by modifying the system with synthetic GFAP probe DNA oligonucleotides. Moreover, since complexed sample preparation step such as purification are not necessary for assaying biological samples, our developed graphene-Au hybrid SERS array can bring a breakthrough for sample-to-answer platform for the analysis of biomarkers even with complexed bio-samples. Collectively, we believe that our graphene-Au hybrid SERS array system will not only be used for high-quality screening assay and will help us to understand associated condition such as disease as well and lead to more effective therapeutic treatments.

Chapter 5: Multidimensional Nanoscaffolds for Developing Design Principles in Nanomedicine

5.1 Mapping Nanotopography-regulated Stem Cell Behaviors

5.1.1 Introduction

In the past three decades, nanotechnology has revolutionized many fields in physics and biology such as electronics, photonics, material science, biosensing, biomechanics and therapeutics[577-585]. To establish design principles and achieve most optimal results from these nanotechnology-enabled studies and applications, one primary task is to study structure (e.g. shape and size) dependent effects on the physical and biological properties of nanomaterials[586-592]. Currently, most work has been based on the optimization of several pre-selected parameters to draw a conclusion[593-596]; however, the selection of parameters may not always be representative, can be cherry-picking and occasionally leads to contradictory conclusions. Given the broad applications of nanotechnology and the benefits of establishing systematic structure-property in large numbers of nanostructures, there is a clear need to develop a reliable method which can directly guide the design for nanotechnology-based applications.

Several approaches have been applied for creating combinatorial nanoarrays to study effects of nanostructures in physical or biological systems. E-beam lithography is the mostly used approach to precisely create different nanostructures[597-599]. Similarly, dip-pen can also produce high-resolution nanopatterns with high flexibility[600-604]. However, these methods become less suitable for generating large-scale nanoarrays with increasing amounts of nanostructures to the scale of hundreds[128,600]. Photolithography,

nanoimprinting and nano-contact printing lithography are also commonly used for generating combinatorial types of nanostructures, but most of these fabrication techniques have to start from a mask created by e-beam lithography. Multi-photon lithography and 3D printing generate large-scale nanostructures with high structural tunability by using digital masks. However, it's challenging for them to achieve a high-resolution in the submicrometer ranges. Self-assembly, magentolithography, candle soots and porous silicon gradients are also useful to obtain a large number of combinatorial nanostructures. Ultimately, they didn't produce large-scale nanoarrays with precisely controlled and ordered shapes[128].

Recently, nanotopographies-based control of stem cell behaviors has raised intense interest in cell biology and demonstrated good potential for clinical applications[605-612]. By regulating integrin clustering with sizes ranging from tens to hundreds of nanometers, nanotopographies of extracellular matrix (ECM) direct stem cell polarization, control stem cell proliferation and guide stem cell differentiation by inducing cytoskeletal remodeling and nucleus epigenetic changes. It's generally known that modulating stem cell behaviors can be achieved by manipulating nanostructures in the ECM; nanotopographies exist in natural or artificial ECM typically cover a wide range from sub-100 nm to above 10 um[613-617]. However, there is a lack of effective and efficient approach to systematically correlate stem cell behaviors with a broad and continuous spectrum of nanotopographies for systematically instructing ECM-based biomaterial design.

Herein, we developed a lithographical tool that generates a library of large-scale nanoarrays with ordered, precisely controlled and biologically-relevant nanostructures (Figure 5-1). Based on this platform, we map the nanotopography-regulated stem cell behaviors in a

broad and continuous spectrum of nanotopographies existing in natural and artificial ECM. Remarkably, our mask-free nanolithographic tool is enabled by an infinite series of dynamic light interference event and implemented by multiscale optical simulations. The generated library of nanoarrays can be precisely and versatilely engineered and cover wide ranges of biologically relevant nanotopographies from lines, dots to grids, from sub-100 nm to above 10 um sizes on a single substrate. As a proof-of-concept for stem cell applications, we mapped nanotopography-regulated axonal alignment from stem cell-derived neurons on a representative 1D combinatorial nanoarray. By identifying most optimal topographical conditions to guide axonal alignment from the mapping, we further demonstrated the potential of our nanoarray platform for instructing the design of clinically relevant cell-transplantation biomaterials.

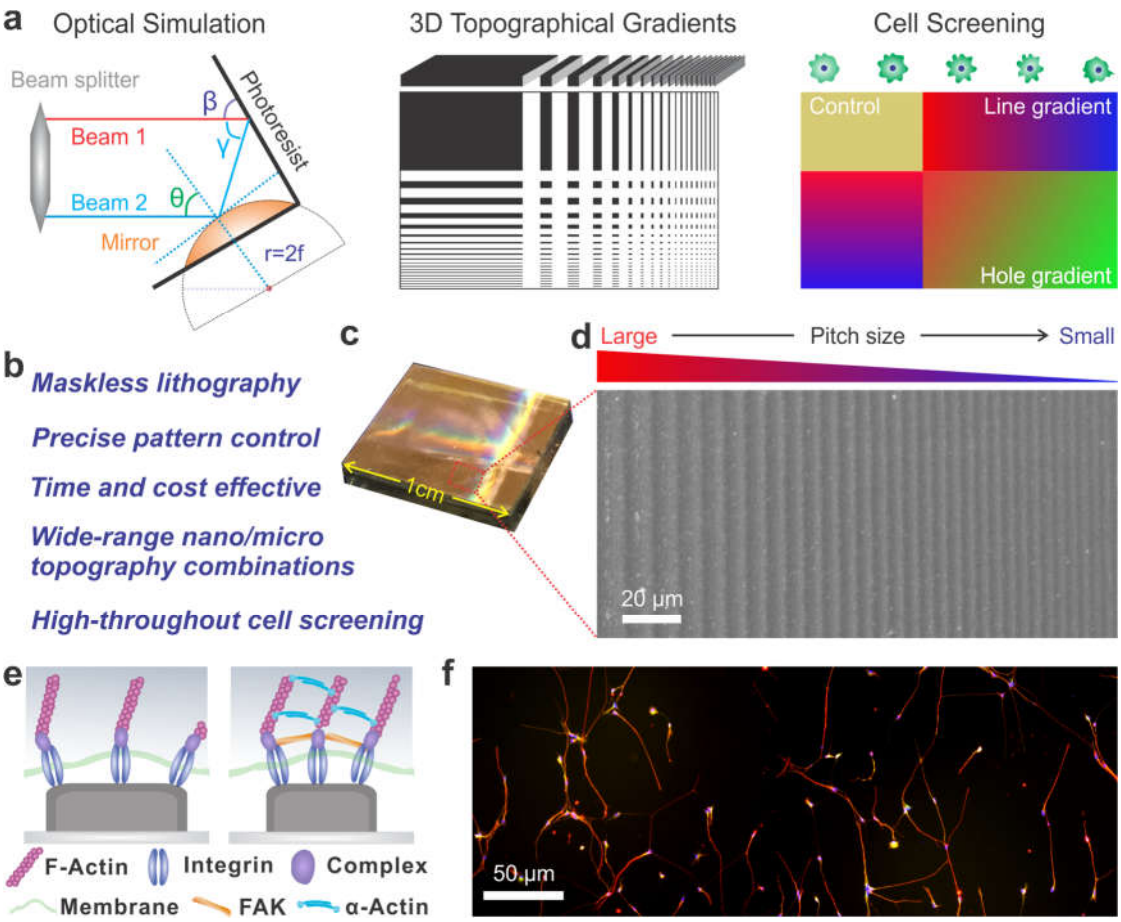

Figure 5-1. Generating libraries of combinatorial nanoarray by GIL for high throughput screening of nanotopographically regulated cell behaviors. a, High-throughout cell screening based on the optical simulation, development of interference lithography and stem cell analysis. b, Advantages of the nanotopographical chip-based mapping of cell behaviors. c-d, Photograph (c) and SEM (d) of the nanotopographical chip generated by GIL. e-f, Schematic diagram of differential control over cytoskeletal arrangement of stem cells (e) and immunostaining results indicating the differential neuronal differentiation and axonal alignment of differentiated neurons (f) on the nanotopographical chip.

5.1.2 Methods

Synthesis of nanotopographical hybrid nanoarrays

On a glass substrate, a photoresist (AZ 2020) diluted by EBR solvent was spin-coated. Then the substrate was baked at 100 degrees on a hot plate before it undergoes exposure under UV interference. To create the regular nanoarrays, vertical setup of interferometer and substrate was used. To generate the gradient nanotopographical arrays, an aluminum-coated and curved mirror with different focal lengths was used. In a typical synthesis, laser exposure of 15 seconds was used for the generation of line patterns. To fabricate nanodot patterns, double exposure with rotation of substrate with different angles was used. After the laser exposure, one minute post-baking at 120 degree on a hot plate was performed. Afterwards, the nanotopographies was developed using a developer solution directly purchased from the company.

Mapping of neuronal differentiation from neural stem cells

To map the nanotopography-regulated stem cell behaviors, human neural progenitor cells (hNPC, Millipore) were used as a proof-of-concept. Polymer-based nanotopographical chip was first incubated with Matrigel (Thermo Fisher) at a concentration of 50 ug/ml for one hour, then hNPC was seeded at a density of 40k/cm^2. Then the cells were allowed to differentiate on the chip for one week before fixation and immunostaining were performed. The conditions of cell culture, fixation and immunostaining were kept the same as mentioned in the above sections. TuJ1 antibody and MAP2 antibody were purchased from Biolegend. Large image collection on the nanotopographical chip was collected using Nikon Ti series fluorescent microscope. Axonal directionality was analyzed using Image J.

5.1.3 Results and discussion

Generation of combinatorial nanoarray

Our method to generate large-scale combinatorial nanoarray covering wide-range of nanostructures is achieved by: i) creating a series of dynamic interference events with continuously changing of interference angles; and ii) exposing light-sensitive polymers to the dynamic light interfering fields and converting them into 3D nanotopographical gradients. To synthesize nanostructures with a high resolution, ultraviolet (UV) lasers were used as the interference light source. Conventionally, after passing through light splitter, one beam (Beam 2) of the slotted UV laser will be directed to a linear mirror and then interfere with the original laser beam (Beam 1) at a constant angle, thereby generating a static interference field throughout the whole substrate to form the homogenous nanostructures[618,619]. To break the static interference into dynamic interference events, we added convex mirror operation and splitted the optical pathways of Beam 2 into a series of light waves with spatially differential reflecting angles. Then the splitted light waves will interfere with the static light beam (Beam 1) in a continuous manner. Efforts have been dedicated to fabricating heterogenous nanostructures through unsymmetrical interference pathways; however, no successful attempts have been made to yield a significant nanotopographical change (more than 100 nm or 10% in pitch changes) that are essential for most practical applications[17,145,157,176,353,370,379,388,393,620]. To this end, we first performed descriptive and quantitative optical simulations to design interference pathways for achieving combinatorial nanoarrays covering a wide spectrum of topographies (Figure 5-2). From our simulation results, there is a dramatic difference on the interference patterns resulted from the mirror geometry: within the same distance of light field and with identical

focal lengths, convex mirror-based interferometer generates higher degree changes of interference angle compared to the concave mirror-based interferometer. Also, changes on the relative angle between the mirror and the interference plane lead to fundamentally different interference pattern as well. For example, when the angle is above a certain value, all the interference light (Beam 2) will be reflected away from the collecting plane (in the experiment, light-sensitive polymers will be at this plane). As a result, no interference will happen on the surface of the collection plane. On the other hand, when the angle is below a certain value, multiple (more than 3) beams start to interfere with each other randomly, leading to disordered and chaotic light fields. When the angles are in between, the changing speed of interference angles varies upon the angle between Beam 1 and the collection plane, suggesting their roles in controlling our nanotopographical patterns. While there are more parameters (e.g., focal lengths of the mirror) to be considered, these simulation results collectively provide the theoretical possibility and identified the critical parameters for achieving large-scale combinatorial nanoarrays.

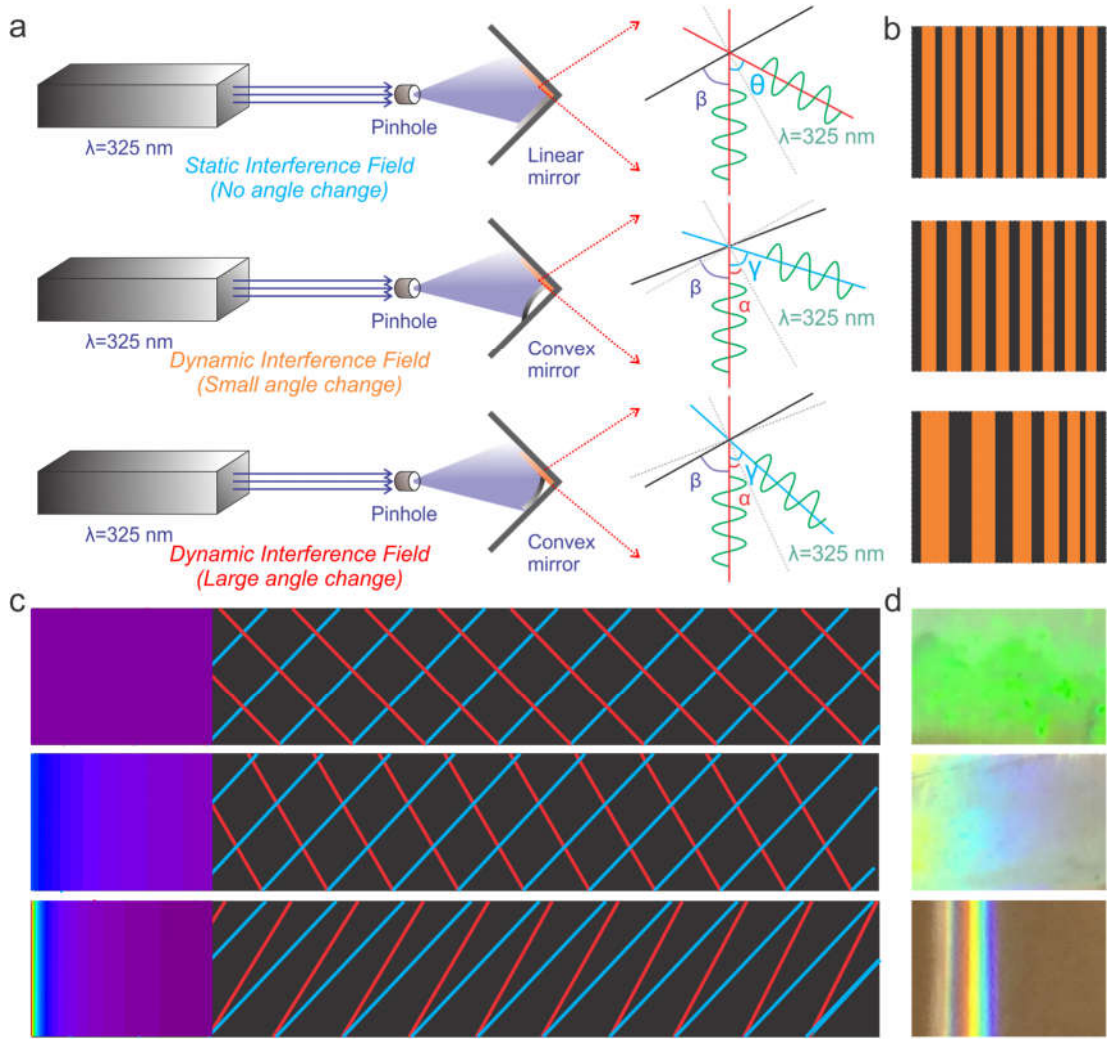

Figure 5-2. Design principles for GIL based mask-free generation of large-scale combinatorial nanoarrays. a-b, Optical setup (a) and expected topographies (b) of the regular and gradient interference lithography. c-d, Descriptive and quantitative optical simulation (c) guided design of optical setup for the GIL and the successful appearance of differential nanotopographies from the different optical setup (d).

Based on our in silico simulation results, we then set up the interference paths and synthesized our combinatorial nanoarrays (Figure 5-3). Immediately after the development of the exposed light-sensitive polymer, we observed a distinctive gradient hologram in the direction of interference angle changes (y-direction). On the vertical direction (x-direction), the hologram remains homogenous throughout the substrate (2.0 cm), indicating no change of pattern structures. As a control, patterns generated by conventional optical interference setup under the same light exposure settings showed no change of hologram on any of the directions. Under the optical microscope, a large number of 1D-line shaped nano- and micro- structures appear on the gradient pattern with the line-width constantly decreasing till beyond the optical detection limits (<500 nm) following y-direction. This trend well matches and supports the predictions in the simulation. Interestingly, while interference lithography has been widely applied for creating line-shaped nanostructures, such nanostructure with line-width above 10 um has not been achieved until the current work. To investigate the structures of smaller (<500 nm) nanotopographies and the resolution of our lithographical technique, we further performed field-emission scanning electron microscopy (FESEM) and atomic force microscopy (AFM)-based topographical mapping. Consistent with our observations under the optical microscope, nanotopographies remain in 1D-lined shape and continuously decrease their line widths following the y-direction until they achieve a minimum. Given the largest line widths of above 20 um and the typical fibrous structures of cell ECM, the nanoarrays fabricated using our lithography cover most of the ECM relevant nanotopographies. Such large numbers of nanotopographies in the scale of thousands would be much beneficial for systematically investigating ECM-dependent cellular behaviors. In addition, the line width within individual lines is highly

consistent for the large and medium nanoarrays with a slight decrease in the smaller pattern regions, which are better than most cutting-edge photolithography techniques and suggesting a good resolution, especially in the sub-um ranges. While e-beam lithography and dip-pen lithography can achieve better resolution and synthesize smaller nanotopographical arrays, it's very challenging for them to synthesize nanoarrays with thousands distinctive nanostructures ranging from sub-100 nm to 10 um, let alone the longitude direction of our nanoarray reaching the centimeter scale in length. Considering the relative large sizes of cells and the benefits of reproducing the nanotopographical effects on many cells, our large-scale and ordered combinatorial nanoarray serves as a unique platform for systematically mapping and studying topographies-regulated cell behaviors.

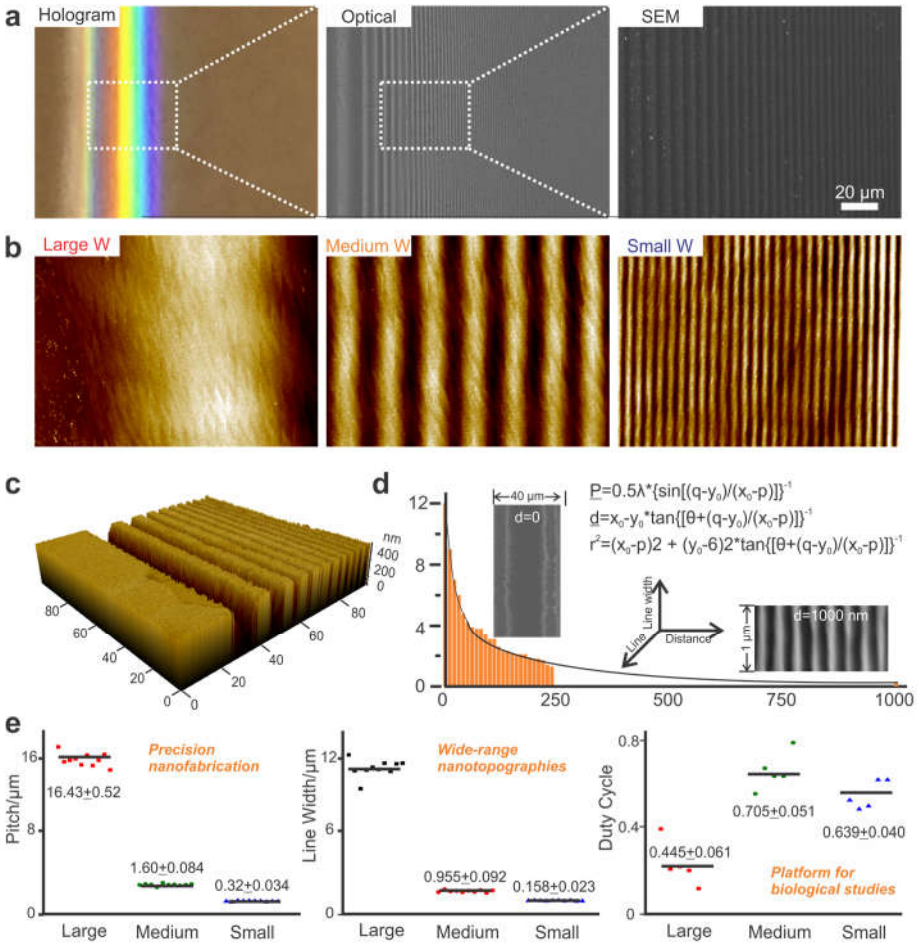

Figure 5-3. Large-scale, ordered and wide-range combinatorial nanoarrays precisely produced by GIL. a, Zoomed out photograph (left), zoomed in optical image (middle) and SEM images of the generated nanotopographical arrays. b, AFM images of the nanotopographical array at different regions of the chip, confirming the wide coverage of the nanotopographies in a single chip for high throughput cell mapping. c, 3D height profile of AFM images for the nanotopographical array. d, Wide distribution of nanotopographies of the nanoarray covering line width of sub 100 nm to above 20 μm. e, Statistical analysis on the nanoarray suggest the precision fabrication, wide-range nanotopographies and relatively constant duty cycle for reliable biological screening using the nanotopographical arrays.

A comprehensive library of combinatorial nanoarray

Not only precisely generates combinatorial nanotopographies in large scale and wide ranges, our method can also synthesize versatile combinatorial nanopatterns to meet the diverse needs in biological and physical systems despite being mask-free lithography (Figure 5-4). For example, nanostructures of natural and synthetic ECM can exist not only in aligned forms but also in a grid form. Similarly, depending on the speed of fiber diameter changes in the ECM, cellular behaviors such as migration may vary differentially in vitro and in vivo. A wide-range of the aspect ratio of nanostructures have also been reported with distinctively different biological and physical behaviors. For instance, localized surface plasmonic resonance widely used for waveguides and biosensors dramatically shift their extinction peaks from visible light to near-infrared with an increase of aspect-ratio. To demonstrate the versatile applications of our nanolithography, we generated a library of combinatorial nanoarrays. This library includes: i) 1D nanopatterns with varying speeds of pitch changing (NA 1-3); ii) 2D-grid shaped nanopatterns with varying pitch distributions (NA 4-6); iii) 0D-dotted nanopatterns with varying size distributions and aspect ratios (NA 7-8); iv) 2D-grid shaped nanopatterns with varying interlinking angles (NA 9); v) 0D-dotted nanopatterns with unidirectional change of size distributions (NA 10). Synthesis of these libraries of nanoarrays is guided by our optical simulation and achieved through the modulation of optical pathways (Methods). Considering the broad interests on these 0D, 1D and 2D nanostructures for cutting-edge biological or physical applications, and the importance of systematically correlating properties with a large number of nanostructures, the library of combinatorial nanoarrays we created represents a distinctive, comprehensive and versatile platform to identify optimal nanotopographies for

advanced applications. As a proof-of-concept, we applied the line-shaped and grid-shaped nanoarrays for studying NSC-nanotopography interactions and for guiding the design of clinical-relevant cell-transplantation scaffolds.

Figure 5-4. A comprehensive library of ordered combinatorial nanoarrays for versatile applications. a-d, Varying categories of 1D nanotopographical arrays with different speed of changing over the line widths. e-h, A wide range of 2D nanotopographical arrays with different shape, crosslinking angle, single anisotropic changes and grid patterns through molding.

Combinatorial nanoarray for axonal mapping

Recently, ECM nanotopography has been identified as one of the critical physical cues for regulating NSC proliferation, migration, differentiation and alignment[605-612]. Among them, guiding NSC differentiation into mature neurons with aligned axons using a biomaterial approach is of high interest for applications such as treating spinal cord injury (SCI)[275,451,621-623]. As such, many studies have been focused on identifying optimal topographies of artificial ECM for guiding neuronal differentiation of NSCs and for the alignment of axons. However, conclusions from these studies are not always consistent. For example, some report suggests grid patterns for most efficient neuronal differentiation and some others suggest line patterns[52,56,64,65,68,82,95,100,108,123,139,142,145,152,158,204,219,222,241-243,245,259,276,309,354,382,386,393,397,403,418,420-423,432,436,439,442,450,451,458,478,501,503]. Such inconsistency can be further compounded by the heterogeneous types of NSCs used for in vivo transplantations, requiring a case-by-case systematic investigation of nanotopographical-regulated NSC behaviors. To this end, we fabricated a combinatorial nanopattern with both line-shapes and grid-shapes and with dimensions ranging differently. The topographical variations are minimized to insignificant levels (<5% within the cell size of 10 um) to avoid undesired cellular polarization. Using neural stem cell derived from human hippocampus as a representative endogenous stem cell line, we then performed stem cell differentiation assay on laminin-coated nanoarray for 7 days (Figure 5-5). By immunostaining the cells differentiated on the nanoarray using neuronal markers such as TuJ1 and MAP2, the neuronal differentiation process and axonal alignment on thousands of different nanotopographies can be directly imaged and mapped on a single substrate. From our results, as expected, we found a dramatic higher level of axonal alignment in the line

patterned areas, which are consistent with most literature reports. Within the grid-patterned area, however, the nanotopographical effects on axonal alignment showed a much more complicated pattern. For example, when the vertically interlinked lines have similar width with high values (>1 um), the axons tend to align either directions with similar probabilities instead of following the 45 degree direction. On the other hand, when they have similar width with low values (<500 nm), the trend of axons growth was reversed. People may also be curious, when the vertically interlinked lines vary in widths, will the axons follow the line direction with larger width or smaller width? From our results, it appears that the line with larger width will be directing the axons more dominantly, especially when the difference in widths are high. Compared to the axonal alignment, less significant differences on the expression of neuronal markers (TuJ1 and MAP2) were found between different nanotopographies, except for the areas with very small line widths on both vertical directions. Such smaller differences could be attributed to the nature of the hippocampus-derived neural stem cells, which tend to differentiate into neurons in our defined media formulation. A higher expression of neuronal markers on the low-width grid nanopatterns, on the other hand, could be originated from the high focal adhesion levels on such small grid nanostructures with similar sizes to focal adhesion complex, which are known to upregulate downstream neuronal pathways. From these results, we identified some of the general rules for axonal alignment for neurons and neuronal differentiation for NSCs when they're interfaced with varying nanotopographies.

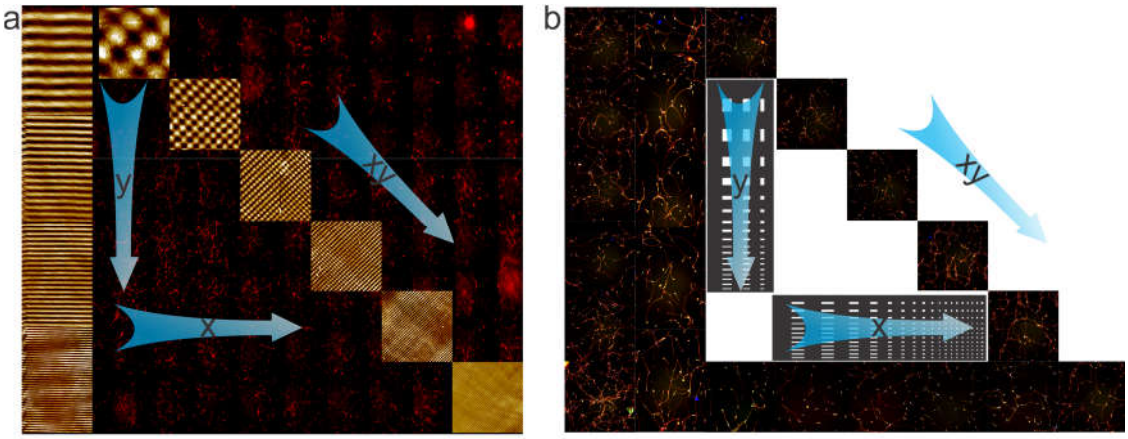

Figure 5-5. GIL-enabled systematic studies on wide-range of nanotopographically regulated cell behaviors. a, A collection of dot nanoarray library for the high throughput mapping of stem cell differentiation. Each AFM image cover an area of 50 by 50 μm2. b, The immunohistological data collected on the nanotopographical array, which can be used for further correlation with the nanotopographies. Each immunostaining image cover an area of 1328 by 1328 μm^2.

To establish more quantitative correlations for precision biomaterial design for axonal alignment, we then moved on to correlate the neuronal behaviors on our nanoarray in a more quantitative model (Figure 5-6). As we observed a significant effect of nanotopography-regulated axonal alignment, we focused on a nanoline pattern. By repeating the stem cell assay on the nanoarray for 7 days, we imaged the axons and nuclei using TuJ1 immunostaining and DAPI staining. By tracing axons in the representative areas and dividing all traced axons into subsections with length of 3 um, we then generated a function [$\theta=f(y)$] between position (y) and axonal alignment angle (θ). As we have already mapped and obtained a function [$w=f(y)$] between position (y) and nanotopography (line width, w), we can then generate the following function: $\theta=f(w)$ and provide a map

directly correlating w and θ. Additionally, as our line patterns are unlimited in length in the x-direction, we can have a large number of axonal behavioral replicates to get probability distributions on a specific pattern geometry, which are desired as certain level of randomness always existing in individual cell behaviors. Strictly following these steps, we successfully provided a systematic mapping of axonal alignment probabilities in response to varying nanotopographies (x-direction is set as 0 degree). From our probability map, plain substrates show no specific angle distributions. However, right across the boundary of nanopatterns, we observed an instant accumulation in the region below 45-degree, indicating a significant increase of alignment on this nanotopography. Such increases in alignment is expected, as both micro-sized and nanosized line patterns have shown to guide axonal alignment. This alignment continued with decreasing the line widths, with a further increase. When it reaches below certain pitch, however, a second boundary seems to appear, with alignment angles shifting more towards in the 40-90 degree region, which corresponds to a reduced level of alignment. Interestingly, while we are not clear about the behind mechanism, the second boundary located width that is similar to the diameters of axons and seems related to the change of neuronal behaviors. To better understand how specific nanotopographies lead to varying level of axonal alignment, further experiments are clearly essential. However, using our nanoarray-based platform, we can gain more insights into the role of topographical cues and better identify the proper nanostructures for controlling neuronal behavior or stem cell behaviors in a high throughput manner.

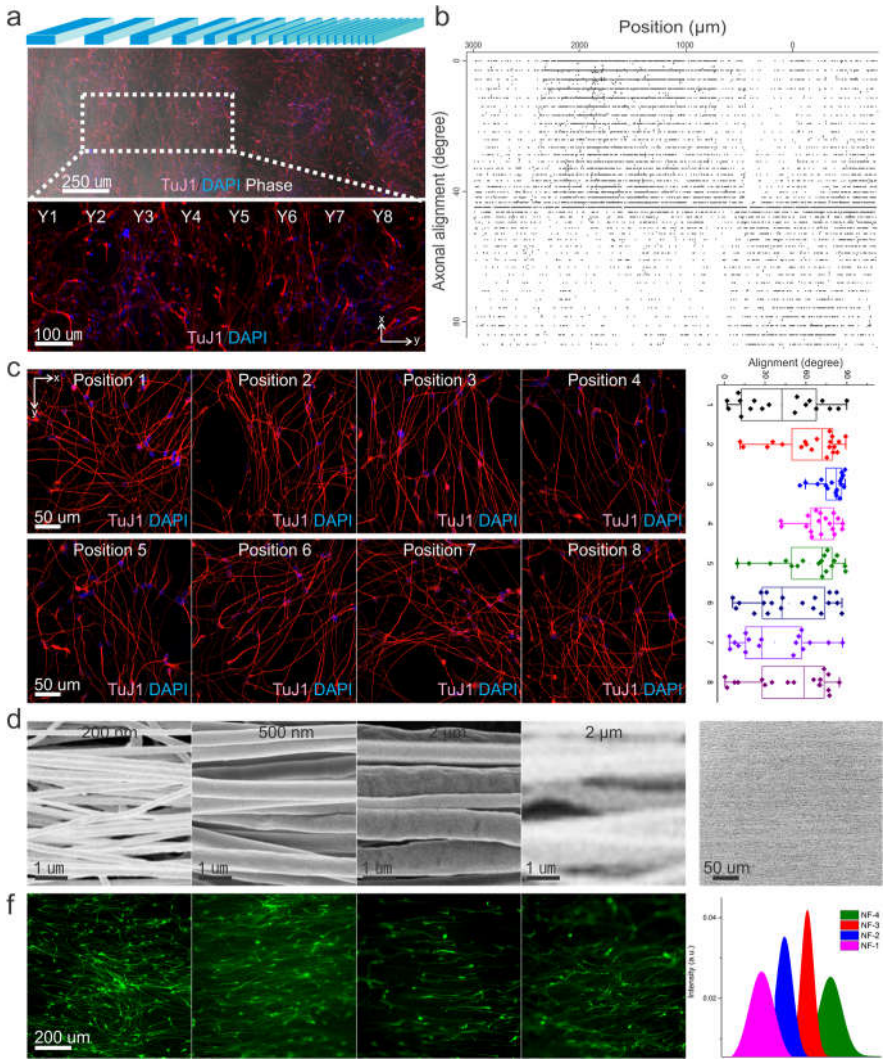

Figure 5-6. GIL-enabled quantitative mapping of axonal behaviors for guiding design of clinically relevant cell-transplantation bioscaffolds. a, 1D nanotopographical array-based mapping of neuronal differentiation from neural stem cells. b, Directionality map derived from the mapping result in a. c, Representative immunostaining images in the zoomed in position listed in a and the corresponding statistical analysis (graph on the right). d, Aligned nanofibers with varying diameters as a modeling biomaterial system to validate the mapping results. f, Immunostaining images on the neurons differentiated from neural stem cells for one week and the summarized directionality statistics on these nanofibers.

Combinatorial nanoarray for guiding biomaterial design

Nanotopography have become one of the most important factors in designing scaffolds both for in vitro stem cell research and for in vivo stem cell transplantation. One example is aligned nanofiber with varying fiber diameters can lead to differential responses from neurons polarization. Given the wide range and large numbers of nanotopographies existing in natural ECM and biomaterials, the combinatorial nanoarray generated by our lithography technique could provide a suitable platform for systematical identification of nanotopographical cues. To test our hypothesis, we generated aligned nanofibers with diameters nearby the optimal regions (500 nm, denoted as NF 500) identified by our nanoarray platform. Specifically, polycaprolactone (PCL) was selected as the polymer source as it has been clinically applied for biomedical sutures and PCL nanofibers have been under intensive development for clinical cell transplantation applications. On PCL NF 500, stem cells were cultured and differentiated for 7 days and then fixed and immunostained under the same condition as nanoarray experiments. As control groups, stem cell assays on nanofibers with different diameters of 200 nm, 1000 nm and 2000 nm (denoted as NF 200, NF 1000 and NF 2000, respectively) were also performed. By analyzing the level of axonal alignment using Image J, in general, better alignment can be found on the nanofibers compared to the nanoarrays with similar line widths. This could be attributed to the significantly higher (>300 nm) topographies in the nanofibers compared to our substrates (around or smaller than 100 nm). However, among the 4 different nanofibers, the one around 500 nm clearly showed the highest level of alignment, which well matches the trend predicted on our combinatorial nanoarray. To check whether such predictions could be applicable for other stem cell lines, we further repeated the

experiments on nanoarrays and nanofibers using an iPSC derived NSC, which has a higher clinical relevance for cell transplantation applications. From the axonal mapping results on nanoarrays, optimal alignment regions were downshifted to around 500 nm, which could be due to thinner axon diameters of neurons differentiated from iPSC-NSCs. Consistent with this result, neurons differentiated on NF 500 demonstrate the highest level of axonal alignment compared to all the other 3 controls, thereby supporting the positive correlation between axonal mapping and results from transplantable tissue-engineering scaffolds. Collectively, these results suggest the potential of the combinatorial nanoarray for identifying optimal ranges of nanotopographies for designing clinical relevant cell transplantation scaffolds, despite the many variables existing between the nanoarray and nanofibers.

5.1.4 Conclusions and Outlook

Nanotopographical regulation over cellular fates are fundamental for regenerative medicine and understanding diseases and injuries. However, current approach to study such process has not been satisfactory towards comprehensive, systematic and unbiased understanding on nanotopographical effects. Addressing this critical challenge, we integrated optical simulation and developed a new lithographical tool which can generate wide range biologically relevant nanotopographies in a highly precise and controlled manner. The successful creation of this large scale and comprehensive library of nanotopography enabled the systematic mapping of substrate regulated stem cell behaviors covering wide range of substrate parameters, thereby paving the way towards high throughput screening of nanotopographies for tissue engineering scaffolds. Our established

method can be widely applicable for the study of other nanotopographies regulated biological processes such as disease development and cancer migration. We also expect the developed nanolithographic method will facilitate the optimization of nanostructure substrate in many other fields of nanotechnology such as nanoplasmonics.

Chapter 6: Summary and Perspectives

In the past two decades, people have witnessed the fast development of the field of nanomedicine. Taking advantages of the large surface area and the unique physicochemical properties of nanomaterials, nanomedicine has shown great promise and clinical potential in many important fields of medicine which includes cancer therapy, regenerative medicine and disease diagnosis and biosensing. For these various types of applications, current material design principles have been mostly based on tailoring the size, shape, dimensionality, composition, functionalization and assembly of the nanomaterials to achieve properties on demand for the treatment of diseases or injuries. Among them, dimensionality is one of the most critical and general aspects as it directly determines the cellular uptake in vitro, circulation in vivo and the quantum confinement in many optical and electronic materials, providing the guidance of nanomaterial-based physical therapy, imaging and sensing functions in a direct manner. Considering this and bearing the ultimate goal of nanomedicine in mind, which is eventually to understand and cure human diseases and injuries, the 0D, 1D and 2D nanomaterials-based applications in cancer therapy, stem cell therapy and biosensing were reviewed in the introduction. As these important topics cover broad areas in chemistry and biology, representative examples that are relevant to my Ph.D. work are focused in each section to provide certain guideline regarding the design of nanomaterials for different applications. For cancer therapy, gold nanoparticle-based biomimicry systems, nanoneedle-based cellular injection-based drug delivery systems and MnO_2 nanosheets-based chemodynamic therapy system were discussed as examples for the 0D, 1D and 2D nanotherapeutics. For stem cell therapy, which is the major focus of my Ph.D. study, the background of regenerative medicine was comprehensively discussed. 0D

biomimetic nanoparticles, actuation nanoparticles, 1D polymeric nanofibers and 2D graphene-based scaffolds were used as examples in explaining the unique applications of nanomaterials in tissue engineering based on dimensionalities. For biosensing, the 0D plasmonic biosensors, 1D silicone nanowire-based electronic sensors and 2D graphene-based biosensors were also briefly covered. Collectively, these examples of multidimensional nanomaterials for different applications suggest the importance of dimensionality in nanomedicine and provide some general principles into how to design nanomaterials for specific disease treatment. Based on these design principles, I carried out my Ph.D. work by integrating the different types of nanomaterials into nanohybrids for in vitro and in vivo cancer killing, for advanced stem cell therapy and optical based biosensing applications. Among them, the most significant scientific contribution from me is the successful development of a category of biodegradable 2D nanomaterial-assembled 3D nanoscaffolds for tissue engineering. Overall, I led or co-led eight projects during the Ph.D. course, which are discussed in the following four chapters.

In the first chapter, three projects focusing on the development of 0D-2D hybrid nanomaterials for cancer therapy was discussed. One of the unique advantages of nanomaterials-based cancer killing is that nanomaterials can provide unique physical properties to present stress to cancer directly. For example, by converting tissue-transparent NIR optical signals into thermal energy, both carbon-based and noble metal-based NIR photothermal therapy have been explored. Taking advantage of the mechanical flexibility of 2D carbon nanomaterials, we successfully synthesized 2D graphene nanosheets encapsulated gold nanoparticle for photothermal therapy. In the first project, the photothermal therapy was tested on a cancer spheroid model, which is generated by

polymeric templating over microwells. In the second project, gene therapy based on single strand DNA was further incorporated into the therapeutic modality, and active targeting ligand of RGD was conjugated through non-covalent binding, leading to the success of in vivo cancer therapy with tumor suppression over 90%. In the third project, chemodynamic therapy based on the depletion of glutathione and induction of Fenton reaction was adapted into the photothermal therapy by replacing graphene with MnO_2 nanosheets and replacing gold nanoparticles with iron oxide nanoparticles embedded in a graphite matrix. The step-by-step advancement of the hybrid nanoparticle system eventually lead to the near 100% ablation of tumor with simultaneous in vivo cancer imaging modality included in a single platform, thereby providing promising alternatives to current nanomedicine-based cancer theranostics. In the future, we're planning to further improve the photothermal efficiency by replacing the 0D plasmonic nanostructures with 1D gold nanorods, which have stronger electromagnetic enhancement of light in the NIR region compared to 0D gold nanoparticles. As a material chemist, the unique property of graphene for cancer therapy inspired my exploration of graphene-based regenerative medicine applications. However, the sp2 bonded carbon structure determines the slow - if any - biodegradation nature of graphene-based cell scaffolds, which not only impede the integration of stem cells into the injury sites but also induce chronic inflammation. To this end, a new scaffold based on the assembly of 2D MnO_2 nanosheets and ECM components were developed for bioapplications, which is discussed in Chapter 2. Similar to graphene-based scaffolds, MnO_2-based nanoscaffolds enhance stem cell neuronal differentiation through the strong binding with laminin proteins and by delivering neurogenic drugs. However, MnO_2-nanoscaffold is biodegradable by cells alone without requiring any toxic exogenous cues

and in a highly controlled manner. By modulating the biodegradation rates, rate of drug delivery can be controlled to meet the needs of different applications. Using the developed MnO_2-nanoscaffold, and incorporating a Notch inhibitor DAPT, the successful transplantation of iPSC-NSCs were achieved in vivo, leading to improvements on the neurological functions and suggesting its potential for clinical stem cell therapy. In the second part of the chapter, MnO_2 nanoscaffolds were used with similar composition, but develop stem cell therapy from the perspective of scaffold-free tissue engineering. Scaffold-free tissue engineering is recently developed and advantageous as no toxic degradation product or fibrosis associated with in vivo transplantation of biomaterials will occur. Taking advantage of the highly controllable degradation of MnO_2 nanoscaffolds, the cells assembled on a porous MnO_2 substrate can be transformed into scaffold-free form by simple treatment of biocompatible reductants such as Vitamin C. In addition, by modulating the porosity of the substrate, we can use negative pressure to guide the assembly of cells into biomimicry patterns, which are desired for cell modeling as well as more advanced tissue regeneration where multiple cell types need to be organized in a spatially controlled manner. Moving forward, it is critical to explore other biodegradable candidates of 2D nanomaterials as building blocks of the hybrid nanoscaffold, which allows a further dimension of tuning the biodegradation of scaffolds and may further fasten the cleavage under the Vitamin C under biocompatible conditions. Meanwhile, as a new composition for tissue engineering, I also expect the rapid expansion of the library of MnO_2-based nanoscaffolds. For example, we're currently developing the 1D MnO_2 nanotubes-assembled hybrid scaffolds, MnO_2-chitosan and PCL-based nanoscaffolds and any other polymeric components that have hydrophobic, hydrogen bonding-based or metal

π interactions with MnO_2. These scaffolds are being applied for a variety of applications other than CNS, which include cardiomyocyte differentiation, muscle differentiation, osteogenesis and many others.

While treating disease and injuries are the ultimate goal of nanomedicine, biosensing provides information for such therapeutic process. In Chapter 3, I focused on one example on SERS-based gene detection for monitoring stem cell differentiation. The SERS substrate is composed of 1D plasmonic nanostructured encapsulated by 2D graphene sheets. By combining the gold-based electromagnetic enhancement and graphene-based chemical enhancement mechanisms, we can achieve a highly sensitive DNA detection. Based on the unique and reversible graphene-oligonucleotide interactions, selective DNA detection can be achieved. Such highly sensitive and selective gene detection was further successfully applied for monitoring the neuronal differentiation of stem cells, which is essential for clinical stem cell therapy. Currently, we're also applying this system for the monitoring of live cells and also developing flexible electronics and optics for more clinical relevant biosensing applications.

In the first three chapters, hybrids of 0D, 1D and 2D nanomaterials were developed and applied for cancer therapy, stem cell therapy and biosensing. Even though there is clear rationale for the selection of nanomaterials of different shape and sizes, there is still lacking general design principles and high throughput screening tool for directly and quantitatively identifying the proper range of nanostructures in nanomedicine. To this end, in Chapter 4, a platform that maps the cellular responses to different nanostructures was developed. This platform is enabled by advanced interference optics-based synthesis of a large library of nanostructure in the order of hundreds of thousands, from sub 100 nm to above 20 μm,

from 0D nanodots, 1D nanolines to 2D grids. Utilizing this platform, the systematic and quantitative mapping of neuronal differentiation from stem cells is directly allowed for providing direct design principles in scaffold-based stem cell transplantation. As a general platform, the nanotopographical chip can be widely applied for screening the nanostructure-dependent biological applications. For example, we're investigating the nanotopographies-dependent biosensing based on the Raman intensities or the metal-enhanced fluorescence effects.

In conclusion, to advance nanomedicine towards clinical applications in cancer therapy, stem cell therapy and biosensing, multidimensional hybrid nanomaterials were developed. The basic design principles behind such advancement in theranostics are also extensively discussed and supported. By further improving the efficiency in the treatment and diagnosis in vivo, I'm hoping to see some of the product can contribute to the human healthcare in more clinical settings.

1 Sy-Tsong Dean Chueng, L. Y., Yixiao Zhang, Ki-Bum Lee. Multidimensional nanomaterials for the control of stem cell fate. *Nano Convergence* **3** (2016).

2 Hare, J. I. *et al.* Challenges and strategies in anti-cancer nanomedicine development: an industry perspective. *Advanced drug delivery reviews* **108**, 25-38 (2017).

3 Juliano, R. Nanomedicine: is the wave cresting? *Nature reviews Drug discovery* **12**, 171 (2013).

4 Min, Y., Caster, J. M., Eblan, M. J. & Wang, A. Z. Clinical translation of nanomedicine. *Chemical reviews* **115**, 11147-11190 (2015).

5 Porter, A. L. & Youtie, J. Where does nanotechnology belong in the map of science? *Nature Nanotechnology* **4**, 534 (2009).

6 Pelaz, B. *et al.* Diverse Applications of Nanomedicine. *ACS Nano* **11**, 2313-2381, doi:10.1021/acsnano.6b06040 (2017).

7 Huang, W. *et al.* Nanomedicine-based combination anticancer therapy between nucleic acids and small-molecular drugs. *Advanced drug delivery reviews* **115**, 82-97 (2017).

8 Jain, R. K. & Stylianopoulos, T. Delivering nanomedicine to solid tumors. *Nature reviews Clinical oncology* **7**, 653 (2010).

9 Tong, R. & Kohane, D. S. New strategies in cancer nanomedicine. *Annual review of pharmacology and toxicology* **56**, 41-57 (2016).

10 Zhang, S., Geryak, R., Geldmeier, J., Kim, S. & Tsukruk, V. V. Synthesis, assembly, and applications of hybrid nanostructures for biosensing. *Chemical reviews* **117**, 12942-13038 (2017).

11 Chen, Y., Tan, C., Zhang, H. & Wang, L. Two-dimensional graphene analogues for biomedical applications. *Chemical Society Reviews* **44**, 2681-2701 (2015).

12 Zhou, H., Liu, J., Xu, J.-J., Zhang, S.-S. & Chen, H.-Y. Optical nano-biosensing interface via nucleic acid amplification strategy: construction and application. *Chemical Society Reviews* **47**, 1996-2019 (2018).

13 Mejía-Salazar, J. & Oliveira Jr, O. N. Plasmonic Biosensing: Focus Review. *Chemical reviews* **118**, 10617-10625 (2018).

14 Chen, P., Huang, N.-T., Chung, M.-T., Cornell, T. T. & Kurabayashi, K. Label-free cytokine micro-and nano-biosensing towards personalized medicine of systemic inflammatory disorders. *Advanced drug delivery reviews* **95**, 90-103 (2015).

15 Zhang, A. & Lieber, C. M. Nano-bioelectronics. *Chemical reviews* **116**, 215-257 (2015).

16 Shi, J., Kantoff, P. W., Wooster, R. & Farokhzad, O. C. Cancer nanomedicine: progress, challenges and opportunities. *Nature Reviews Cancer* **17**, 20 (2017).

17 Kim, J., Kim, J., Jeong, C. & Kim, W. J. Synergistic nanomedicine by combined gene and photothermal therapy. *Advanced drug delivery reviews* **98**, 99-112 (2016).

18 Zhang, S., Geryak, R., Geldmeier, J., Kim, S. & Tsukruk, V. V. Synthesis, assembly, and applications of hybrid nanostructures for biosensing. *Chemical reviews* **117**, 12942-13038 (2017).

19 Chen, Y., Tan, C., Zhang, H. & Wang, L. Two-dimensional graphene analogues for biomedical applications. *Chemical Society Reviews* **44**, 2681-2701 (2015).

20 Onoshima, D., Yukawa, H. & Baba, Y. Multifunctional quantum dots-based cancer diagnostics and stem cell therapeutics for regenerative medicine. *Advanced drug delivery reviews* **95**, 2-14 (2015).

21 Liu, X. & Wang, S. Three-dimensional nano-biointerface as a new platform for guiding cell fate. *Chemical Society Reviews* **43**, 2385-2401 (2014).

22 Urie, R., Ghosh, D., Ridha, I. & Rege, K. Inorganic Nanomaterials for Soft Tissue Repair and Regeneration. *Annual review of biomedical engineering* **20**, 353-374 (2018).

23 Peng, S. *et al.* Multi-functional electrospun nanofibres for advances in tissue regeneration, energy conversion & storage, and water treatment. *Chemical Society Reviews* **45**, 1225-1241 (2016).

24 Saraniti, M. Artificial cells: Designing biomimetic nanomachines. *Nature nanotechnology* **3**, 647 (2008).

25 Yoo, J.-W., Irvine, D. J., Discher, D. E. & Mitragotri, S. Bio-inspired, bioengineered and biomimetic drug delivery carriers. *Nature reviews Drug discovery* **10**, 521 (2011).

26 Green, J. J. & Elisseeff, J. H. Mimicking biological functionality with polymers for biomedical applications. *Nature* **540**, 386 (2016).

27 Stewart, M. P. *et al.* In vitro and ex vivo strategies for intracellular delivery. *Nature* **538**, 183 (2016).

28 Parodi, A. *et al.* Synthetic nanoparticles functionalized with biomimetic leukocyte membranes possess cell-like functions. *Nature nanotechnology* **8**, 61 (2013).

29 Yin, P. T., Shah, S., Chhowalla, M. & Lee, K. B. Design, Synthesis, and Characterization of Graphene-Nanoparticle Hybrid Materials for Bioapplications. *Chemical Reviews* **115**, 2483-2531, doi:10.1021/cr500537t (2015).

30 Solanki, A., Kim, J. D. & Lee, K. B. Nanotechnology for regenerative medicine: nanomaterials for stem cell imaging. *Nanomedicine* **3**, 567-578, doi:10.2217/17435889.3.4.567 (2008).

31 Sawyers, C. Targeted cancer therapy. *Nature* **432**, 294 (2004).

32 Blau, H. M., Brazelton, T. & Weimann, J. The evolving concept of a stem cell: entity or function? *Cell* **105**, 829-841 (2001).

33 Dvir, T., Timko, B. P., Kohane, D. S. & Langer, R. Nanotechnological strategies for engineering complex tissues. *Nature nanotechnology* **6**, 13 (2011).

34 Willets, K. A. & Van Duyne, R. P. Localized surface plasmon resonance spectroscopy and sensing. *Annu. Rev. Phys. Chem.* **58**, 267-297 (2007).

35 Chueng, S.-T. D., Yang, L., Zhang, Y. & Lee, K.-B. Multidimensional nanomaterials for the control of stem cell fate. *Nano convergence* **3**, 23 (2016).

36 Meyer, R. A. & Green, J. J. Shaping the future of nanomedicine: anisotropy in polymeric nanoparticle design. *Wiley Interdisciplinary Reviews: Nanomedicine and Nanobiotechnology* **8**, 191-207 (2016).

37 Blanco, E., Shen, H. & Ferrari, M. Principles of nanoparticle design for overcoming biological barriers to drug delivery. *Nature biotechnology* **33**, 941 (2015).

38 Truong, N. P., Whittaker, M. R., Mak, C. W. & Davis, T. P. The importance of nanoparticle shape in cancer drug delivery. *Expert opinion on drug delivery* **12**, 129-142 (2015).

39 Behzadi, S. *et al.* Cellular uptake of nanoparticles: journey inside the cell. *Chemical Society Reviews* **46**, 4218-4244 (2017).

40 Salatin, S., Maleki Dizaj, S. & Yari Khosroushahi, A. Effect of the surface modification, size, and shape on cellular uptake of nanoparticles. *Cell biology international* **39**, 881-890 (2015).

41 Calderón, L. *et al.* Release of airborne particles and Ag and Zn compounds from nanotechnology-enabled consumer sprays: Implications for inhalation exposure. *Atmospheric environment* **155**, 85-96 (2017).

42 Calderon, L., Yang, L. Y., Lee, K.-B. & Mainelis, G. Characterization of Airborne Particle Release from Nanotechnology-enabled Clothing Products. *Journal of Nanoparticle Research* (2018).

43 Christopher Rathnam, S.-T. D. C., Letao Yang, Ki-Bum Lee. Advanced Gene Manipulation Methods for Stem Cell Theranostics. *Theranostics* **7**, 2775-2793 (2017).

44 Dey, G., Yang, L., Lee, K. B. & Wang, L. Characterizing Molecular Adsorption on Biodegradable MnO2 Nanoscaffolds. *The Journal of Physical Chemistry* (2018).

45 Jinping Lai, A. Y., Letao Yang, Yixiao Zhang, Birju P Shah, Ki-Bum Lee. Development of Photoactivated Fluorescent N-Hydroxyoxindoles and Their Application for Cell-Selective Imaging. *Chemistry–A European Journal* (2016).

46 Jinping Lai, B. P. S., Yixiao Zhang, Letao Yang, Ki-Bum Lee. Real-Time Monitoring of ATP-Responsive Drug Release Using Mesoporous-Silica-Coated Multicolor Upconversion Nanoparticles. *ACS Nano* **9**, 5234-5245 (2015).

47 Kim, T.-H. *et al.* Controlling Differentiation of Adipose-Derived Stem Cells Using Combinatorial Graphene Hybrid-Pattern Arrays. *ACS Nano* **9**, 3780-3790 (2015).

48 Lee, J. H. *et al.* Nondestructive Real-Time Monitoring of Enhanced Stem Cell Differentiation Using a Graphene-Au Hybrid Nanoelectrode Array. *Advanced Materials* **30**, 1802762 (2018).

49 Lee, J. H. *et al.* Stem Cell Differentiation: Nondestructive Real-Time Monitoring of Enhanced Stem Cell Differentiation Using a Graphene-Au Hybrid Nanoelectrode Array (Adv. Mater. 39/2018). *Advanced Materials* **30**, 1870290 (2018).

50 Lee, J. M. *et al.* Generation of uniform-sized multicellular tumor spheroids using hydrogel microwells for advanced drug screening. *Scientific Reports* **8**, 17145 (2018).

51 Letao Yang, S.-T. D. C., Ying Li, Misaal Patel, Christopher Rathnam, Gangotri Dey, Lu Wang, Li Cai, Ki-Bum Lee. A biodegradable hybrid inorganic nanoscaffold for advanced stem cell therapy. *Nature Communications* (2018).

52 Shah, S. *et al.* Guiding Stem Cell Differentiation into Oligodendrocytes Using Graphene-Nanofiber Hybrid Scaffolds. *Advanced materials* **26**, 3673-3680 (2014).

53 Taewon T. Han, L. Y., Ki-Bum Lee, Gediminas Mainelis. Design and Development of a Novel Nanofiber Nasal Filter (NNF) to Improve Respiratory Health. *Aerosol and Air Quality Research* **18** (2018).

54 Yuan, S. *et al.* Preparation and Lithium Storage Performances of Mesoporous Fe3O4@ C Microcapsules. *ACS Applied Materials & Interfaces* (2011).

55 Zhang, H. *et al.* Synthesis and catalytic properties of Sb2S3 nanowire bundles as counter electrodes for dye-sensitized solar cells. *The Journal of Physical Chemistry C* **117**, 10285-10290 (2013).

56 Zhang, H. *et al.* Facet-dependent activity of bismuth sulfide as low-cost counter-electrode materials for dye-sensitized solar cells. *Journal of Materials Chemistry* **22**, 18572-18577 (2012).

57 Zhang, J. J., Lee, K.B., He, L., Seiffert, J., Subramaniam, P., Yang, L., Chen, S., Maguire, P., Mainelis, G., Schwander, S. & Tetley, T. D. Effects of a Nanoceria Fuel Additive on Physicochemical Properties of Diesel Exhaust Particles. *Environmental Science: Processes & Impacts* (2016).

58 Kim, T. H. *et al.* Controlling differentiation of adipose-derived stem cells using combinatorial graphene hybrid-pattern arrays. *ACS Nano* **9**, 3780-3790, doi:10.1021/nn5066028 (2015).

59 Shah, B. P. *et al.* Core-shell nanoparticle-based peptide therapeutics and combined hyperthermia for enhanced cancer cell apoptosis. *ACS Nano* **8**, 9379-9387, doi:10.1021/nn503431x (2014).

60 Qiu, H., Min, Y., Rodgers, Z., Zhang, L. & Wang, A. Z. Nanomedicine approaches to improve cancer immunotherapy. *Wiley Interdisciplinary Reviews: Nanomedicine and Nanobiotechnology* **9**, e1456 (2017).
61 Yallapu, M. M., Jaggi, M. & Chauhan, S. C. Curcumin nanoformulations: a future nanomedicine for cancer. *Drug Discovery Today* **17**, 71-80, doi:10.1016/j.drudis.2011.09.009 (2012).
62 Wicki, A., Witzigmann, D., Balasubramanian, V. & Huwyler, J. Nanomedicine in cancer therapy: Challenges, opportunities, and clinical applications. *Journal of Controlled Release* **200**, 138-157, doi:10.1016/j.jconrel.2014.12.030 (2015).
63 Wang, M. & Thanou, M. Targeting nanoparticles to cancer. *Pharmacological Research* **62**, 90-99, doi:10.1016/j.phrs.2010.03.005 (2010).
64 Wang, A. Z., Langer, R. & Farokhzad, O. C. in *Annual Review of Medicine, Vol 63* Vol. 63 *Annual Review of Medicine* (eds C. T. Caskey, C. P. Austin, & J. A. Hoxie) 185-198 (2012).
65 Valencia, P. M., Farokhzad, O. C., Karnik, R. & Langer, R. Microfluidic technologies for accelerating the clinical translation of nanoparticles. *Nature Nanotechnology* **7**, 623-629, doi:10.1038/nnano.2012.168 (2012).
66 Torchilin, V. P. Targeted pharmaceutical nanocarriers for cancer therapy and Imaging. *Aaps Journal* **9**, E128-E147, doi:10.1208/aapsj0902015 (2007).
67 Sutton, D., Nasongkla, N., Blanco, E. & Gao, J. M. Functionalized micellar systems for cancer targeted drug delivery. *Pharmaceutical Research* **24**, 1029-1046, doi:10.1007/s11095-006-9223-y (2007).
68 Sun, T. M. *et al.* Engineered Nanoparticles for Drug Delivery in Cancer Therapy. *Angewandte Chemie-International Edition* **53**, 12320-12364, doi:10.1002/anie.201403036 (2014).
69 Shi, J. J., Kantoff, P. W., Wooster, R. & Farokhzad, O. C. Cancer nanomedicine: progress, challenges and opportunities. *Nature Reviews Cancer* **17**, 20-37, doi:10.1038/nrc.2016.108 (2017).
70 Rosenholm, J. M., Sahlgren, C. & Linden, M. Towards multifunctional, targeted drug delivery systems using mesoporous silica nanoparticles - opportunities & challenges. *Nanoscale* **2**, 1870-1883, doi:10.1039/c0nr00156b (2010).
71 Park, J. H. *et al.* Polymeric nanomedicine for cancer therapy. *Progress in Polymer Science* **33**, 113-137, doi:10.1016/j.progpolymsci.2007.09.003 (2008).
72 Oerlemans, C. *et al.* Polymeric Micelles in Anticancer Therapy: Targeting, Imaging and Triggered Release. *Pharmaceutical Research* **27**, 2569-2589, doi:10.1007/s11095-010-0233-4 (2010).
73 Naksuriya, O., Okonogi, S., Schiffelers, R. M. & Hennink, W. E. Curcumin nanoformulations: A review of pharmaceutical properties and preclinical studies and clinical data related to cancer treatment. *Biomaterials* **35**, 3365-3383, doi:10.1016/j.biomaterials.2013.12.090 (2014).
74 Moghimi, S. M., Hunter, A. C. & Murray, J. C. Nanomedicine: current status and future prospects. *Faseb Journal* **19**, 311-330, doi:10.1096/fj.04-2747rev (2005).
75 Melancon, M. P., Zhou, M. & Li, C. Cancer Theranostics with Near-Infrared Light-Activatable Multimodal Nanoparticles. *Accounts of Chemical Research* **44**, 947-956, doi:10.1021/ar200022e (2011).

76 MaHam, A., Tang, Z. W., Wu, H., Wang, J. & Lin, Y. H. Protein-Based Nanomedicine Platforms for Drug Delivery. *Small* **5**, 1706-1721, doi:10.1002/smll.200801602 (2009).

77 Maeda, H., Bharate, G. Y. & Daruwalla, J. Polymeric drugs for efficient tumor-targeted drug delivery based on EPR-effect. *European Journal of Pharmaceutics and Biopharmaceutics* **71**, 409-419, doi:10.1016/j.ejpb.2008.11.010 (2009).

78 Maeda, H. Macromolecular therapeutics in cancer treatment: The EPR effect and beyond. *Journal of Controlled Release* **164**, 138-144, doi:10.1016/j.jconrel.2012.04.038 (2012).

79 Liu, Y. Y., Miyoshi, H. & Nakamura, M. Nanomedicine for drug delivery and imaging: A promising avenue for cancer therapy and diagnosis using targeted functional nanoparticles. *International Journal of Cancer* **120**, 2527-2537, doi:10.1002/ijc.22709 (2007).

80 Liu, J. *et al.* pH-Sensitive nano-systems for drug delivery in cancer therapy. *Biotechnology Advances* **32**, 693-710, doi:10.1016/j.biotechadv.2013.11.009 (2014).

81 Li, N., Zhao, P. X. & Astruc, D. Anisotropic Gold Nanoparticles: Synthesis, Properties, Applications, and Toxicity. *Angewandte Chemie-International Edition* **53**, 1756-1789, doi:10.1002/anie.201300441 (2014).

82 Lammers, T., Kiessling, F., Hennink, W. E. & Storm, G. Drug targeting to tumors: Principles, pitfalls and (pre-) clinical progress. *Journal of Controlled Release* **161**, 175-187, doi:10.1016/j.jconrel.2011.09.063 (2012).

83 Lammers, T., Aime, S., Hennink, W. E., Storm, G. & Kiessling, F. Theranostic Nanomedicine. *Accounts of Chemical Research* **44**, 1029-1038, doi:10.1021/ar200019c (2011).

84 Kim, B. Y. S., Rutka, J. T. & Chan, W. C. W. Current Concepts: Nanomedicine. *New England Journal of Medicine* **363**, 2434-2443, doi:10.1056/NEJMra0912273 (2010).

85 Johnstone, T. C., Suntharalingam, K. & Lippard, S. J. The Next Generation of Platinum Drugs: Targeted Pt(II) Agents, Nanoparticle Delivery, and Pt(IV) Prodrugs. *Chemical Reviews* **116**, 3436-3486, doi:10.1021/acs.chemrev.5b00597 (2016).

86 Jain, R. K. & Stylianopoulos, T. Delivering nanomedicine to solid tumors. *Nature Reviews Clinical Oncology* **7**, 653-664, doi:10.1038/nrclinonc.2010.139 (2010).

87 He, C. B., Liu, D. M. & Lin, W. B. Nanomedicine Applications of Hybrid Nanomaterials Built from Metal-Ligand Coordination Bonds: Nanoscale Metal-Organic Frameworks and Nanoscale Coordination Polymers. *Chemical Reviews* **115**, 11079-11108, doi:10.1021/acs.chemrev.5b00125 (2015).

88 Gullotti, E. & Yeo, Y. Extracellularly Activated Nanocarriers: A New Paradigm of Tumor Targeted Drug Delivery. *Molecular Pharmaceutics* **6**, 1041-1051, doi:10.1021/mp900090z (2009).

89 Greco, F. & Vicent, M. J. Combination therapy: Opportunities and challenges for polymer-drug conjugates as anticancer nanomedicines. *Advanced Drug Delivery Reviews* **61**, 1203-1213, doi:10.1016/j.addr.2009.05.006 (2009).

90 Firme, C. P. & Bandaru, P. R. Toxicity issues in the application of carbon nanotubes to biological systems. *Nanomedicine-Nanotechnology Biology and Medicine* **6**, 245-256, doi:10.1016/j.nano.2009.07.003 (2010).

91 Farokhzad, O. C. & Langer, R. Nanomedicine: Developing smarter therapeutic and diagnostic modalities. *Advanced Drug Delivery Reviews* **58**, 1456-1459, doi:10.1016/j.addr.2006.09.011 (2006).

92 Ernsting, M. J., Murakami, M., Roy, A. & Li, S. D. Factors controlling the pharmacokinetics, biodistribution and intratumoral penetration of nanoparticles. *Journal of Controlled Release* **172**, 782-794, doi:10.1016/j.jconrel.2013.09.013 (2013).

93 Duncan, R. & Gaspar, R. Nanomedicine(s) under the Microscope. *Molecular Pharmaceutics* **8**, 2101-2141, doi:10.1021/mp200394t (2011).

94 Dreaden, E. C., Mackey, M. A., Huang, X. H., Kang, B. & El-Sayed, M. A. Beating cancer in multiple ways using nanogold. *Chemical Society Reviews* **40**, 3391-3404, doi:10.1039/c0cs00180e (2011).

95 Doane, T. L. & Burda, C. The unique role of nanoparticles in nanomedicine: imaging, drug delivery and therapy. *Chemical Society Reviews* **41**, 2885-2911, doi:10.1039/c2cs15260f (2012).

96 Della Rocca, J., Liu, D. M. & Lin, W. B. Nanoscale Metal-Organic Frameworks for Biomedical Imaging and Drug Delivery. *Accounts of Chemical Research* **44**, 957-968, doi:10.1021/ar200028a (2011).

97 Delcea, M., Mohwald, H. & Skirtach, A. G. Stimuli-responsive LbL capsules and nanoshells for drug delivery. *Advanced Drug Delivery Reviews* **63**, 730-747, doi:10.1016/j.addr.2011.03.010 (2011).

98 Danhier, F., Feron, O. & Preat, V. To exploit the tumor microenvironment: Passive and active tumor targeting of nanocarriers for anti-cancer drug delivery. *Journal of Controlled Release* **148**, 135-146, doi:10.1016/j.jconrel.2010.08.027 (2010).

99 Cheng, Y. Y., Zhao, L. B., Li, Y. W. & Xu, T. W. Design of biocompatible dendrimers for cancer diagnosis and therapy: current status and future perspectives. *Chemical Society Reviews* **40**, 2673-2703, doi:10.1039/c0cs00097c (2011).

100 Chen, Y., Chen, H. R. & Shi, J. L. In Vivo Bio-Safety Evaluations and Diagnostic/Therapeutic Applications of Chemically Designed Mesoporous Silica Nanoparticles. *Advanced Materials* **25**, 3144-3176, doi:10.1002/adma.201205292 (2013).

101 Cai, W. B. & Chen, X. Y. Nanoplatforms for targeted molecular imaging in living subjects. *Small* **3**, 1840-1854, doi:10.1002/smll.200700351 (2007).

102 Bozzuto, G. & Molinari, A. Liposomes as nanomedical devices. *International Journal of Nanomedicine* **10**, 975-999, doi:10.2147/ijn.s68861 (2015).

103 Boisselier, E. & Astruc, D. Gold nanoparticles in nanomedicine: preparations, imaging, diagnostics, therapies and toxicity. *Chemical Society Reviews* **38**, 1759-1782, doi:10.1039/b806051g (2009).

104 Bertrand, N., Wu, J., Xu, X. Y., Kamaly, N. & Farokhzad, O. C. Cancer nanotechnology: The impact of passive and active targeting in the era of modern

cancer biology. *Advanced Drug Delivery Reviews* **66**, 2-25, doi:10.1016/j.addr.2013.11.009 (2014).

105 Batrakova, E. V. & Kabanov, A. V. Pluronic block copolymers: Evolution of drug delivery concept from inert nanocarriers to biological response modifiers. *Journal of Controlled Release* **130**, 98-106, doi:10.1016/j.jconrel.2008.04.013 (2008).

106 Bareford, L. A. & Swaan, P. W. Endocytic mechanisms for targeted drug delivery. *Advanced Drug Delivery Reviews* **59**, 748-758, doi:10.1016/j.addr.2007.06.008 (2007).

107 Ambrogio, M. W., Thomas, C. R., Zhao, Y. L., Zink, J. I. & Stoddartt, J. F. Mechanized Silica Nanoparticles: A New Frontier in Theranostic Nanomedicine. *Accounts of Chemical Research* **44**, 903-913, doi:10.1021/ar200018x (2011).

108 Allen, T. M. & Cullis, P. R. Liposomal drug delivery systems: From concept to clinical applications. *Advanced Drug Delivery Reviews* **65**, 36-48, doi:10.1016/j.addr.2012.09.037 (2013).

109 Al-Jamal, W. T. & Kostarelos, K. Liposomes: From a Clinically Established Drug Delivery System to a Nanoparticle Platform for Theranostic Nanomedicine. *Accounts of Chemical Research* **44**, 1094-1104, doi:10.1021/ar200105p (2011).

110 Acharya, S. & Sahoo, S. K. PLGA nanoparticles containing various anticancer agents and tumour delivery by EPR effect. *Advanced Drug Delivery Reviews* **63**, 170-183, doi:10.1016/j.addr.2010.10.008 (2011).

111 Torchilin, V. P. Micellar nanocarriers: Pharmaceutical perspectives. *Pharmaceutical Research* **24**, 1-16, doi:10.1007/s11095-006-9132-0 (2007).

112 Shi, J. J., Kantoff, P. W., Wooster, R. & Farokhzad, O. C. Cancer nanomedicine: progress, challenges and opportunities. *Nature Reviews Cancer* **17**, 20-37, doi:10.1038/nrc.2016.108 (2017).

113 Duncan, R. Polymer conjugates as anticancer nanomedicines. *Nature Reviews Cancer* **6**, 688-701, doi:10.1038/nrc1958 (2006).

114 Euliss, L. E., DuPont, J. A., Gratton, S. & DeSimone, J. Imparting size, shape, and composition control of materials for nanomedicine. *Chemical Society Reviews* **35**, 1095-1104 (2006).

115 Burda, C., Chen, X., Narayanan, R. & El-Sayed, M. A. Chemistry and properties of nanocrystals of different shapes. *Chemical reviews* **105**, 1025-1102 (2005).

116 Xia, Y. N., Xiong, Y. J., Lim, B. & Skrabalak, S. E. Shape-Controlled Synthesis of Metal Nanocrystals: Simple Chemistry Meets Complex Physics? *Angewandte Chemie-International Edition* **48**, 60-103, doi:10.1002/anie.200802248 (2009).

117 Yin, Y. & Alivisatos, A. P. Colloidal nanocrystal synthesis and the organic-inorganic interface. *Nature* **437**, 664-670, doi:10.1038/nature04165 (2005).

118 Tao, A. R., Habas, S. & Yang, P. D. Shape control of colloidal metal nanocrystals. *Small* **4**, 310-325, doi:10.1002/smll.200701295 (2008).

119 Murphy, C. J. *et al.* Anisotropic metal nanoparticles: Synthesis, assembly, and optical applications. *Journal of Physical Chemistry B* **109**, 13857-13870, doi:10.1021/jp0516846 (2005).

120 Shah, S. *et al.* Hybrid upconversion nanomaterials for optogenetic neuronal control. *Nanoscale* **7**, 16571-16577, doi:10.1039/c5nr03411f (2015).

121 Lai, J. P., Zhang, Y. X., Pasquale, N. & Lee, K. B. An Upconversion Nanoparticle with Orthogonal Emissions Using Dual NIR Excitations for Controlled Two-Way

Photoswitching. *Angewandte Chemie-International Edition* **53**, 14419-14423, doi:10.1002/anie.201408219 (2014).

122 Lai, J. P., Shah, B. R., Zhang, Y. X., Yang, L. T. & Lee, K. B. Real-Time Monitoring of ATP-Responsive Drug Release Using Mesoporous-Silica-Coated Multicolor Upconversion Nanoparticles. *ACS Nano* **9**, 5234-5245, doi:10.1021/acsnano.5b00641 (2015).

123 Subramaniam, P. *et al.* Generation of a Library of Non-Toxic Quantum Dots for Cellular Imaging and siRNA Delivery. *Advanced Materials* **24**, 4014-4019, doi:10.1002/adma.201201019 (2012).

124 Kim, T. H., Cho, H. Y., Lee, K. B., Kim, S. U. & Choi, J. W. Electrically Controlled Delivery of Cargo into Single Human Neural Stem Cell. *Acs Applied Materials & Interfaces* **6**, 20709-20716, doi:10.1021/am504498x (2014).

125 Frens, G. Controlled nucleation for the regulation of the particle size in monodisperse gold suspensions. *Nature physical science* **241**, 20 (1973).

126 Tao, A. R., Habas, S. & Yang, P. D. Shape control of colloidal metal nanocrystals. *Small* **4**, 310-325, doi:10.1002/smll.200701295 (2008).

127 Stewart, M. E. *et al.* Nanostructured plasmonic sensors. *Chemical Reviews* **108**, 494-521, doi:10.1021/cr068126n (2008).

128 Rosi, N. L. & Mirkin, C. A. Nanostructures in biodiagnostics. *Chemical Reviews* **105**, 1547-1562, doi:10.1021/cr030067f (2005).

129 Robinson, J. T. *et al.* Ultrasmall Reduced Graphene Oxide with High Near-Infrared Absorbance for Photothermal Therapy. *Journal of the American Chemical Society* **133**, 6825-6831, doi:10.1021/ja2010175 (2011).

130 Loo, C., Lowery, A., Halas, N. J., West, J. & Drezek, R. Immunotargeted nanoshells for integrated cancer imaging and therapy. *Nano Letters* **5**, 709-711, doi:10.1021/nl050127s (2005).

131 Jain, P. K., Lee, K. S., El-Sayed, I. H. & El-Sayed, M. A. Calculated absorption and scattering properties of gold nanoparticles of different size, shape, and composition: Applications in biological imaging and biomedicine. *Journal of Physical Chemistry B* **110**, 7238-7248, doi:10.1021/jp057170o (2006).

132 Jain, P. K., Huang, X. H., El-Sayed, I. H. & El-Sayed, M. A. Noble Metals on the Nanoscale: Optical and Photothermal Properties and Some Applications in Imaging, Sensing, Biology, and Medicine. *Accounts of Chemical Research* **41**, 1578-1586, doi:10.1021/ar7002804 (2008).

133 Huang, X. H., Neretina, S. & El-Sayed, M. A. Gold Nanorods: From Synthesis and Properties to Biological and Biomedical Applications. *Advanced Materials* **21**, 4880-4910, doi:10.1002/adma.200802789 (2009).

134 Huang, X. H., Jain, P. K., El-Sayed, I. H. & El-Sayed, M. A. Plasmonic photothermal therapy (PPTT) using gold nanoparticles. *Lasers in Medical Science* **23**, 217-228, doi:10.1007/s10103-007-0470-x (2008).

135 Huang, X. H., El-Sayed, I. H., Qian, W. & El-Sayed, M. A. Cancer cell imaging and photothermal therapy in the near-infrared region by using gold nanorods. *Journal of the American Chemical Society* **128**, 2115-2120, doi:10.1021/ja057254a (2006).

136 Hu, M. *et al.* Gold nanostructures: engineering their plasmonic properties for biomedical applications. *Chemical Society Reviews* **35**, 1084-1094, doi:10.1039/b517615h (2006).
137 Dreaden, E. C., Alkilany, A. M., Huang, X. H., Murphy, C. J. & El-Sayed, M. A. The golden age: gold nanoparticles for biomedicine. *Chemical Society Reviews* **41**, 2740-2779, doi:10.1039/c1cs15237h (2012).
138 Boisselier, E. & Astruc, D. Gold nanoparticles in nanomedicine: preparations, imaging, diagnostics, therapies and toxicity. *Chemical Society Reviews* **38**, 1759-1782, doi:10.1039/b806051g (2009).
139 Yang, X. J. *et al.* Near-Infrared Light-Triggered, Targeted Drug Delivery to Cancer Cells by Aptamer Gated Nanovehicles. *Advanced Materials* **24**, 2890-2895, doi:10.1002/adma.201104797 (2012).
140 Xiao, Z. Y. *et al.* DNA Self-Assembly of Targeted Near-Infrared-Responsive Gold Nanoparticles for Cancer Thermo-Chemotherapy. *Angewandte Chemie-International Edition* **51**, 11853-11857, doi:10.1002/anie.201204018 (2012).
141 Luo, Y. L., Shiao, Y. S. & Huang, Y. F. Release of Photoactivatable Drugs from Plasmonic Nanoparticles for Targeted Cancer Therapy. *ACS Nano* **5**, 7796-7804, doi:10.1021/nn201592s (2011).
142 Huschka, R. *et al.* Gene Silencing by Gold Nanoshell-Mediated Delivery and Laser-Triggered Release of Antisense Oligonucleotide and siRNA. *ACS Nano* **6**, 7681-7691, doi:10.1021/nn301135w (2012).
143 Eustis, S. & El-Sayed, M. A. Why gold nanoparticles are more precious than pretty gold: noble metal surface plasmon resonance and its enhancement of the radiative and nonradiative properties of nanocrystals of different shapes. *Chemical society reviews* **35**, 209-217 (2006).
144 Dreaden, E. C., Alkilany, A. M., Huang, X., Murphy, C. J. & El-Sayed, M. A. The golden age: gold nanoparticles for biomedicine. *Chemical Society Reviews* **41**, 2740-2779 (2012).
145 Wang, Z. *et al.* Biomimetic RNA-Silencing Nanocomplexes: Overcoming Multidrug Resistance in Cancer Cells. *Angewandte Chemie International Edition* **53**, 1997-2001 (2014).
146 Petree, J. R. *et al.* Site-Selective RNA Splicing Nanozyme: DNAzyme and RtcB Conjugates on a Gold Nanoparticle. *Acs Chemical Biology* **13**, 215-224, doi:10.1021/acschembio.7b00437 (2018).
147 Wang, K., Fishman, H. A., Dai, H. & Harris, J. S. Neural stimulation with a carbon nanotube microelectrode array. *Nano letters* **6**, 2043-2048 (2006).
148 Zhou, J. *et al.* Functionalized gold nanorods for nanomedicine: Past, present and future. *Coordination Chemistry Reviews* **352**, 15-66 (2017).
149 Lau, A. Y., Hung, P. J., Wu, A. R. & Lee, L. P. Open-access microfluidic patch-clamp array with raised lateral cell trapping sites. *Lab on a Chip* **6**, 1510-1515 (2006).
150 Hai, A. *et al.* Spine-shaped gold protrusions improve the adherence and electrical coupling of neurons with the surface of micro-electronic devices. *Journal of The Royal Society Interface* **6**, 1153-1165 (2009).
151 Hai, A., Shappir, J. & Spira, M. E. In-cell recordings by extracellular microelectrodes. *Nature methods* **7**, 200 (2010).

152 Robinson, J. T. *et al.* Vertical nanowire electrode arrays as a scalable platform for intracellular interfacing to neuronal circuits. *Nature nanotechnology* **7**, 180 (2012).

153 Shalek, A. K. *et al.* Vertical silicon nanowires as a universal platform for delivering biomolecules into living cells. *Proceedings of the National Academy of Sciences* (2010).

154 Chiappini, C. *et al.* Biodegradable silicon nanoneedles delivering nucleic acids intracellularly induce localized in vivo neovascularization. *Nature materials* **14**, 532 (2015).

155 Wang, C., Ye, Y., Hochu, G. M., Sadeghifar, H. & Gu, Z. Enhanced cancer immunotherapy by microneedle patch-assisted delivery of anti-PD1 antibody. *Nano letters* **16**, 2334-2340 (2016).

156 Xu, A. M., Wang, D. S., Shieh, P., Cao, Y. H. & Melosh, N. A. Direct Intracellular Delivery of Cell-Impermeable Probes of Protein Glycosylation by Using Nanostraws. *Chembiochem* **18**, 623-628, doi:10.1002/cbic.201600689 (2017).

157 Xu, A. M., Kim, S. A., Wang, D. S., Aalipour, A. & Melosh, N. A. Temporally resolved direct delivery of second messengers into cells using nanostraws. *Lab on a Chip* **16**, 2434-2439, doi:10.1039/c6lc00463f (2016).

158 Xu, A. M., Aalipour, A. & Melosh, N. A. Nanostraw-Mediated Intracellular Delivery: Direct Observation of Cell/Nanotube Interfaces. *Biophysical Journal* **104**, 194A-194A, doi:10.1016/j.bpj.2012.11.1092 (2013).

159 Xu, A. M. *et al.* Quantification of nanowire penetration into living cells. *Nature Communications* **5**, doi:10.1038/ncomms4613 (2014).

160 Xie, X. *et al.* Nanostraw-Electroporation System for Highly Efficient Intracellular Delivery and Transfection. *ACS Nano* **7**, 4351-4358, doi:10.1021/nn400874a (2013).

161 Fox, C. B. *et al.* Fabrication of Sealed Nanostraw Microdevices for Oral Drug Delivery. *ACS Nano* **10**, 5873-5881, doi:10.1021/acsnano.6b00809 (2016).

162 Cao, Y. H. *et al.* Nondestructive nanostraw intracellular sampling for longitudinal cell monitoring. *Proceedings of the National Academy of Sciences of the United States of America* **114**, E1866-E1874, doi:10.1073/pnas.1615375114/-/DCSupplemental (2017).

163 Cao, Y. *et al.* Universal intracellular biomolecule delivery with precise dosage control. *Science Advances* **4**, doi:10.1126/sciadv.aat8131 (2018).

164 Nicolosi, V., Chhowalla, M., Kanatzidis, M. G., Strano, M. S. & Coleman, J. N. Liquid exfoliation of layered materials. *Science* **340**, 1226419 (2013).

165 Liu, T., Cheng, L. & Liu, Z. Two Dimensional Transitional Metal Dichalcogenides for Biomedical Applications. *Acta Chimica Sinica* **73**, 902-912, doi:10.6023/a15040283 (2015).

166 Khalil, I., Julkapli, N. M., Yehye, W. A., Basirun, W. J. & Bhargava, S. K. Graphene-Gold Nanoparticles Hybrid-Synthesis, Functionalization, and Application in a Electrochemical and Surface-Enhanced Raman Scattering Biosensor. *Materials* **9**, doi:10.3390/ma9060406 (2016).

167 D'Agata, R., Giuffrida, M. C. & Spoto, G. Peptide Nucleic Acid-Based Biosensors for Cancer Diagnosis. *Molecules* **22**, doi:10.3390/molecules22111951 (2017).

168 Chen, H., Liu, T. J., Su, Z. Q., Shang, L. & Wei, G. 2D transition metal dichalcogenide nanosheets for photo/thermo-based tumor imaging and therapy. *Nanoscale Horizons* **3**, 74-89, doi:10.1039/c7nh00158d (2018).

169 Yang, L. *et al.* A biodegradable hybrid inorganic nanoscaffold for advanced stem cell therapy. *Nature Communications* **9**, 3147, doi:10.1038/s41467-018-05599-2 (2018).

170 Zhu, W. W. *et al.* Modulation of Hypoxia in Solid Tumor Microenvironment with MnO2 Nanoparticles to Enhance Photodynamic Therapy. *Advanced Functional Materials* **26**, 5490-5498, doi:10.1002/adfm.201600676 (2016).

171 Zhao, Z. L. *et al.* Activatable Fluorescence/MRI Bimodal Platform for Tumor Cell Imaging via MnO2 Nanosheet-Aptamer Nanoprobe. *Journal of the American Chemical Society* **136**, 11220-11223, doi:10.1021/ja5029364 (2014).

172 Zhang, Y. *et al.* Nanozyme Decorated Metal-Organic Frameworks for Enhanced Photodynamic Therapy. *ACS Nano* **12**, 651-661, doi:10.1021/acsnano.7b07746 (2018).

173 Yi, X. *et al.* Core-shell Au@MnO2 nanoparticles for enhanced radiotherapy via improving the tumor oxygenation. *Nano Research* **9**, 3267-3278, doi:10.1007/s12274-016-1205-8 (2016).

174 Yang, G. B. *et al.* Hollow MnO2 as a tumor-microenvironment-responsive biodegradable nano-platform for combination therapy favoring antitumor immune responses. *Nature Communications* **8**, doi:10.1038/s41467-017-01050-0 (2017).

175 Wu, D. *et al.* Corallite-like Magnetic Fe3O4@MnO2@Pt Nanocomposites as Multiple Signal Amplifiers for the Detection of Carcinoembryonic Antigen. *Acs Applied Materials & Interfaces* **7**, 18786-18793, doi:10.1021/acsami.5b05443 (2015).

176 Park, J.-i. *et al.* Scaffold-Free Coculture Spheroids of Human Colonic Adenocarcinoma Cells and Normal Colonic Fibroblasts Promote Tumorigenicity in Nude Mice. *Translational Oncology* **9**, 79-88, doi:http://dx.doi.org/10.1016/j.tranon.2015.12.001 (2016).

177 Song, M. L., Liu, T., Shi, C. R., Zhang, X. Z. & Chen, X. Y. Bioconjugated Manganese Dioxide Nanoparticles Enhance Chemotherapy Response by Priming Tumor-Associated Macrophages toward M1-like Phenotype and Attenuating Tumor Hypoxia. *ACS Nano* **10**, 633-647, doi:10.1021/acsnano.5b06779 (2016).

178 Saeed, M., Rogan, E. & Cavalieri, E. Mechanism of metabolic activation and DNA adduct formation by the human carcinogen diethylstilbestrol: The defining link to natural estrogens. *International Journal of Cancer* **124**, 1276-1284, doi:10.1002/ijc.24113 (2009).

179 Prasad, P. *et al.* Multifunctional Albumin-MnO2 Nanoparticles Modulate Solid Tumor Microenvironment by Attenuating Hypoxia, Acidosis, Vascular Endothelial Growth Factor and Enhance Radiation Response. *ACS Nano* **8**, 3202-3212, doi:10.1021/nn405773r (2014).

180 Peng, J. R. *et al.* "One-for-AII"-Type, Biodegradable Prussian Blue/Manganese Dioxide Hybrid Nanocrystal for Trimodal Imaging-Guided Photothermal Therapy

and Oxygen Regulation of Breast Cancer. *Acs Applied Materials & Interfaces* **9**, 13875-13886, doi:10.1021/acsami.7b01365 (2017).

181 Ou, M. *et al.* MnO2 nanosheet mediated "DD-A" FRET binary probes for sensitive detection of intracellular mRNA. *Chemical Science* **8**, 668-673, doi:10.1039/c6sc03162e (2017).

182 Meng, H. M. *et al.* Multiple Functional Nanoprobe for Contrast-Enhanced Bimodal Cellular Imaging and Targeted Therapy. *Analytical Chemistry* **87**, 4448-4454, doi:10.1021/acs.analchem.5b00337 (2015).

183 Ma, Z. F. *et al.* MnO2 Gatekeeper: An Intelligent and O-2-Evolving Shell for Preventing Premature Release of High Cargo Payload Core, Overcoming Tumor Hypoxia, and Acidic H2O2-Sensitive MRI. *Advanced Functional Materials* **27**, doi:10.1002/adfm.201604258 (2017).

184 Liu, J. J. *et al.* Nanoscale-Coordination-Polymer-Shelled Manganese Dioxide Composite Nanoparticles: A Multistage Redox/pH/H2O2-Responsive Cancer Theranostic Nanoplatform. *Advanced Functional Materials* **27**, doi:10.1002/adfm.201605926 (2017).

185 Li, L. *et al.* Growth of gold-manganese oxide nanostructures on a 3D origami device for glucose-oxidase label based electrochemical immunosensor. *Biosensors & Bioelectronics* **61**, 76-82, doi:10.1016/j.bios.2014.05.012 (2014).

186 Li, J., Li, D. X., Yuan, R. & Xiang, Y. Biodegradable MnO2 Nanosheet-Mediated Signal Amplification in Living Cells Enables Sensitive Detection of Down-Regulated Intracellular MicroRNA. *Acs Applied Materials & Interfaces* **9**, 5717-5724, doi:10.1021/acsami.6b13073 (2017).

187 Huang, Y. Y. *et al.* Self-Assembly of Multi-nanozymes to Mimic an Intracellular Antioxidant Defense System. *Angewandte Chemie-International Edition* **55**, 6646-6650, doi:10.1002/anie.201600868 (2016).

188 Gordijo, C. R. *et al.* Design of Hybrid MnO2-Polymer-Lipid Nanoparticles with Tunable Oxygen Generation Rates and Tumor Accumulation for Cancer Treatment. *Advanced Functional Materials* **25**, 1858-1872, doi:10.1002/adfm.201404511 (2015).

189 Gao, S. *et al.* Oxygen-generating hybrid nanoparticles to enhance fluorescent/photoacoustic/ultrasound imaging guided tumor photodynamic therapy. *Biomaterials* **112**, 324-335, doi:10.1016/j.biomaterials.2016.10.030 (2017).

190 Fan, W. P. *et al.* Intelligent MnO2 Nanosheets Anchored with Upconversion Nanoprobes for Concurrent pH-/H2O2-Responsive UCL Imaging and Oxygen-Elevated Synergetic Therapy. *Advanced Materials* **27**, 4155-4161, doi:10.1002/adma.201405141 (2015).

191 Fan, H. H. *et al.* A Smart Photosensitizer-Manganese Dioxide Nanosystem for Enhanced Photodynamic Therapy by Reducing Glutathione Levels in Cancer Cells. *Angewandte Chemie-International Edition* **55**, 5477-5482, doi:10.1002/anie.201510748 (2016).

192 Chu, C. C. *et al.* Tumor Microenvironment-Triggered Supramolecular System as an In Situ Nanotheranostic Generator for Cancer Phototherapy. *Advanced Materials* **29**, doi:10.1002/adma.201605928 (2017).

193 Chen, Y. *et al.* Break-up of Two-Dimensional MnO2 Nanosheets Promotes Ultrasensitive pH-Triggered Theranostics of Cancer. *Advanced Materials* **26**, 7019-+, doi:10.1002/adma.201402572 (2014).

194 Chen, Q. *et al.* Intelligent Albumin-MnO2 Nanoparticles as pH-/H2O2-Responsive Dissociable Nanocarriers to Modulate Tumor Hypoxia for Effective Combination Therapy. *Advanced Materials* **28**, 7129-+, doi:10.1002/adma.201601902 (2016).

195 Wang, H. C. R. & Choudhary, S. Reactive oxygen species-mediated therapeutic control of bladder cancer. *Nature Reviews Urology* **8**, 608-616, doi:10.1038/nrurol.2011.135 (2011).

196 Trachootham, D., Alexandre, J. & Huang, P. Targeting cancer cells by ROS-mediated mechanisms: a radical therapeutic approach? *Nature Reviews Drug Discovery* **8**, 579-591, doi:10.1038/nrd2803 (2009).

197 Sabharwal, S. S. & Schumacker, P. T. Mitochondrial ROS in cancer: initiators, amplifiers or an Achilles' heel? *Nature Reviews Cancer* **14**, 709-721, doi:10.1038/nrc3803 (2014).

198 Krysko, D. V. *et al.* Immunogenic cell death and DAMPs in cancer therapy. *Nature Reviews Cancer* **12**, 860-875, doi:10.1038/nrc3380 (2012).

199 Gorrini, C., Harris, I. S. & Mak, T. W. Modulation of oxidative stress as an anticancer strategy. *Nature Reviews Drug Discovery* **12**, 931-947, doi:10.1038/nrd4002 (2013).

200 Block, K. & Gorin, Y. Aiding and abetting roles of NOX oxidases in cellular transformation. *Nature Reviews Cancer* **12**, 627-637, doi:10.1038/nrc3339 (2012).

201 Wang, L. Y., Huo, M. F., Chen, Y. & Shi, J. L. Tumor Microenvironment-Enabled Nanotherapy. *Advanced Healthcare Materials* **7**, doi:10.1002/adhm.201701156 (2018).

202 Liu, Y. X., Jia, Q., Guo, Q. W., Wei, W. & Zhou, J. Simultaneously activating highly selective ratiometric MRI and synergistic therapy in response to intratumoral oxidability and acidity. *Biomaterials* **180**, 104-116, doi:10.1016/j.biomaterials.2018.07.025 (2018).

203 Lin, L. S. *et al.* Simultaneous Fenton-like Ion Delivery and Glutathione Depletion by MnO2-Based Nanoagent to Enhance Chemodynamic Therapy. *Angewandte Chemie-International Edition* **57**, 4902-4906, doi:10.1002/anie.201712027 (2018).

204 Zhao, P. *et al.* Multifunctional MnO2 nanosheet-modified Fe3O4@SiO2/NaYF4:Yb, Er nanocomposites as novel drug carriers. *Dalton Transactions* **43**, 451-457, doi:10.1039/c3dt52066h (2014).

205 Yuan, J. *et al.* MnO2-Nanosheet-Modified Upconversion Nanosystem for Sensitive Turn-On Fluorescence Detection of H2O2 and Glucose in Blood. *Acs Applied Materials & Interfaces* **7**, 10548-10555, doi:10.1021/acsami.5b02188 (2015).

206 Fan, W. P. *et al.* Intelligent MnO2 Nanosheets Anchored with Upconversion Nanoprobes for Concurrent pH-/H2O2-Responsive UCL Imaging and Oxygen-Elevated Synergetic Therapy. *Advanced Materials* **27**, 4155-4161, doi:10.1002/adma.201405141 (2015).

207 Deng, R. R., Xie, X. J., Vendrell, M., Chang, Y. T. & Liu, X. G. Intracellular Glutathione Detection Using MnO2-Nanosheet-Modified Upconversion Nanoparticles. *Journal of the American Chemical Society* **133**, 20168-20171, doi:10.1021/ja2100774 (2011).

208 Wang, C. H., Cherng, W. J. & Verma, S. Drawbacks to stem cell therapy in cardiovascular diseases. *Future Cardiol* **4**, 399-408, doi:10.2217/14796678.4.4.399 (2008).

209 Medvedev, S. P., Shevchenko, A. I. & Zakian, S. M. Induced Pluripotent Stem Cells: Problems and Advantages when Applying them in Regenerative Medicine. *Acta Naturae* **2**, 18-27 (2010).

210 Liu, C. *et al.* The effect of the fibre orientation of electrospun scaffolds on the matrix production of rabbit annulus fibrosus-derived stem cells. *Bone Res* **3**, 15012, doi:10.1038/boneres.2015.12 (2015).

211 Solanki, A., Kim, J. D. & Lee, K. B. Nanotechnology for regenerative medicine: nanomaterials for stem cell imaging. *Nanomedicine (Lond)* **3**, 567-578, doi:10.2217/17435889.3.4.567 (2008).

212 Patel, S. & Lee, K. B. Probing stem cell behavior using nanoparticle-based approaches. *Wiley Interdiscip Rev Nanomed Nanobiotechnol* **7**, 759-778, doi:10.1002/wnan.1346 (2015).

213 Pulavendran, S., Rajam, M., Rose, C. & Mandal, A. B. Hepatocyte growth factor incorporated chitosan nanoparticles differentiate murine bone marrow mesenchymal stem cell into hepatocytes in vitro. *IET Nanobiotechnology* **4**, 51-60 (2010). <http://digital-library.theiet.org/content/journals/10.1049/iet-nbt.2009.0014>.

214 Pulavendran, S., Rose, C. & Mandal, A. B. Hepatocyte growth factor incorporated chitosan nanoparticles augment the differentiation of stem cell into hepatocytes for the recovery of liver cirrhosis in mice. *J Nanobiotechnology* **9**, 15, doi:10.1186/1477-3155-9-15 (2011).

215 Neumann, A., Christel, A., Kasper, C. & Behrens, P. BMP2-loaded nanoporous silica nanoparticles promote osteogenic differentiation of human mesenchymal stem cells. *Rsc Adv* **3**, 24222-24230, doi:10.1039/c3ra44734k (2013).

216 Garcia-Bennett, A. E. *et al.* Delivery of differentiation factors by mesoporous silica particles assists advanced differentiation of transplanted murine embryonic stem cells. *Stem Cells Transl Med* **2**, 906-915, doi:10.5966/sctm.2013-0072 (2013).

217 Maia, J. *et al.* Controlling the neuronal differentiation of stem cells by the intracellular delivery of retinoic acid-loaded nanoparticles. *ACS Nano* **5**, 97-106, doi:10.1021/nn101724r (2011).

218 Shah, B., Yin, P. T., Ghoshal, S. & Lee, K. B. Multimodal magnetic core-shell nanoparticles for effective stem-cell differentiation and imaging. *Angew Chem Int Ed Engl* **52**, 6190-6195, doi:10.1002/anie.201302245 (2013).

219 Yau, W. W., Rujitanaroj, P. O., Lam, L. & Chew, S. Y. Directing stem cell fate by controlled RNA interference. *Biomaterials* **33**, 2608-2628, doi:10.1016/j.biomaterials.2011.12.021 (2012).

220 Shah, S., Solanki, A., Sasmal, P. K. & Lee, K. B. Single vehicular delivery of siRNA and small molecules to control stem cell differentiation. *J Am Chem Soc* **135**, 15682-15685, doi:10.1021/ja4071738 (2013).

221 Leader, B., Baca, Q. J. & Golan, D. E. Protein therapeutics: a summary and pharmacological classification. *Nat Rev Drug Discov* **7**, 21-39, doi:10.1038/nrd2399 (2008).

222 Spitz, F. & Furlong, E. E. Transcription factors: from enhancer binding to developmental control. *Nat Rev Genet* **13**, 613-626, doi:10.1038/nrg3207 (2012).

223 Patel, S. *et al.* NanoScript: A Nanoparticle-Based Artificial Transcription Factor for Effective Gene Regulation. *ACS Nano* **8**, 8959-8967, doi:10.1021/nn501589f (2014).

224 Park, J. *et al.* 2D and 3D Hybrid Systems for Enhancement of Chondrogenic Differentiation of Tonsil-Derived Mesenchymal Stem Cells. *Advanced Functional Materials* **25**, 2573-2582, doi:10.1002/adfm.201500299 (2015).

225 Patel, S. & Lee, K. B. Probing stem cell behavior using nanoparticle-based approaches. *Wiley Interdisciplinary Reviews-Nanomedicine and Nanobiotechnology* **7**, 759-778, doi:10.1002/wnan.1346 (2015).

226 Patel, S. *et al.* Induction of Stem-Cell-Derived Functional Neurons by NanoScript-Based Gene Repression. *Angewandte Chemie-International Edition* **54**, 11983-11988, doi:10.1002/anie.201504902 (2015).

227 Santos, L. J., Reis, R. L. & Gomes, M. E. Harnessing magnetic-mechano actuation in regenerative medicine and tissue engineering. *Trends Biotechnol* **33**, 471-479, doi:10.1016/j.tibtech.2015.06.006 (2015).

228 Dalby, M. J., Gadegaard, N. & Oreffo, R. O. Harnessing nanotopography and integrin-matrix interactions to influence stem cell fate. *Nat Mater* **13**, 558-569, doi:10.1038/nmat3980 (2014).

229 Murphy, W. L., McDevitt, T. C. & Engler, A. J. Materials as stem cell regulators. *Nat Mater* **13**, 547-557, doi:10.1038/nmat3937 (2014).

230 Yuge, L. *et al.* Physical stress by magnetic force accelerates differentiation of human osteoblasts. *Biochem Biophys Res Commun* **311**, 32-38, doi:http://dx.doi.org/10.1016/j.bbrc.2003.09.156 (2003).

231 Dobson, J. Remote control of cellular behaviour with magnetic nanoparticles. *Nat Nanotechnol* **3**, 139-143, doi:10.1038/nnano.2008.39 (2008).

232 Matthews, B. D., Overby, D. R., Mannix, R. & Ingber, D. E. Cellular adaptation to mechanical stress: role of integrins, Rho, cytoskeletal tension and mechanosensitive ion channels. *J Cell Sci* **119**, 508-518, doi:10.1242/jcs.02760 (2006).

233 Hughes, S., McBain, S., Dobson, J. & El Haj, A. J. Selective activation of mechanosensitive ion channels using magnetic particles. *J R Soc Interface* **5**, 855-863, doi:10.1098/rsif.2007.1274 (2008).

234 Henstock, J. R., Rotherham, M., Rashidi, H., Shakesheff, K. M. & El Haj, A. J. Remotely Activated Mechanotransduction via Magnetic Nanoparticles Promotes Mineralization Synergistically With Bone Morphogenetic Protein 2: Applications for Injectable Cell Therapy. *Stem Cells Transl Med* **3**, 1363-1374, doi:10.5966/sctm.2014-0017 (2014).

235 Hu, B., El Haj, A. J. & Dobson, J. Receptor-targeted, magneto-mechanical stimulation of osteogenic differentiation of human bone marrow-derived mesenchymal stem cells. *Int J Mol Sci* **14**, 19276-19293, doi:10.3390/ijms140919276 (2013).

236 Hu, B., Dobson, J. & El Haj, A. J. Control of smooth muscle alpha-actin (SMA) up-regulation in HBMSCs using remote magnetic particle mechano-activation. *Nanomedicine* **10**, 45-55, doi:10.1016/j.nano.2013.06.014 (2014).

237 Geim, A. K. & Novoselov, K. S. The rise of graphene. *Nat Mater* **6**, 183-191, doi:10.1038/nmat1849 (2007).

238 Allen, M. J., Tung, V. C. & Kaner, R. B. Honeycomb carbon: a review of graphene. *Chem Rev* **110**, 132-145, doi:10.1021/cr900070d (2010).

239 Sun, X. *et al.* Nano-Graphene Oxide for Cellular Imaging and Drug Delivery. *Nano Res.* **1**, 203-212, doi:10.1007/s12274-008-8021-8 (2008).

240 Chimene, D., Alge, D. L. & Gaharwar, A. K. Two-Dimensional Nanomaterials for Biomedical Applications: Emerging Trends and Future Prospects. *Adv. Mater.* **27**, 7261-7284, doi:10.1002/adma.201502422 (2015).

241 Park, S. Y. *et al.* Enhanced differentiation of human neural stem cells into neurons on graphene. *Adv. Mater.* **23**, H263-267, doi:10.1002/adma.201101503 (2011).

242 Li, N. *et al.* The promotion of neurite sprouting and outgrowth of mouse hippocampal cells in culture by graphene substrates. *Biomaterials* **32**, 9374-9382, doi:10.1016/j.biomaterials.2011.08.065 (2011).

243 Wang, Y. *et al.* Fluorinated graphene for promoting neuro-induction of stem cells. *Adv. Mater.* **24**, 4285-4290, doi:10.1002/adma.201200846 (2012).

244 Zhang, T. *et al.* Enhanced proliferation and osteogenic differentiation of human mesenchymal stem cells on biomineralized three-dimensional graphene foams. *Carbon* **105**, 233-243, doi:10.1016/j.carbon.2016.04.027 (2016).

245 Ku, S. H. & Park, C. B. Myoblast differentiation on graphene oxide. *Biomaterials* **34**, 2017-2023, doi:10.1016/j.biomaterials.2012.11.052 (2013).

246 Yoon, H. H. *et al.* Dual Roles of Graphene Oxide in Chondrogenic Differentiation of Adult Stem Cells: Cell-Adhesion Substrate and Growth Factor-Delivery Carrier. *Advanced Functional Materials* **24**, 6455-6464, doi:10.1002/adfm.201400793 (2014).

247 Park, J. *et al.* Graphene-regulated cardiomyogenic differentiation process of mesenchymal stem cells by enhancing the expression of extracellular matrix proteins and cell signaling molecules. *Adv. Healthc. Mater.* **3**, 176-181, doi:10.1002/adhm.201300177 (2014).

248 Lee, W. C. *et al.* Origin of enhanced stem cell growth and differentiation on graphene and graphene oxide. *ACS Nano* **5**, 7334-7341, doi:10.1021/nn202190c (2011).

249 Guo, W. *et al.* Self-Powered Electrical Stimulation for Enhancing Neural Differentiation of Mesenchymal Stem Cells on Graphene-Poly(3,4-ethylenedioxythiophene) Hybrid Microfibers. *ACS Nano* **10**, 5086-5095, doi:10.1021/acsnano.6b00200 (2016).

250 Akhavan, O. & Ghaderi, E. The use of graphene in the self-organized differentiation of human neural stem cells into neurons under pulsed laser stimulation. *J Mater Chem B* **2**, 5602-5611, doi:10.1039/c4tb00668b (2014).

251 Akhavan, O. & Ghaderi, E. Flash photo stimulation of human neural stem cells on graphene/TiO2 heterojunction for differentiation into neurons. *Nanoscale* **5**, 10316-10326, doi:10.1039/c3nr02161k (2013).

252 Li, N. *et al.* The promotion of neurite sprouting and outgrowth of mouse hippocampal cells in culture by graphene substrates. *Biomaterials* **32**, 9374-9382, doi:http://dx.doi.org/10.1016/j.biomaterials.2011.08.065 (2011).

253 Kim, T. H., Lee, K. B. & Choi, J. W. 3D graphene oxide-encapsulated gold nanoparticles to detect neural stem cell differentiation. *Biomaterials* **34**, 8660-8670, doi:10.1016/j.biomaterials.2013.07.101 (2013).

254 Solanki, A. *et al.* Axonal alignment and enhanced neuronal differentiation of neural stem cells on graphene-nanoparticle hybrid structures. *Adv. Mater.* **25**, 5477-5482, doi:10.1002/adma.201302219 (2013).

255 Shin, S. R. *et al.* Layer-by-layer assembly of 3D tissue constructs with functionalized graphene. *Adv. Funct. Mater.* **24**, 6136-6144, doi:10.1002/adfm.201401300 (2014).

256 Fujie, T. *et al.* Micropatterned polymeric nanosheets for local delivery of an engineered epithelial monolayer. *Adv. Mater.* **26**, 1699-1705, doi:10.1002/adma.201304183 (2014).

257 Gattazzo, F., Urciuolo, A. & Bonaldo, P. Extracellular matrix: a dynamic microenvironment for stem cell niche. *Biochim Biophys Acta* **1840**, 2506-2519, doi:10.1016/j.bbagen.2014.01.010 (2014).

258 Leung, V. & Ko, F. Biomedical applications of nanofibers. *Polymers for Advanced Technologies* **22**, 350-365, doi:10.1002/pat.1813 (2011).

259 Zhang, Z., Hu, J. & Ma, P. X. Nanofiber-based delivery of bioactive agents and stem cells to bone sites. *Adv Drug Deliv Rev* **64**, 1129-1141, doi:10.1016/j.addr.2012.04.008 (2012).

260 Rho, K. S. *et al.* Electrospinning of collagen nanofibers: effects on the behavior of normal human keratinocytes and early-stage wound healing. *Biomaterials* **27**, 1452-1461, doi:10.1016/j.biomaterials.2005.08.004 (2006).

261 Jeong, L. *et al.* Plasma-treated silk fibroin nanofibers for skin regeneration. *Int J Biol Macromol* **44**, 222-228, doi:10.1016/j.ijbiomac.2008.12.008 (2009).

262 Zhou, Y. *et al.* Electrospun water-soluble carboxyethyl chitosan/poly(vinyl alcohol) nanofibrous membrane as potential wound dressing for skin regeneration. *Biomacromolecules* **9**, 349-354, doi:10.1021/bm7009015 (2008).

263 Dhandayuthapani, B., Krishnan, U. M. & Sethuraman, S. Fabrication and characterization of chitosan-gelatin blend nanofibers for skin tissue engineering. *J Biomed Mater Res B Appl Biomater* **94**, 264-272, doi:10.1002/jbm.b.31651 (2010).

264 Ma, K. *et al.* Effects of nanofiber/stem cell composite on wound healing in acute full-thickness skin wounds. *Tissue Eng Part A* **17**, 1413-1424, doi:10.1089/ten.TEA.2010.0373 (2011).

265 Mata, A. *et al.* Bone regeneration mediated by biomimetic mineralization of a nanofiber matrix. *Biomaterials* **31**, 6004-6012, doi:10.1016/j.biomaterials.2010.04.013 (2010).

266 Cui, H., Webber, M. J. & Stupp, S. I. Self-assembly of peptide amphiphiles: from molecules to nanostructures to biomaterials. *Biopolymers* **94**, 1-18, doi:10.1002/bip.21328 (2010).

267 Venugopal, J. R., Low, S., Choon, A. T., Kumar, A. B. & Ramakrishna, S. Nanobioengineered electrospun composite nanofibers and osteoblasts for bone regeneration. *Artif Organs* **32**, 388-397, doi:10.1111/j.1525-1594.2008.00557.x (2008).

268 Yoshimoto, H., Shin, Y. M., Terai, H. & Vacanti, J. P. A biodegradable nanofiber scaffold by electrospinning and its potential for bone tissue engineering. *Biomaterials* **24**, 2077-2082, doi:http://dx.doi.org/10.1016/S0142-9612(02)00635-X (2003).

269 Vunjak-Novakovic, G., Altman, G., Horan, R. & Kaplan, D. L. Tissue engineering of ligaments. *Annu Rev Biomed Eng* **6**, 131-156, doi:10.1146/annurev.bioeng.6.040803.140037 (2004).

270 Yin, Z. *et al.* The regulation of tendon stem cell differentiation by the alignment of nanofibers. *Biomaterials* **31**, 2163-2175, doi:10.1016/j.biomaterials.2009.11.083 (2010).

271 Lee, C. H. *et al.* Nanofiber alignment and direction of mechanical strain affect the ECM production of human ACL fibroblast. *Biomaterials* **26**, 1261-1270, doi:10.1016/j.biomaterials.2004.04.037 (2005).

272 Feng, Z. Q. *et al.* The effect of nanofibrous galactosylated chitosan scaffolds on the formation of rat primary hepatocyte aggregates and the maintenance of liver function. *Biomaterials* **30**, 2753-2763, doi:10.1016/j.biomaterials.2009.01.053 (2009).

273 Piryaei, A., Valojerdi, M. R., Shahsavani, M. & Baharvand, H. Differentiation of bone marrow-derived mesenchymal stem cells into hepatocyte-like cells on nanofibers and their transplantation into a carbon tetrachloride-induced liver fibrosis model. *Stem Cell Rev* **7**, 103-118, doi:10.1007/s12015-010-9126-5 (2011).

274 Gelain, F., Bottai, D., Vescovi, A. & Zhang, S. Designer self-assembling peptide nanofiber scaffolds for adult mouse neural stem cell 3-dimensional cultures. *PLoS One* **1**, e119, doi:10.1371/journal.pone.0000119 (2006).

275 Silva, G. A. *et al.* Selective differentiation of neural progenitor cells by high-epitope density nanofibers. *Science* **303**, 1352-1355, doi:10.1126/science.1093783 (2004).

276 Shah, S. *et al.* Guiding stem cell differentiation into oligodendrocytes using graphene-nanofiber hybrid scaffolds. *Adv. Mater.* **26**, 3673-3680, doi:10.1002/adma.201400523 (2014).

277 Beniash, E., Hartgerink, J. D., Storrie, H., Stendahl, J. C. & Stupp, S. I. Self-assembling peptide amphiphile nanofiber matrices for cell entrapment. *Acta Biomaterialia* **1**, 387-397, doi:http://dx.doi.org/10.1016/j.actbio.2005.04.002 (2005).

278 Li, L. s. & Stupp, S. I. One-Dimensional Assembly of Lipophilic Inorganic Nanoparticles Templated by Peptide-Based Nanofibers with Binding Functionalities. *Angewandte Chemie International Edition* **44**, 1833-1836 (2005).

279 Natu, M. V., de Sousa, H. C. & Gil, M. Effects of drug solubility, state and loading on controlled release in bicomponent electrospun fibers. *International journal of pharmaceutics* **397**, 50-58 (2010).

280 Willets, K. A. & Van Duyne, R. P. Localized surface plasmon resonance spectroscopy and sensing. *Annual Review of Physical Chemistry* **58**, 267-297, doi:10.1146/annurev.physchem.58.032806.104607 (2007).

281 Stiles, P. L., Dieringer, J. A., Shah, N. C. & Van Duyne, R. R. Surface-Enhanced Raman Spectroscopy. *Annual Review of Analytical Chemistry* **1**, 601-626, doi:10.1146/annurev.anchem.1.031207.112814 (2008).

282 Sherry, L. J. *et al.* Localized surface plasmon resonance spectroscopy of single silver nanocubes. *Nano Letters* **5**, 2034-2038, doi:10.1021/nl0515753 (2005).

283 Sharma, B., Frontiera, R. R., Henry, A. I., Ringe, E. & Van Duyne, R. P. SERS: Materials, applications, and the future. *Materials Today* **15**, 16-25, doi:10.1016/s1369-7021(12)70017-2 (2012).

284 McFarland, A. D. & Van Duyne, R. P. Single silver nanoparticles as real-time optical sensors with zeptomole sensitivity. *Nano Letters* **3**, 1057-1062, doi:10.1021/nl034372s (2003).

285 Malinsky, M. D., Kelly, K. L., Schatz, G. C. & Van Duyne, R. P. Chain length dependence and sensing capabilities of the localized surface plasmon resonance of silver nanoparticles chemically modified with alkanethiol self-assembled monolayers. *Journal of the American Chemical Society* **123**, 1471-1482, doi:10.1021/ja003312a (2001).

286 Jensen, T. R., Malinsky, M. D., Haynes, C. L. & Van Duyne, R. P. Nanosphere lithography: Tunable localized surface plasmon resonance spectra of silver nanoparticles. *Journal of Physical Chemistry B* **104**, 10549-10556, doi:10.1021/jp002435e (2000).

287 Haynes, C. L. & Van Duyne, R. P. Nanosphere lithography: A versatile nanofabrication tool for studies of size-dependent nanoparticle optics. *Journal of Physical Chemistry B* **105**, 5599-5611, doi:10.1021/jp010657m (2001).

288 Haes, A. J. & Van Duyne, R. P. A nanoscale optical blosensor: Sensitivity and selectivity of an approach based on the localized surface plasmon resonance spectroscopy of triangular silver nanoparticles. *Journal of the American Chemical Society* **124**, 10596-10604, doi:10.1021/ja020393x (2002).

289 Anker, J. N. *et al.* Biosensing with plasmonic nanosensors. *Nature Materials* **7**, 442-453, doi:10.1038/nmat2162 (2008).

290 Yu, C. X. & Irudayaraj, J. Multiplex biosensor using gold nanorods. *Analytical Chemistry* **79**, 572-579, doi:10.1021/ac061730d (2007).

291 Wu, C. H. *et al.* Fano-resonant asymmetric metamaterials for ultrasensitive spectroscopy and identification of molecular monolayers. *Nature Materials* **11**, 69-75, doi:10.1038/nmat3161 (2012).

292 Stewart, M. E. *et al.* Nanostructured plasmonic sensors. *Chemical Reviews* **108**, 494-521, doi:10.1021/cr068126n (2008).

293 Sherry, L. J., Jin, R. C., Mirkin, C. A., Schatz, G. C. & Van Duyne, R. P. Localized surface plasmon resonance spectroscopy of single silver triangular nanoprisms. *Nano Letters* **6**, 2060-2065, doi:10.1021/nl061286u (2006).
294 Rodrigo, D. *et al.* Mid-infrared plasmonic biosensing with graphene. *Science* **349**, 165-168, doi:10.1126/science.aab2051 (2015).
295 Li, D., Song, S. P. & Fan, C. H. Target-Responsive Structural Switching for Nucleic Acid-Based Sensors. *Accounts of Chemical Research* **43**, 631-641, doi:10.1021/ar900245u (2010).
296 Langhammer, C., Schwind, M., Kasemo, B. & Zoric, I. Localized surface plasmon resonances in aluminum nanodisks. *Nano Letters* **8**, 1461-1471, doi:10.1021/nl080453i (2008).
297 Haes, A. J. *et al.* Plasmonic materials for surface-enhanced sensing and spectroscopy. *Mrs Bulletin* **30**, 368-375, doi:10.1557/mrs2005.100 (2005).
298 Chan, G. H., Zhao, J., Hicks, E. M., Schatz, G. C. & Van Duyne, R. P. Plasmonic properties of copper nanoparticles fabricated by nanosphere lithography. *Nano Letters* **7**, 1947-1952, doi:10.1021/nl070648a (2007).
299 Anker, J. N. *et al.* Biosensing with plasmonic nanosensors. *Nature Materials* **7**, 442-453, doi:10.1038/nmat2162 (2008).
300 Cao, Y. W. C., Jin, R. C. & Mirkin, C. A. Nanoparticles with Raman spectroscopic fingerprints for DNA and RNA detection. *Science* **297**, 1536-1540, doi:10.1126/science.297.5586.1536 (2002).
301 Uetz, P. *et al.* A comprehensive analysis of protein-protein interactions in Saccharomyces cerevisiae. *Nature* **403**, 623-627, doi:10.1038/35001009 (2000).
302 Tyagi, S. & Kramer, F. R. Molecular beacons: Probes that fluoresce upon hybridization. *Nature Biotechnology* **14**, 303-308, doi:10.1038/nbt0396-303 (1996).
303 Redon, R. *et al.* Global variation in copy number in the human genome. *Nature* **444**, 444-454, doi:10.1038/nature05329 (2006).
304 Mortazavi, A., Williams, B. A., McCue, K., Schaeffer, L. & Wold, B. Mapping and quantifying mammalian transcriptomes by RNA-Seq. *Nature Methods* **5**, 621-628, doi:10.1038/nmeth.1226 (2008).
305 Lockhart, D. J. *et al.* Expression monitoring by hybridization to high-density oligonucleotide arrays. *Nature Biotechnology* **14**, 1675-1680, doi:10.1038/nbt1296-1675 (1996).
306 Kononen, J. *et al.* Tissue microarrays for high-throughput molecular profiling of tumor specimens. *Nature Medicine* **4**, 844-847, doi:10.1038/nm0798-844 (1998).
307 Ho, Y. *et al.* Systematic identification of protein complexes in Saccharomyces cerevisiae by mass spectrometry. *Nature* **415**, 180-183, doi:10.1038/415180a (2002).
308 Abecasis, G. R., Cherny, S. S., Cookson, W. O. & Cardon, L. R. Merlin-rapid analysis of dense genetic maps using sparse gene flow trees. *Nature Genetics* **30**, 97-101, doi:10.1038/ng786 (2002).
309 Calderon, L. *et al.* Release of airborne particles and Ag and Zn compounds from nanotechnology-enabled consumer sprays: Implications for inhalation exposure. *Atmospheric Environment* **155**, 85-96, doi:10.1016/j.atmosenv.2017.02.016 (2017).

310 Wagner, R. & Ellis, W. Vapor-liquid-solid mechanism of single crystal growth. *Applied Physics Letters* **4**, 89-90 (1964).
311 Perepichka, I. F., Perepichka, D. F., Meng, H. & Wudl, F. Light-emitting polythiophenes. *Advanced Materials* **17**, 2281-2305, doi:10.1002/adma.200500461 (2005).
312 Muccini, M. A bright future for organic field-effect transistors. *Nature Materials* **5**, 605-613, doi:10.1038/nmat1699 (2006).
313 Misewich, J. A. *et al.* Electrically induced optical emission from a carbon nanotube FET. *Science* **300**, 783-786, doi:10.1126/science.1081294 (2003).
314 Fan, Z. Y., Wang, D. W., Chang, P. C., Tseng, W. Y. & Lu, J. G. ZnO nanowire field-effect transistor and oxygen sensing property. *Applied Physics Letters* **85**, 5923-5925, doi:10.1063/1.1836870 (2004).
315 Chang, D. E., Sorensen, A. S., Demler, E. A. & Lukin, M. D. A single-photon transistor using nanoscale surface plasmons. *Nature Physics* **3**, 807-812, doi:10.1038/nphys708 (2007).
316 Brown, P. J. *et al.* Effect of interchain interactions on the absorption and emission of poly(3-hexylthiophene). *Physical Review B* **67**, doi:10.1103/PhysRevB.67.064203 (2003).
317 Avouris, P., Freitag, M. & Perebeinos, V. Carbon-nanotube photonics and optoelectronics. *Nature Photonics* **2**, 341-350, doi:10.1038/nphoton.2008.94 (2008).
318 Kang, S. J. *et al.* High-performance electronics using dense, perfectly aligned arrays of single-walled carbon nanotubes. *Nature Nanotechnology* **2**, 230-236, doi:10.1038/nnano.2007.77 (2007).
319 Hu, L., Hecht, D. S. & Gruner, G. Percolation in transparent and conducting carbon nanotube networks. *Nano Letters* **4**, 2513-2517, doi:10.1021/nl048435y (2004).
320 Avouris, P., Chen, Z. H. & Perebeinos, V. Carbon-based electronics. *Nature Nanotechnology* **2**, 605-615, doi:10.1038/nnano.2007.300 (2007).
321 Akimov, A. V. *et al.* Generation of single optical plasmons in metallic nanowires coupled to quantum dots. *Nature* **450**, 402-406, doi:10.1038/nature06230 (2007).
322 Marcano, D. C. *et al.* Improved Synthesis of Graphene Oxide. *ACS Nano* **4**, 4806-4814, doi:10.1021/nn1006368 (2010).
323 Zhu, Y. W. *et al.* Graphene and Graphene Oxide: Synthesis, Properties, and Applications. *Advanced Materials* **22**, 3906-3924, doi:10.1002/adma.201001068 (2010).
324 Stankovich, S. *et al.* Synthesis of graphene-based nanosheets via chemical reduction of exfoliated graphite oxide. *Carbon* **45**, 1558-1565, doi:10.1016/j.carbon.2007.02.034 (2007).
325 Dreyer, D. R., Park, S., Bielawski, C. W. & Ruoff, R. S. The chemistry of graphene oxide. *Chemical Society Reviews* **39**, 228-240, doi:10.1039/b917103g (2010).
326 Grimme, S., Antony, J., Ehrlich, S. & Krieg, H. A consistent and accurate ab initio parametrization of density functional dispersion correction (DFT-D) for the 94 elements H-Pu. *Journal of Chemical Physics* **132**, doi:10.1063/1.3382344 (2010).

327 Balandin, A. A. *et al.* Superior thermal conductivity of single-layer graphene. *Nano Letters* **8**, 902-907, doi:10.1021/nl0731872 (2008).

328 Stoller, M. D., Park, S. J., Zhu, Y. W., An, J. H. & Ruoff, R. S. Graphene-Based Ultracapacitors. *Nano Letters* **8**, 3498-3502, doi:10.1021/nl802558y (2008).

329 Kim, K. S. *et al.* Large-scale pattern growth of graphene films for stretchable transparent electrodes. *Nature* **457**, 706-710, doi:10.1038/nature07719 (2009).

330 Novoselov, K. S. *et al.* Two-dimensional gas of massless Dirac fermions in graphene. *Nature* **438**, 197-200, doi:10.1038/nature04233 (2005).

331 Stankovich, S. *et al.* Graphene-based composite materials. *Nature* **442**, 282-286, doi:10.1038/nature04969 (2006).

332 Zhang, Y. B., Tan, Y. W., Stormer, H. L. & Kim, P. Experimental observation of the quantum Hall effect and Berry's phase in graphene. *Nature* **438**, 201-204, doi:10.1038/nature04235 (2005).

333 Geim, A. K. & Novoselov, K. S. The rise of graphene. *Nature Materials* **6**, 183-191, doi:10.1038/nmat1849 (2007).

334 Schedin, F. *et al.* Detection of individual gas molecules adsorbed on graphene. *Nature Materials* **6**, 652-655, doi:10.1038/nmat1967 (2007).

335 Bae, S. *et al.* Roll-to-roll production of 30-inch graphene films for transparent electrodes. *Nature Nanotechnology* **5**, 574-578, doi:10.1038/nnano.2010.132 (2010).

336 Li, D., Muller, M. B., Gilje, S., Kaner, R. B. & Wallace, G. G. Processable aqueous dispersions of graphene nanosheets. *Nature Nanotechnology* **3**, 101-105, doi:10.1038/nnano.2007.451 (2008).

337 Radisavljevic, B., Radenovic, A., Brivio, J., Giacometti, V. & Kis, A. Single-layer MoS2 transistors. *Nature Nanotechnology* **6**, 147-150, doi:10.1038/nnano.2010.279 (2011).

338 Wang, Q. H., Kalantar-Zadeh, K., Kis, A., Coleman, J. N. & Strano, M. S. Electronics and optoelectronics of two-dimensional transition metal dichalcogenides. *Nature Nanotechnology* **7**, 699-712, doi:10.1038/nnano.2012.193 (2012).

339 Ferrari, A. C. *et al.* Raman spectrum of graphene and graphene layers. *Physical Review Letters* **97**, doi:10.1103/PhysRevLett.97.187401 (2006).

340 Mak, K. F., Lee, C., Hone, J., Shan, J. & Heinz, T. F. Atomically Thin MoS2: A New Direct-Gap Semiconductor. *Physical Review Letters* **105**, doi:10.1103/PhysRevLett.105.136805 (2010).

341 Novoselov, K. S. *et al.* Two-dimensional atomic crystals. *Proceedings of the National Academy of Sciences of the United States of America* **102**, 10451-10453, doi:10.1073/pnas.0502848102 (2005).

342 Castro Neto, A. H., Guinea, F., Peres, N. M. R., Novoselov, K. S. & Geim, A. K. The electronic properties of graphene. *Reviews of Modern Physics* **81**, 109-162, doi:10.1103/RevModPhys.81.109 (2009).

343 Geim, A. K. Graphene: Status and Prospects. *Science* **324**, 1530-1534, doi:10.1126/science.1158877 (2009).

344 Lee, C., Wei, X. D., Kysar, J. W. & Hone, J. Measurement of the elastic properties and intrinsic strength of monolayer graphene. *Science* **321**, 385-388, doi:10.1126/science.1157996 (2008).

345 Li, X. S. *et al.* Large-Area Synthesis of High-Quality and Uniform Graphene Films on Copper Foils. *Science* **324**, 1312-1314, doi:10.1126/science.1171245 (2009).

346 Novoselov, K. S. *et al.* Electric field effect in atomically thin carbon films. *Science* **306**, 666-669, doi:10.1126/science.1102896 (2004).

347 Mohanty, N. & Berry, V. Graphene-based single-bacterium resolution biodevice and DNA transistor: interfacing graphene derivatives with nanoscale and microscale biocomponents. *Nano letters* **8**, 4469-4476 (2008).

348 Society, A. C. *Cancer Facts & Figures 2017*. (American Cancer Society, 2017).

349 Torre, L. A., Siegel, R. L., Ward, E. M. & Jemal, A. Global Cancer Incidence and Mortality Rates and Trends—An Update. *Cancer Epidemiology Biomarkers & Prevention* **25**, 16-27, doi:10.1158/1055-9965.epi-15-0578 (2016).

350 Paul, S. M. *et al. How to improve R&D productivity: the pharmaceutical industry's grand challenge*. (Nat Rev Drug Discov. 2010 Mar;9(3):203-14. doi: 10.1038/nrd3078. Epub 2010 Feb 19.).

351 Administration, U. F. a. D. *Innovation or stagnation: challenge and opportunity on the critical path to new medical products*. (2004).

352 Nath, S. & Devi, G. R. Three-dimensional culture systems in cancer research: Focus on tumor spheroid model. *Pharmacology & Therapeutics* **163**, 94-108, doi:https://doi.org/10.1016/j.pharmthera.2016.03.013 (2016).

353 Ishiguro, T. *et al.* Tumor-derived spheroids: Relevance to cancer stem cells and clinical applications. *Cancer Science* **108**, 283-289, doi:10.1111/cas.13155 (2017).

354 Ma, H. L. *et al.* Multicellular tumor spheroids as an in vivo-like tumor model for three-dimensional imaging of chemotherapeutic and nano material cellular penetration. *Mol Imaging* **11**, 487-498 (2012).

355 Kato, Y., Iwamoto, M., Koike, T., Suzuki, F. & Takano, Y. Terminal differentiation and calcification in rabbit chondrocyte cultures grown in centrifuge tubes: regulation by transforming growth factor beta and serum factors. *Proceedings of the National Academy of Sciences of the United States of America* **85**, 9552-9556 (1988).

356 Ivascu, A. & Kubbies, M. Rapid generation of single-tumor spheroids for high-throughput cell function and toxicity analysis. *J Biomol Screen* **11**, 922-932 (2006).

357 Tung, Y. C. *et al.* High-throughput 3D spheroid culture and drug testing using a 384 hanging drop array. *Analyst* **136**, 473-478 (2011).

358 Nyberg, S. L. *et al.* Rapid, large-scale formation of porcine hepatocyte spheroids in a novel spheroid reservoir bioartificial liver. *Liver Transpl* **11**, 901-910 (2005).

359 Haisler, W. L. *et al.* Three-dimensional cell culturing by magnetic levitation. *Nat Protoc* **8**, 1940-1949 (2013).

360 Vadivelu, R., Kamble, H., Shiddiky, M. & Nguyen, N.-T. Microfluidic Technology for the Generation of Cell Spheroids and Their Applications. *Micromachines* **8**, 94 (2017).

361 Kim, S.-H., Lee, G. H. & Park, J. Y. Microwell fabrication methods and applications for cellular studies. *Biomedical Engineering Letters* **3**, 131-137, doi:10.1007/s13534-013-0105-z (2013).

362 Kang, A., Seo, H. I., Chung, B. G. & Lee, S.-H. Concave microwell array-mediated three-dimensional tumor model for screening anticancer drug-loaded nanoparticles. *Nanomedicine: Nanotechnology, Biology and Medicine* **11**, 1153-1161, doi:http://dx.doi.org/10.1016/j.nano.2015.02.009 (2015).

363 Cui, X., Hartanto, Y. & Zhang, H. Advances in multicellular spheroids formation. *Journal of The Royal Society Interface* **14**, doi:10.1098/rsif.2016.0877 (2017).

364 Jun Hyuk, B., Jong Min, L. & Bong Geun, C. Hydrogel-encapsulated 3D microwell array for neuronal differentiation. *Biomedical Materials* **11**, 015019 (2016).

365 Shubin, A. D., Felong, T. J., Graunke, D., Ovitt, C. E. & Benoit, D. S. Development of poly(ethylene glycol) hydrogels for salivary gland tissue engineering applications. *Tissue Eng Part A* **21**, 1733-1751 (2015).

366 Lee, B. H. *et al.* Modulation of Huh7.5 Spheroid Formation and Functionality Using Modified PEG-Based Hydrogels of Different Stiffness. *PLoS ONE* **10**, e0118123, doi:10.1371/journal.pone.0118123 (2015).

367 Du, Y., Lo, E., Ali, S. & Khademhosseini, A. Directed assembly of cell-laden microgels for fabrication of 3D tissue constructs. *Proceedings of the National Academy of Sciences* **105**, 9522-9527, doi:10.1073/pnas.0801866105 (2008).

368 Au, S. H., Chamberlain, M. D., Mahesh, S., Sefton, M. V. & Wheeler, A. R. Hepatic organoids for microfluidic drug screening. *Lab on a Chip* **14**, 3290-3299, doi:10.1039/c4lc00531g (2014).

369 Futrega, K., Atkinson, K., Lott, W. B. & Doran, M. R. Spheroid Coculture of Hematopoietic Stem/Progenitor Cells and Monolayer Expanded Mesenchymal Stem/Stromal Cells in Polydimethylsiloxane Microwells Modestly Improves In Vitro Hematopoietic Stem/Progenitor Cell Expansion. *Tissue Eng Part C Methods* **23**, 200-218 (2017).

370 Liu, Y. *et al.* Promoting hepatocyte spheroid formation and functions by coculture with fibroblasts on micropatterned electrospun fibrous scaffolds. *J Mater Chem B* **2**, 3029-3040, doi:10.1039/c3tb21779e (2014).

371 Cheon, Y. A., Bae, J. H. & Chung, B. G. Reduced Graphene Oxide Nanosheet for Chemo-photothermal Therapy. *Langmuir* **32**, 2731-2736, doi:10.1021/acs.langmuir.6b00315 (2016).

372 Lee, J. M., Seo, H. I., Bae, J. H. & Chung, B. G. Hydrogel microfluidic co-culture device for photothermal therapy and cancer migration. *Electrophoresis* **38**, 1318-1324, doi:10.1002/elps.201600540 (2017).

373 Yin, P. T., Shah, S., Chhowalla, M. & Lee, K.-B. Design, Synthesis, and Characterization of Graphene–Nanoparticle Hybrid Materials for Bioapplications. *Chemical Reviews* **115**, 2483-2531, doi:10.1021/cr500537t (2015).

374 Kim, T.-H., Lee, K.-B. & Choi, J.-W. 3D graphene oxide-encapsulated gold nanoparticles to detect neural stem cell differentiation. *Biomaterials* **34**, 8660-8670, doi:http://dx.doi.org/10.1016/j.biomaterials.2013.07.101 (2013).

375 Wang, C. *et al.* Gold Nanoclusters and Graphene Nanocomposites for Drug Delivery and Imaging of Cancer Cells. *Angewandte Chemie* **123**, 11848-11852, doi:10.1002/ange.201105573 (2011).

376 Kim, J.-e., Lee, J. M. & Chung, B. G. Microwell arrays for uniform-sized embryoid body-mediated endothelial cell differentiation. *Biomedical Microdevices* **16**, 559-566, doi:10.1007/s10544-014-9858-0 (2014).

377 Niidome, T., Nakashima, K., Takahashi, H. & Niidome, Y. Preparation of primary amine-modified gold nanoparticles and their transfection ability into cultivated cells. *Chemical Communications*, 1978-1979 (2004).

378 Lin, R.-Z., Chou, L.-F., Chien, C.-C. M. & Chang, H.-Y. Dynamic analysis of hepatoma spheroid formation: roles of E-cadherin and β1-integrin. *Cell and Tissue Research* **324**, 411-422, doi:10.1007/s00441-005-0148-2 (2006).

379 Ito, K. *et al.* Temporal Transition of Mechanical Characteristics of HUVEC/MSC Spheroids Using a Microfluidic Chip with Force Sensor Probes. *Micromachines* **7**, 221 (2016).

380 Chithrani, B. D., Ghazani, A. A. & Chan, W. C. Determining the size and shape dependence of gold nanoparticle uptake into mammalian cells. *Nano Lett* **6**, 662-668, doi:10.1021/nl052396o (2006).

381 Paredes, J. I., Villar-Rodil, S., Martinez-Alonso, A. & Tascon, J. M. Graphene oxide dispersions in organic solvents. *Langmuir* **24**, 10560-10564, doi:10.1021/la801744a (2008).

382 Kim, J. A., Aberg, C., Salvati, A. & Dawson, K. A. Role of cell cycle on the cellular uptake and dilution of nanoparticles in a cell population. *Nat Nano* **7**, 62-68, doi:http://www.nature.com/nnano/journal/v7/n1/abs/nnano.2011.191.html#supplementary-information (2012).

383 Field, S. B. & Bleehen, N. M. Hyperthermia in the treatment of cancer. *Cancer Treatment Reviews* **6**, 63-94, doi:http://dx.doi.org/10.1016/S0305-7372(79)80043-2 (1979).

384 van der Zee, J. Heating the patient: a promising approach? *Annals of Oncology* **13**, 1173-1184, doi:10.1093/annonc/mdf280 (2002).

385 Rosi, N. L. *et al.* Oligonucleotide-modified gold nanoparticles for intracellular gene regulation. *Science* **312**, 1027-1030, doi:10.1126/science.1125559 (2006).

386 Cutler, J. I., Auyeung, E. & Mirkin, C. A. Spherical Nucleic Acids. *Journal of the American Chemical Society* **134**, 1376-1391, doi:10.1021/ja209351u (2012).

387 Cutler, J. I. *et al.* Polyvalent Nucleic Acid Nanostructures. *Journal of the American Chemical Society* **133**, 9254-9257, doi:10.1021/ja203375n (2011).

388 Choi, K. Y. *et al.* A nanoparticle formula for delivering siRNA or miRNAs to tumor cells in cell culture and in vivo. *Nat. Protocols* **9**, 1900-1915, doi:10.1038/nprot.2014.128

http://www.nature.com/nprot/journal/v9/n8/abs/nprot.2014.128.html#supplementary-information (2014).

389 Gilleron, J. *et al.* Image-based analysis of lipid nanoparticle-mediated siRNA delivery, intracellular trafficking and endosomal escape. *Nat Biotech* **31**, 638-646, doi:10.1038/nbt.2612

http://www.nature.com/nbt/journal/v31/n7/abs/nbt.2612.html#supplementary-information (2013).

390 Patel, S., Yin, P. T., Sugiyama, H. & Lee, K. B. Inducing Stem Cell Myogenesis Using NanoScript. *ACS Nano* **9**, 6909-6917, doi:10.1021/acsnano.5b00709 (2015).
391 Ryoo, S. R. *et al.* Quantitative and Multiplexed MicroRNA Sensing in Living Cells Based on Peptide Nucleic Acid and Nano Graphene Oxide (PANGO). *ACS Nano* **7**, 5882-5891, doi:10.1021/nn401183s (2013).
392 Thi, E. P. *et al.* Lipid nanoparticle siRNA treatment of Ebola-virus-Makona-infected nonhuman primates. *Nature* **521**, 362-365, doi:10.1038/nature14442 (2015).
393 Wang, Z. L. *et al.* Biomimetic RNA-Silencing Nanocomplexes: Overcoming Multidrug Resistance in Cancer Cells. *Angewandte Chemie-International Edition* **53**, 1997-2001, doi:10.1002/anie.201309985 (2014).
394 Yin, P. T., Shah, B. P. & Lee, K. B. Combined Magnetic Nanoparticle-based MicroRNA and Hyperthermia Therapy to Enhance Apoptosis in Brain Cancer Cells. *Small* **10**, 4106-4112, doi:10.1002/smll.201400963 (2014).
395 Zheng, J. *et al.* A Spherical Nucleic Acid Platform Based on Self-Assembled DNA Biopolymer for High-Performance Cancer Therapy. *ACS Nano* **7**, 6545-6554, doi:10.1021/nn402344v (2013).
396 Chen, A. M. *et al.* Co-delivery of Doxorubicin and Bcl-2 siRNA by Mesoporous Silica Nanoparticles Enhances the Efficacy of Chemotherapy in Multidrug-Resistant Cancer Cells. *Small* **5**, 2673-2677, doi:10.1002/smll.200900621 (2009).
397 Kole, R., Krainer, A. R. & Altman, S. RNA therapeutics: beyond RNA interference and antisense oligonucleotides. *Nat Rev Drug Discov* **11**, 125-140, doi:10.1038/nrd3625 (2012).
398 Gottesman, M. M., Fojo, T. & Bates, S. E. Multidrug resistance in cancer: Role of ATP-dependent transporters. *Nature Reviews Cancer* **2**, 48-58, doi:10.1038/nrc706 (2002).
399 Szakacs, G., Paterson, J. K., Ludwig, J. A., Booth-Genthe, C. & Gottesman, M. M. Targeting multidrug resistance in cancer. *Nature Reviews Drug Discovery* **5**, 219-234, doi:10.1038/nrd1984 (2006).
400 Cory, S. & Adams, J. M. The Bcl2 family: regulators of the cellular life-or-death switch. *Nature reviews. Cancer* **2**, 647-656, doi:10.1038/nrc883 (2002).
401 Thomadaki, H. & Scorilas, A. BCL2 family of apoptosis-related genes: Functions and clinical implications in cancer. *Crit. Rev. Clin. Lab. Sci.* **43**, 1-67, doi:10.1080/10408360500295626 (2006).
402 Frenzel, A., Grespi, F., Chmelewskij, W. & Villunger, A. Bcl2 family proteins in carcinogenesis and the treatment of cancer. *Apoptosis* **14**, 584-596, doi:10.1007/s10495-008-0300-z (2009).
403 Zhu, W. *et al.* miR-200bc/429 cluster modulates multidrug resistance of human cancer cell lines by targeting BCL2 and XIAP. *Cancer Chemother. Pharmacol.* **69**, 723-731, doi:10.1007/s00280-011-1752-3 (2012).
404 Lai, J. P. *et al.* Development of Photoactivated Fluorescent N-Hydroxyoxindoles and Their Application for Cell-Selective Imaging. *Chemistry-a European Journal* **22**, 6361-6367, doi:10.1002/chem.201600547 (2016).
405 Islam, T. & Harisinghani, M. G. Overview of nanoparticle use in cancer imaging. *Cancer Biomark.* **5**, 61-67, doi:10.3233/cbm-2009-0578 (2009).

406 Shah, B., Yin, P. T., Ghoshal, S. & Lee, K. B. Multimodal Magnetic Core-Shell Nanoparticles for Effective Stem-Cell Differentiation and Imaging. *Angewandte Chemie-International Edition* **52**, 6190-6195, doi:10.1002/anie.201302245 (2013).

407 Santra, S., Dutta, D., Walter, G. A. & Moudgil, B. M. Fluorescent nanoparticle probes for cancer imaging. *Technol. Cancer Res. Treat.* **4**, 593-602 (2005).

408 Yin, P. T., Shah, S., Chhowalla, M. & Lee, K. B. Design, synthesis, and characterization of graphene-nanoparticle hybrid materials for bioapplications. *Chemical reviews* **115**, 2483-2531, doi:10.1021/cr500537t (2015).

409 Ma, X. *et al.* Graphene oxide wrapped gold nanoparticles for intracellular Raman imaging and drug delivery. *J Mater Chem B* **1**, 6495-6500, doi:10.1039/c3tb21385d (2013).

410 Robinson, J. T. *et al.* Ultrasmall reduced graphene oxide with high near-infrared absorbance for photothermal therapy. *J Am Chem Soc* **133**, 6825-6831, doi:10.1021/ja2010175 (2011).

411 Zedan, A. F., Moussa, S., Terner, J., Atkinson, G. & El-Shall, M. S. Ultrasmall Gold Nanoparticles Anchored to Graphene and Enhanced Photothermal Effects by Laser Irradiation of Gold Nanostructures in Graphene Oxide Solutions. *ACS Nano* **7**, 627-636, doi:10.1021/nn304775h (2013).

412 Dembereldorj, U. *et al.* Gold nanorod-assembled PEGylated graphene-oxide nanocomposites for photothermal cancer therapy. *Photochemistry and photobiology* **90**, 659-666, doi:10.1111/php.12212 (2014).

413 Xu, C. *et al.* Encapsulating gold nanoparticles or nanorods in graphene oxide shells as a novel gene vector. *ACS Appl Mater Interfaces* **5**, 2715-2724, doi:10.1021/am400212j (2013).

414 Wang, C. *et al.* Gold nanoclusters and graphene nanocomposites for drug delivery and imaging of cancer cells. *Angew Chem Int Ed Engl* **50**, 11644-11648, doi:10.1002/anie.201105573 (2011).

415 Turcheniuk, K., Boukherroub, R. & Szunerits, S. Gold-graphene nanocomposites for sensing and biomedical applications. *J Mater Chem B* **3**, 4301-4324, doi:10.1039/c5tb00511f (2015).

416 Lim, D. K. *et al.* Enhanced photothermal effect of plasmonic nanoparticles coated with reduced graphene oxide. *Nano Lett* **13**, 4075-4079, doi:10.1021/nl4014315 (2013).

417 Yin, P. T., Kim, T. H., Choi, J. W. & Lee, K. B. Prospects for graphene-nanoparticle-based hybrid sensors. *Physical chemistry chemical physics : PCCP* **15**, 12785-12799, doi:10.1039/c3cp51901e (2013).

418 Huang, X., Qi, X., Boey, F. & Zhang, H. Graphene-based composites. *Chem Soc Rev* **41**, 666-686, doi:10.1039/c1cs15078b (2012).

419 Loh, K. P., Bao, Q., Eda, G. & Chhowalla, M. Graphene oxide as a chemically tunable platform for optical applications. *Nature chemistry* **2**, 1015-1024, doi:10.1038/nchem.907 (2010).

420 Chen, D., Feng, H. & Li, J. Graphene oxide: preparation, functionalization, and electrochemical applications. *Chem Rev* **112**, 6027-6053, doi:10.1021/cr300115g (2012).

421 Novoselov, K. S. *et al.* A roadmap for graphene. *Nature* **490**, 192-200, doi:10.1038/nature11458 (2012).

422 Myung, S. *et al.* Graphene-encapsulated nanoparticle-based biosensor for the selective detection of cancer biomarkers. *Adv. Mater.* **23**, 2221-2225, doi:10.1002/adma.201100014 (2011).

423 Zhong, Y. R. *et al.* Orderly Packed Anodes for High-Power Lithium-Ion Batteries with Super-Long Cycle Life: Rational Design of MnCO3/Large-Area Graphene Composites. *Advanced Materials* **27**, 806-812, doi:10.1002/adma.201404611 (2015).

424 Jing, Y., Zhou, Z., Cabrera, C. R. & Chen, Z. F. Graphene, inorganic graphene analogs and their composites for lithium ion batteries. *J. Mater. Chem. A* **2**, 12104-12122, doi:10.1039/c4ta01033g (2014).

425 Yang, K., Feng, L., Shi, X. & Liu, Z. Nano-graphene in biomedicine: theranostic applications. *Chem Soc Rev* **42**, 530-547, doi:10.1039/c2cs35342c (2013).

426 Tang, L. H., Wang, Y. & Li, J. H. The graphene/nucleic acid nanobiointerface. *Chemical Society Reviews* **44**, 6954-6980, doi:10.1039/c4cs00519h (2015).

427 Dong, H. F., Ding, L., Yan, F., Ji, H. X. & Ju, H. X. The use of polyethylenimine-grafted graphene nanoribbon for cellular delivery of locked nucleic acid modified molecular beacon for recognition of microRNA. *Biomaterials* **32**, 3875-3882, doi:10.1016/j.biomaterials.2011.02.001 (2011).

428 Paul, A. *et al.* Injectable Graphene Oxide/Hydrogel-Based Angiogenic Gene Delivery System for Vasculogenesis and Cardiac Repair. *ACS Nano* **8**, 8050-8062, doi:10.1021/nn5020787 (2014).

429 Hung, A. H. *et al.* Graphene Oxide Enhances Cellular Delivery of Hydrophilic Small Molecules by Co-incubation. *ACS Nano* **8**, 10168-10177, doi:10.1021/nn502986e (2014).

430 Tian, B., Wang, C., Zhang, S., Feng, L. Z. & Liu, Z. Photothermally Enhanced Photodynamic Therapy Delivered by Nano-Graphene Oxide. *ACS Nano* **5**, 7000-7009, doi:10.1021/nn201560b (2011).

431 Sydlik, S. A., Jhunjhunwala, S., Webber, M. J., Anderson, D. G. & Langer, R. In Vivo Compatibility of Graphene Oxide with Differing Oxidation States. *ACS Nano* **9**, 3866-3874, doi:10.1021/acsnano.5b01290 (2015).

432 Yang, K. *et al.* The influence of surface chemistry and size of nanoscale graphene oxide on photothermal therapy of cancer using ultra-low laser power. *Biomaterials* **33**, 2206-2214, doi:10.1016/j.biomaterials.2011.11.064 (2012).

433 Mao, H. Y. *et al.* Graphene: promises, facts, opportunities, and challenges in nanomedicine. *Chem Rev* **113**, 3407-3424, doi:10.1021/cr300335p (2013).

434 Anker, J. N. *et al.* Biosensing with plasmonic nanosensors. *Nature Materials* **7**, 442-453, doi:10.1038/nmat2162 (2008).

435 Zhang, X. M., Chen, Y. L., Liu, R. S. & Tsai, D. P. Plasmonic photocatalysis. *Rep. Prog. Phys.* **76**, 41, doi:10.1088/0034-4885/76/4/046401 (2013).

436 Fan, W. *et al.* Graphene oxide and shape-controlled silver nanoparticle hybrids for ultrasensitive single-particle surface-enhanced Raman scattering (SERS) sensing. *Nanoscale* **6**, 4843-4851, doi:10.1039/c3nr06316j (2014).

437 Chang, H. X., Tang, L. H., Wang, Y., Jiang, J. H. & Li, J. H. Graphene Fluorescence Resonance Energy Transfer Aptasensor for the Thrombin Detection. *Analytical Chemistry* **82**, 2341-2346, doi:10.1021/ac9025384 (2010).

438 Xie, L. M., Ling, X., Fang, Y., Zhang, J. & Liu, Z. F. Graphene as a Substrate To Suppress Fluorescence in Resonance Raman Spectroscopy. *Journal of the American Chemical Society* **131**, 9890-+, doi:10.1021/ja9037593 (2009).

439 Albanese, A., Tang, P. S. & Chan, W. C. The effect of nanoparticle size, shape, and surface chemistry on biological systems. *Annu Rev Biomed Eng* **14**, 1-16, doi:10.1146/annurev-bioeng-071811-150124 (2012).

440 Jansen, B. *et al.* Chemosensitisation of malignant melanoma by BCL2 antisense therapy. *Lancet* **356**, 1728-1733, doi:10.1016/S0140-6736(00)03207-4 (2000).

441 Wust, P. *et al.* Hyperthermia in combined treatment of cancer. *The Lancet. Oncology* **3**, 487-497, doi:10.1016/s1470-2045(02)00818-5 (2002).

442 Vanneman, M. & Dranoff, G. Combining immunotherapy and targeted therapies in cancer treatment. *Nature Reviews Cancer* **12**, 237-251, doi:10.1038/nrc3237 (2012).

443 Arap, W., Pasqualini, R. & Ruoslahti, E. Cancer treatment by targeted drug delivery to tumor vasculature in a mouse model. *Science* **279**, 377-380, doi:10.1126/science.279.5349.377 (1998).

444 Kim, C., Shah, B. P., Subramaniam, P. & Lee, K. B. Synergistic Induction of Apoptosis in Brain Cancer Cells by Targeted Codelivery of siRNA and Anticancer Drugs. *Molecular Pharmaceutics* **8**, 1955-1961, doi:10.1021/mp100460h (2011).

445 Liu, Z., Tabakman, S. M., Chen, Z. & Dai, H. Preparation of carbon nanotube bioconjugates for biomedical applications. *Nat Protoc* **4**, 1372-1382, doi:10.1038/nprot.2009.146 (2009).

446 Choi, J.-s. *et al.* Distance-dependent magnetic resonance tuning as a versatile MRI sensing platform for biological targets. *Nature Materials* (2017).

447 Lin, L. S. *et al.* Simultaneous Fenton-like Ion Delivery and Glutathione Depletion by MnO2-Based Nanoagent to Enhance Chemodynamic Therapy. *Angewandte Chemie-International Edition* **57**, 4902-4906, doi:10.1002/anie.201712027 (2018).

448 Fan, W. P. *et al.* Intelligent MnO2 Nanosheets Anchored with Upconversion Nanoprobes for Concurrent pH-/H2O2-Responsive UCL Imaging and Oxygen-Elevated Synergetic Therapy. *Advanced Materials* **27**, 4155-4161, doi:10.1002/adma.201405141 (2015).

449 Schlücker, S. Surface-Enhanced raman spectroscopy: Concepts and chemical applications. *Angewandte Chemie International Edition* **53**, 4756-4795 (2014).

450 Shah, S. *et al.* Graphene: Guiding Stem Cell Differentiation into Oligodendrocytes Using Graphene-Nanofiber Hybrid Scaffolds (Adv. Mater. 22/2014). *Advanced Materials* **26**, 3570-3570 (2014).

451 Shah, S. *et al.* Guiding Stem Cell Differentiation into Oligodendrocytes Using Graphene-Nanofiber Hybrid Scaffolds. *Advanced Materials* **26**, 3673-3680, doi:10.1002/adma.201400523 (2014).

452 Yang, L. T. *et al.* A biodegradable hybrid inorganic nanoscaffold for advanced stem cell therapy. *Nature Communications* **9**, doi:10.1038/s41467-018-05599-2 (2018).
453 Rubiano, A. M., Carney, N., Chesnut, R. & Puyana, J. C. Global neurotrauma research challenges and opportunities. *Nature* **527**, S193-S197, doi:10.1038/nature16035 (2015).
454 Tran, A. P. & Silver, J. Neuroscience. Systemically treating spinal cord injury. *Science* **348**, 285-286, doi:10.1126/science.aab1615 (2015).
455 Bouton, C. E. *et al.* Restoring cortical control of functional movement in a human with quadriplegia. *Nature* **533**, 247-+, doi:10.1038/nature17435 (2016).
456 Lu, P. *et al.* Long-distance growth and connectivity of neural stem cells after severe spinal cord injury. *Cell* **150**, 1264-1273 (2012).
457 Ruschel, J. *et al.* Axonal regeneration. Systemic administration of epothilone B promotes axon regeneration after spinal cord injury. *Science* **348**, 347-352, doi:10.1126/science.aaa2958 (2015).
458 van den Brand, R. *et al.* Restoring voluntary control of locomotion after paralyzing spinal cord injury. *Science* **336**, 1182-1185, doi:10.1126/science.1217416 (2012).
459 Tsuji, O. *et al.* Therapeutic potential of appropriately evaluated safe-induced pluripotent stem cells for spinal cord injury. *Proc. Natl. Acad. Sci. U. S. A.* **107**, 12704-12709, doi:10.1073/pnas.0910106107 (2010).
460 McDonald, J. W. *et al.* Transplanted embryonic stem cells survive, differentiate and promote recovery in injured rat spinal cord. *Nat. Med.* **5**, 1410-1412, doi:10.1038/70986 (1999).
461 Lindvall, O. & Kokaia, Z. Stem cells for the treatment of neurological disorders. *Nature* **441**, 1094-1096 (2006).
462 Park, K. I., Teng, Y. D. & Snyder, E. Y. The injured brain interacts reciprocally with neural stem cells supported by scaffolds to reconstitute lost tissue. *Nature biotechnology* **20**, 1111-1117 (2002).
463 Thuret, S., Moon, L. D. & Gage, F. H. Therapeutic interventions after spinal cord injury. *Nature Reviews Neuroscience* **7**, 628 (2006).
464 Kan, E. M., Ling, E. A. & Lu, J. Stem cell therapy for spinal cord injury. *Curr. Med. Chem.* **17**, 4492-4510 (2010).
465 Griffin, D. R., Weaver, W. M., Scumpia, P. O., Di Carlo, D. & Segura, T. Accelerated wound healing by injectable microporous gel scaffolds assembled from annealed building blocks. *Nature materials* **14**, 737-744 (2015).
466 Huebsch, N. *et al.* Matrix elasticity of void-forming hydrogels controls transplanted-stem-cell-mediated bone formation. *Nature materials* **14**, 1269-1277 (2015).
467 Murphy, W. L., McDevitt, T. C. & Engler, A. J. Materials as stem cell regulators. *Nature materials* **13**, 547-557 (2014).
468 Carlson, A. L. *et al.* Generation and transplantation of reprogrammed human neurons in the brain using 3D microtopographic scaffolds. *Nature communications* **7** (2016).

469 Meyer, R. A. & Green, J. J. Shaping the future of nanomedicine: anisotropy in polymeric nanoparticle design. *Wiley Interdisciplinary Reviews: Nanomedicine and Nanobiotechnology* **8**, 191-207 (2016).
470 Kang, H.-W. *et al.* A 3D bioprinting system to produce human-scale tissue constructs with structural integrity. *Nature biotechnology* **34**, 312-319 (2016).
471 DeForest, C. A. & Tirrell, D. A. A photoreversible protein-patterning approach for guiding stem cell fate in three-dimensional gels. *Nature materials* **14**, 523-531 (2015).
472 DeForest, C. A., Polizzotti, B. D. & Anseth, K. S. Sequential click reactions for synthesizing and patterning three-dimensional cell microenvironments. *Nature materials* **8**, 659-664 (2009).
473 Luo, Y. & Shoichet, M. S. A photolabile hydrogel for guided three-dimensional cell growth and migration. *Nature materials* **3**, 249-253 (2004).
474 Kim, T. H. *et al.* Controlling Differentiation of Adipose-Derived Stem Cells Using Combinatorial Graphene Hybrid-Pattern Arrays. *ACS Nano* **9**, 3780-3790, doi:10.1021/nn5066028 (2015).
475 Park, S. Y. *et al.* Enhanced differentiation of human neural stem cells into neurons on graphene. *Advanced Materials* **23** (2011).
476 Laurenti, M. *et al.* Two-Dimensional Magnesium Phosphate Nanosheets Form Highly Thixotropic Gels That Up-Regulate Bone Formation. *Nano letters* **16**, 4779-4787 (2016).
477 Aldinucci, A. *et al.* Carbon nanotube scaffolds instruct human dendritic cells: modulating immune responses by contacts at the nanoscale. *Nano letters* **13**, 6098-6105 (2013).
478 Dvir, T. *et al.* Nanowired three-dimensional cardiac patches. *Nature nanotechnology* **6**, 720-725 (2011).
479 Dvir, T., Timko, B. P., Kohane, D. S. & Langer, R. Nanotechnological strategies for engineering complex tissues. *Nature nanotechnology* **6**, 13 (2011).
480 Kai, K. *et al.* Room-temperature synthesis of manganese oxide monosheets. *Journal of the American Chemical Society* **130**, 15938-15943 (2008).
481 Marchetto, M. C. N. *et al.* A Model for Neural Development and Treatment of Rett Syndrome Using Human Induced Pluripotent Stem Cells. *Cell* **143**, 527-539, doi:http://dx.doi.org/10.1016/j.cell.2010.10.016 (2010).
482 Meijering, E. *et al.* Design and validation of a tool for neurite tracing and analysis in fluorescence microscopy images. *Cytometry Part A* **58**, 167-176 (2004).
483 Perdew, J. P., Burke, K. & Ernzerhof, M. Generalized gradient approximation made simple (vol 77, pg 3865, 1996). *Physical Review Letters* **78**, 1396-1396, doi:10.1103/PhysRevLett.78.1396 (1997).
484 Grimme, S., Antony, J., Ehrlich, S. & Krieg, H. A consistent and accurate ab initio parametrization of density functional dispersion correction (DFT-D) for the 94 elements H-Pu. *J. Chem. Phys.* **132**, 19, doi:10.1063/1.3382344 (2010).
485 Wang, L., Maxisch, T. & Ceder, G. Oxidation energies of transition metal oxides within the GGA+U framework. *Physical Review B* **73**, 6, doi:10.1103/PhysRevB.73.195107 (2006).

486 Wang, Y. C., Chen, Z. H. & Jiang, H. The local projection in the density functional theory plus U approach: A critical assessment. *Journal of Chemical Physics* **144**, 9, doi:10.1063/1.4945608 (2016).

487 Sun, C. H., Wang, Y., Zou, J. & Smith, S. C. A formation mechanism of oxygen vacancies in a MnO2 monolayer: a DFT+U study. *Physical Chemistry Chemical Physics* **13**, 11325-11328, doi:10.1039/c1cp20634f (2011).

488 Luchetti, S. *et al.* Comparison of immunopathology and locomotor recovery in C57BL/6, BUB/BnJ, and NOD-SCID mice after contusion spinal cord injury. *Journal of neurotrauma* **27**, 411-421 (2010).

489 Dalby, M. J., Gadegaard, N. & Oreffo, R. O. Harnessing nanotopography and integrin-matrix interactions to influence stem cell fate. *Nature materials* **13**, 558-569 (2014).

490 Wang, S. *et al.* A Nanostructured Molybdenum Disulfide Film for Promoting Neural Stem Cell Neuronal Differentiation: toward a Nerve Tissue-Engineered 3D Scaffold. *Advanced Biosystems* (2017).

491 Takahashi, K. & Yamanaka, S. Induction of pluripotent stem cells from mouse embryonic and adult fibroblast cultures by defined factors. *Cell* **126**, 663-676, doi:10.1016/j.cell.2006.07.024 (2006).

492 López-Dolado, E. *et al.* Subacute tissue response to 3D graphene oxide scaffolds implanted in the injured rat spinal cord. *Advanced healthcare materials* **4**, 1861-1868 (2015).

493 Halliwell, B. & Gutteridge, J. M. C. The antioxidants of human extracellular fluids. *Arch. Biochem. Biophys.* **280**, 1-8, doi:10.1016/0003-9861(90)90510-6 (1990).

494 Khetan, S. *et al.* Degradation-mediated cellular traction directs stem cell fate in covalently crosslinked three-dimensional hydrogels. *Nat Mater* **12**, 458-465, doi:10.1038/nmat3586 (2013).

495 Yu, X., Dillon, G. P. & Bellamkonda, R. V. A laminin and nerve growth factor-laden three-dimensional scaffold for enhanced neurite extension. *Tissue engineering* **5**, 291-304 (1999).

496 Wang, Q. *et al.* High-water-content mouldable hydrogels by mixing clay and a dendritic molecular binder. *Nature* **463**, 339-343, doi:http://www.nature.com/nature/journal/v463/n7279/suppinfo/nature08693_S1.html (2010).

497 O'Neill, H. S. *et al.* Biomaterial-Enhanced Cell and Drug Delivery: Lessons Learned in the Cardiac Field and Future Perspectives. *Advanced Materials* (2016).

498 Tam, R. Y., Fuehrmann, T., Mitrousis, N. & Shoichet, M. S. Regenerative Therapies for Central Nervous System Diseases: a Biomaterials Approach. *Neuropsychopharmacology* **39**, 169-188, doi:10.1038/npp.2013.237 (2014).

499 Hollister, S. J. Porous scaffold design for tissue engineering. *Nature materials* **4**, 518-524 (2005).

500 Li, J. & Mooney, D. J. Designing hydrogels for controlled drug delivery. *Nature Reviews Materials* **1**, 16071 (2016).

501 El Bejjani, R. & Hammarlund, M. Notch Signaling Inhibits Axon Regeneration. *Neuron* **73**, 268-278, doi:10.1016/j.neuron.2011.11.017 (2012).

502 Androutsellis-Theotokis, A. *et al.* Notch signalling regulates stem cell numbers in vitro and in vivo. *Nature* **442**, 823-826 (2006).
503 Tzatzalos, E. *et al.* A cis-element in the Notch1 locus is involved in the regulation of gene expression in interneuron progenitors. *Developmental biology* **372**, 217-228 (2012).
504 Lu, P. *et al.* Prolonged human neural stem cell maturation supports recovery in injured rodent CNS. *The Journal of clinical investigation* **127**, 3287-3299 (2017).
505 Führmann, T. *et al.* Combined delivery of chondroitinase ABC and human induced pluripotent stem cell-derived neuroepithelial cells promote tissue repair in an animal model of spinal cord injury. *Biomedical Materials* **13**, 024103 (2018).
506 Bentley, S. D. *et al.* Complete genome sequence of the model actinomycete Streptomyces coelicolor A3(2). *Nature* **417**, 141-147, doi:10.1038/417141a (2002).
507 Drury, J. L. & Mooney, D. J. Hydrogels for tissue engineering: scaffold design variables and applications. *Biomaterials* **24**, 4337-4351, doi:10.1016/s0142-9612(03)00340-5 (2003).
508 Greiner, A. & Wendorff, J. H. Electrospinning: A fascinating method for the preparation of ultrathin fibres. *Angewandte Chemie-International Edition* **46**, 5670-5703, doi:10.1002/anie.200604646 (2007).
509 Hollister, S. J. Porous scaffold design for tissue engineering. *Nature Materials* **4**, 518-524, doi:10.1038/nmat1421 (2005).
510 Hutmacher, D. W. Scaffolds in tissue engineering bone and cartilage. *Biomaterials* **21**, 2529-2543, doi:10.1016/s0142-9612(00)00121-6 (2000).
511 Langer, R. & Vacanti, J. P. TISSUE ENGINEERING. *Science* **260**, 920-926, doi:10.1126/science.8493529 (1993).
512 Lee, K. Y. & Mooney, D. J. Hydrogels for tissue engineering. *Chemical Reviews* **101**, 1869-1879, doi:10.1021/cr000108x (2001).
513 Li, W. J., Laurencin, C. T., Caterson, E. J., Tuan, R. S. & Ko, F. K. Electrospun nanofibrous structure: A novel scaffold for tissue engineering. *Journal of Biomedical Materials Research* **60**, 613-621, doi:10.1002/jbm.10167 (2002).
514 Liu, X. Y., Chu, P. K. & Ding, C. X. Surface modification of titanium, titanium alloys, and related materials for biomedical applications. *Materials Science & Engineering R-Reports* **47**, 49-121, doi:10.1016/j.mser.2004.11.001 (2004).
515 Lutolf, M. P. & Hubbell, J. A. Synthetic biomaterials as instructive extracellular microenvironments for morphogenesis in tissue engineering. *Nature Biotechnology* **23**, 47-55, doi:10.1038/nbt1055 (2005).
516 Rezwan, K., Chen, Q. Z., Blaker, J. J. & Boccaccini, A. R. Biodegradable and bioactive porous polymer/inorganic composite scaffolds for bone tissue engineering. *Biomaterials* **27**, 3413-3431, doi:10.1016/j.biomaterials.2006.01.039 (2006).
517 Sill, T. J. & von Recum, H. A. Electro spinning: Applications in drug delivery and tissue engineering. *Biomaterials* **29**, 1989-2006, doi:10.1016/j.biomaterials.2008.01.011 (2008).
518 Stevens, M. M. & George, J. H. Exploring and engineering the cell surface interface. *Science* **310**, 1135-1138, doi:10.1126/science.1106587 (2005).

519 Tomasek, J. J., Gabbiani, G., Hinz, B., Chaponnier, C. & Brown, R. A. Myofibroblasts and mechano-regulation of connective tissue remodelling. *Nature Reviews Molecular Cell Biology* **3**, 349-363, doi:10.1038/nrm809 (2002).
520 Zuk, P. A. *et al.* Multilineage cells from human adipose tissue: Implications for cell-based therapies. *Tissue Engineering* **7**, 211-228, doi:10.1089/107632701300062859 (2001).
521 Anderson, J. M., Rodriguez, A. & Chang, D. T. Foreign body reaction to biomaterials. *Seminars in Immunology* **20**, 86-100, doi:10.1016/j.smim.2007.11.004 (2008).
522 Nair, L. S. & Laurencin, C. T. Biodegradable polymers as biomaterials. *Progress in Polymer Science* **32**, 762-798, doi:10.1016/j.progpolymsci.2007.05.017 (2007).
523 Yamato, M. & Okano, T. Cell sheet engineering. *Materials today* **7**, 42-47 (2004).
524 Yang, J. *et al.* Cell sheet engineering: recreating tissues without biodegradable scaffolds. *Biomaterials* **26**, 6415-6422 (2005).
525 Du, L. H. *et al.* Flexible supercapacitors based on carbon nanotube/MnO2 nanotube hybrid porous films for wearable electronic devices. *Journal of Materials Chemistry A* **2**, 17561-17567, doi:10.1039/c4ta04431b (2014).
526 Liu, G. *et al.* Interphase strengthening birnessite MnO2 coating on three-dimensional Ni foam for soot removal. *Applied Catalysis a-General* **568**, 157-167, doi:10.1016/j.apcata.2018.10.003 (2018).
527 Zhu, Q. F., Zhang, B. B., Wang, T. T. & Feng, X. D. Synthesis and properties of porous delta-MnO2/polymer millimeter-sized beads for Ni(II) removal. *Microporous and Mesoporous Materials* **273**, 90-98, doi:10.1016/j.micromeso.2018.07.001 (2019).
528 Lee, K.-B. & Yang, L. (US Patent App. PCT/US18/61,301, 2018).
529 Han, T. T., Yang, L. T., Lee, K. B. & Mainelis, G. Design and Development of a Novel Nanofiber Nasal Filter (NNF) to Improve Respiratory Health. *Aerosol and Air Quality Research* **18**, 2064-2076, doi:10.4209/aaqr.2018.03.0086 (2018).
530 Wang, S. Q., Yang, L. T., Zhang, Q. Y. & Lee, K. B. A novel biodegradable multifunctional nanoplatform synergistically overcome multidrug resistance. *Abstracts of Papers of the American Chemical Society* **256** (2018).
531 Hsiao, S. C. *et al.* Direct Cell Surface Modification with DNA for the Capture of Primary Cells and the Investigation of Myotube Formation on Defined Patterns. *Langmuir* **25**, 6985-6991, doi:10.1021/la900150n (2009).
532 Zuk, P. A. *et al.* Multilineage cells from human adipose tissue: Implications for cell-based therapies. *Tissue Engineering* **7**, 211-228, doi:10.1089/107632701300062859 (2001).
533 Kane, R. S., Takayama, S., Ostuni, E., Ingber, D. E. & Whitesides, G. M. Patterning proteins and cells using soft lithography. *Biomaterials* **20**, 2363-2376, doi:10.1016/s0142-9612(99)00165-9 (1999).
534 Todhunter, M. E. *et al.* Programmed synthesis of three-dimensional tissues. *Nature Methods* **12**, 975-981, doi:10.1038/nmeth.3553 (2015).
535 Gartner, Z. J. & Bertozzi, C. R. Programmed assembly of 3-dimensional microtissues with defined cellular connectivity. *Proceedings of the National Academy of Sciences of the United States of America* **106**, 4606-4610, doi:10.1073/pnas.0900717106 (2009).

536 Mironov, V. *et al.* Organ printing: tissue spheroids as building blocks. *Biomaterials* **30**, 2164-2174 (2009).
537 Mironov, V., Kasyanov, V. & Markwald, R. R. Organ printing: from bioprinter to organ biofabrication line. *Current opinion in biotechnology* **22**, 667-673 (2011).
538 Shen, Q. *et al.* Adult SVZ stem cells lie in a vascular niche: A quantitative analysis of niche cell-cell interactions. *Cell Stem Cell* **3**, 289-300, doi:10.1016/j.stem.2008.07.026 (2008).
539 Schlondorff, J. & Blobel, C. P. Metalloprotease-disintegrins: modular proteins capable of promoting cell-cell interactions and triggering signals by protein-ectodomain shedding. *Journal of Cell Science* **112**, 3603-3617 (1999).
540 Gao, W. Q., Heintz, N. & Hatten, M. E. CEREBELLAR GRANULE CELL NEUROGENESIS IS REGULATED BY CELL CELL-INTERACTIONS INVITRO. *Neuron* **6**, 705-715, doi:10.1016/0896-6273(91)90168-y (1991).
541 Lim, D. A. & Alvarez-Buylla, A. Interaction between astrocytes and adult subventricular zone precursors stimulates neurogenesis. *Proceedings of the National Academy of Sciences of the United States of America* **96**, 7526-7531, doi:10.1073/pnas.96.13.7526 (1999).
542 Bullmore, E. T. & Sporns, O. Complex brain networks: graph theoretical analysis of structural and functional systems. *Nat. Rev. Neurosci.* **10**, 186-198, doi:10.1038/nrn2575 (2009).
543 Anderson, M. A. *et al.* Astrocyte scar formation aids central nervous system axon regeneration. *Nature* **532**, 195 (2016).
544 Song, H., Stevens, C. F. & Gage, F. H. Astroglia induce neurogenesis from adult neural stem cells. *Nature* **417**, 39 (2002).
545 Greenhalgh, D. G., Sprugel, K. H., Murray, M. J. & Ross, R. PDGF AND FGF STIMULATE WOUND-HEALING IN THE GENETICALLY DIABETIC MOUSE. *American Journal of Pathology* **136**, 1235-1246 (1990).
546 Falanga, V. Wound healing and its impairment in the diabetic foot. *Lancet* **366**, 1736-1743, doi:10.1016/s0140-6736(05)67700-8 (2005).
547 Jeffcoate, W. J. & Harding, K. G. Diabetic foot ulcers. *Lancet* **361**, 1545-1551, doi:10.1016/s0140-6736(03)13169-8 (2003).
548 Chen, L. W., Tredget, E. E., Wu, P. Y. G. & Wu, Y. J. Paracrine Factors of Mesenchymal Stem Cells Recruit Macrophages and Endothelial Lineage Cells and Enhance Wound Healing. *Plos One* **3**, doi:10.1371/journal.pone.0001886 (2008).
549 Eming, S. A., Martin, P. & Tomic-Canic, M. Wound repair and regeneration: Mechanisms, signaling, and translation. *Science Translational Medicine* **6**, doi:10.1126/scitranslmed.3009337 (2014).
550 Wu, Y. J., Chen, L., Scott, P. G. & Tredget, E. E. Mesenchymal stem cells enhance wound healing through differentiation and angiogenesis. *Stem Cells* **25**, 2648-2659, doi:10.1634/stemcells.2007-0226 (2007).
551 Maxson, S., Lopez, E. A., Yoo, D., Danilkovitch-Miagkova, A. & Leroux, M. A. Concise Review: Role of Mesenchymal Stem Cells in Wound Repair. *Stem Cells Translational Medicine* **1**, 142-149, doi:10.5966/sctm.2011-0018 (2012).
552 Rosi, N. L. & Mirkin, C. A. Nanostructures in biodiagnostics. *Chemical Reviews* **105**, 1547-1562, doi:10.1021/cr030067f (2005).

553 Orita, M., Suzuki, Y., Sekiya, T. & Hayashi, K. RAPID AND SENSITIVE DETECTION OF POINT MUTATIONS AND DNA POLYMORPHISMS USING THE POLYMERASE CHAIN-REACTION. *Genomics* **5**, 874-879, doi:10.1016/0888-7543(89)90129-8 (1989).

554 Vermes, I., Haanen, C., Steffensnakken, H. & Reutelingsperger, C. A NOVEL ASSAY FOR APOPTOSIS - FLOW CYTOMETRIC DETECTION OF PHOSPHATIDYLSERINE EXPRESSION ON EARLY APOPTOTIC CELLS USING FLUORESCEIN-LABELED ANNEXIN-V. *Journal of Immunological Methods* **184**, 39-51, doi:10.1016/0022-1759(95)00072-i (1995).

555 Bustin, S. A. Absolute quantification of mRNA using real-time reverse transcription polymerase chain reaction assays. *Journal of Molecular Endocrinology* **25**, 169-193, doi:10.1677/jme.0.0250169 (2000).

556 Gardes, M. & Bruns, T. D. ITS PRIMERS WITH ENHANCED SPECIFICITY FOR BASIDIOMYCETES - APPLICATION TO THE IDENTIFICATION OF MYCORRHIZAE AND RUSTS. *Molecular Ecology* **2**, 113-118, doi:10.1111/j.1365-294X.1993.tb00005.x (1993).

557 Ho, Y. *et al.* Systematic identification of protein complexes in Saccharomyces cerevisiae by mass spectrometry. *Nature* **415**, 180-183, doi:10.1038/415180a (2002).

558 Lockhart, D. J. *et al.* Expression monitoring by hybridization to high-density oligonucleotide arrays. *Nature Biotechnology* **14**, 1675-1680, doi:10.1038/nbt1296-1675 (1996).

559 Yoneyama, M. *et al.* The RNA helicase RIG-I has an essential function in double-stranded RNA-induced innate antiviral responses. *Nature Immunology* **5**, 730-737, doi:10.1038/ni1087 (2004).

560 Kononen, J. *et al.* Tissue microarrays for high-throughput molecular profiling of tumor specimens. *Nature Medicine* **4**, 844-847, doi:10.1038/nm0798-844 (1998).

561 Lowe, T. M. & Eddy, S. R. tRNAscan-SE: A program for improved detection of transfer RNA genes in genomic sequence. *Nucleic Acids Research* **25**, 955-964, doi:10.1093/nar/25.5.955 (1997).

562 Vos, P. *et al.* AFLP - A NEW TECHNIQUE FOR DNA-FINGERPRINTING. *Nucleic Acids Research* **23**, 4407-4414, doi:10.1093/nar/23.21.4407 (1995).

563 Li, C. & Wong, W. H. Model-based analysis of oligonucleotide arrays: Expression index computation and outlier detection. *Proceedings of the National Academy of Sciences of the United States of America* **98**, 31-36, doi:10.1073/pnas.011404098 (2001).

564 Orita, M., Iwahana, H., Kanazawa, H., Hayashi, K. & Sekiya, T. DETECTION OF POLYMORPHISMS OF HUMAN DNA BY GEL-ELECTROPHORESIS AS SINGLE-STRAND CONFORMATION POLYMORPHISMS. *Proceedings of the National Academy of Sciences of the United States of America* **86**, 2766-2770, doi:10.1073/pnas.86.8.2766 (1989).

565 Chan, W. C. W. & Nie, S. M. Quantum dot bioconjugates for ultrasensitive nonisotopic detection. *Science* **281**, 2016-2018, doi:10.1126/science.281.5385.2016 (1998).

566 von Maltzahn, G. *et al.* SERS-coded gold nanorods as a multifunctional platform for densely multiplexed near-infrared imaging and photothermal heating. *Advanced Materials* **21**, 3175-3180 (2009).
567 Kneipp, K., Kneipp, H., Itzkan, I., Dasari, R. R. & Feld, M. S. Ultrasensitive chemical analysis by Raman spectroscopy. *Chem Rev* **99**, 2957-2976 (1999).
568 Jeanmaire, D. L. & Van Duyne, R. P. Surface Raman spectroelectrochemistry: Part I. Heterocyclic, aromatic, and aliphatic amines adsorbed on the anodized silver electrode. *Journal of electroanalytical chemistry and interfacial electrochemistry* **84**, 1-20 (1977).
569 Albrecht, M. G. & Creighton, J. A. Anomalously intense Raman spectra of pyridine at a silver electrode. *Journal of the american chemical society* **99**, 5215-5217 (1977).
570 Lv, Y., Qin, Y., Svec, F. & Tan, T. Molecularly imprinted plasmonic nanosensor for selective SERS detection of protein biomarkers. *Biosens Bioelectron* **80**, 433-441, doi:10.1016/j.bios.2016.01.092 (2016).
571 Luo, Y. H., Ma, L., Zhang, X. H., Liang, A. H. & Jiang, Z. L. SERS Detection of Dopamine Using Label-Free Acridine Red as Molecular Probe in Reduced Graphene Oxide/Silver Nanotriangle Sol Substrate. *Nanoscale Res Lett* **10**, 230, doi:ARTN 230

10.1186/s11671-015-0937-9 (2015).
572 Wang, P. *et al.* Label-Free SERS Selective Detection of Dopamine and Serotonin Using Graphene-Au Nanopyramid Heterostructure. *Analytical Chemistry* **87**, 10255-10261, doi:10.1021/acs.analchem.5b01560 (2015).
573 Schatz, G. C. & Van Duyne, R. P. Electromagnetic mechanism of surface-enhanced spectroscopy. *Handbook of vibrational spectroscopy* (2002).
574 Zhou, M., Zhai, Y. & Dong, S. Electrochemical sensing and biosensing platform based on chemically reduced graphene oxide. *Anal Chem* **81**, 5603-5613, doi:10.1021/ac900136z (2009).
575 Tang, L. H. *et al.* Preparation, Structure, and Electrochemical Properties of Reduced Graphene Sheet Films. *Advanced Functional Materials* **19**, 2782-2789, doi:10.1002/adfm.200900377 (2009).
576 Alwarappan, S., Erdem, A., Liu, C. & Li, C. Z. Probing the Electrochemical Properties of Graphene Nanosheets for Biosensing Applications. *J Phys Chem C* **113**, 8853-8857, doi:10.1021/jp9010313 (2009).
577 Farokhzad, O. C. & Langer, R. Impact of Nanotechnology on Drug Delivery. *ACS Nano* **3**, 16-20, doi:10.1021/nn900002m (2009).
578 Duncan, T. V. Applications of nanotechnology in food packaging and food safety: Barrier materials, antimicrobials and sensors. *Journal of Colloid and Interface Science* **363**, 1-24, doi:10.1016/j.jcis.2011.07.017 (2011).
579 Maynard, A. D. *et al.* Safe handling of nanotechnology. *Nature* **444**, 267-269, doi:10.1038/444267a (2006).
580 Sarikaya, M., Tamerler, C., Jen, A. K. Y., Schulten, K. & Baneyx, F. Molecular biomimetics: nanotechnology through biology. *Nature Materials* **2**, 577-585, doi:10.1038/nmat964 (2003).
581 Ferrari, M. Cancer nanotechnology: Opportunities and challenges. *Nature Reviews Cancer* **5**, 161-171, doi:10.1038/nrc1566 (2005).

582 Paul, D. R. & Robeson, L. M. Polymer nanotechnology: Nanocomposites. *Polymer* **49**, 3187-3204, doi:10.1016/j.polymer.2008.04.017 (2008).
583 Qu, X. L., Alvarez, P. J. J. & Li, Q. L. Applications of nanotechnology in water and wastewater treatment. *Water Research* **47**, 3931-3946, doi:10.1016/j.watres.2012.09.058 (2013).
584 Zhang, Q. F., Uchaker, E., Candelaria, S. L. & Cao, G. Z. Nanomaterials for energy conversion and storage. *Chemical Society Reviews* **42**, 3127-3171, doi:10.1039/c3cs00009e (2013).
585 Klaine, S. J. *et al.* Nanomaterials in the environment: Behavior, fate, bioavailability, and effects. *Environmental Toxicology and Chemistry* **27**, 1825-1851, doi:10.1897/08-090.1 (2008).
586 Roduner, E. Size matters: why nanomaterials are different. *Chemical Society Reviews* **35**, 583-592, doi:10.1039/b502142c (2006).
587 Burda, C., Chen, X. B., Narayanan, R. & El-Sayed, M. A. Chemistry and properties of nanocrystals of different shapes. *Chemical Reviews* **105**, 1025-1102, doi:10.1021/cr030063a (2005).
588 Kelly, K. L., Coronado, E., Zhao, L. L. & Schatz, G. C. The optical properties of metal nanoparticles: The influence of size, shape, and dielectric environment. *Journal of Physical Chemistry B* **107**, 668-677, doi:10.1021/jp026731y (2003).
589 Bettinger, C. J., Langer, R. & Borenstein, J. T. Engineering Substrate Topography at the Micro- and Nanoscale to Control Cell Function. *Angewandte Chemie-International Edition* **48**, 5406-5415, doi:10.1002/anie.200805179 (2009).
590 Hoffman-Kim, D., Mitchel, J. A. & Bellamkonda, R. V. in *Annual Review of Biomedical Engineering, Vol 12* Vol. 12 *Annual Review of Biomedical Engineering* (eds M. L. Yarmush, J. S. Duncan, & M. L. Gray) 203-231 (2010).
591 Clark, P., Connolly, P., Curtis, A. S. G., Dow, J. A. T. & Wilkinson, C. D. W. CELL GUIDANCE BY ULTRAFINE TOPOGRAPHY INVITRO. *Journal of Cell Science* **99**, 73-77 (1991).
592 Hoch, H. C., Staples, R. C., Whitehead, B., Comeau, J. & Wolf, E. D. SIGNALING FOR GROWTH ORIENTATION AND CELL-DIFFERENTIATION BY SURFACE-TOPOGRAPHY IN UROMYCES. *Science* **235**, 1659-1662, doi:10.1126/science.235.4796.1659 (1987).
593 Zamani, Y., Rabiee, M., Shokrgozar, M. A., Bonakdar, S. & Tahriri, M. Response of Human Mesenchymal Stem Cells to Patterned and Randomly Oriented Poly(Vinyl Alcohol) Nano-fibrous Scaffolds Surface-Modified with Arg-Gly-Asp (RGD) Ligand. *Applied Biochemistry and Biotechnology* **171**, 1513-1524, doi:10.1007/s12010-013-0442-5 (2013).
594 Yang, Y. J. *et al.* Regulation of mesenchymal stem cell functions by micro-nano hybrid patterned surfaces. *Journal of Materials Chemistry B* **6**, 5424-5434, doi:10.1039/c8tb01621f (2018).
595 Wu, Y., Law, J. B. K., Yang, Z., Lee, E. H. & Low, H. Y. Enhanced mesenchymal stem cell chondrogenesis using controlled nano-topography patterned on polycaprolactone scaffolds. *Journal of Tissue Engineering and Regenerative Medicine* **6**, 360-360 (2012).
596 Paul, A. *et al.* Micro- and nano-patterned elastin-like polypeptide hydrogels for stem cell culture. *Soft Matter* **13**, 5665-5675, doi:10.1039/c7sm00487g (2017).

597 Golzhauser, A. *et al.* Chemical nanolithography with electron beams. *Advanced Materials* **13**, 806-+, doi:10.1002/1521-4095(200106)13:11%3c803::aid-adma806%3e3.0.co;2-w (2001).

598 Tseng, A. A., Chen, K., Chen, C. D. & Ma, K. J. Electron beam lithography in nanoscale fabrication: recent development. *Ieee Transactions on Electronics Packaging Manufacturing* **26**, 141-149, doi:10.1109/tepm.2003.817714 (2003).

599 Chou, S. Y., Krauss, P. R., Zhang, W., Guo, L. J. & Zhuang, L. Sub-10 nm imprint lithography and applications. *Journal of Vacuum Science & Technology B* **15**, 2897-2904, doi:10.1116/1.589752 (1997).

600 Geissler, M. & Xia, Y. N. Patterning: Principles and some new developments. *Advanced Materials* **16**, 1249-1269, doi:10.1002/adma.200400835 (2004).

601 Ginger, D. S., Zhang, H. & Mirkin, C. A. The evolution of dip-pen nanolithography. *Angewandte Chemie-International Edition* **43**, 30-45, doi:10.1002/anie.200300608 (2004).

602 Hong, S. H., Zhu, J. & Mirkin, C. A. Multiple ink nanolithography: Toward a multiple-pen nano-plotter. *Science* **286**, 523-525, doi:10.1126/science.286.5439.523 (1999).

603 Lee, K. B., Park, S. J., Mirkin, C. A., Smith, J. C. & Mrksich, M. Protein nanoarrays generated by dip-pen nanolithography. *Science* **295**, 1702-1705, doi:10.1126/science.1067172 (2002).

604 Piner, R. D., Zhu, J., Xu, F., Hong, S. H. & Mirkin, C. A. "Dip-pen" nanolithography. *Science* **283**, 661-663, doi:10.1126/science.283.5402.661 (1999).

605 Chen, W. Q. *et al.* Nanotopography Influences Adhesion, Spreading, and Self-Renewal of Human Embryonic Stem Cells. *ACS Nano* **6**, 4094-4103, doi:10.1021/nn3004923 (2012).

606 Teo, B. K. K. *et al.* Nanotopography Modulates Mechanotransduction of Stem Cells and Induces Differentiation through Focal Adhesion Kinase. *ACS Nano* **7**, 4785-4798, doi:10.1021/nn304966z (2013).

607 Kim, H. N. *et al.* Nanotopography-guided tissue engineering and regenerative medicine. *Advanced Drug Delivery Reviews* **65**, 536-558, doi:10.1016/j.addr.2012.07.014 (2013).

608 Yim, E. K. F., Darling, E. M., Kulangara, K., Guilak, F. & Leong, K. W. Nanotopography-induced changes in focal adhesions, cytoskeletal organization, and mechanical properties of human mesenchymal stem cells. *Biomaterials* **31**, 1299-1306, doi:10.1016/j.biomaterials.2009.10.037 (2010).

609 Yim, E. K. F., Pang, S. W. & Leong, K. W. Synthetic nanostructures inducing differentiation of human mesenchymal stem cells into neuronal lineage. *Experimental Cell Research* **313**, 1820-1829, doi:10.1016/j.yexcr.2007.02.031 (2007).

610 Kim, D. H., Provenzano, P. P., Smith, C. L. & Levchenko, A. Matrix nanotopography as a regulator of cell function. *Journal of Cell Biology* **197**, 351-360, doi:10.1083/jcb.201108062 (2012).

611 Dalby, M. J., Gadegaard, N. & Oreffo, R. O. C. Harnessing nanotopography and integrin-matrix interactions to influence stem cell fate. *Nature Materials* **13**, 558-569, doi:10.1038/nmat3980 (2014).

612 Oh, S. *et al.* Stem cell fate dictated solely by altered nanotube dimension. *Proceedings of the National Academy of Sciences of the United States of America* **106**, 2130-2135, doi:10.1073/pnas.0813200106 (2009).

613 Sill, T. J. & von Recum, H. A. Electro spinning: Applications in drug delivery and tissue engineering. *Biomaterials* **29**, 1989-2006, doi:10.1016/j.biomaterials.2008.01.011 (2008).

614 Li, W. J., Laurencin, C. T., Caterson, E. J., Tuan, R. S. & Ko, F. K. Electrospun nanofibrous structure: A novel scaffold for tissue engineering. *Journal of Biomedical Materials Research* **60**, 613-621, doi:10.1002/jbm.10167 (2002).

615 Shoulders, M. D. & Raines, R. T. Collagen Structure and Stability. *Annual Review of Biochemistry* **78**, 929-958, doi:10.1146/annurev.biochem.77.032207.120833 (2009).

616 Kadler, K. E., Holmes, D. F., Trotter, J. A. & Chapman, J. A. Collagen fibril formation. *Biochemical Journal* **316**, 1-11 (1996).

617 Vanderrest, M. & Garrone, R. COLLAGEN FAMILY OF PROTEINS. *Faseb Journal* **5**, 2814-2823 (1991).

618 Campbell, M., Sharp, D. N., Harrison, M. T., Denning, R. G. & Turberfield, A. J. Fabrication of photonic crystals for the visible spectrum by holographic lithography. *Nature* **404**, 53-56 (2000).

619 Boto, A. N. *et al.* Quantum interferometric optical lithography: Exploiting entanglement to beat the diffraction limit. *Physical Review Letters* **85**, 2733-2736, doi:10.1103/PhysRevLett.85.2733 (2000).

620 Zhang, B. *et al.* Biodegradable scaffold with built-in vasculature for organ-on-a-chip engineering and direct surgical anastomosis. *Nature materials* (2016).

621 Gelain, F. *et al.* Transplantation of Nanostructured Composite Scaffolds Results in the Regeneration of Chronically Injured Spinal Cords. *ACS Nano* **5**, 227-236, doi:10.1021/nn102461w (2011).

622 Panseri, S. *et al.* Electrospun micro- and nanofiber tubes for functional nervous regeneration in sciatic nerve transections. *Bmc Biotechnology* **8**, doi:10.1186/1472-6750-8-39 (2008).

623 Corey, J. M. *et al.* Aligned electrospun nanofibers specify the direction of dorsal root ganglia neurite growth. *Journal of Biomedical Materials Research Part A* **83A**, 636-645, doi:10.1002/jbm.a.31285 (2007).